

THE ELECTRICAL AND OPTICAL PROPERTIES

OF AMORPHOUS FILMS OF Si:Au AND Si:Cu

John Macneil

A thesis submitted to the University of  
Leicester for the degree of Doctor of  
Philosophy

June 1985

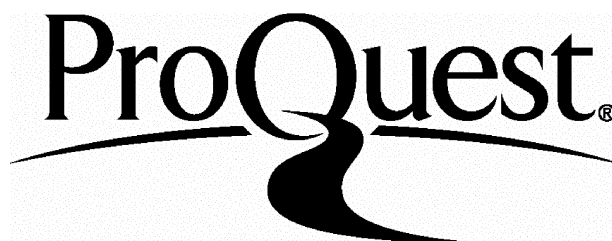
ProQuest Number: U360098

All rights reserved

INFORMATION TO ALL USERS

The quality of this reproduction is dependent upon the quality of the copy submitted.

In the unlikely event that the author did not send a complete manuscript and there are missing pages, these will be noted. Also, if material had to be removed, a note will indicate the deletion.



ProQuest U360098

Published by ProQuest LLC(2015). Copyright of the Dissertation is held by the Author.

All rights reserved.

This work is protected against unauthorized copying under Title 17, United States Code.  
Microform Edition © ProQuest LLC.

ProQuest LLC  
789 East Eisenhower Parkway  
P.O. Box 1346  
Ann Arbor, MI 48106-1346



**To my parents**

## CONTENTS

Acknowledgements

Abstract

	Page
<u>Chapter 1, Introduction to Amorphous Semiconductors</u>	1
1.1 Introduction	2
1.2 Structure of Amorphous Solids	3
1.2.1 Preparation methods	4
1.2.2 Determination of structure	6
1.2.3 Stability	9
1.3 The effect of disorder on electronic states	11
1.3.1 D.C. Conduction Mechanisms	14
1.3.2 Thermoelectric Power	19
1.3.3 The Metal-Insulator Transition	22
1.4 Optical Properties	25
1.4.1 Vibrational Spectra	25
1.4.2 Absorption Edge	27
<u>Chapter 2, Review of Current Work</u>	30
2.1 Sputtered a-Si:H - a brief review	31
2.2 Amorphous Si-Au	34
2.2.1 Introduction	34
2.2.2 Structure and Stability	35
2.2.3 Electronic and Optical Properties	38
2.2.4 Other Properties	47
2.3 Amorphous Si - M - A brief review	49

	Page
<u>Chapter 3, Experimental Methods</u>	54
3.1 Film Preparation	55
3.1.1 Sputtering Process	55
3.1.2 Sputtering System	56
3.1.3 Preparation Conditions	59
3.2 Electronic Transport Measurement	61
3.2.1 D.C. "dark" Conductivity	61
3.2.2 Thermoelectric Power	63
3.3 Optical Measurements	64
3.3.1 Visible-Ultraviolet	64
3.3.2 Infrared	65
3.4 Electron Microscopy	65
3.5 Other Measurements	67
<u>Chapter 4, Experimental Results</u>	68
4.1 a-Si:H	69
4.2 a-Si:Cu:H and Si:Cu Alloys	73
4.2.1 D.C. Conductivity	73
4.2.2 Optical Absorption	78
4.2.3 Structural Measurements	80
4.2.4 Discussion	82
4.3 a-Si:Au:H Alloys	85
4.3.1 D.C. Conductivity and Thermopower	85
4.3.2 Optical Absorption	92
4.3.3 Structural Measurements	95
4.3.4 Discussion	100

	Page
<u>Chapter 5. Photoemission</u>	107
5.1 Introduction	108
5.2 Experimental	112
5.3 Results and Discussion	113
<u>Chapter 6. Conclusions and suggestions for further work</u>	119
6.1 Conclusions	120
6.2 Suggestions for further work	122
References	124
Appendix	133

## ACKNOWLEDGEMENTS

I would like to thank my supervisor, Prof. E. A. Davis, for supervision throughout the course of this work.

I would also like to thank the SERC for the provision of a studentship.

I have been greatly assisted by the expert technical support of Mr. J. S. G. Taylor and the staff of both the Mechanical and Electronic Workshops within the Department.

During the early stages of this project discussions with Drs. R. J. Newport and K. Shimakawa were especially rewarding.

Assistance from Mr. R. Assumpcao in the TEM measurements made on the Si:Cu alloys is acknowledged.

I have benefitted from discussions with all members of the CMP Group, most notably Dr. C. Norris, Dr. R. A. Howe and Dr. C. Binns.

Some of the diagrams in this work result from the skills of Mrs. R. Littler and Mr. J. Kerruish to whom thanks are due. Finally I would like to thank Mrs. S. M. Sherlock for her careful and neat typing of this thesis.

## ABSTRACT

Amorphous films of a-Si: Au and a-Si: Cu have been prepared by radio-frequency sputtering in an argon/hydrogen plasma and their properties studied by various techniques. The object of the investigation was to study the behaviour of deep impurity states in a-Si: H and to explore the nature of the metal-insulator transition which occurs in these alloys for sufficiently high concentrations of incorporated metal atoms.

A transmission electron microscope investigation of the  $a\text{-Si}_{1-x}\text{Au}_x$  alloys confirmed that the films were amorphous in a composition range up to and beyond the metal-insulator transition, which occurs at  $x = 0.14$ . For low concentration of Au, the electrical conductivity rises with increasing  $x$  and the temperature dependence shows activated behaviour. Beyond  $x \sim 0.05$ ,  $T^{-1}$  behaviour, indicative of hopping conduction, is observed. The metal-insulator transition appears to be continuous and values of the conductivity less than the "minimum metallic conductivity" are observed at helium temperatures. Optical absorption measurements show that an optical gap remains when  $x \gtrsim 0.14$  and it is concluded that the transition to the metallic state occurs in Au-related impurity levels. Photoemission studies suggest that these levels lie at the top of the host Si valence band.

The  $a\text{-Si}_{1-x}\text{Cu}_x$  alloys also display an increase in electrical conductivity with increasing  $x$  but evidence from electrical and optical measurements, suggests that in this alloy the impurity states lie near the centre of the gap. For  $x$  greater than a few percent the films exhibit phase separation and crystallization.

## CHAPTER 1

### Introduction to Amorphous Semiconductors

- 1.1 Introduction
  
- 1.2 Structure of Amorphous Solids
  - 1.2.1 Preparation methods
  - 1.2.2 Determination of Structure
  - 1.2.3 Stability
  
- 1.3 The effect of disorder on electronic states
  - 1.3.1 D.C. conduction mechanisms
  - 1.3.2 Thermoelectric power
  - 1.3.3 The Metal-Insulator Transition
  
- 1.4 Optical Properties
  - 1.4.1 Vibrational Spectra
  - 1.4.2 Absorption Edge

## CHAPTER 1

### 1.1 Introduction

Solid state physics has, until quite recently, been devoted to the study of crystals. Most theoretical treatments of crystalline solids are based on the knowledge that a crystal is a three-dimensional periodic array of atoms. The existence of Long Range Order (LRO) in the crystalline lattice greatly simplifies the problem of, say, the electronic states and transport, enabling concepts such as Bloch waves and Brillouin Zones to be applied. In an amorphous (or non-crystalline) solid LRO no longer exists and many of the concepts developed to understand crystalline solids no longer apply. It is the Short Range Order (SRO), which is still present due to chemical bonding, that dominates the properties of these materials.

Ordinary "window" glass, probably the best known non-crystalline material, has been known to exist for many thousands of years, although it was not until the 1960's that its transparency was explained. The term "glass" or "vitreous" is usually applied to an amorphous material which has been rapidly cooled from its liquid phase. Indeed the disordered state of the liquid is frozen into the glass. Non-crystalline materials are therefore thermodynamically metastable and tend to relax to the energetically more favourable crystalline state given sufficient time or energy.

It has not solely been for academic interest that the field of non-crystalline materials has developed so rapidly in the last decade. With the realization that amorphous materials can have widespread

technological applications, industry has been deeply involved also. In fact it is probably the technological usefulness of some amorphous materials that has governed much work on non-crystalline solids. The discovery of two switching effects in multicomponent chalcogenide glasses by Ovshinsky [ 1 ] generated a great deal of interest in chalcogenide glasses. Though perhaps the greatest experimental stimulus to the study of amorphous materials was the announcement by Spear and LeComber in 1975 that [ 2 ] amorphous silicon, prepared by the glow-discharge decomposition of silane ( $\text{SiH}_4$ ), could be successfully doped by the incorporation of small amounts of diborane ( $\text{B}_2\text{H}_6$ ) or phosphene ( $\text{PH}_3$ ) into the discharge. This discovery opened up the possibility of fabricating cheap large area electronic devices which would otherwise have been prohibitively expensive. This bond between fundamental research and industry is one of the features of non-crystalline materials which is bound to continue in years to come.

## 1.2 Structure

The physical properties of many non-crystalline materials are strongly dependent on the method of preparation. This is found to be true not only for the tetrahedral semiconductors such as a-Si, a-Ge and a-C (where the incorporation of H into the lattice in various configurations complicates the matter), but also for the chalcogenide alloys prepared from the melt or by thermal evaporation [ 3 ]. Major difficulties exist in experimentally preparing some amorphous materials by different techniques to exhibit the same electronic and optical properties. This may be due to various factors eg the incorporation of an additive intentionally or unintentionally into

the material or the growth processes may differ sufficiently to affect the bulk structure of the material [4] which may be evident in gross features such as columnar growth/voids etc as reported by Knights. A particularly striking example of the sensitivity of a material's properties with respect to the deposition process can be seen in the preparation of a-C:H films by the glow-discharge decomposition of CH<sub>4</sub> [5]. Here by varying the deposition temperature between T<sub>RM</sub> and 300°C, the graphite or diamond-like forms of carbon, or a mixture of both are obtained.

Significant difficulties occur when any attempt at direct structural determination is carried out. Unlike the crystalline case where long-range periodicity enables investigation by a number of techniques such as X-ray diffraction or X-ray topography, for amorphous materials where LRO is absent, by definition, and which are essentially isotropic, the results of the above techniques are either averaged out in the diffraction experiment or rendered useless in the case of X-ray topography.

### 1.2.1 Preparation

Amorphous materials may be prepared by a great number of methods. A brief description of some of the most widely used techniques is presented in this section.

#### (i) Glass Formation by cooling a liquid [ 6 ]

The formation of a glass by quenching from a melt requires the prevention of the nucleation and growth processes responsible for crystallization. Hence, in principle, if sufficiently rapid cooling rates can be achieved, any liquid should be capable of forming

a glass. In practice however quench rates as great as  $10^7$  °C/sec., which are achieved in "splat quenching" are not sufficient to inhibit crystallization in the elementary semiconductors Si and Ge. (Table I - contains data on quench rates etc.).

In the formation of a glass, if the rate of decrease of temperature is sufficient to prevent crystallization, first-order thermodynamic quantities such as volume  $V$ , entropy  $S$  and enthalpy  $H$  change continuously. Only a change in slope of these quantities is observed as the transition from a liquid to a solid occurs. (Fig. 1.1) The temperature at which this occurs is called the glass transition temperature  $T_g$ . This quantity is not particularly well defined and is dependent on the cooling rates and the thermal history of the sample. Second-order thermodynamic quantities such as expansion coefficient and specific heat  $C_p$  do however change discontinuously (Fig. 1.1, insert). Hence the glass transformation is sometimes seen as a second-order transition [7] although this is probably at best an oversimplification of the situation.

(ii) Thermal evaporation

This is one of the most frequently employed methods of fabrication of amorphous thin films. A source material is evaporated by electron-beam bombardment or by resistance heating in a high-vacuum chamber  $p < 10^{-6}$   $\tau$ . The subsequent vapour is condensed onto a substrate held at a fixed temperature. This technique has a number of drawbacks that restrict its use to certain materials. Multi-component alloys are difficult to produce as evaporation rates of individual components differ dramatically, though the use

TABLE 1.1

Experimental cooling rates	
Technique	Rate ( $K s^{-1}$ )
Annealing: Large telescope mirrors	$10^{-5}$
Optical glasses	$\sim 3 \times 10^{-4}$
Ordinary glasses	$10^{-3} - 10^{-2}$
Air quenching ( $10^1$ 's of gms)	1-10
Small drops (1-100mgms) into 1-Hg	$10^2 - 10^3$
Strip furnace (mgm batches)	$10^3 - 10^4$
Splat cooling	$10^5 - 10^7$
LMQ	$\sim 10^{10}$

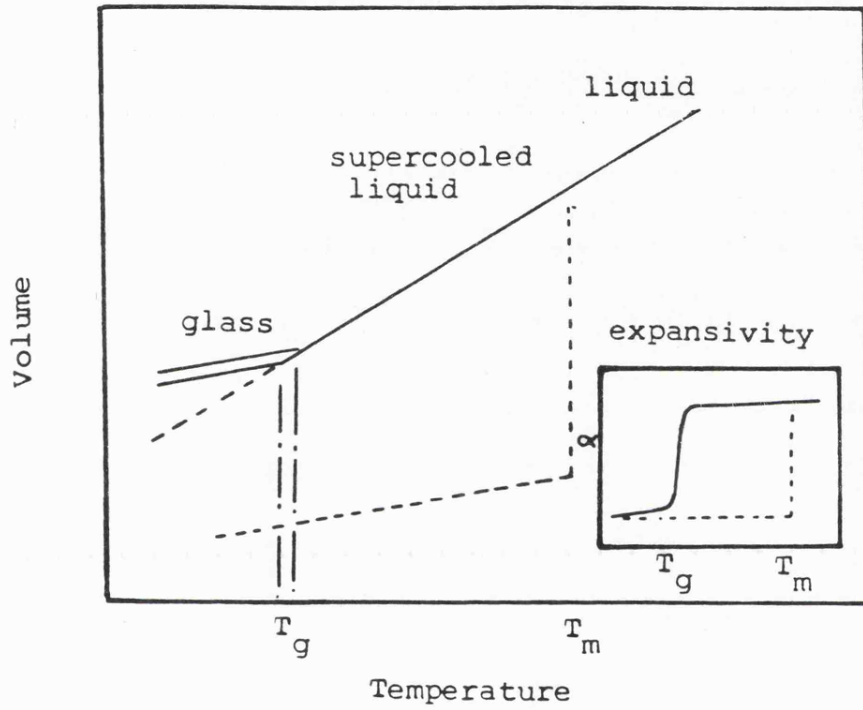


Fig 1.1 Schematic variation of volume vs temperature for a glass forming material.

of several crucibles or flash evaporation can sometimes circumvent this problem. Perhaps more limiting is the inability to incorporate reactive gases such as hydrogen directly into evaporated thin films.

(iii) Glow-discharge decomposition

If the energy from a radio frequency generator is coupled inductively or capacitively to a gas at a sufficiently low pressure, usually  $p \sim 0.1 \text{ Torr}$ , a glow discharge can be achieved. Through the decomposition of silane gas  $\text{SiH}_4$  by the above process, high-quality samples of  $\alpha\text{-Si:H}$  have been prepared by Spear and LeComber [ 2 ] by careful control of deposition conditions.

(iv) Sputtering

As this process was employed to prepare samples for this study it will be described in detail in Chapter 3, where experimental techniques are reported.

### 1.2.2 Structural determination

Although long-range order is absent in non-crystalline materials some degree of local order must exist because of geometric constraints imposed by the packing together of atoms or any steric constraints imposed by the binding forces between atoms. Direct measurement of the structure that exists in amorphous materials can best be experimentally examined by either diffraction techniques (X-ray, electron or neutron) or by Extended X-ray Absorption Fine Structure (EXAFS).

The broad haloes or rings, vanishing rapidly with increasing angle of diffraction, which are the result of a diffraction experiment are a standard characteristic of an amorphous material. The precise

conditions under which the Bragg condition is satisfied in the crystalline case no longer hold. Structural information from a diffracting experiment is usually expressed in terms of the Radial Distribution Function (RDF)  $G(r)$ .

$$G(r) = \frac{2}{\pi} \int (i(k) - 1) kr \sin(kr) dr + 4\pi r^2 \rho_0 \quad (1.1)$$

where  $i(k)$  is the interference function,  $k = 4\pi \sin \theta/\lambda$  and  $\rho_0$  is the average atomic density:  $G(r)$  indicates the average atomic density at a given distance from an arbitrary atom. The radial distribution function is therefore achieved by applying a Fourier Transform to the interference function - a product of atomic scattering factor  $f(k)$  and the angular distribution of the scattered intensity  $I(k)$ .

A wealth of information can be obtained from the RDF, the position of peaks indicating the average separation of nearest neighbours, second-nearest neighbours and so on from an arbitrarily chosen atom. The width of peaks, after correction for thermal broadening, describes the radial fluctuations in the corresponding interatomic distances and the integrated area below each peak equals the number of atoms contained in the respective coordination shell. (See Fig. 1.2).

A number of problems make the determination of an accurate RDF a non-trivial matter, strongly dependent on the details of the experiment. The separation of elastic and inelastic scattering, correction for multiple scattering and the limited nature of the range of  $k$  for the Fourier transform, necessitates careful reduction of the data. Further complications arise when the material to be investigated is a binary alloy for which three partial interference functions are required to describe the atomic arrangement.

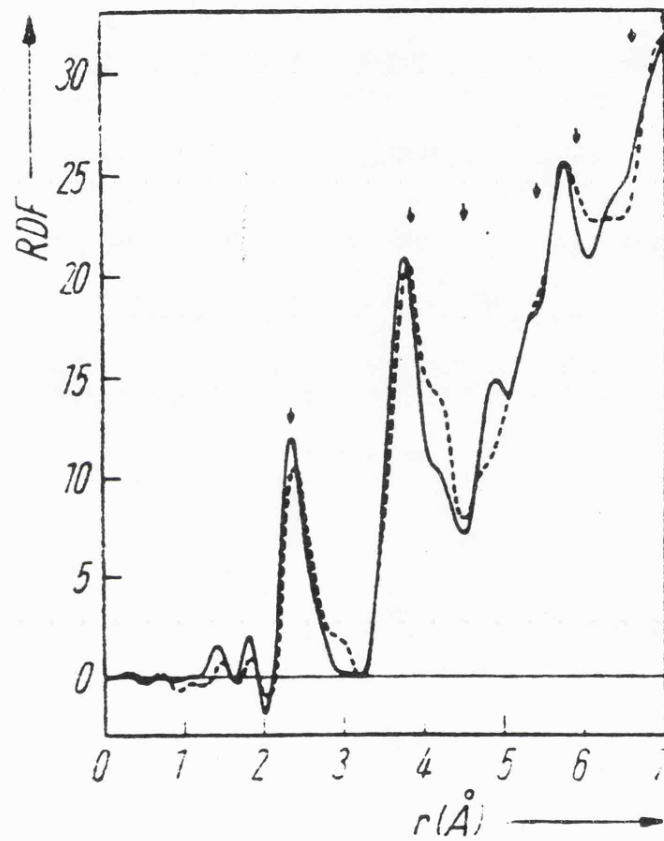


Fig 1.2 RDF of a-Si; glow discharge(—), evaporated(--).Arrows mark crystalline positions. (8) .

EXAFS provides another method of determining the RDF of a material by the measurement of the energy dependence of the absorption coefficient beyond an X-ray absorption edge. Although the analysis of the data is not as straightforward as that of a diffraction experiment this technique has the advantage that it can be successfully applied to alloys as each atom has its own absorption edge and associated fine structure. [ 9 ], [ 10 ]. EXAFS arises from the ejection of photoelectrons from a deep state which are scattered by surrounding atoms and interfere with the outgoing wave. This introduces variations in the X-ray absorption coefficient, which can be Fourier transformed as in Fig. 1.3.

Further techniques such as Raman and infrared spectroscopy offer less direct measurement of atomic bonding by evaluating various vibrational modes which are governed by atomic mass, force constants and local atomic environment.

Another approach to the study of amorphous structure has been through model building, constructed by hand or with the aid of a computer. By comparing the RDF and the density of the model with the experimentally determined values of an amorphous solid the suitability of the model may be decided. The RDF however does not uniquely specify a structural representation and it is generally found that a number of models fit the experimental RDF.

The types of models proposed broadly fall into two categories;

(a) Microcrystallite Models

In the models the non-crystalline solid is considered to consist of

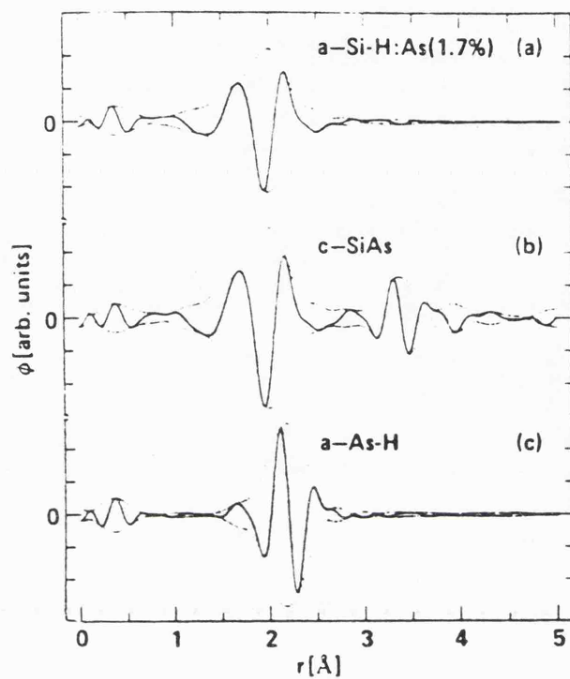


Fig 1.3 The real part(—) and the magnitude of the Fourier transform  $\phi(r)$  of the EXAFS on the As K-shell absorption in (a) 1.7 % As in a-Si:H;(b) c-SiAs, and (c) a-As:H. (10).

crystallites of one of the real or potential polymorphs of the same element or compound. Ordered domains are connected together so as to maintain both incoherent diffraction between themselves and to minimise the number of broken bonds. The main problem with this approach is that, for the size of domain indicated by diffraction experiments [11], about half the atoms would have to reside on the surface of the crystallites. Unless there is some mechanism to satisfy these bonds the increase in energy would be intolerably high and it is normally considered that an amorphous tissue connects the crystallites.

(b) Continuous Random Network (CRN) Models

In the CRN, the amorphous material is considered to consist of a continuous, non-periodic, connecting network in which atoms are linked together by the same types of chemical bonds as in the corresponding crystal. Hence the corresponding CRN for a solid which is metallic, where there is essentially non-directional bonding, and a covalent solid, where the bonding is strongly directional, are different. The random close-packing of spheres is appropriate for the former and the approximate preservation of nearest-neighbour bond lengths and angles of the crystal occurs in the latter. The covalently bonded structures should show a greater degree of short-range order than the Bernal type [12] of structures associated with metals. CRN models have proved to be most successful with the three- and four-fold coordinated elemental materials (As, Si, Ge, etc.) and for  $\text{SiO}_2$ . [13], [14].

1.2.3 Stability

The topics discussed in this section have been concerned with

the preparation methods required to produce non-crystalline materials and the subsequent structural examination of these materials. An interesting question arises - why do certain materials, with certain kinds of local atomic arrangements, form non-crystalline structures when prepared by a specific technique, while others prepared in a similar manner result in crystalline structures? This problem has been tackled by Phillips [15], [16], using a topological approach. The glass-forming tendency of any material can be optimized by matching the number of degrees of freedom per atom,  $N_d$ , and the number of constraints  $N_{CON}$ . ie

$$N_{CON} = N_d \quad (1.2)$$

For a three-dimensional solid, if  $\Delta S$  ( $S$  amorph -  $S$  crystal) = 0, then  $N_d = 3$ . The number of constraints  $N_{CON}$  is related to the average coordination number  $m$ , for a binary alloy  $A_x B_{1-x}$ , in the following manner

$$m = xz(A) + (1-x)z(B) \quad (1.3)$$

where  $z(A)$  and  $z(B)$  are the usual coordination numbers for the elements A and B. The number of constraints,  $N_{CON}$ , per atom as a function of the average coordination number  $m$  is then

$$N_{CON}(m) = \frac{m}{2} + \frac{m(m-1)}{2} = \frac{m^2}{2} \quad (1.4)$$

where the first term is due to bond-stretching interactions and the second is due to bond-bonding interactions. Thus if the glass-forming condition (1.2) is satisfied the average coordination number  $m = m_c = 2.45$ . Materials with  $m > m_c$ , the tetrahedral semiconductors Si and Ge for example, will have highly strained lattices and as a result can only be

prepared by deposition from the vapour phase. The incorporation of hydrogen into these structures will reduce  $m$  and hence enhance the glass-forming abilities of the materials. This can be seen as the hydrogen produces a more flexible CRN structure and hence reduces internal strain. Alternatively for materials with an average coordination number  $m < m_c$ , Se for example, will have a high degree of entropy and will tend to dissociate into molecular fragments (eg  $Se_8$  rings). When  $m = m_c$  glass formation will occur readily and any of the techniques discussed in 1.2.1 will produce a non-crystalline solid.

### 1.3 The effect of disorder on electronic states

As disorder is gradually introduced into the lattice of a crystalline semiconductor, by neutron bombardment for example, the Bloch wavefunctions that initially extend throughout the infinite lattice are scattered by defects which limit the lifetime of the electrons. At this stage the mean free path ( $L$ ) is much greater than the average interatomic spacing  $a$  ( $L \gg a$ ) See Fig. 1.4(a). Further disorder will eventually reduce  $L$  until  $L \sim a$ : the phase coherence of the wavefunction is lost in a few scattering events though the wavefunction is still extended throughout the structure without attenuation (See Fig. 1.4(b)). The fact that phenomena frequently occur in disordered semiconductors in which electrons have energies for which  $kL \sim 1$  ( $k$  = wavevector) illustrates one of the most important differences between the theories of crystalline and non-crystalline materials. Under such conditions the  $\underline{k}$  selection rule breaks down, as can be witnessed in the smearing out of detail in the optical density of states (Fig. 1.5). Values of  $L < a$  cannot

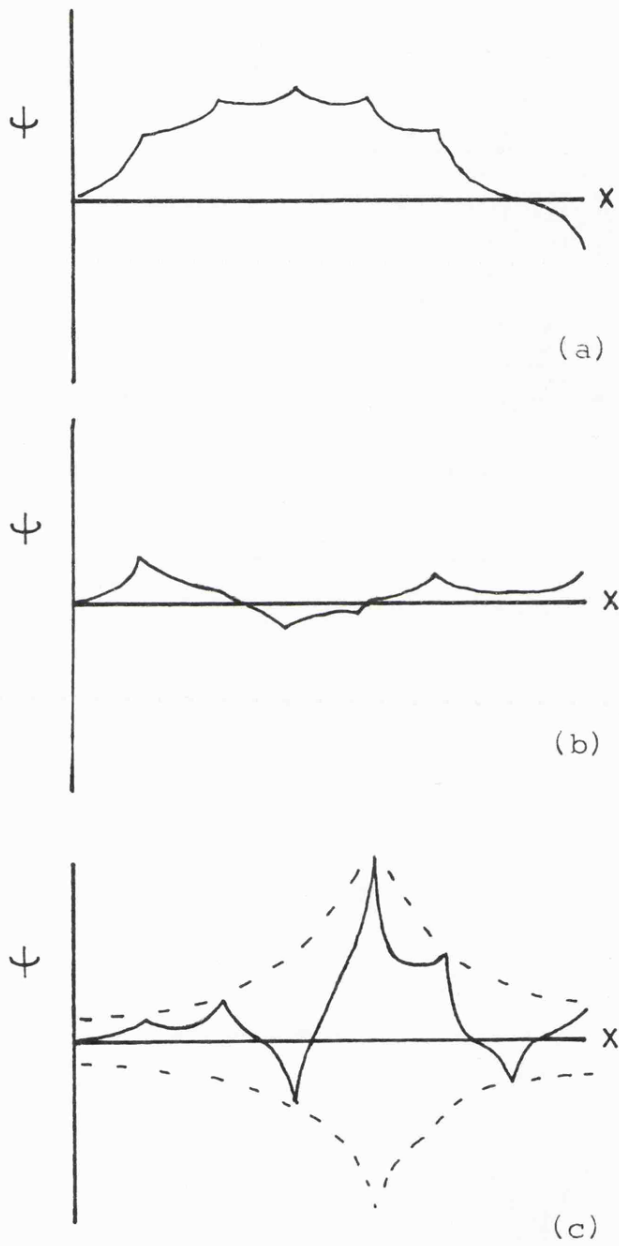


Fig 1.4 Form of the wavefunction when  
 (a)  $L \gg a$  ; (b)  $L \sim a$  ; (c)  $L \sim a$  ;  
 wavefunction localized

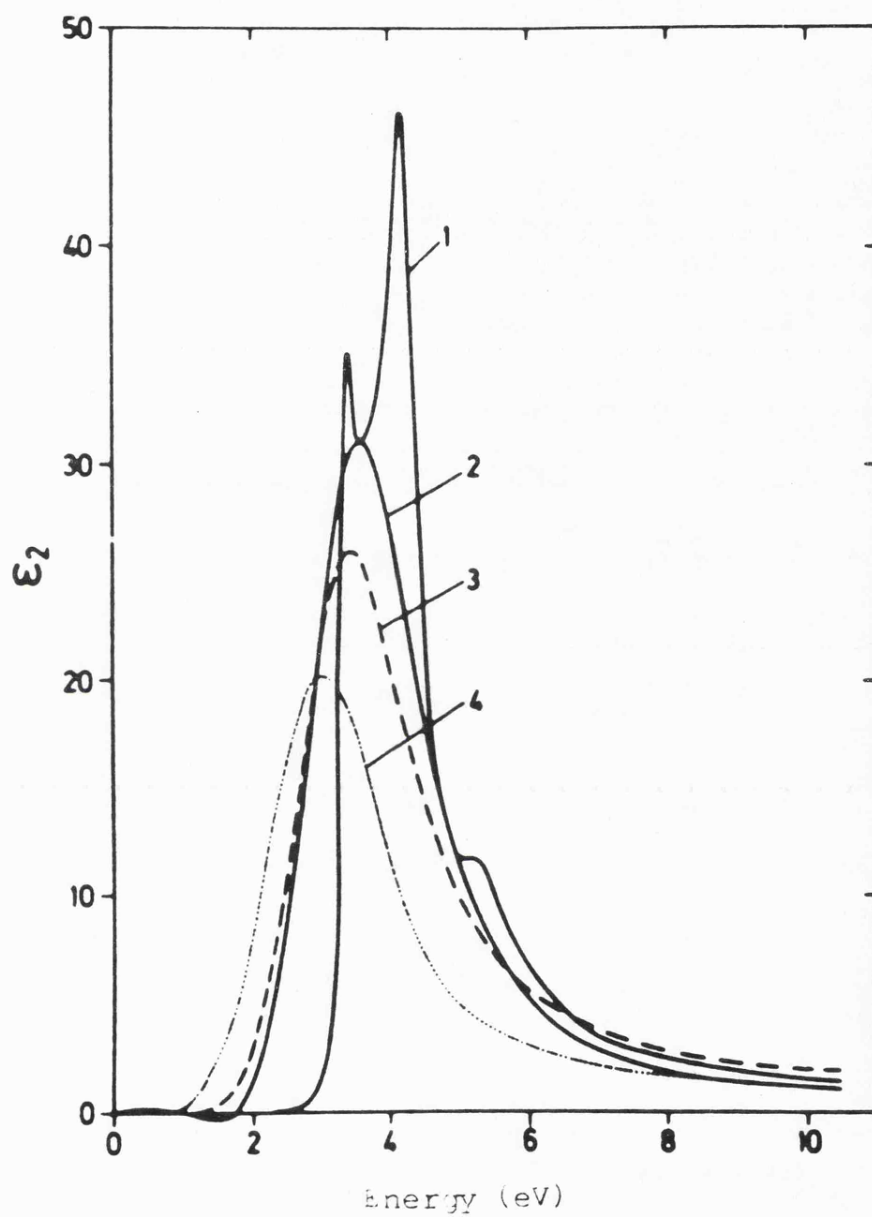
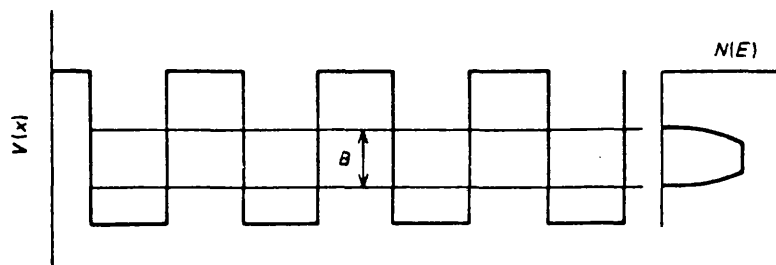


Fig 1.5 Spectrum of the imaginary part of the dielectric constant  $\epsilon_2$ , for (1) c-Si (2) g.d a-Si:H,  $T_d=400^\circ\text{C}$ , (3) CVD a-Si and (4) evaporated a-Si. (17).

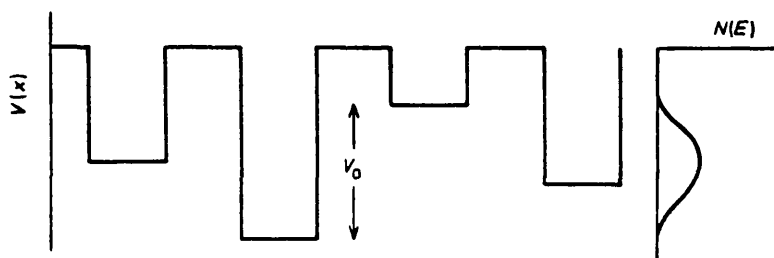
exist, as pointed out by Ioffe and Regal [ 18 ], though further disorder may be introduced into the lattice, the final result of which is the localization of the wavefunction (see Fig. 1.4(c)). The existence of a continuous density of localized states, where at zero temperature the mobility vanishes even though the wavefunctions of localized states overlap, is one of the important new concepts for amorphous materials.

Anderson [19] in 1958 was the first to obtain a quantitative description of localization for a carrier moving in the three-dimensional potential energy indicated in Fig. 1.6, where  $V_0$  is the range of disorder and  $B$  is the width of the band when  $V_0 = 0$  (and when no positional disorder exists), all states within the band would be localized for  $V_0/B \gtrsim 5$ . Later work by a number of authors, Edwards [20] and Mott and Davis [7] for example, consider the value to be close to 2. Gubanov [21] suggested that localized states occur near the edges of valence and conduction bands. Mott [22] pointed out that if  $V_0/B$  was less than the critical value for localization of a band, states in the tails of the band could still be localized below a sharp value  $E_c$ . Owing to the vast change in mobility for carriers on either side of  $E_c$ , separating extended from localized states, Cohen, Fritzsche and Ovshinsky [23] designated the energy  $E_c$  as the "mobility edge".

In certain non-crystalline materials where  $N(E_f) \neq 0$ , if the Fermi level can be moved from its position within the gap through a mobility edge by application of stress, a magnetic field or change of composition, a transition from hopping to metallic conduction occurs.



(a)



(b)

Fig 1.6 Potential energy of an electron in a lattice with diagonal disorder. (a) with  $V_0=0$  ; (b) with finite value of  $V_0$ .

The accompanying change in conductivity at  $T = 0$  will be a dramatic increase at  $E_c$

$$\begin{aligned} E < E_c & \quad \langle \sigma(E) \rangle = 0 \\ E > E_c & \quad \langle \sigma(E) \rangle \neq 0 \end{aligned}$$

where  $\langle \rangle$  is a configurational average. This is known as an Anderson transition. The nature of this transition, whether it is continuous or not, is still a question of much debate and will be described in more detail later 1.3.3. If it occurs as a discontinuity, a minimum value of conductivity 'The Minimum Metallic Conductivity',  $\sigma_{\min}$ , defined by Mott [24] must occur at  $E_c$ , below which the conductivity will fall abruptly to zero when  $T = 0$

Various models for the density of states of an amorphous semiconductor have been suggested based on the concepts described previously and on experimentally observed phenomena. Cohen, Fritzsche and Ovshinsky [23] in 1969 proposed a model, which was originally suggested for multicomponent chalcogenide glasses (eg STAG glasses), where the band tails extended through the mobility gap in a featureless distribution. Overlap of these states occurs near the centre of the gap and the experimentally observed pinning of the Fermi level can be explained with the aid of this model. (See Fig. 1.7(a)) Whether or not this type of model is perhaps suitable for a multicomponent system, a more readily accepted description of elemental and compound amorphous semiconductors has been proposed by Davis and Mott [25]. (See Fig. 1.7(b)) In this case discrete states within the mobility gap are associated with specific defects and pin the Fermi level. The defects may, for example, be 'dangling bonds' within the CRN structure. This model, although simplistic, provides a suitable starting point to describe

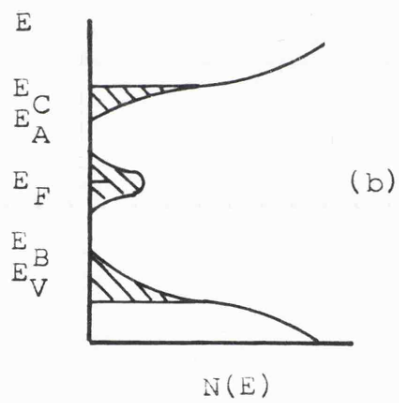
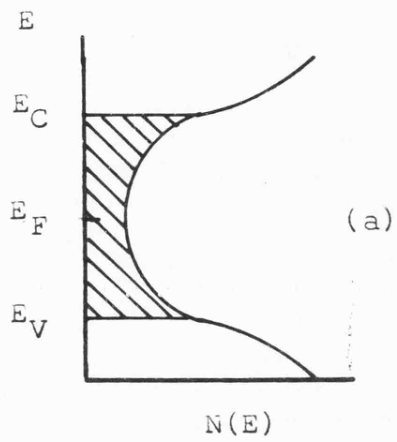


Fig 1.7 Schematic density of states diagrams for amorphous semiconductors - (a) CFO model, (b) Davis-Mott model

some of the fundamental properties for non-crystalline semiconductors.

### 1.3.1 D.C. conduction mechanisms

If one starts from the assumption of a band model of Davis and Mott type (Fig. 1.7(b)), it is evident that three basically different channels of conduction may exist: extended-state conduction above the mobility edge, conduction in the localized band-tail states and thermally-assisted tunnelling between localized states at the Fermi level. The relative contribution of each of the above processes to the total conductivity is strongly dependent on temperature and the following treatment of the d.c. conduction mechanisms pays particular emphasis to the temperature dependence of the conductivity. Unless otherwise stated the majority carriers are electrons, though extension of the treatment to holes is straightforward.

#### (i) Extended State Conduction

The total conductivity for any semiconductor in which the current is carried by excited electrons rather than being determined by those at the Fermi level, can be expressed in terms of the density of states  $N(E)$ , the mobility  $\mu(E)$  and the occupancy of the states  $f(E)$  as

$$\sigma = -e \int N(E) \mu(E) kT \frac{\partial f(E)}{\partial E} dE \quad (1.5)$$

where  $f(E)$  is the Fermi Dirac distribution function

$$f(E) = \frac{1}{1 + \exp \left[ \frac{(E - E_F)}{kT} \right]} \quad (1.6)$$

and  $k$  = the Boltzmann constant.

When the states involved in the conductivity are far above the Fermi level,  $E - E_F \gg kT$ , as in extended-state conduction, the Fermi

Dirac function approximates to

$$f(E) \approx \exp \left[ -(E - E_F)/kT \right] \quad (1.7)$$

The conductivity due to carriers excited beyond  $E_c$ , assuming constant  $N(E)$  and  $\mu(E)$ , after substitution of equation (1.7) into (1.5), is given by

$$\sigma_1 = eN(E_c)kT\mu_c \exp \left[ -(E_c - E_F)/kT \right] \quad (1.8)$$

where  $\sigma_1$  is the extended state conductivity and  $\mu_c$  is the average mobility. The above expression (1.8) does not describe the temperature dependence of  $(E_c - E_F)$ . Optical measurements (to be discussed in detail in 1.4) indicate that the band gap decreases with increasing temperature. A similar linear temperature dependence is assumed for  $(E_c - E_F)$ , ie

$$E_c - E_F = (E_c - E_F)_0 - \gamma T \quad (1.9)$$

so that

$$\sigma_1 = C_0 \exp \frac{\gamma}{k} \exp \left[ -(E_c - E_F)_0/kT \right] \quad (1.10)$$

where  $\gamma$  is the temperature coefficient of  $(E_c - E_F)$  and  $(E_c - E_F)_0$  is the extrapolated energy separation at  $T = 0$

A plot of  $\ln \sigma$  against  $1/T$  of (1.10) will yield a straight line with slope  $(E_c - E_F)_0$  and a  $\sigma(T = 0)$  intercept of  $C_0 \exp (\gamma/k)$ .

Experimental values of  $\sigma_{10}$  are  $10^3 - 10^5 (\Omega \text{ cm})^{-1}$  where

$$\sigma_{10} = C_0 \exp \left( \frac{\gamma}{k} \right) \quad (1.11)$$

for most materials though, without a precise determination of  $\gamma$ , it is difficult to evaluate  $C_0$  accurately.

(ii) Conduction in Localized Tail States

With the wavefunction of the electron localized in the tail states, conduction can only occur if carriers are thermally excited into new localized states. Mobility in this regime may be described by an activated process such as

$$\mu_2 = \mu_0 \exp(-W/kT) \quad (1.12)$$

with the pre-exponential

$$\mu_0 = \frac{1}{6} \frac{eR^2}{kT} v_{ph} \quad (1.13)$$

where  $R$  is the hopping distance,  $v_{ph}$  the phonon frequency and  $W$  the thermal activation energy. Typical values of  $v_{ph} \approx 10^{13} \text{ s}^{-1}$  and  $W \approx kT$  suggest that the mobility in this regime is  $\mu_2 \approx 10^{-2} \text{ cm}^2 \text{ v}^{-1} \text{ s}^{-1}$  ie several orders of magnitude down on the mobility found above  $E_c$  in extended states [ $\mu_1 \approx 10 \text{ cm}^2 \text{ v}^{-1} \text{ s}^{-1}$ ].

To evaluate the conductivity, since it is an integral over all available energy states, some knowledge of the energy distribution of the density of states  $N(E)$  in the band tail is necessary. Following Nagels [26] the distribution can be approximated to a density of states of the form

$$N(E) = \frac{N(E_c)}{\Delta E^s} (E - E_A)^s \quad (1.14)$$

where  $\Delta E = E_c - E_A$ , the conductivity within the tailstates,  $\sigma_2$ , can be derived from (1.5) as

$$\sigma_2 = \sigma_{20} \left( \frac{kT}{\Delta E} \right)^s A \exp[-(E_A - E_F + W)/kT] \quad (1.15)$$

with

$$\sigma_{20} = \frac{1}{6} e^2 R^2 N(E_c) v_{ph} \quad (1.16)$$

and

$$A = s! - \left[ \frac{\Delta E}{kT} \right]^s \exp \left[ -\frac{\Delta E}{kT} \right] \left[ 1 + s \frac{kT}{\Delta E} + s(s-1) \frac{kT^2}{\Delta E^2} + \dots \right] \quad (1.17)$$

Hence for a linear variation of  $N(E)$  in the band tail ( $s = 1$ )

$$\sigma_2 = \sigma_{20} \frac{kT}{\Delta E} A_1 \exp \left[ -[E_A - E_F + W]/kT \right] \quad (1.18)$$

with

$$A_1 = 1 - \exp \left[ \frac{-\Delta E}{kT} \right] \left[ 1 + (\Delta E/kT) \right] \quad (1.19)$$

Ultimately similar expressions for  $\sigma_2$  are achieved if one follows the treatments of Grant and Davis [27] or Butcher [28].

A plot of  $\ln \sigma$  against  $1/T$  should yield a straight line with slope  $[E_A - E_F + W]_0$ , following the same arguments for the temperature variation of the band gap as in (i), and a  $\sigma(T = 0)$  intercept of the pre-exponential in equation (1.18) with an  $\exp(\gamma/k)$  factor. The value of the pre-exponential factor,  $\sigma_{20}$ , is expected to be  $\sim 10^2 - 10^3$  times lower than  $C_1$  in extended states. This is not only due to the density of states distribution but also to the lower mobility of carriers.

### (iii) Conduction in Localized States at the Fermi Level

When a finite density of localized states exists at the Fermi level, carriers can contribute to conduction by phonon-assisted tunnelling. The probability that an electron will hop to another localized state of energy difference  $W$  and spatial separation  $R$ , with decay length  $\alpha^{-1}$ , can be written in the form.

$$p \sim v_{ph} \exp \left[ -2\alpha R - W/kT \right] \quad (1.20)$$

This follows because the probability of finding a phonon with energy

equal to  $W$  is proportional to  $\exp[-W/kT]$ . The phonon attempt frequency must be less than the maximum phonon frequency ( $\sim 10^{13} \text{ s}^{-1}$ ) and the overlap of the wavefunction will behave as  $\exp(-2\alpha R)$ .

From the Einstein relation

$$\mu = eD/kT \quad (1.21)$$

with  $D = 1/6pR^2$  and assuming only electrons within  $\sim kT$  of the Fermi level contribute to conductivity:

$$\sigma_3 \sim \frac{1}{6} e^2 R^2 v_{ph} N(E_F) \exp[-2\alpha R - W/kT] \quad (1.22)$$

This form of hopping conduction about the Fermi level is known as "Nearest Neighbour" or "Miller-Abrahams" [7] hopping, after the work of the authors on impurity-band conduction [29].

Hopping conduction obeying (1.22) will only be observed if  $\alpha R_0 \gg 1$ , where  $R_0$  is the average distance to a nearest neighbour. If  $\alpha R_0 \lesssim 1$ , or if the temperature is sufficiently low, carriers will tend to hop to sites that are closer energetically though spatially at a distance greater than  $R_0$ . This process, known as "Variable-Range Hopping" conduction was first pointed out by Mott [22]. Following Mott and Davis [7] pp 34 the optimum value of  $R$  is obtained as follows. In a sphere of radius  $R$  there are  $(4/3) \pi R^3 N(E_F) \Delta E$  states in the energy range  $\Delta E$ . The average energy spacing between states near the Fermi level is thus

$$W = \frac{3}{4\pi R^3 N(E_F)} \quad (1.23)$$

with  $W$  being the Hopping energy and the average hopping distance  $R$

$$R = \frac{4}{3} \left( \int_0^R r 4\pi r^2 dr \right) / \left( \int 4\pi r^2 dr \right) \quad (1.24)$$

Substituting equations (1.23) and (1.24) into (1.20) we find

$$p \sim v_{ph} \exp \left[ -\frac{3\alpha R}{2} - \frac{3}{(4\pi N(E_F)R^3 kT)} \right] \quad (1.25)$$

To maximize the jump probability,  $p$ , the exponent is maximized to give the optimum hopping distance  $R_m$ .

$$R_m = \left[ \frac{3}{2\pi\alpha N(E_F)kT} \right]^{\frac{1}{3}} \quad (1.26)$$

hence

$$\sigma_{VRH} = \frac{1}{6} e^2 R^2 v_{ph} N(E_F) \exp - [T_0/T^{\frac{1}{3}}] \quad (1.27)$$

where

$$T_0 = 2 \left( \frac{3}{2} \pi \right)^{\frac{1}{3}} \left[ \frac{\alpha^3}{kN(E_F)} \right]^{\frac{1}{3}} \quad (1.28)$$

Plotting  $\ln \sigma$  against  $(1/T)^{\frac{1}{3}}$  should yield a term  $T_0$ , which in turn can be used to determine  $\alpha^3/N(E_F)$ .

In two dimensions, the above equation (1.27) reduces to

$$\sigma_{2D} = \sigma_0 \exp \left( -\frac{B}{T^{\frac{1}{2}}} \right) \quad (1.29)$$

after [30].

### 1.3.2 Thermoelectric Power

The thermopower,  $S$ , is related to the Peltier coefficient,  $\pi$ , by

$$S = \pi/T \quad (1.30)$$

The Peltier coefficient is the energy carried by the electrons per unit charge, measured relative to the Fermi level. The contribution of an electron to  $\pi$  is directly proportional to its contribution to the total conductivity. The weighting factor for electrons in a range

$dE$  at  $E$  is thus  $\sigma(E) dE/\sigma$ . Hence [31]

$$\pi = -\frac{1}{e} \int (E - E_c) \sigma(E)/\sigma dE \quad (1.31)$$

where  $\sigma(E) dE$  is the conductivity in the energy range  $dE$  at  $E$  and  $\sigma$  is the total conductivity; thus

$$S = \frac{-k}{e} \int \frac{E - E_F}{kT} \frac{\sigma(E)}{\sigma} dE \quad (1.32)$$

By convention, in semiconductors,  $S$  is positive for carriers with  $E > E_F$  and negative for  $E < E_F$ . The behaviour of the thermopower is strongly dependent on the dominant conduction process.

(i) Conduction in Extended States

Through the substitution of (1.5) into (1.32) and assuming a constant density of states, with an energy-independent mobility, it can be shown that

$$S = \frac{-k}{e} \left[ \frac{E_c - E_A}{kT} + A_c \right] \quad (1.33)$$

where  $A_c$  depends on the nature of the scattering process and is normally in the range 2 - 4 for crystalline semiconductors. By equation (1.9)

$$S = \frac{-k}{e} \left[ \frac{(E_c - E_F)_0}{kT} - \frac{Y}{k} + A_c \right] \quad (1.34)$$

(The above treatment can readily be applied to conduction by holes.)

It can be seen that graphical representation of equation (1.31) and the corresponding d.c. conductivity relationship on the appropriate axes should yield the same activation energy  $(E_c - E_F)_0$

(ii) Conduction in Band Tail States

Derivation of formula describing thermopower due to carriers conducting in the localized tail states between  $E_c$  and  $E_A$  for electrons and  $E_v$  and  $E_B$  for holes, follows closely the argument used in (i) for

extended state conduction. The density of localized states is again assumed to behave like some power  $S$  of the energy  $E$  as applied in the corresponding d.c. conduction process. One finds [26].

$$S = \frac{-k}{e} \left[ \frac{E_A - E_f}{kT} + \frac{C^*}{N(E)} \right] \quad (1.35)$$

where  $N(E)$  is defined by equation (1.14) and

$$C^* = \int_0^{\frac{\Delta E}{kT}} \exp(-x) x^{S+1} dx \quad (1.36)$$

where  $\Delta E$  is the band-tail width  $E_c - E_A$  and  $x = (E - E_A)/kT$ . For a linear variation of the density of states described in equation (1.14) with  $S = 1$ .

$$S = \frac{-k}{e} \left[ \frac{(E_A - E_f)_0}{kT} - \frac{y}{k} + \frac{C_1^*}{C_1} \right] \quad (1.37)$$

with

$$C_1^* = 2 - \{ \exp(-\Delta E/kT) [2 + 2(\Delta E/kT) + (\Delta E/kT)^2] \} \quad (1.38)$$

and

$$C_1 = 1 - \{ \exp(-\Delta E/kT) [1 + (\Delta E/kT)] \} \quad (1.39)$$

Plots of  $S$  versus  $1/T$  and  $\ln \sigma$  versus  $1/T$  for band-tail conduction should yield a difference of slope  $\sim W$ , the hopping energy

### (iii) Conduction in Localized States Near the Fermi-Level

At low temperatures, when the conduction process is electron tunnelling between states at the Fermi level, the thermoelectric power may be described by [32]

$$S = \frac{\pi^2}{3} \frac{k^2 T}{e} \left[ \frac{d(\ln \sigma)}{dE} \right]_{E = E_f} \quad (1.40)$$

This is identical to the equation used for metallic conduction. The thermopower is expected to be small. In this regime the sign of the thermopower is dependent on the density of states distribution near the Fermi level. The temperature dependence of the thermoelectric power in the variable-range hopping regime has been calculated by a number of workers [33], [34]. Different investigators suggest  $S$  increases with  $T^{\frac{1}{2}}$  or  $T^{\frac{1}{4}}$  and that it is proportional to  $d \ln(N(E))/dE$  for  $E = E_F$ .

### 1.3.3 Metal-Insulator Transition

A non-crystalline semiconductor or insulator with a finite density of localized states  $N(E_F)$  at the Fermi level is said to undergo an Anderson transition when the states at the Fermi level are delocalized and the material becomes a metal. This non-metal to metal transition can be initiated experimentally when some parameter  $x$ , such as the application of a magnetic or electric field, stress, or a change in chemical composition, is varied. An example of an Anderson transition can be seen in Fig. 1.8 where the activated conduction at high temperature and variable-range hopping conduction at low temperature of the semiconductor slowly transforms to metallic-type conduction,  $\sigma$  tending to a finite value as the temperature tends to zero. Strictly speaking two types of Anderson transition are found to occur in amorphous solids [7]. The most commonly observed Anderson transition (Type I) happens when  $x$  is varied in such a way that,  $\Delta E = E_c - E_F$ , changes sign, the Fermi level moving through the mobility edge. In the previous example as  $x$  is increased,  $E_F$  moves through the localized gap states through  $E_c$ , the mobility-edge, into extended

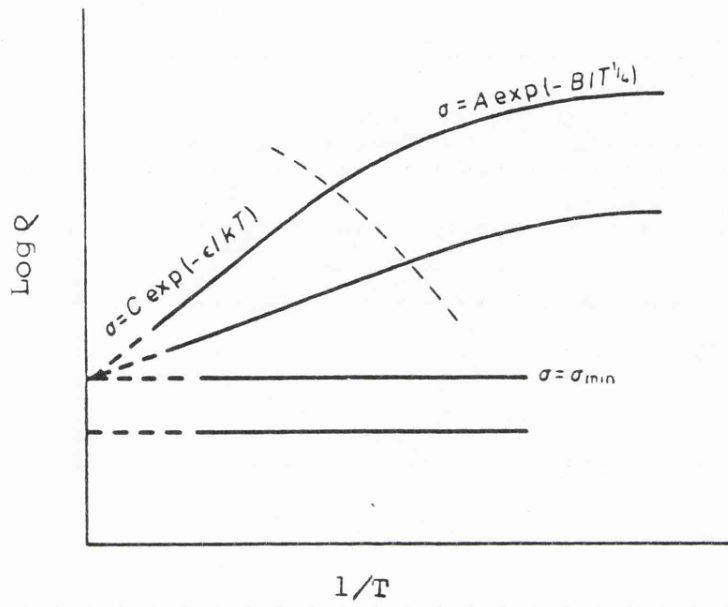


Fig 1.3 Typical behaviour of the resistivity  $Q$  of a degenerate electron gas showing an Anderson transition.

states and is represented in Fig. 1.9. Another type of Anderson transition (Type II) is indicated in Fig. 1.10 where localized states in a half-full band (not strongly correlated) become delocalized as the parameter  $x$  is increased, mobility edges forming on either side of the Fermi level  $E_F$  in the band. Conduction in this case will be from variable-range hopping about the Fermi level to metallic conduction with no activated region.

Mott [24] in 1972 proposed the existence of a quantity "the minimum metallic conductivity",  $\sigma_{\min}$ , in non-crystalline systems. When an Anderson transition occurs in an amorphous material it was asserted that the conductivity, if it remains finite as  $T \rightarrow 0$ , cannot be less than  $\sigma_{\min}$ . The conductivity attains this value when the Fermi level lies at the mobility edge. In type I systems, where conduction is due to electrons excited to a mobility edge, as discussed in 1.3.1(i) the minimum metallic conductivity is defined as

$$\sigma_1 = \sigma_{\min} \exp\left(\frac{Y}{k}\right) \exp\left[-\frac{(E_c - E_f)_0}{kT}\right] \quad (1.41)$$

Thus the constant  $C_0$  of equation (1.10) is  $\sigma_{\min}$ .

and

$$\sigma_{\min} = C_3 e^2 / \hbar a_E \quad (1.42)$$

with  $a_E$  defined as (1.43)

$$\left[\frac{a_E}{a}\right]^3 = \int_{-\infty}^E N(E) dE / \int_{-\infty}^{\infty} N(E) dE \quad (1.43)$$

$a$  being the distance between potential wells, in the model of Anderson [19]. Mott finds  $C_3 \sim 0.025 - 0.05$ , hence  $\sigma_{\min}$  values, depending on

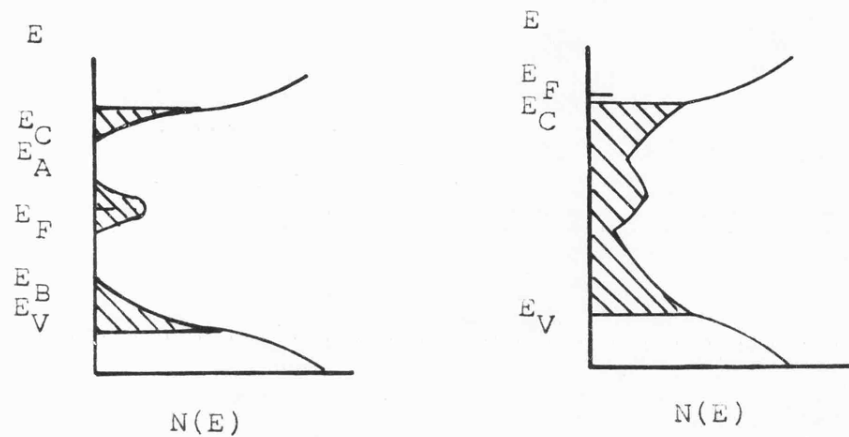


Fig 1.9 Anderson transition (type I) with increase in  $x$  (impurity concentration)  $E_F$  moves through  $E_C$ .

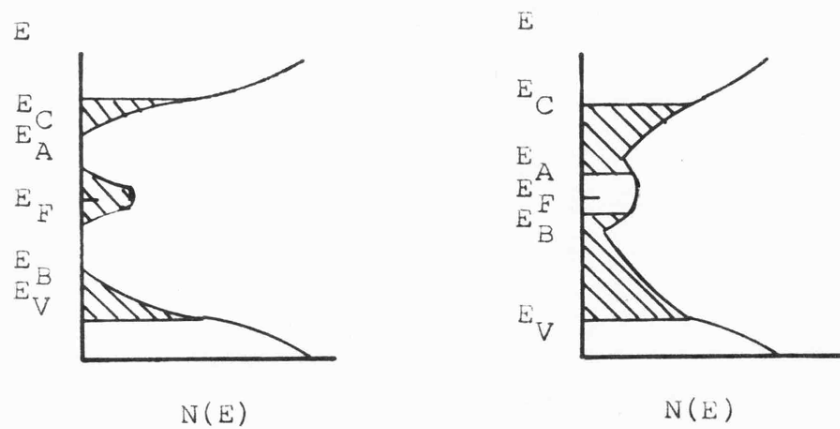


Fig 1.10 Anderson transition (type II) with increase in  $x$  the states at  $E_F$  become delocalized.

the approximations used, are generally found to be  $\sim 100$  to  $600 \Omega^{-1} \text{cm}^{-1}$ . These values compare favourably, in most cases, with the experimentally determined values of  $\sigma_{\min}$ . A plot of conductivity as a function of  $x$  for a system displaying a  $\sigma_{\min}$  can be seen in Fig. 1.11 (full line). It can be seen that at a finite value  $x_0$ ,  $\sigma$  falls discontinuously to zero as the system becomes a semiconductor.

Recently a number of workers have suggested that the transition is of a continuous nature (Fig. 1.11 - dotted line), and a series of experimental values of  $\sigma < \sigma_{\min}$  have been presented as evidence that the quantity  $\sigma_{\min}$  does not exist. [35], [36]. A number of complex theoretical treatments have been presented to explain the existence of conductivity values that fall continuously to zero. The scaling theory arguments of Abrahams et al [37] describe conduction as following the relation

$$\sigma(E) \sim \sigma_c \left\{ (E - E_c)/B \right\}^{\nu} \quad (1.44)$$

where  $B$  is the band width and  $\nu$  is a constant of order unity. Grötze, applying a memory function approach [38], finds

$$\sigma(E) = \sigma_0 \left\{ (E - E_c)/E_c \right\}^{\frac{1}{2}} \quad (1.45)$$

Both treatments indicate that the conductivity will fall continuously to zero as  $T \rightarrow 0$  and hence  $\sigma_{\min}$  does not exist.

Mott [39] has expanded upon his earlier work and predicts that the existence of  $\sigma_{\min}$  depends on the index  $S$ , defined if the radius of an Anderson-localized state at energy  $E$  tends to infinity as  $(E_c - E)^S$ . He states that the quantity  $\sigma_{\min}$  exists only if  $S > \frac{2}{3}$ . Hence if  $S \approx 0.6$  the conductivity would fall continuously to zero

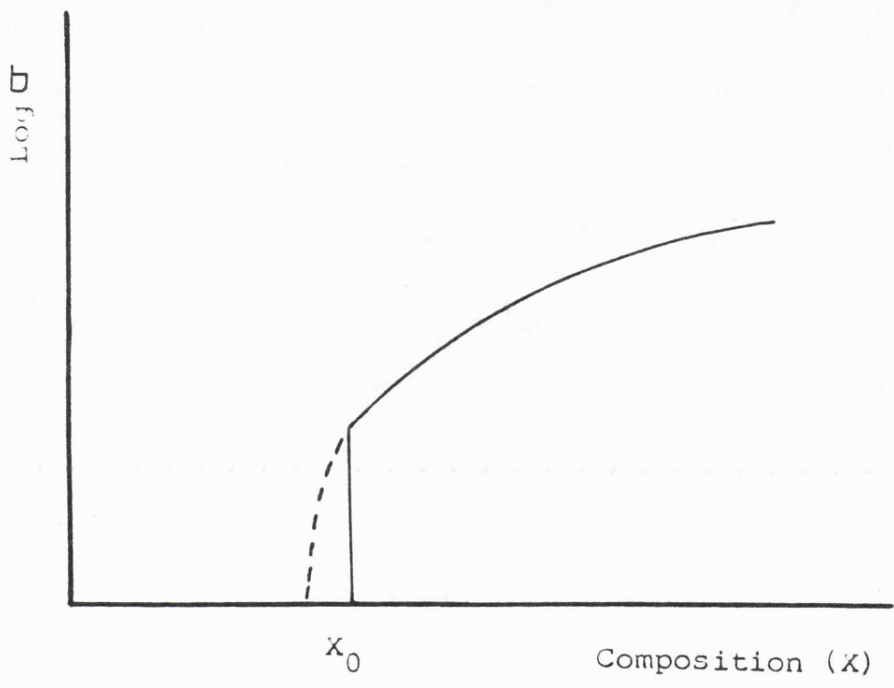


Fig 1.11 Conductivity at  $T=0$

- if  $\sigma_{\min}$  exists
- if  $\sigma_{\min}$  does not exist

and  $\sigma_{\min}$  would not exist.

Although there is still a great deal of controversy about the existence of  $\sigma_{\min}$  as  $T \rightarrow 0$ , at high  $T$  the concept of a minimum metallic conductivity remains valid and the equations derived in 1.3.1(i) will accurately describe conduction at a mobility edge.

#### 1.4 Optical Properties

With loss of long-range order, the sharp structure observed in the fundamental optical spectra of crystals both electronic and vibrational, is lost. The broad features of the spectra are similar only if short-range order is maintained with the introduction of disorder. A particularly fine example of this can be seen in Fig. 1.12 where the broad features of the crystalline spectra are maintained in the amorphous state when the nearest-neighbour coordination is still 4, but are lost when germanium becomes a liquid metal with a coordination number  $\sim 8$ .

##### 1.4.1 Vibrational Spectra

###### (i) Fundamental Vibrational Spectra

The degree to which the fundamental vibrational absorption processes are retained for non-crystalline materials depends strongly on the type of material. For tetrahedrally connected networks Si, Ge and III - VI compounds, a 'distorted-lattice model' [43] has been suggested where the amorphous solid is viewed as a disordered crystal. With the breakdown of crystalline selection rules, except the conservation of energy, the one-photon absorption process will dominate the spectrum and the absorption curve will reflect the phonon density of states. This can be seen to be the case in Fig. 1.13 [44] when the

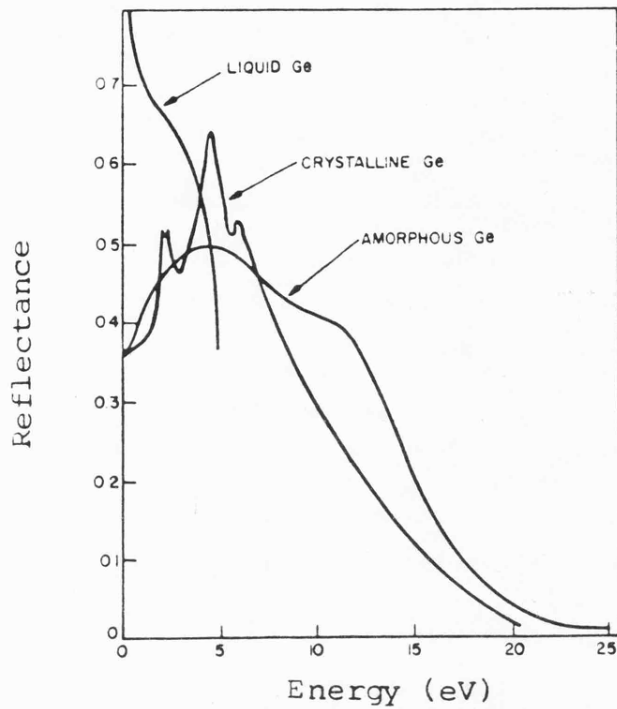


Fig 1.12 Fundamental reflectivity spectra of l-Ge (42) ; a-Ge (41) ; c-Ge(40).

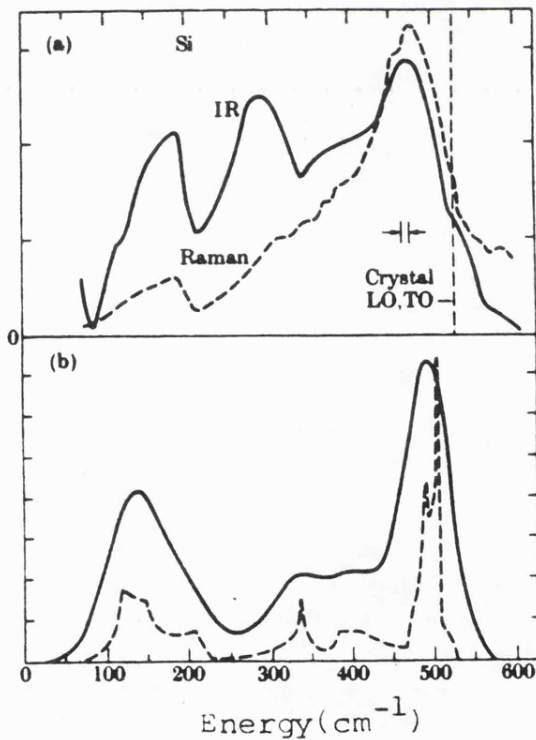


Fig 1.13 (a) Raman and I.R spectra for a-Si (b) Phonon density of states for c-Si as determined from neutron scattering. The broken curve has been Gaussian broadened to produce the solid curve(44).

phonon density of states of crystalline silicon has been convoluted with a gaussian of half-width  $30\text{cm}^{-1}$  to approximate the variation of band angles required in the CRN of amorphous silicon. The similarities between the two sets of curves (a) and (b) indicate that to a first approximation the distorted-lattice model is appropriate for this class of non-crystalline material.

A contrasting approach has been successfully employed in interpreting vibrational spectra of chalcogenide glasses such as  $\text{As}_2\text{Se}_3$ . The localized or 'molecular' model requires that some structural elements in the non-crystalline material are able to vibrate as independent units (or 'molecules'), as opposed to the rigid CRN assumed for the model described previously. If these structural elements are maintained from the crystalline to amorphous phase, then the corresponding vibrations are usually found at approximately the same energy, though again fine structure is lost [7].

(ii) Vibrations of impurities and defects

Vibrational spectroscopy provides a powerful technique for detecting small traces ( $\sim 1\text{ppm}$ ) of impurities such as oxygen or hydrogen in non-crystalline semiconductors. It has long been acknowledged that only with great care can some chalcogenide glasses be prepared without the accidental incorporation of OH. More recently I.R. spectroscopy has been used in detailed studies of hydrogen incorporated in elemental tetrahedral amorphous semiconductors such as a-Ge:H [45] and a-Si:H [46]. This interest results from the 'improved' electronic and optical properties of the hydrogenated

material when prepared by glow-discharge decomposition of silane (or germane) or by reactive sputtering. Estimates of the total hydrogen content and hydrogen bonding configuration can be achieved by analysis of the various absorption modes. [46], [47].

In a CRN structure there may exist atomic configurations which may be described as defects. Tauc [43] and Chittick [48] describe an absorption band at  $560\text{cm}^{-1}$  in the absorption spectrum of a-Ge, prepared by a number of different techniques, as a defect intrinsic to a-Ge.

#### 1.4.2 Absorption Edge

The optical absorption edge of many amorphous semiconductors can be conveniently separated into three regions (see Fig. 1.14). Regions A and B are due to transitions within the CRN, perturbed to some extent by defects, while C results from transitions involving defect states directly.

##### Region A: High-Absorption Region

Interband transitions in an amorphous semiconductor in the absence of any electric field or excitonic effects, may be described by [7].

$$\alpha(\omega) = \frac{8\pi^2 e^2 \hbar a}{n_0^2 \text{cm}^2} \int \frac{N_v(E) N_c(E + \hbar\omega)}{\hbar\omega} dE \quad (1.46)$$

where the integral is over all pairs of states in the valence and conduction bands separated by  $\hbar\omega$ . If the density of states at the band edges are represented by power laws:

$$N_c(E) = \text{const} (E - E_A)^P \quad (1.47)$$

$$N_v(E) = \text{const} (E_B - E)^Q \quad (1.48)$$

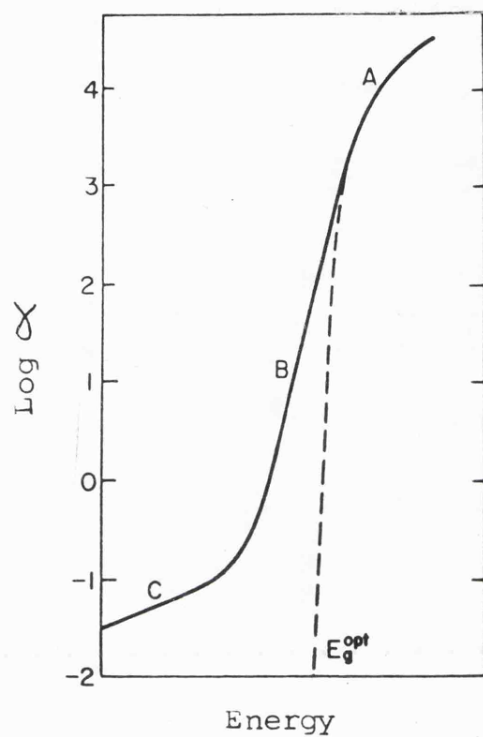


Fig 1.14 Schematic representation of the absorption spectrum of amorphous semiconductors.

it can be shown [7] that

$$\alpha(\omega) = \text{const } (\hbar\omega - E_0)^{p+q+1} / \hbar\omega \quad (1.49)$$

where  $E_0 = E_A - E_B$

If one assumes parabolic bands  $p = q = \frac{1}{2}$  then (1.49) simplifies to

$$\hbar\omega \alpha(\omega) = \text{const } (\hbar\omega - E_0)^2 \quad (1.50)$$

Many amorphous materials show this type of behaviour in the region above the absorption edge, though the quadratic frequency dependence is by no means absolute. Amorphous Se [49] and some STAG glasses [7] being notable exceptions showing power law relationships to the first and third powers respectively. Davis and Mott [25] by assuming  $N(E)$  to be linear in both the band edges and forbidding transitions between localized states derived the relationship (1.49) but now  $E_0 = E_A - E_V$  or  $E_0 = E_C - E_B$  whichever is the smaller.

#### Region B: Exponential Absorption Region

At energies below  $E_0$  the absorption of almost all materials obey the so called 'Spectral Urbach Rule' [50].

$$\alpha(\omega) = \text{const exp } [\Gamma \hbar\omega] \quad (1.51)$$

where  $\Gamma$  is a quantity which describes the steepness of the edges. Values of  $\Gamma$  at 300K vary from  $10-25\text{eV}^{-1}$  and are constant up to near the glass transition temperature  $T_g$ . It is also observed that  $\Gamma$  for a given material is insensitive to preparation conditions.

Despite the widespread observation of this exponential absorption the precise origin is not certain. The exponential dependence of  $\alpha$  with photon energy  $\hbar\omega$  has been attributed to exponential tails of states in the valence and conduction bands [51] or to phonon-assisted tunnelling in the presence of potential fluctuations [52] or a

combination of both [53]. Field-Broadened exciton effects have also been proposed as an explanation [7].

#### Region C: Weak Absorption Tail

A weak absorption tail is observed for energies below the exponential region B (where  $\alpha \lesssim 1\text{cm}^{-1}$ ). Its shape is found to be dependent on preparation, purity and thermal history of the sample [54]. It seems probable that this low-absorption tail is associated with transitions into or out of energy levels associated with specific defect centres. Photothermal deflection spectroscopy has been used to provide evidence for this interpretation.

## CHAPTER 2

### Review of Current Work

- 2.1 Sputtered a-Si:H - a brief review
- 2.2 Amorphous silicon - gold
  - 2.2.1 Introduction
  - 2.2.2 Structure and stability
  - 2.2.3 Electronic and optical properties
  - 2.2.4 Other properties
- 2.3 a-Si:M - a brief review

## 2.1 Sputtered hydrogenated amorphous silicon - a brief review

Since the successful doping of a-Si:H with boron and phosphorus in 1976 [ 2 ] research on hydrogenated amorphous silicon, prepared primarily by the glow-discharge decomposition of silane has boomed. A brief review of some properties of sputtered hydrogenated amorphous silicon is presented in this section, though when necessary reference will be made to material prepared by other techniques.

Early work on sputtered and evaporated amorphous silicon indicated a material with a large density of structural defects ranging from single dangling bonds to macroscopic voids. A correspondingly high density of states in the gap was observed as indicated by the variable-range hopping conduction behaviour (fig. 2.1), and the large density of paramagnetic centres ( $\sim 10^{19} - 10^{20} \text{ cm}^{-3}$ ) detected by ESR. Following the work of Lewis et al [ 45 ] on a-Ge:H prepared by reactive sputtering in an argon-hydrogen atmosphere, where spin density and room temperature hopping conductivity were reduced by several orders of magnitude, a-Si:H has been prepared in a similar manner by a number of groups [ 56 ], [ 57 ], [ 46 ]. The incorporation of hydrogen into the CRN lattice of amorphous silicon drastically reduces the number of dangling bond defects in the band gap and hence produces a silicon-hydride alloy with a density of states as indicated in fig. 2.2. It is an oversimplification of the problem to say that hydrogen only 'passivates' dangling bonds. Depending on how the thin films are prepared, hydrogen may be incorporated in different bonding configurations, in different quantities and affect the structural, electronic and optical properties of the alloy [ 57 ].

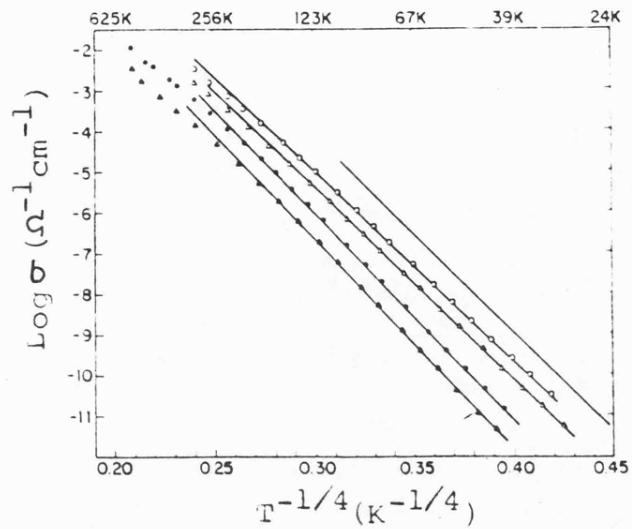


Fig 2.1  $\text{Log } \sigma$  vs  $T^{-1/4}$  for as-deposited a-Si ( $\Delta, \circ$ ) and for annealed films at 250 c for 1 hr ( $\blacktriangle, \bullet$ ). The solid line represents the  $T^{-1/4}$  regime for an as-deposited a-Ge film. (55).

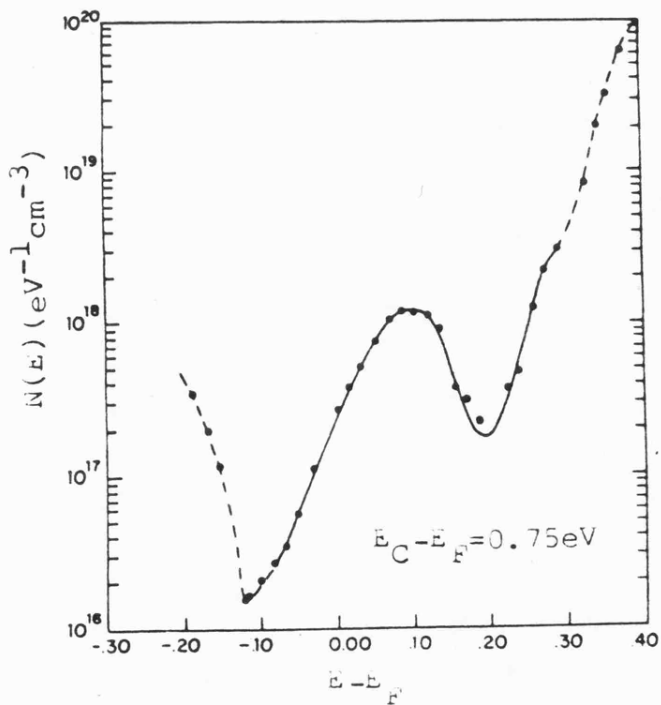


Fig 2.2 The density of states derived from field effect measurements on sputtered a-Si:H (57).

### Preparation

In the sputtering process a large number of parameters such as deposition temperature, argon and hydrogen pressures, r.f. power, d.c. bias and cathode-anode separation all affect the properties of the amorphous film to a greater or lesser degree [ 57 ], [ 58 ]. Experimentally the best material is found to be produced at low argon-hydrogen pressures  $\sim 5-10$  m $\tau$ , high deposition temperature  $T_d = 200 - 350^\circ\text{C}$  and low power densities  $\sim 0.5 - 3.0$  Wcm $^{-2}$ . Even this type of material contains 10 - 30 at % H, requiring a large amount of the hydrogen to be undesirably bonded in the silicon lattice. Attempts to reduce the amount of excess hydrogen incorporated into the lattice by the application of different types of sputtering techniques such as bias sputtering [ 59 ] and magnetron sputtering [ 60 ] have been investigated with some degree of success.

### Structure and microstructure

X-ray [ 61 ], electron [ 8 ] and neutron [ 62 ] scattering experiments have been carried out on a-Si:H. The RDFs when determined, compare well with those of CRN models. These techniques, however, are not sensitive enough to detect the slight changes in structure that could be the result of excess hydrogen in the silicon CRN lattice. Microstructure in the form of voids ( $\sim 30$  Å) have been observed by SANS [ 63 ] on films produced at  $400^\circ\text{C}$  and by TEM and SEM where columnar growth structures, similar to that observed by Knights [ 4 ] on glow-discharge a-Si:H, has been reported. A parallel between glow-discharge and sputtered material has been suggested in that at high  $T_d$  and low powers the columnar structures may be avoided. This however has been questioned by Moustakas [ 64 ], who claims that

sputtered films are improved, in some cases, by increasing the power of the discharge, contrary to the findings in the glow-discharge a-Si:H films.

### Electronic properties

Although the role of hydrogen is not well understood, its incorporation in amorphous silicon results in dangling bond passivation and a widening of the optical gap to  $\sim 1.8\text{eV}$ . Conductivity and thermopower measurements indicate thermally activated conduction, with  $E_{\sigma} \sim 0.75 - 1.05\text{eV}$ ,  $E_{\sigma} - E_s \sim 0.15\text{eV}$  and  $\sigma_{RT} \sim 10^{-10} - 10^{-12} \Omega^{-1} \text{cm}^{-1}$ ; suggesting extended-state conduction in the conduction band. The subsequent reduction of the density of states, as determined by the Field Effect experiment [7] (fig. 2.2) is confirmed by ESR measurements from which spin densities ( $N_s$ ) of the order  $10^{16} \text{cm}^{-3}$  are deduced [57]. Photoemission studies [65] indicate that the structure of the valence band can be affected by the incorporation of hydrogen under certain conditions.

### Optical properties

The optical absorption spectrum of sputtered a-Si:H has been studied in some detail from the infrared to the visible/ultra violet. A typical I.R. spectrum is shown in fig. 2.3. Three distinct groups of absorption bands at  $2100 - 2000 \text{cm}^{-1}$ ,  $890 - 850 \text{cm}^{-1}$  and a broad band at  $650 \text{cm}^{-1}$ , being designated respectively as silicon hydride stretching, bending and rocking, wagging and rolling modes [46]. The spectral response of the absorption edge follows the form described in Chapter 1, exhibiting a defect tail, Urbach edge and a high-energy region from which an optical gap of  $\sim 1.7 - 2.1\text{eV}$  can be derived. Films may also exhibit a strong photoconductivity response

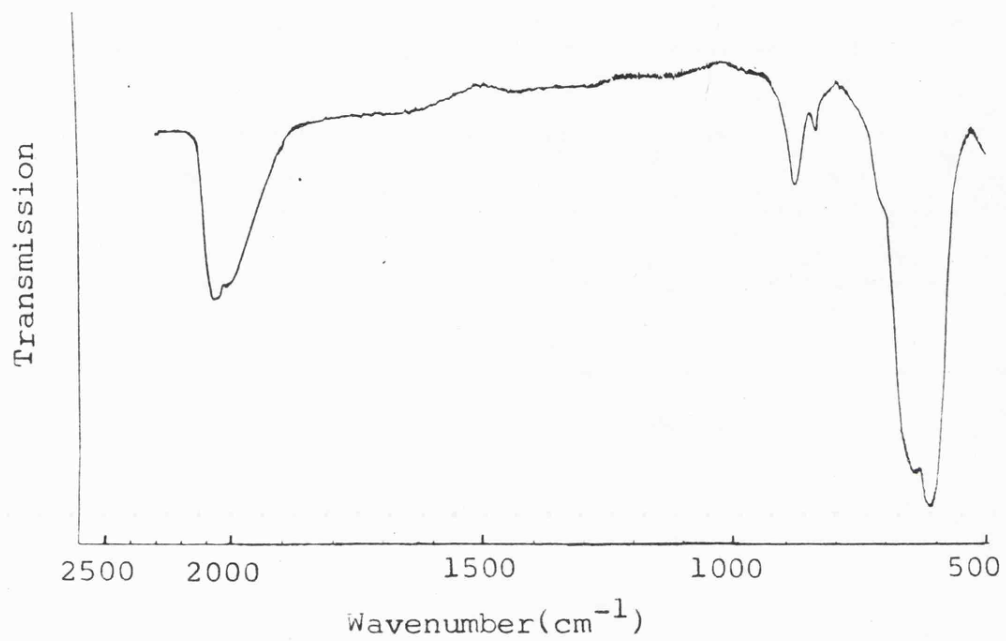


Fig 2.3 IR Transmission spectra for a-Si:H

and show photoluminescence as indicated in fig. 2.4 and fig. 2.5. All of these properties are strongly dependent on hydrogen content and deposition parameters.

## 2.2 Amorphous silicon-gold

### 2.2.1 Introduction

Non-crystalline silicon-gold alloys have been prepared by three basically different methods:-

i) Quenching from the liquid:  $g - Si_{1-x}Au_x$

In 1960 Klement et al [ 66 ] reported the first amorphous silicon-gold alloy [ 25% Si ] prepared by the splat quench technique; indeed this proved to be the first metallic glass. Though even with the most rapid conventional quenching techniques ( $10^5 - 10^7 \text{ Ks}^{-1}$ ) available at present, the range of composition that remains stable, even at reduced temperatures, is limited to an area close to the eutectic composition. The degree to which the liquid-like nature is frozen into the glass has been studied near the eutectic, and comparative studies between liquid and glassy silicon-gold (l - Si: Au and g - Si: Au) have proved to be very useful in explaining properties of the amorphous system.

Recently the LMQ technique (laser-induced melting, mixing and quenching) has extended the range of stable amorphous silicon-gold alloys to  $x = 0.09 - 0.91$  [ 67 ]. By applying short laser pulses  $\sim 30\text{ns}$  to a multilayer structure, cooling rates  $\sim 10^{10} \text{ Ks}^{-1}$  are achieved and the range of glass formation is greatly enhanced.

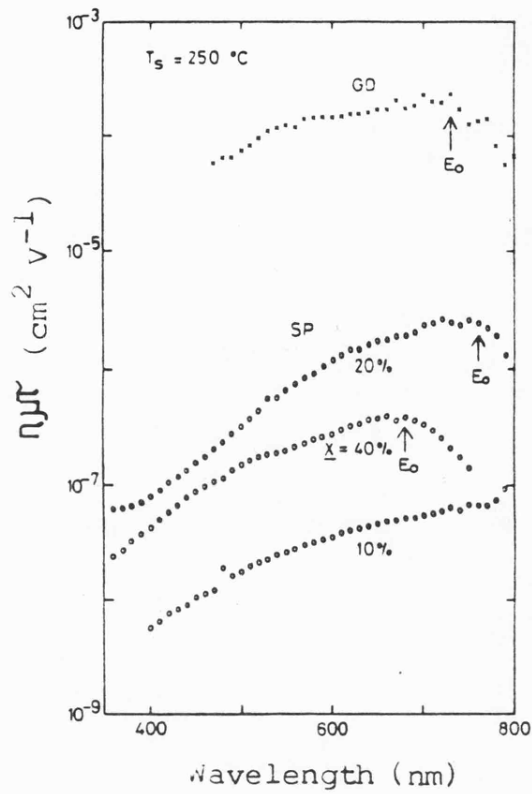


Fig 2.4 Normalized photoconductivity ( $\bar{\eta}\bar{\mu}\bar{\tau}$ ) vs wavelength (nm) for sp and gd a-Si:H (53).

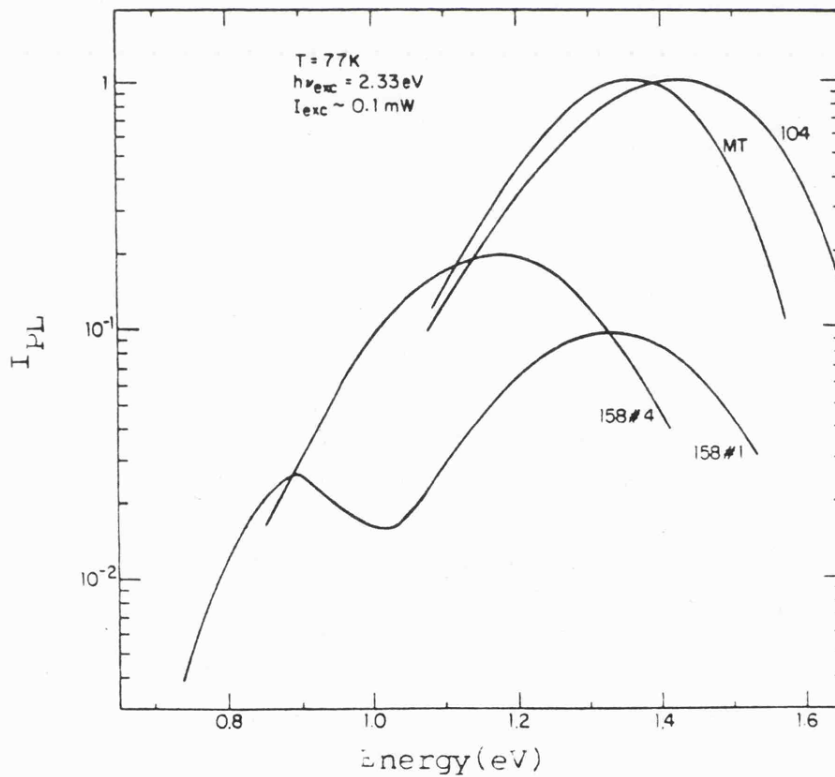


Fig 2.5 Steady-state P.L spectra for sp (153-4, 104, 153-1 are low, medium, high  $P_H$  respectively) and gd (MT) a-Si:H (57).

ii) Evaporation: ev -  $\text{Si}_{1-x}\text{Au}_x$

Workers have employed single [68] and double crucible [69] evaporation in high vacuum and UHV conditions onto various types of substrates at various temperatures. Thin films  $\sim 0.1 - 2\mu\text{m}$  have been prepared over a wide range of composition  $x = 0 - 0.8$ .

iii) Sputtering: sp -  $\text{Si}_{1-x}\text{Au}_x$

Thin films  $\sim 0.01 - 1\mu\text{m}$  of amorphous silicon-gold have been prepared by the sputtering technique in argon [70] and argon +  $\chi$  ( $\chi = \text{oxygen or hydrogen}$ ) [71] atmospheres. At present the true range of composition available to this method is not known.

### 2.2.2 Structure and Stability

The compositional range of existence of amorphous silicon-gold alloys prepared by several different techniques is summarised in fig. 2.6. It can be seen that, by judicious choice of deposition parameters, stable amorphous alloys can be prepared from amorphous silicon ( $x = 0$ ) to  $\text{Si}_{0.09}\text{Au}_{0.91}$  before the alloy becomes unstable and begins to crystallize. Much of the early work on the Si:Au system was centred near the eutectic in the equilibrium phase diagram (see fig. 2.7), as a liquid with a deep eutectic and high viscosity is in general favourable for rapid quenching for the formation of a non-crystalline solid [69]. Indeed it is only in the range  $x = 0.6 - 0.83$ , which is accessible to conventional glass-forming techniques, that structural comparisons between glassy (g), vapour-deposited (ev) and sputtered (sp) materials can be made.

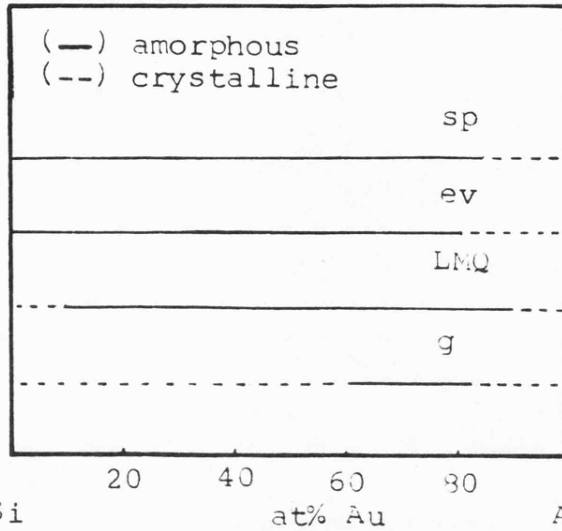


Fig 2.6 Compositional range of non-crystalline Si-Au.

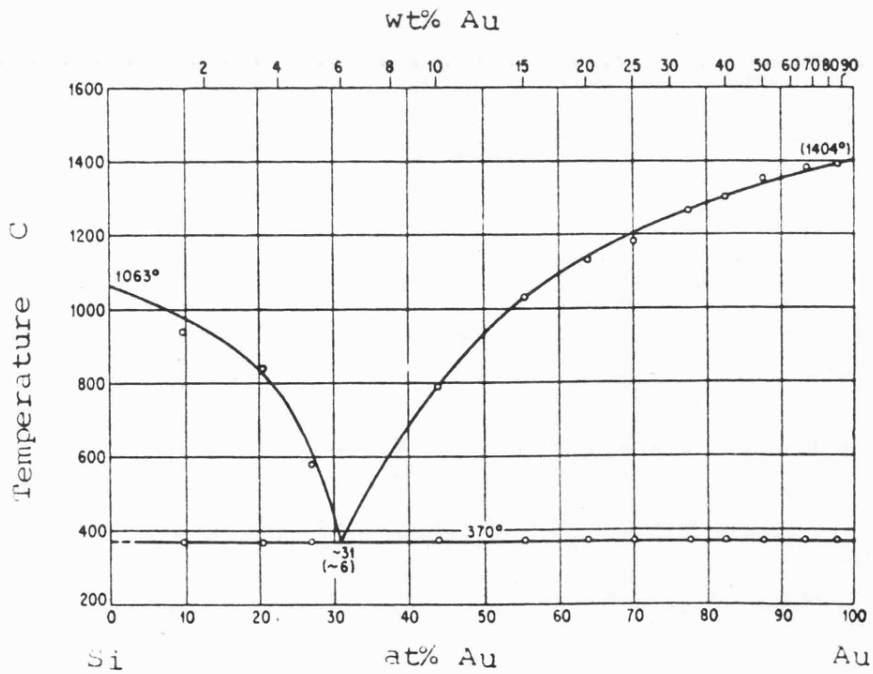


Fig 2.7 Equilibrium phase diagram for Au-Si (130).

The interference function  $J(k)$  obtained from electron diffraction experiments on  $\text{ev - Si}_{1-x}\text{Au}_x$  deposited at 77K can be seen in fig. 2.8. At the Au-rich composition the interference functions have a sharp maximum at  $k_p \approx 2.78\text{\AA}^{-1}$  with a weaker unsplit maximum at  $k_p' \approx 4.9\text{\AA}^{-1}$  [ 69 ]. Silicon enrichment first results in broadening of the first peak followed by the appearance of two satellite peaks, situated on either side of  $k_p$ , at  $k_1 \approx 2.10\text{\AA}^{-1}$  and  $k_2 = 3.60\text{\AA}^{-1}$ . At gold concentrations below 9 at% Au  $k_p$  is lost and only  $k_1$  and  $k_2$ , the major maximum of the interference function of pure silicon, remain [ 8 ].

Electron diffraction traces for  $\text{ev - Si}_{1-x}\text{Au}_x$  alloys evaporated onto substrates at 300K [ 68 ] are shown in fig. 2.9. For  $x < 0.24$  the diffraction pattern is similar to pure amorphous silicon, though when the Au content exceeds  $\sim 30$  at % Au ( $x > 0.3$ ) broad peaks appear at positions that correspond to crystalline gold. These gold peaks have been interpreted by the authors as microcrystallites of gold  $\sim 20 - 30\text{\AA}$  in diameter.

X-ray diffraction patterns of Chen and Turnbull [ 72 ] on  $\text{g - Si}_{0.185}\text{Au}_{0.815}$  show a broad peak centred at  $k_p \sim 2.76\text{\AA}^{-1}$  which is in qualitative agreement with the work of Dixmier and Guinier [ 73 ] on  $\text{g - Si}_{0.3}\text{Au}_{0.7}$ . Structural measurements on sputtered silicon-gold alloys, deposited at 77K, have been carried out by Hauser and Tauc [ 70 ] for the compositional range  $0.5 < x < 0.87$ . Their published work was again limited to the first diffraction ring only. For compositions between 87 - 69 at % Au, a broad peak at  $k_p \approx 2.76\text{\AA}^{-1}$  is found. Below 69 at % Au, significant broadening of the peak occurs,

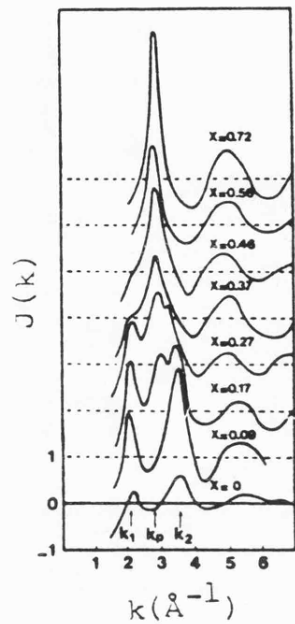


Fig 2.8 Interference functions  $J(k)$  for  $ev\text{-Au}_x\text{Si}_{1-x}$ . (69)

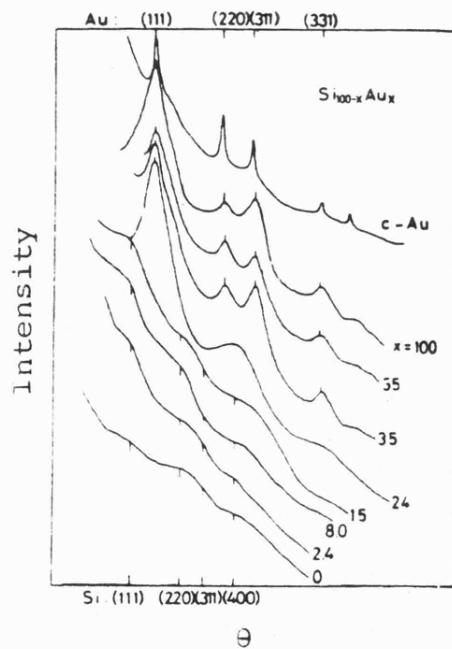


Fig 2.9 Electron diffraction patterns for  $ev\text{-Si}_{1-x}\text{Au}_x$ . (68). The Bragg reflections are shown on the abscissa.

especially on the short-wavelength side, and it finally splits into two maxima situated approximately at  $k_p \approx 2.9\text{\AA}^{-1}$  and  $k_p' \approx 2.25\text{\AA}^{-1}$ .

There is broad agreement between structural measurements on material prepared by all three techniques in that near the eutectic composition the interference function has a broad maxima at  $k_p \approx 2.75 - 2.78\text{\AA}^{-1}$  and when reported, the second maxima is unsplit and centred at  $k_p' \approx 4.9\text{\AA}^{-1}$ . These results are very similar to those obtained from X-ray diffraction experiments on  $1 - \text{Si}_{0.185}\text{Au}_{0.815}$  by Waghorne et al [ 74 ]. As can be seen in fig. 2.10, maxima were found at  $k_p \approx 2.75\text{\AA}^{-1}$  and  $k_p' \approx 4.8\text{\AA}^{-1}$ . At the other end of the compositional range, for low gold concentrations  $0 < x < 0.3$ , there is qualitative agreement that the structure becomes dominated by the strong covalent tetrahedral bonding of amorphous silicon. The composition at which the peak at  $k_p \approx 2.76\text{\AA}^{-1}$  disappears apparently depends on deposition parameters. These results have been interpreted by Ph Mangin et al [69 ] as representing, near the eutectic, a close-packed metallic structure (a -  $\mu$  phase) while alloys at the silicon-rich end exhibit a more open continuous random network structure (a-Si phase). The amorphous alloys in the intermediate compositional range are suggested as being an intricate mixture of the two phases. Mass density measurements carried out by these authors indicate that for alloys of low Au content, Au enters the tetrahedral silicon lattice in interstitial sites. A free-energy diagram, as shown in fig. 2.11, representing the relative stability of the various phases, is proposed for this model.

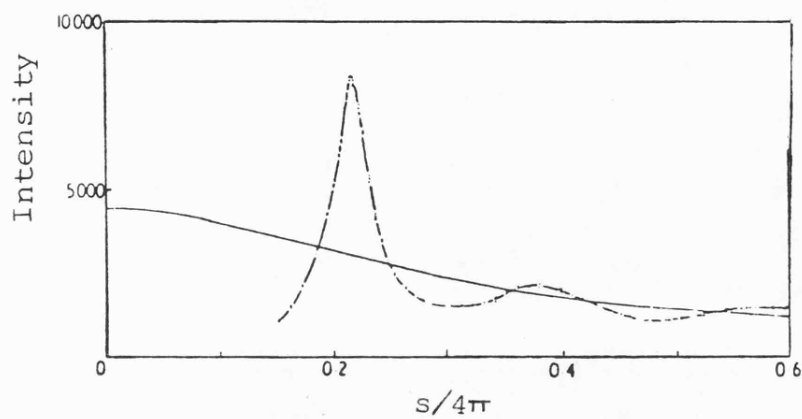


Fig 2.10 Diffraction profile for  $l\text{-Si}_{13.5}\text{Au}_{81.5}$  at 390 C (74).

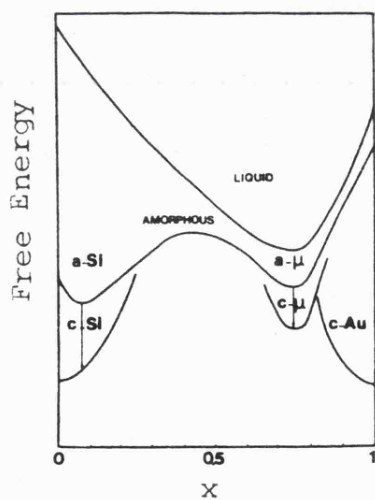


Fig 2.11 Hypothetical free-energy diagram for  $\text{Si}_{1-x}\text{Au}_x$ . (69).

### 2.2.3 Electrical and optical properties

D.C. conductivity studies have been carried out on evaporated, sputtered and LMQ silicon-gold alloys [69] [70] [67], over a wide range of composition and temperature. Ph Mangin et al [69] reports the conductivity behaviour from the deposition temperature of 77K to above the crystallization point of various evaporated alloys. Typical results are indicated in fig. 2.12 where 0 → 1 and 1 → 3 correspond to irreversible relaxation to more stable amorphous states, and 1 ⇌ 2 and 3 ⇌ 4 correspond to two way reversible sequences. Only if  $x > 0.3$  (fig. 2.12(a)) can a TCR be evaluated from the conductivity data. For  $x < 0.3$ , as can be seen in fig. 2.12(b), the processes are thermally activated. The sharp irreversible decrease in resistivity at  $T_c$  (crystallization temperature) 3 → 5 corresponds to crystallization into a metastable phase whose TCR can be measured on 5 ⇌ 6. Subsequent heating of the sample  $T_7$  results in a second irreversible transformation in resistivity. For alloys  $x > 0.5$  the resistivity recovery is a decrease and a + ve TCR (which is measured along 7 ⇌ 8) is observed. But for compositions  $x < 0.5$  see fig. 2.12(b) the resistivity change is an increase and the result is again a thermally activated process.

These crystallization mechanisms are explained by Ph Mangin et al by invoking the free-energy diagram of fig. 2.11. The first transition results in a decrease in resistivity due to the crystallization of the  $a - \mu$  phase to a  $c - \mu$  phase. The second transformation, which is controlled by long-range diffusion, is the phase separation of gold and silicon. This transformation can result in a decrease or

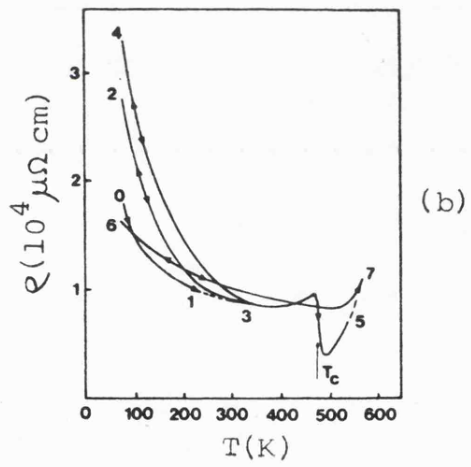
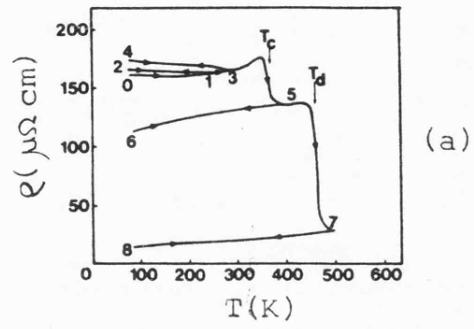


Fig 2.12 Resistivity behaviour in  $ev\text{-AuSi}_{1-x}$   
 (a)  $x=0.715$  (b)  $x=0.174$ . (69)<sup>x</sup>

increase in resistivity depending on which phase, Si or Au, is predominant.

Conductivity measurements on  $\text{ev} - \text{Si}_{1-x}\text{Au}_x$  thin films deposited at 300K have been made down to temperatures of 10mK by Nishida et al [76] and for compositions of up to  $x \approx 0.42$ . Samples with  $x < 0.3$  exhibit activated conduction at high temperatures ( $> 50\text{K}$ ), as can be seen in fig. 2.13, whose activation energy falls with Au content and becomes zero at  $x \approx 0.3$ . As stated in the previous section for gold concentrations greater than 30 at % microcrystallites of gold form. Below 30 at % Au, the conductivity may again be sub-divided into two regions, namely compositions above and below  $x = 0.14$ , the concentration at which the Metal-Insulator Transition (M.I.T.) is predicted [75]. At low temperatures for  $x < 0.14$ , variable-range hopping conduction ( $T^{\frac{1}{4}}$  hopping) is observed, though for some concentrations there are deviations from this type of behaviour (see fig. 2.14). The conduction behaviour of the two samples  $x = 0.057$  and  $0.08$  in fig. 2.14 has been described by Morigaki [75] in terms of an electron-correlation effect which becomes important at very low temperatures where simultaneous hopping of two electrons is more probable than single-electron hopping. For concentrations  $x > 0.14$  metallic type behaviour exhibiting a  $\sqrt{T}$  dependence is observed, of the form

$$\sigma(T) = \sigma(0) [1 + A\sqrt{T}] \quad (2.1)$$

where A is a dimensionless quantity independent of temperature.

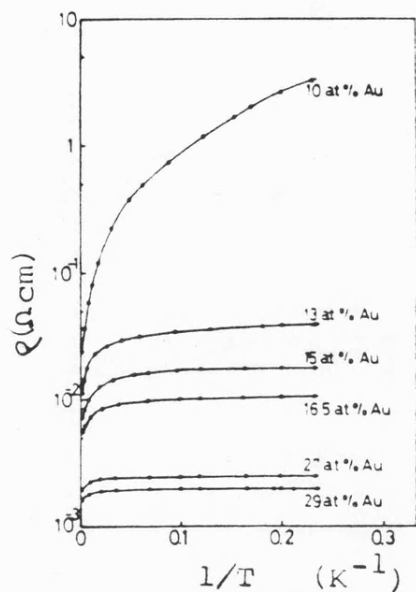


Fig 2.13 Plots of resistivity vs  $1/T$  for  $ev-Si_{1-x}Au_x$ . (76).

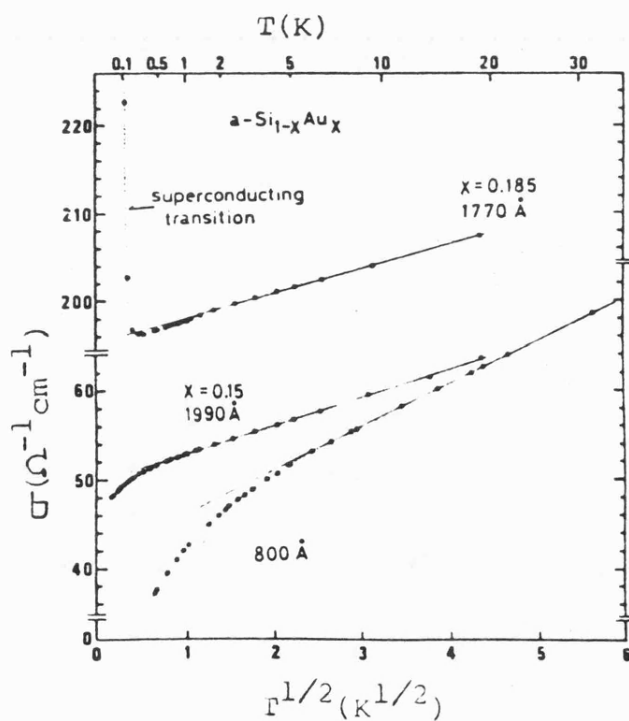


Fig 2.14 Low temperature conductivity behaviour for  $ev-Si_{1-x}Au_x$ . (76).

This conduction process is maintained down to  $\approx 1 - 10\text{K}$  when a  $\ln T$  dependence is followed down to very low temperatures. Recent measurements of  $\sigma(0)$ , the extrapolated zero-temperature conductivity, as indicated in fig. 2.15, show that conductivity values below Mott's minimum metallic conductivity ( $\sigma_{\text{min}} \approx 100 \Omega^{-1} \text{cm}^{-1}$ ) may exist for this alloy system. Kishimoto et al [ 68 ] explain these d.c. conductivity results in terms of de-localization of a gold acceptor band formed in the pseudogap of the material. For  $x < 0.14$  variable-range hopping conduction occurs in a band about the Fermi level, above  $x > 0.14$  gold states within the band become extended and metallic conduction is observed. A schematic density of states, as envisaged by Kishimoto et al [ 68 ] is shown in fig. 2.16. Further techniques were employed to determine the exact position of the gold band and the various other features in the density-of-states diagram.

Superconducting behaviour is observed for a small range of composition at very low temperatures (see fig. 2.14). The mechanism for this behaviour is uncertain at present; the authors tentatively suggest that it is due to metallic electrons in the gold impurity band and not to a metallic silicon phase as proposed to describe similar results in a-Ge:Au [ 77 ].

Resistivity measurements for as-deposited LMQ [ 67 ] amorphous films heated to above the crystallization temperature at  $3^\circ\text{C}/\text{min}$  are shown in fig. 2.17. All samples show an abrupt drop in resistivity between  $300 - 350\text{K}$ , except  $x = 0.91$ , which was irradiated at  $77\text{K}$  and shows a similar discontinuity at  $248\text{K}$ . The drop in resistivity is interpreted as crystallization of the amorphous alloys. X-ray

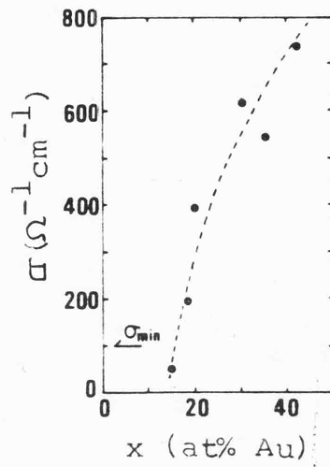


Fig 2.15 Extrapolated zero-temperature conductivity vs x for ev-Si:Au. (75).

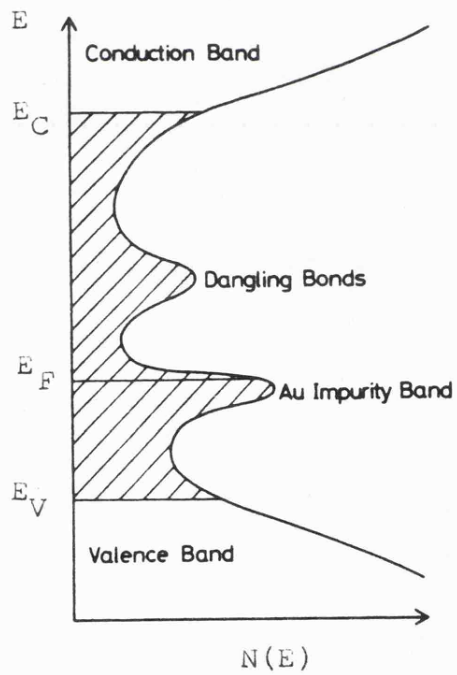


Fig 2.16 Schematic density of states distribution for ev-Si:Au. (63).

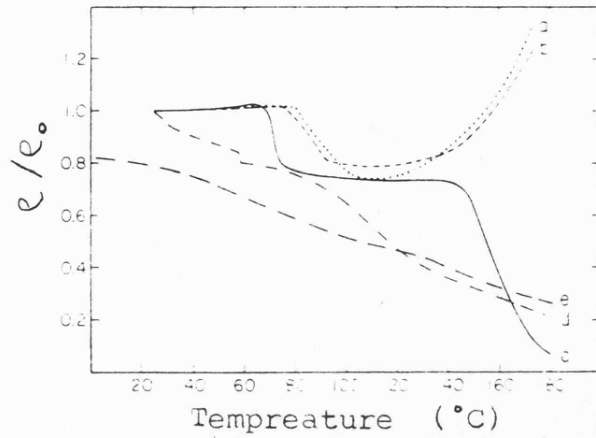


Fig 2.17 Resistivity of LMQ-Si<sub>1-x</sub>Au<sub>x</sub> Films vs temperature measured with constant temperature rise of 3°C min<sup>-1</sup> for x= (a) 9, (b) 17, (c) 50, (d) 33, (e) 91 (67).

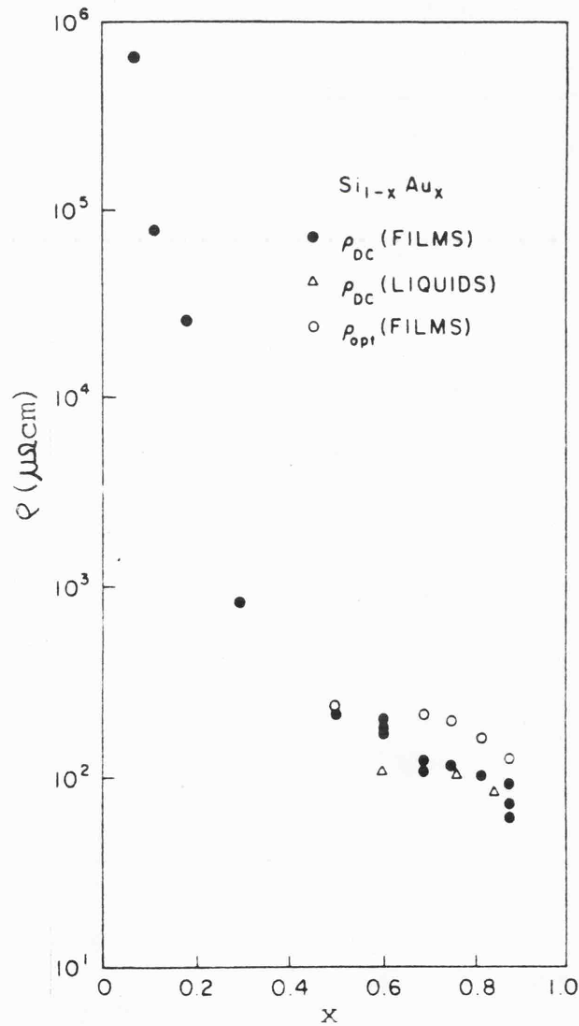


Fig 2.18 The resistivity of sp-Si<sub>1-x</sub>Au<sub>x</sub> as a function of composition (73). The films were measured at room temperature, the liquids at the melting point.

diffraction measurements on the crystallized films indicate the formation of a hexagonal metastable silicide phase.

Thin amorphous films of sputtered Si:Au prepared in argon, argon/oxygen and argon/hydrogen atmospheres have had their d.c. conductivity studied over a wide range of composition. The resistivity of various  $\text{Si}_{1-x}\text{Au}_x$  films prepared by getter sputtering in argon onto liquid-nitrogen cooled substrates is indicated in fig. 2.18 for  $0.07 < x < 0.87$  [78]. The temperature variation of resistivity between room temperature and 4.2K demonstrates variable-range hopping conduction ( $T^{\frac{1}{2}}$ ) for samples with  $x < 0.11$ , though they are still semiconducting up to  $x \approx 0.29$ , followed by metallic conduction above this value. TCRs for the metallic films are indicated in fig. 2.19 where it can be seen that a change in sign of TCR occurs close to the eutectic composition. These authors suggest the high value of the metallic transition is due to non-homogeneity of their films.

Conductivity measurements on reactively sputtered sp-Si:Au (O or H) [71] films broadly fall into two categories depending upon the O/H content of the a-Si:Au films. For a-Si where variable-range hopping is still observed upon introduction of the reactive gas ( $\text{O} < 5$  at % and  $\text{H} < 3$  at %), the addition of Au simply increases  $N(E_F)$  indicated by a subsequent reduction in  $T_0$  (from equation 1.26). If high gas concentrations are used ( $\text{O} > 5$  at% and  $\text{H} > 3$  at%) where insulating  $\text{SiO}_2$  or thermally activated Si:H is formed, Hauser reports the observation of  $T^{\frac{1}{2}}$  conduction. The results in fig. 2.20 are linear down to  $\approx 19\text{K}$ . Hauser speculates this behaviour

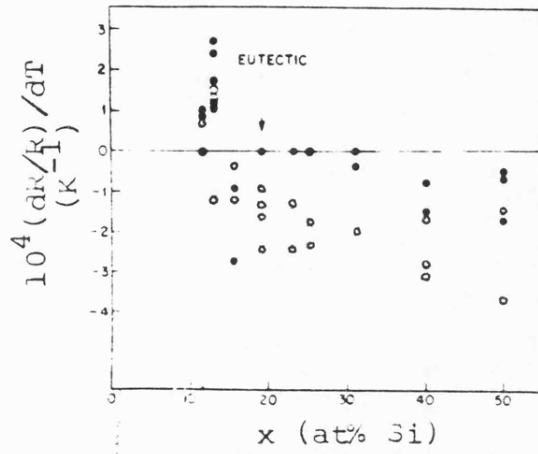


Fig 2.19 TCR values for  $sp\text{-Au}_x\text{Si}_x$  as a function of  $x$ . (73)

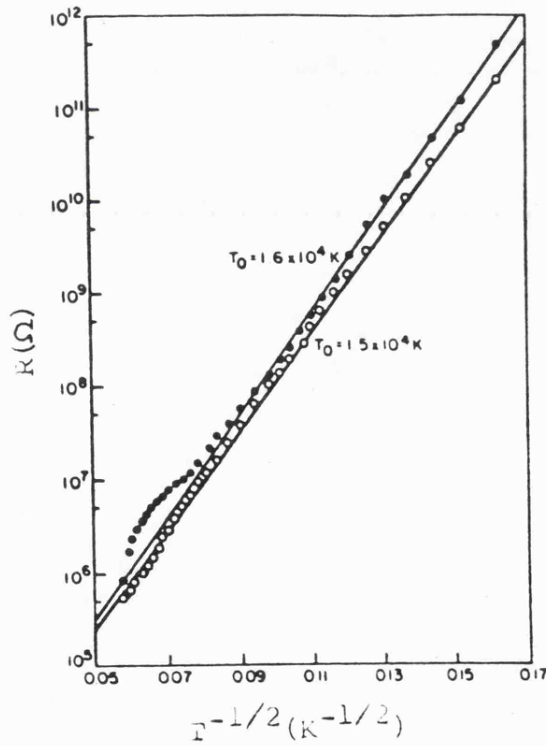


Fig 2.20 Temperature dependence of the resistivity for an  $a\text{-Si}_{92.7}\text{Au}_{7.3}\text{:H}$  film. • = as deposited at 77K. o = annealed at room temperature. (71)

is the result of percolation along quasi 1-dimensional channels in the films.

Macneil and Davis [79], for sputtered a-Si:H films exhibiting thermally activated conduction, report  $T^{\frac{1}{2}}$ , variable-range hopping conduction, for  $0.05 < x < 0.13$ . These results will be reported in detail in Chapter 4.

#### Thermoelectric power [68] and infrared photoconductivity [68]

Measurements on ev-Si:Au in conjunction with conductivity measurements position the gold acceptor band of fig. 2.16 at 0.26eV above the valence band. Below  $x \approx 0.05$  the temperature variation of thermoelectric power, as presented in fig. 2.21 is interpreted in terms of band conduction of free electrons and holes. Between 5 and 14 at% Au variable-range hopping type behaviour is observed, though an almost linear temperature dependence is observed, not the expected  $T^{\frac{1}{2}}$  behaviour. This behaviour is as yet unexplained. At 14 at% Au and above, a linear temperature variation characteristic of metallic conduction is seen to occur. The position of the Fermi level in fig. 2.16 is inferred from the +ve sign of the variable-range hopping thermopower measurements which indicate a negative slope in the density of states  $N(E_F)$ . The two main features in the photoconductivity spectra in fig. 2.22 are the steep increase of photocurrent at 0.30eV, followed by a plateau spectrum, attributed to optical excitation from the valence band to the gold impurity band, and a narrow peak at 0.25eV which is seen as an excitation from the gold impurity band into another narrow band.

ESR measurements [80], for low gold concentrations, show a rapid

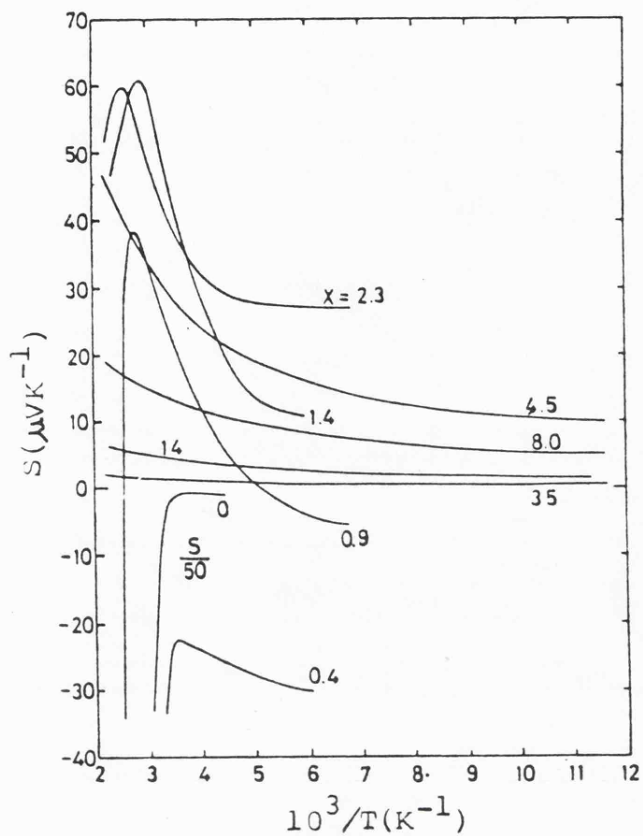


Fig 2.21 Thermopower vs  $10^3/T$  for  $ev-Si_{1-x}Au_x$  (75).

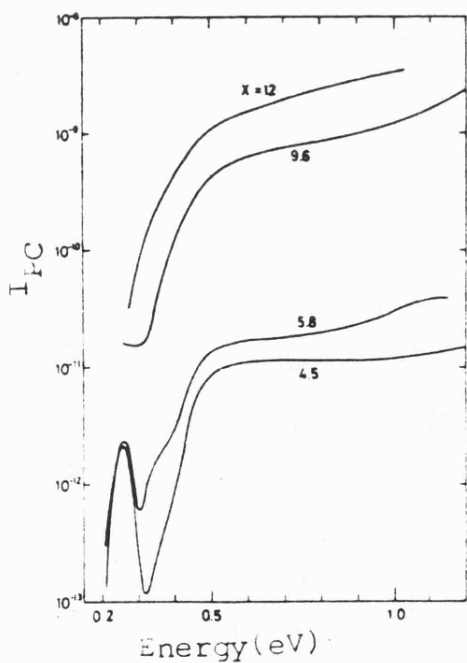


Fig 2.22 IR photoconductivity spectra at 77K for  $ev-Si_{1-x}Au_x$ . Thickness of the samples is  $1-x$  normalized to 2000Å. (68).

decrease in the spin density (fig. 2.23) and an increase in the peak-to-peak linewidth  $\Delta H_{pp}$  (fig. 2.24) with increase in gold content. The g-value of the signal is 2.006, and the lineshape is Lorentzian, just as observed in a-Si [81]. The results of fig. 2.23 can be explained in terms of gold acceptor impurities compensating the a-Si dangling bonds and hence reducing the number of unpaired spins. As the number of mobile electrons increases with x, if the spin-lattice relaxation rate of unpaired electrons is determined by its interaction with mobile electron, the recombination rate will increase with gold content and hence contribute to line broadening.

Spin-dependent conductivity measurements [82], conductivity change due to electron spin resonance and dielectric constant measurements [83] have also been made by the same authors in conjunction with the experiments mentioned above. By measuring the resistance change  $\Delta R$  due to electron spin resonance at 9GHz from 83 - 300K the data in fig. 2.25 were obtained. The resistivity decrease with ESR is interpreted in terms of a spin energy transfer process in which spin energy associated with ESR is transformed from localized spins to carriers and also by the variable-range hopping process in which hopping is enhanced by ESR. The dielectric constant,  $\epsilon$ , of the ev-Si:Au samples was derived by conventional capacitance measurements at low temperature. The asymptotic dielectric constant  $\epsilon_a = \epsilon_o + \epsilon_L$ ,  $\epsilon_o$  and  $\epsilon_L$  are the contributions to the dielectric constant from pure a-Si and localized electrons (or holes) associated with doped impurities, as a function of gold content is plotted in fig. 2.26. The rapid increases of  $\epsilon_a$  with x must be due to the localized electrons in the

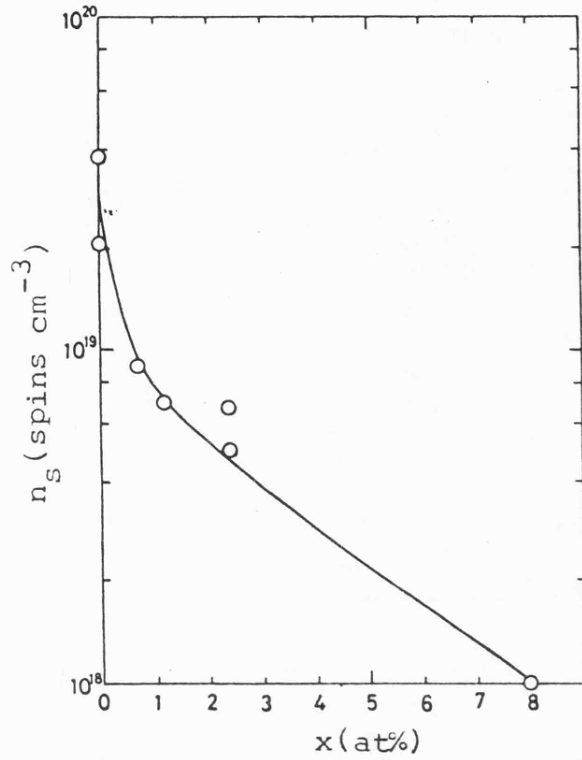


Fig 2.23 ESR vs x for ev-Si<sub>1-x</sub>Au<sub>x</sub>. (30)

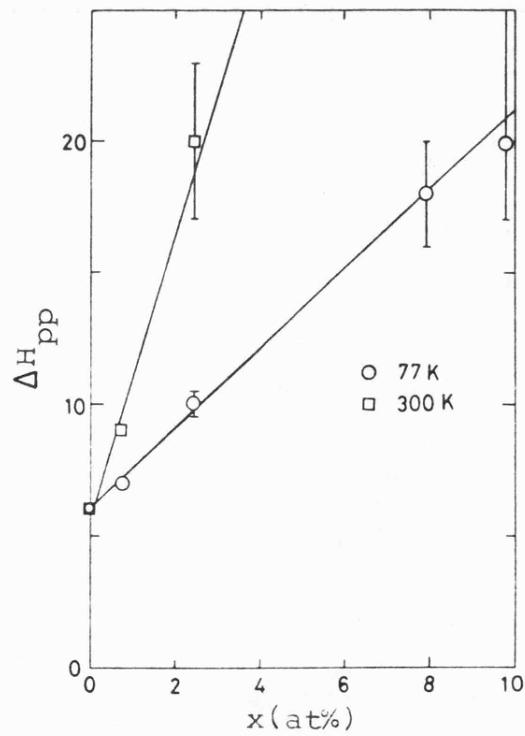


Fig 2.24 Peak-to-peak linewidth  $\Delta H_{pp}$  vs Au content x. (30).

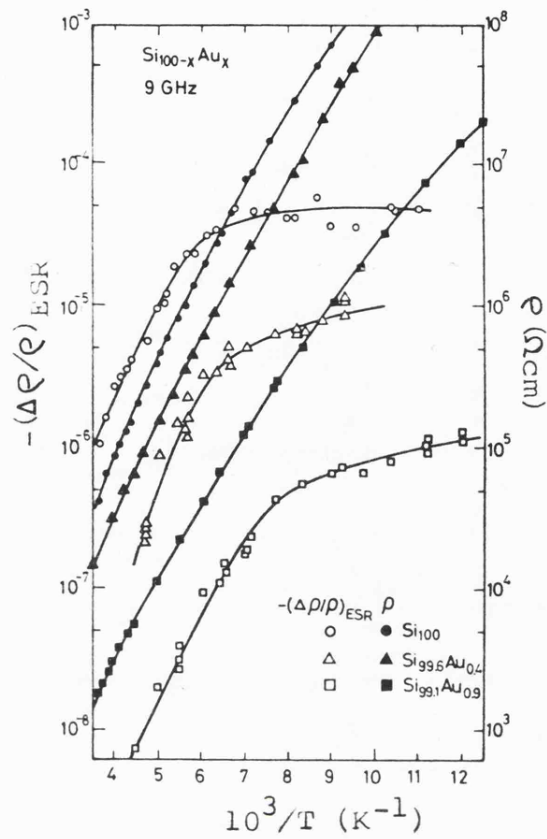


Fig 2.25 Spin-dependent conductivity vs reciprocal temperature for  $\text{ev-Si}_{1-x}\text{Au}_x$ . (75).

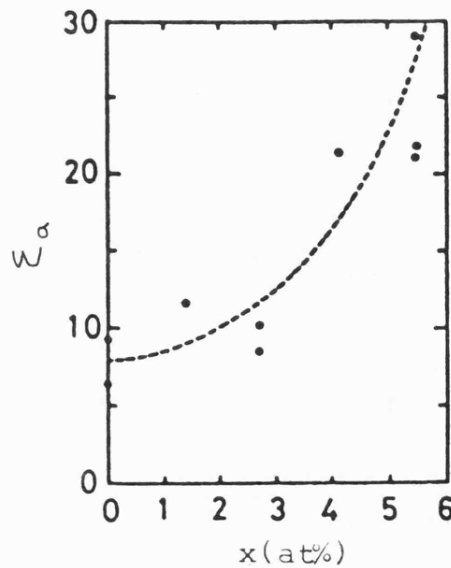


Fig 2.26 Dielectric constant vs Au content for  $\text{ev-Si}_{1-x}\text{Au}_x$ . (83).

Au impurity band, and hence  $\epsilon_L$ . This behaviour cannot be explained solely by the Clausius-Mossotti equation

$$\epsilon - \epsilon_0 = (4\pi N_i \alpha_p) / (1 - (4\pi N_i \alpha_p / 3\epsilon_0)) \quad (2.2)$$

when the impurity content  $N_i$  approaches a critical value of  $3\epsilon_0 / 4\pi \alpha_p$  where  $\epsilon_0$  and  $\alpha_p$  designate the dielectric constant of the host matrix and the polarizability of impurity atoms respectively. Sano et al [83] suggest the following argument to explain the deviation from (2.2). As the Au concentration is increased, the radii of the localized wavefunctions in the Au impurity band become more and more spread out, and the polarization of the impurity atoms is enhanced. Therefore,  $\epsilon_L$  increases rapidly producing the observed rise in  $\epsilon_a$  with  $x$ .

Optical absorption measurements have been made on sputtered [84] [78] and evaporated [68] amorphous films of Si:Au over a large frequency range. Non-crystalline sputtered metallic films of  $sp\text{-Si}_{1-x}\text{Au}_x$ , with  $0.5 < x < 0.87$ , have been examined from the infrared to the near ultraviolet, as can be seen in fig. 2.27, by Hauser et al [84]. Determination of the real and imaginary parts of the dielectric constant was from a Kramers-Kronig analysis of reflectivity data obtained at near-normal incidence. The low frequency data can be described by the Drude formula

$$\epsilon_D = 1 - \omega_p^2 / \omega (\omega + i/\tau) \quad (2.3)$$

where  $\omega_p^2 = 4\pi n e^2 / m^*$ ,  $n$  is the electron concentration,  $m^*$  is the electron effective mass and  $\tau$  is the relaxation time. The best agreement is obtained from a weakly-frequency-dependent  $\tau$ .

$$1/\tau = \omega \epsilon_2 (1 - \epsilon_1) = 1/\tau_0 + a(\hbar\omega)^2 \quad (2.4)$$

where  $a$  is a constant with a minimum close to the eutectic of

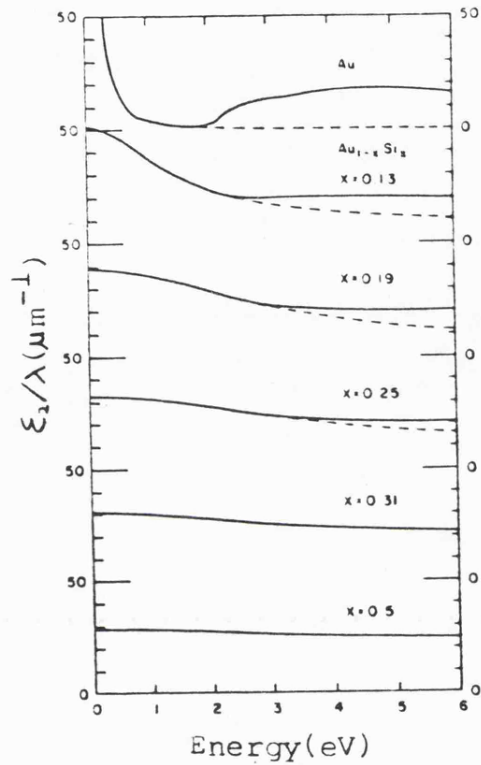


Fig 2.27 Optical absorption  $\epsilon_2/\lambda$  calculated from Kramers-kronig analysis(—) and from the Drude formula(-- ) of Au and a-Si<sub>x</sub>Au<sub>1-x</sub> alloys as a function of energy and composition. (34)

$a = 5 \times 10^{13} \text{ eV}^{-2} \text{ s}^{-1}$ . It can be seen in fig. 2.28 that  $\tau_0^{-1}$  decreases monotonically with decrease in gold content. The energy of the interband transitions, as opposed to the intraband transitions associated with Drude behaviour ( $E_0^{(2)}$  in fig. 2.28), also shows a steady increase with gold concentration. The energy difference,  $E^c$ , between the Au d band and the Fermi level position, as calculated from a simple rigid-band approximation assuming Au contributes one electron and Si four, shows reasonable agreement with the experimentally derived quantity  $E_0^{(2)}$ . The most striking features of the data in fig. 2.27 is the importance of intraband transitions over the whole spectral range and almost complete disappearance of the interband transitions. Since interband transitions, as in pure gold, we expected from the d band to the Fermi level in this system, resulting in a strong absorption in the optical absorption between 2 - 5eV. This effect increases with Si content to the point that samples with  $x = 0.31$  and 0.5 are almost completely described by the Drude term. This type of behaviour is tentatively described in terms of some of the d-band electrons contributing to the Drude term and subsequently reducing the strength of the interband transitions resulting from the very short relaxation lifetimes of electrons of definite momentum at the Fermi level.

Infrared absorption spectra of sputtered films, prepared in a similar manner, have been made over the composition range  $0.07 < x < 0.3$  [78]. A broad absorption band between 0.15 - 0.5eV is attributed to the presence of Au (fig. 2.29), below which the spectra are dominated by the vibrational absorption bands of a-Si and a-SiO<sub>2</sub>. The behaviour of the band was found to obey Mott's formula [ 7 ]

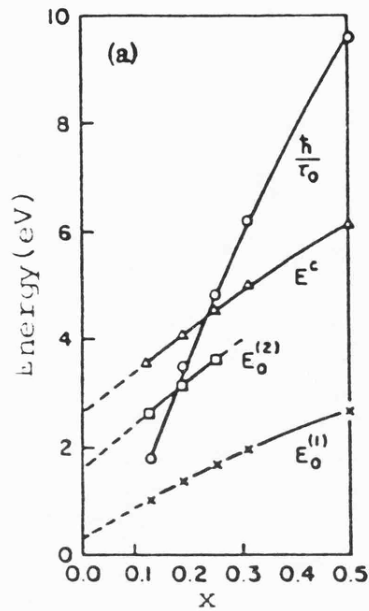


Fig 2.28 Onset of interband transitions for  $\text{Si}_{1-x}\text{Au}_x$  as a function of x compared with  $n/r_0$ .

- $E_0^{(1)}$  = energy of inflection point in reflectivity curve.
- $E_0^{(2)}$  = onset of interband transitions
- $E_c$  = energy calculated with the rigid-band approximation. (84).

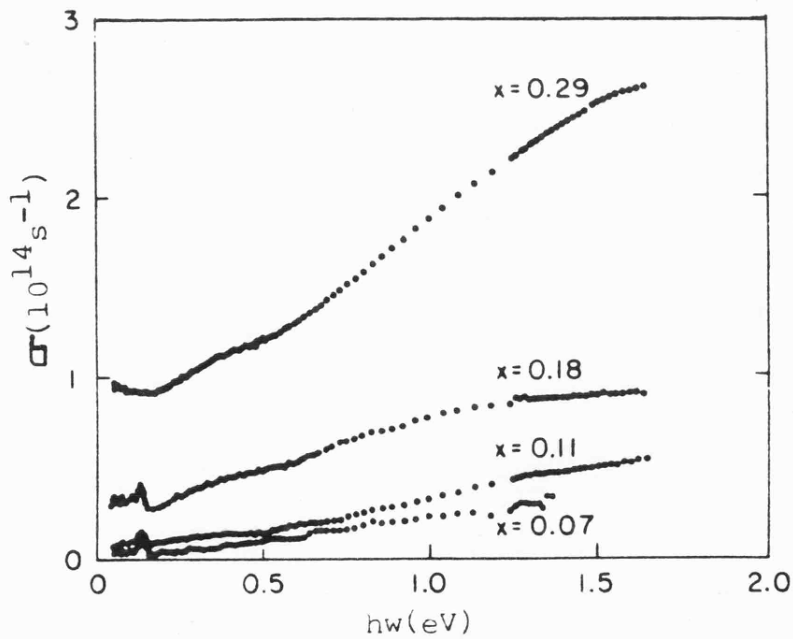


Fig 2.29 Optical conductivity vs photon energy for sp- $\text{Si}_{1-x}\text{Au}_x$  alloys. (78).

$$\sigma(\omega) = e^2 \pi \hbar \omega^2 \alpha^{-5} [N(E_F)]^2 [\ln(I_0/\hbar\omega)]^4 \quad (2.5)$$

where  $\alpha^{-1}$  is the width of the localized wavefunction and  $N(E_F)$  is the density of states of the Fermi level. The absorption is due to a transition in a pair of Au atoms between the states corresponding to the even and odd combinations of their wavefunctions. The energy difference between these states  $I$  is expressed as  $I_0 \exp(-\alpha R)$  where  $R$  is the distance between the centres.  $N(E_F)$  values determined from d.c. conductivity measurements are considerably larger than those obtained from equation (2.5) and experimental optical data, assuming  $\alpha^{-1}$  is the same in both cases. This discrepancy is due to the non-homogeneous nature of the alloy films.

The absorption coefficient has been measured for  $\text{ev-Si}_{1-x}\text{Au}_x$ ,  $0 < x < 0.55$  in the visible (0.5 - 3eV) [68]. The absorption spectra of fig. 2.30 can be broadly divided into two regimes,  $x < 0.3$  and  $x > 0.3$ . For concentrations below 30at% Au the shape of the spectra is similar to that commonly observed for amorphous semiconductors; a high energy region, exponential edge and a low-energy defect tail. The absorption coefficient can be expressed in the form  $(\alpha \hbar\omega)^{\frac{1}{2}} \alpha(\hbar\omega - E)$  as indicated in fig. 2.30, implying that the density of states (to a first approximation) of the host bands are parabolic. The convergence of absorption coefficients for  $x < 0.1$  at 3.0eV is considered to be determined mainly by the Si-Si bond from its insensitivity to Au content. The decrease in optical gap is seen as a result of the weakening of the silicon covalent bond with Au concentration. The existence of a finite

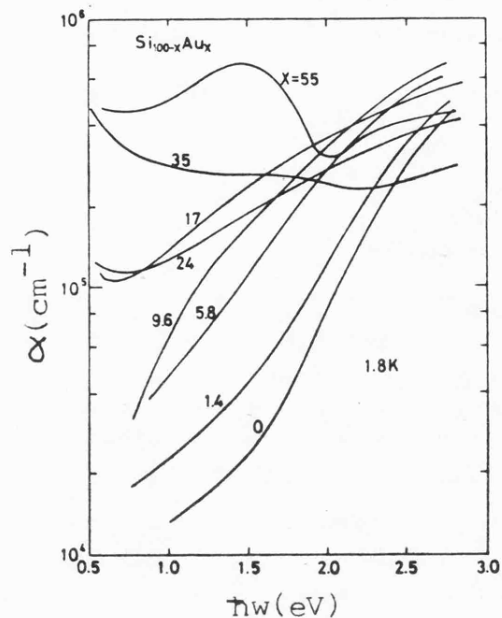


Fig 2.30 Optical absorption spectra at 1.8K for samples of ev-Si<sub>100-x</sub>Au<sub>x</sub> with various Au concentrations. (68)

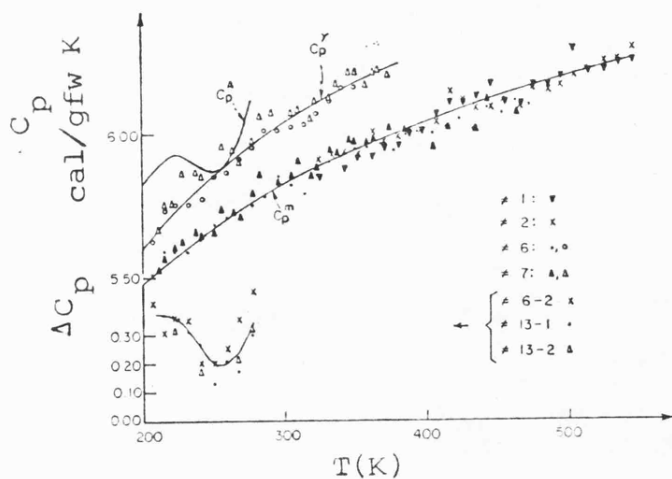


Fig 2.31 Specific heat  $C_p$  of g-Au<sub>31.4</sub>Si<sub>13.6</sub>, where  $\Delta C_p = C_p^A - C_p^m$ . A denotes the amorphous phase; m the solid mixture; Y the intermetallic phase. (72).

optical gap for gold concentrations greater than the 14 at% required for the Metal-Insulator-Transition to occur is due to thermal excitation of carriers from the impurity band to the host band. The M.I.T. is not associated with the disappearance of the host energy gap, but with the transition from localized to extended states in the impurity band as discussed previously. The behaviour of the absorption coefficient, for  $x > 0.3$ , as a function of photon energy changes dramatically. The increase of absorption coefficient at longer wavelengths, as opposed to the behaviour observed for  $x < 0.3$  is interpreted as free-carrier absorption. As microcrystallites of Au are known to exist in this type of material, as described in 2.2.2, the free-carrier effects may not be due to the amorphous Si:Au alloy. It should be noted that the peak at 1.5eV for  $x = 0.55$  is similar to that in pure Au thin films, consisting of very small crystallites, prior to annealing. This peak is attributed to imperfections or impurities in Au [85].

#### 2.2.4. Other properties

The Specific heat,  $C_p$  of  $g\text{-Si}_{0.186}\text{Au}_{0.814}$  has been measured in the temperature range 208 - 278K [72]. At temperatures above 278K the alloy transforms into a metastable crystalline phase  $\delta$ . As indicated in fig. 2.31  $C_p$  rises slowly to 225K, then falls, and then rises again with increasing temperature. It exceeds  $C_p$  of the eutectic solid by 0.2 - 0.4cal/gfw K and is about 0.2 cal/gfw K higher than the  $\delta$  phase at low temperatures. This data, in conjunction with results of measurements on the liquid, indicates that there is a strong tendency for gold and silicon atoms to associate with each other in the metallic state and phase separation to occur in the solid

due to the high stability of silicon in its covalent crystalline form.

Magnetoresistance [75] and Magnetic susceptibility [70]

studies have been performed on samples over a limited range of composition. Some preliminary measurements on magnetoresistance have been made on evaporated non-crystalline films of  $\text{ev-Si}_{1-x}\text{Au}_x$  in the non-metallic region by Morigaki et al [75] (fig. 2.32). The authors suggest that the change from the observed behaviour in a-Si, which is explained in terms of spin-flip hopping of localized electrons [86] associated with dangling bonds, when Au is added is due to hopping conduction taking place in the gold band near the Fermi level. The spin relaxation behaviour of these hopping electrons is expected to differ markedly from the case of dangling bonds in pure a-Si, though a detailed explanation has yet to be proposed. The temperature dependence of the diamagnetic susceptibility of a sputtered amorphous thin film of  $\text{sp-Si}_{0.19}\text{Au}_{0.81}$  has been reported by Hauser and Tauc [70]. Taken in conjunction with magnetic susceptibility measurements on  $1 - \text{Au}_{0.91}\text{Si}_{0.19}$  [87], these authors suggest (fig. 2.33) that the extrapolation from the supercooled liquid to solid indicates similarities between the phases. The increase in the susceptibility at low temperatures is due to a low level of paramagnetic impurities.

Auger Electron Spectroscopy (AES) has been used to investigate the change in the electronic state of the silicon valence electrons with gold concentration by careful study of the silicon (LVV) Auger transition [88]. Fig. 2.34 shows the silicon (LVV) transition for

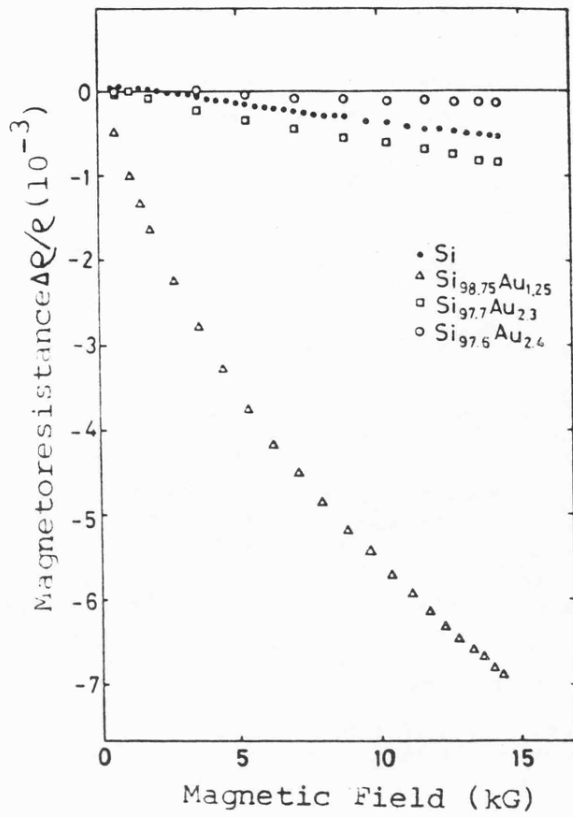


Fig 2.32 Magnetoresistance,  $\Delta\rho/\rho$  (at 300K) vs magnetic field for  $\text{ev-Si}_{100-x}\text{Au}_x$ . (75).

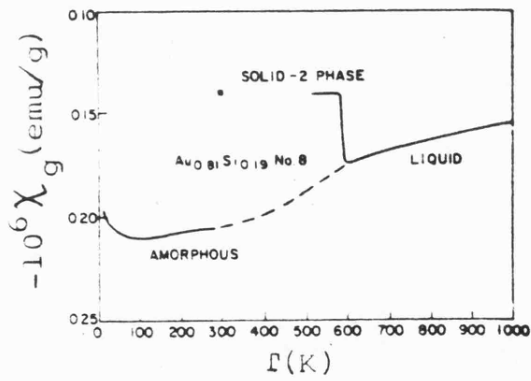


Fig 2.33 Variation of the diamagnetic susceptibility of a-, l-, and c-(two phase solid) with temperature. (70).

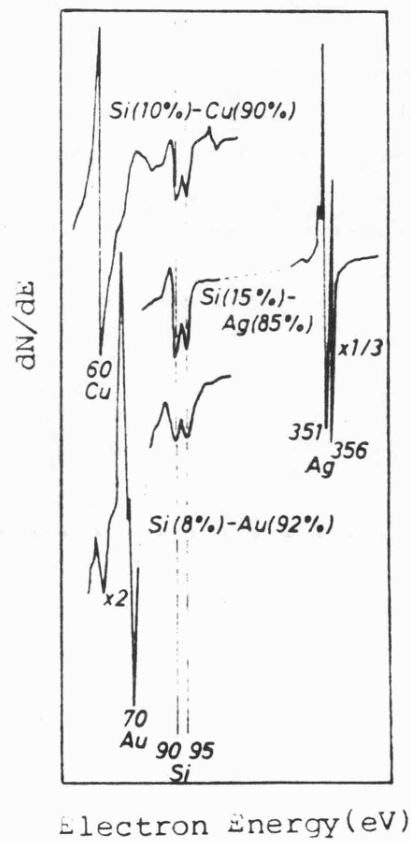


Fig 2.34 Si(LVV) Auger peaks observed in evaporated Ag-Si,Au-Si,Cu-Si.( 88 ).

a-Si (a single peak at 92eV) and  $\text{ev} - \text{Si}_{0.23}\text{Au}_{0.77}$  (with two peaks at 90 and 95 eV). Only for samples with  $x > 0.7$  is the splitting observed in the Auger spectra. This is seen as indicating that the silicon atoms are metallic as one would expect to see in a true frozen - Si:Au liquid. There is a strong tendency for Au-Si bonding in the gold-rich structures, as discussed above, ie for  $x > 0.7$ , though, with increase in silicon content, covalent Si-Si bonds are more readily formed and the single Auger peak at 92eV is observed.

Photoemission measurements on a-Si:H and a-Si<sub>1-x</sub>Au<sub>x</sub>:H will be reported in Chapter 5.

### 2.3 Amorphous silicon M - a brief review

Much of the early work on doping a-Si:H was concerned with the incorporation of shallow impurity centres, such as P and B, into the silicon host, primarily by the glow-discharge technique. In this section a-Si:M applies to a-Si and a-Si:H doped or alloyed with noble or transition metals, which in general behave like deep-level impurities. Table 2.1 summarizes some non-crystalline a-Si:M materials that have been prepared by a number of techniques. It is apparent that a wide range of elements have been incorporated into a-Si, though only Mn alloyed with a-Si:H for doping and alloying purposes. Unfortunately a number of these studies have been brief, preliminary investigations and hence are of limited use for comparative purposes and for determining trends.

Table 2.1

a-Si:M

M	deposition method	electronic configuration	reference
Cu	ev	$3d^{10} 4s^1$	88, 89
Ag	ev	$4d^{10} 5s^1$	88
Mn	sp	$3d^5 4s^2$	90, 91
Fe	sp, ev	$3d^6 4s^2$	90, 92
Co	ev	$3d^7 4s^2$	93
Ni	sp	$3d^8 4s^2$	90
Nb	sp	$4d^4 5s^1$	94
Mo	sp	$4d^5 5s^1$	95
Rh	annealing	$4d^8 5s^1$	96
Pd	g, LMQ	$4d^{10} 5s^0$	97, 98
Ta	ev, sp	$5d^3 6s^2$	99
Pt	LMQ	$5d^9 6s^1$	98

Very little work has been published on the other amorphous silicon - noble metal systems: a-Si:Ag and a-Si:Cu. Auger Electron Spectroscopy (AES) was used by Hiraki et al [88] to study evaporated a-Si<sub>0.1</sub>Cu<sub>0.9</sub> and a-Si<sub>0.15</sub>Ag<sub>0.85</sub> thin films and hence to determine the nature of the chemical state of silicon from the energy and shape of the Auger peaks. The Si (LVV) spectra of both ev -Si:Ag and ev -Si:Cu alloys show essentially the same split peaks at 90 and 95eV as seen in the Si:Au (see fig. 2.34). The splitting of the silicon peak is taken as indicating the valence electronic state of metallic silicon in these alloy systems, though why the splitting occurs in this manner is not known at present.

A detailed Transmission Electron Microscope (TEM) study on ev - Si<sub>1-x</sub>Cu<sub>x</sub> (0 < x < 0.76) has been carried out by Suto et al [89] on electron-beam evaporated Si-Cu at 77K, with particular emphasis on the crystallization process. For the amorphous films ultra fine structure, cellular regions ~ 20Å in diameter surrounded by irregular white rims, were observed. These features may correspond to density-deficient regions or surface roughness due to the nature of the deposition process. Crystallization occurs in a series of steps:

- 1) ~ 100°C, crystallization of the  $\eta$ ' phase (SiCu<sub>3</sub>) is initiated
- 2) ~ 450°C, Si crystallizes; this is over 100°C below the crystallization temperature of pure a-Si
- 3) ~ 500°C, recrystallization of the alloy occurs in the form of equi-axial grain growth and whisker formation. Unfortunately no electrical or optical measurements were performed by these authors on their amorphous films.

Chemical modification of amorphous silicon by addition of a

transition element has been attempted by a number of groups using a variety of deposition techniques as indicated in Table 1. A comprehensive study of a-Si:Mn, Fe and Ni alloys, prepared by high-temperature sputtering, has been carried out by Shimizu et al [90] [91], and conductivity, optical absorption, ESR and thermopower measurements made. The semiconducting films, with metal content 0.1 - 10 at% all displayed variable-range-hopping conduction behaviour. Room temperature conductivity increases with transition element content, though for low impurity levels it is strongly dependent on the argon sputtering pressure (fig. 2.35). Hydrogenation of the Mn alloys results in a significant drop in conductivity for low Mn concentrations (< 1 at%), above which behaviour similar to the argon-sputtered films occurs. The optical gap and the centre density of the ESR signal due to dangling bonds with  $g = 2.0055$  decreases with increase in transition element content. From these measurements, and a small thermoelectric voltage  $\sim \pm 20 \mu\text{V K}^{-1}$  between 300 - 450K, these authors suggest that an impurity level, due to the addition of metallic impurities, is formed near the centre of the gap and the Fermi level is pinned within it. In contrast to the ESR measurements on the ev -Si:Au system, ESR signals due to the transition elements themselves were observed at low temperatures.

Conductivity measurements on metastable crystalline Si:Ni and Si:Co films [93] which exhibit variable-range-hopping transport reveals an exponential decrease in the hopping parameter  $T_0$  as a function of transition element concentration, as observed in the Si:Au system [75]. These authors attribute this behaviour to a linear decrease in the energy gap as a function of transition element

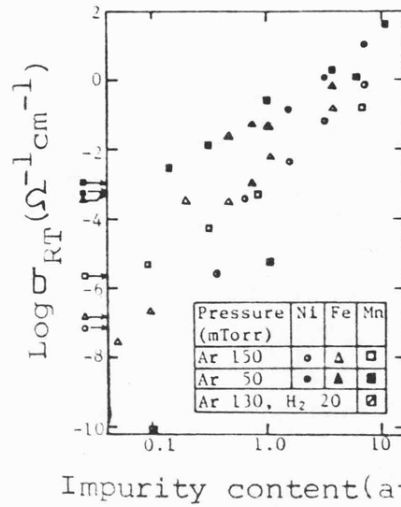


Fig 2.35 The electrical conductivity at room temperature  $\sigma_{RT}$  vs transition element content. Arrows at the ordinate show  $\sigma_{RT}$  for samples without transition element. (90).

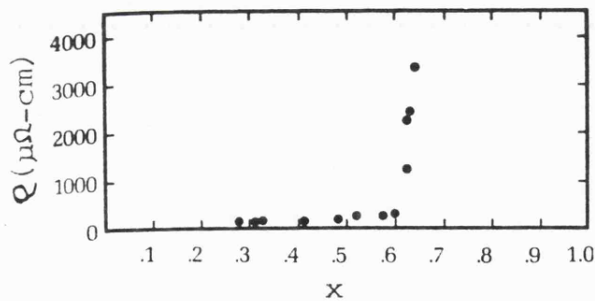


Fig 2.36 Resistivity vs Mo concentration for  $a\text{-Mo}_{1-x}\text{Si}_x$  films. (95).

concentration. This is in contrast with the suggestion of Morigaki et al [75], who describe the exponential dependence in Si:Au as being the result of the decay length of localized wavefunctions of the hopping electrons around the Fermi level which is expected to increase exponentially with the impurity content.

Amorphous silicon-molybdenum [95] and silicon-niobium [94] alloys have been prepared from semiconducting to metallic compositions by co-sputtering in argon. Amorphous  $sp\text{-Si}_{1-x}\text{Mo}_x$  ( $0.23 < x < 0.73$ ) films exhibit superconductivity down to at least 36 at% Mo and at  $x \approx 0.33$  show an abrupt increase in resistivity accompanied by semiconducting behaviour (fig. 2.36). It is suggested that this metal-non-metal transition could be attributed to the conversion of metallically bonded silicon to covalently bonded silicon. There are indications that samples with low Mo content are inhomogeneous; hence data on the semiconducting regime may not be representative of a true  $sp\text{-Si:Mo}$  alloy

Tunnelling and conductivity measurements on amorphous  $\text{Si}_{1-x}\text{Nb}_x$  ( $0.04 < x < 0.2$ ) [94], through the M.I.T., indicate that no minimum metallic conductivity exists in this system. As the Nb concentration is decreased  $\sigma(0)$  decreases smoothly to zero for 11.5 at% Nb. Superconductivity is observed in samples with  $x > 0.18$  and for 20.5 at% Nb, the superconductivity transition temperature  $T_c = 280\text{mK}$ .

With the exception of Si:Pd near the eutectic composition [97], the other transition element impurities Rh, Ta and Pt in a-Si [96] [99] [98] have only been studied in a very limited manner. Only the stability of the alloys, and in some cases crystallization mechanisms, have been investigated.

## CHAPTER 3

### Experimental Methods

- 3.1 Film preparation
  - 3.1.1 Sputtering process
  - 3.1.2 Sputtering system
  - 3.1.3 Preparation conditions
- 3.2 Electronic transport measurements
  - 3.2.1 D.C. "dark" conductivity
  - 3.2.2 Thermoelectric power
- 3.3 Optical measurements
  - 3.3.1 Visible-Ultraviolet
  - 3.3.2 Infrared
- 3.4 Electron microscopy
- 3.5 Other measurements

### 3.1 Film preparation

Amorphous semiconductor-metal alloys have been prepared by a variety of different techniques; evaporation, glow-discharge decomposition of a gas and sputtering being the most popular. The method chosen for this investigation was that of r.f. reactive sputtering, a versatile technique which allows deposition of thin films of metals, insulators and even polymers.

#### 3.1.1 The sputtering process

A low-pressure gas discharge (plasma) can be sustained in a vacuum chamber, containing a partial pressure of an inert gas such as argon, by the application of an r.f. field between two electrodes, an anode and cathode. Owing to the difference in mobilities of the electrons and ions created in the plasma (see fig. 3.1), the electrons being the more mobile, more electrons are attracted to the front surface of the target on the cathode during the positive half of the r.f. cycle than are ions in the negative half cycle. The resultant electron current causes the target surface to acquire a negative bias voltage  $V_B$  for most of the r.f. cycle. The potential on the target surface after a few r.f. cycles can be described as an r.f. potential with a superimposed negative d.c. bias.

Ions in the luminous part of the plasma<sup>4</sup> move around in a random motion. Only those positive ions that enter the target sheath are accelerated to the target (essentially by the bias potential  $V_B$ ) and bombard the target with an energy of the order of  $V_B$  electron volts. In fig. 3.2 the various processes that occur following the ion bombardment of the target are indicated [100]. Target material is emitted

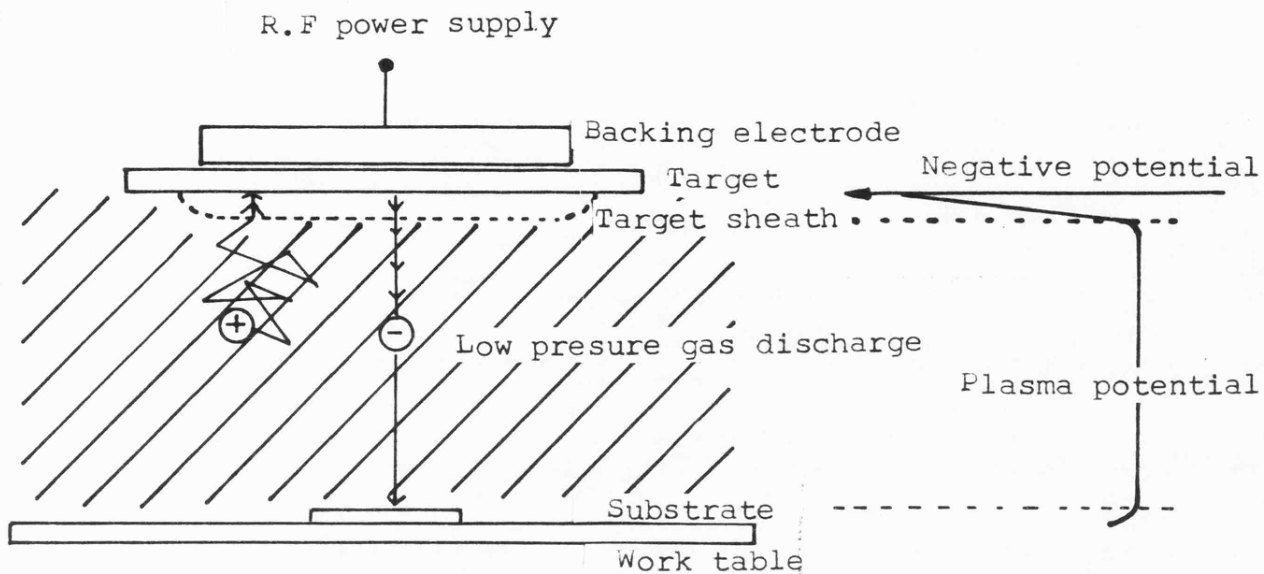


Fig 3.1 Schematic diagram of an r.f sputtering electrode arrangement and potential distribution.

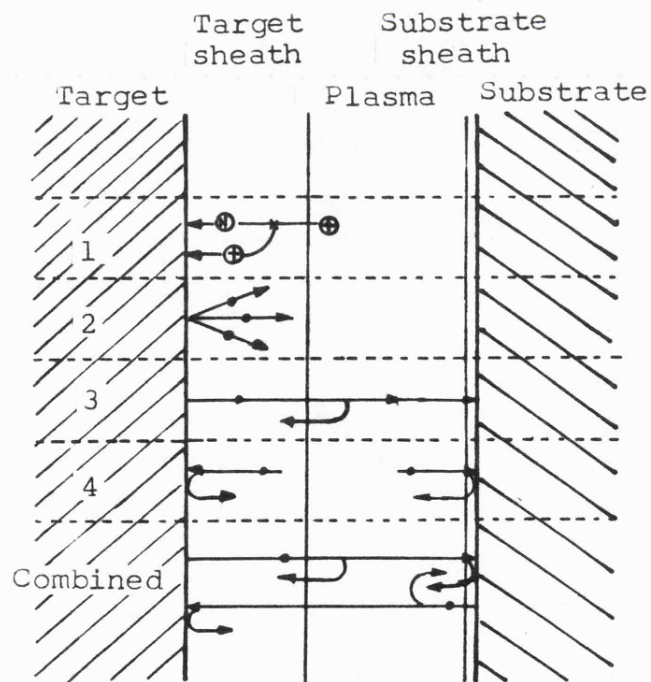


Fig 3.2 Physical processes involved in sputtering(100 )

(2) following bombardment by ions and neutrals (1). In (3) the sputtered material is transported through the plasma to the anode (substrate table) and some backscattering occurs with gas atoms, and finally in (4), when the material reaches the substrate table, re-emission of the target material occurs due to the analogous bombardment of the substrate from ions accelerated through the substrate sheath. This process of re-emission of material deposited on the substrate table can be controlled to some extent by applying a d.c. bias to the substrate electrode, a procedure known as bias sputtering. Several groups, in the United Kingdom (Sheffield) and abroad (Xerox and Lyons) are investigating the influence of a d.c. substrate bias on the quality of sputtered hydrogenated amorphous silicon. Although these studies are in their early stages it seems that bias sputtering offers yet another valuable parameter that can be tuned to obtain high-quality amorphous silicon [101].

By coupling the r.f. power to the substrate electrode and earthing the target, or more usually placing an earthed shutter between target and substrate electrodes, the substrate table can be "sputter-etched". Hence prior to deposition of a film the substrate surfaces may be cleaned by removing the first few atomic layers by ion bombardment. Through the application of photolithographic techniques, line definitions of better than  $1\mu\text{m}$  can be achieved by sputter etching.

### 3.1.2 The sputtering system

The basis of the sputtering system employed in this work was a commercially available Nordiko NM-2000-T8-SE1 sputtering module. (Nordiko Ltd., Havant). Various modifications have been made since its

commissioning in 1980 to tailor the system for the production of amorphous thin films of high purity on a variety of different types of substrates simultaneously. The initial aim was to produce films for structural, optical and electronic measurements, with the necessary electrode fabrication, in one pump-down cycle to minimize variations in preparation conditions in nominally similar films.

Figure 3.3 and the accompanying photograph (Plate 3.1) display the complete system. The stainless steel chamber, 22" in diameter by 15.8" high, contains a multielectrode turret with two sputtering electrodes, one of which is a high-rate magnetron source, and an evaporation source. The electrode is simply chosen by rotation of the turret. The substrate electrode uses a 'lock in' removable copper platen for easy access to samples. This electrode may be heated to  $\sim 400^{\circ}\text{C}$  by a heating element or cooled to nitrogen temperatures by passing  $\text{LN}_2$  through a channel in the electrode. Thermal contact between platen and anode assembly is assisted by the insertion of thin copper gaskets.

The chamber was pumped by a Varian VHS - 6 oil diffusion pump, with a liquid-nitrogen cold trap, backed by a Laybold-Heraeus D60A direct-drive rotary pump. Chamber pressure below  $10^{-7}$  Torr were obtainable by prolonged pumping over approximately one day.

Gas flow into the chamber was controlled by a Vacuum General 78-7 flow ratio and pressure control system, the absolute chamber pressure being measured by a Vacuum General CM capacitive manometer gauge. The analogue signal from the manometer head was fed to the 78-7 which operates piezoelectric valves to maintain chamber pressure.

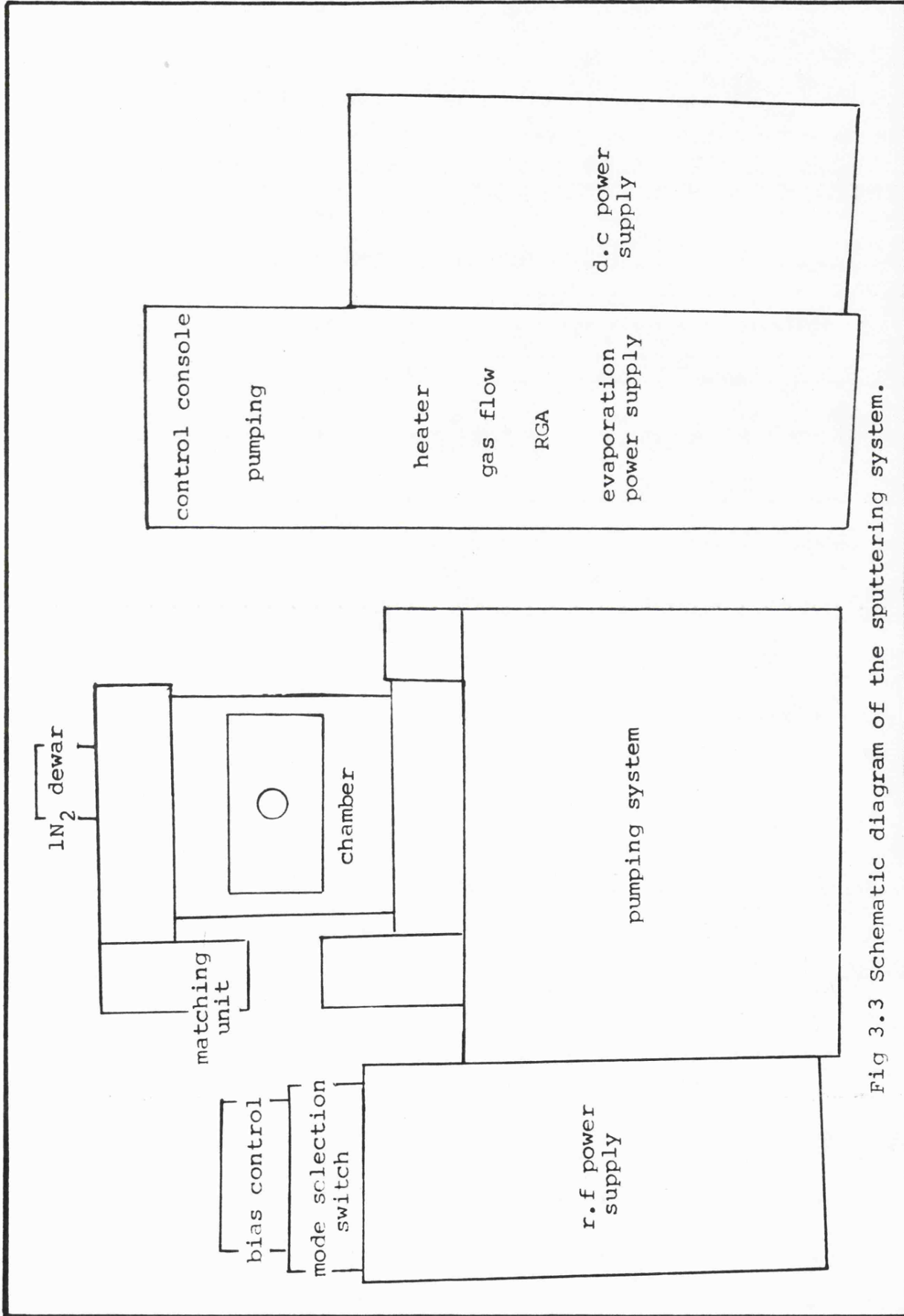
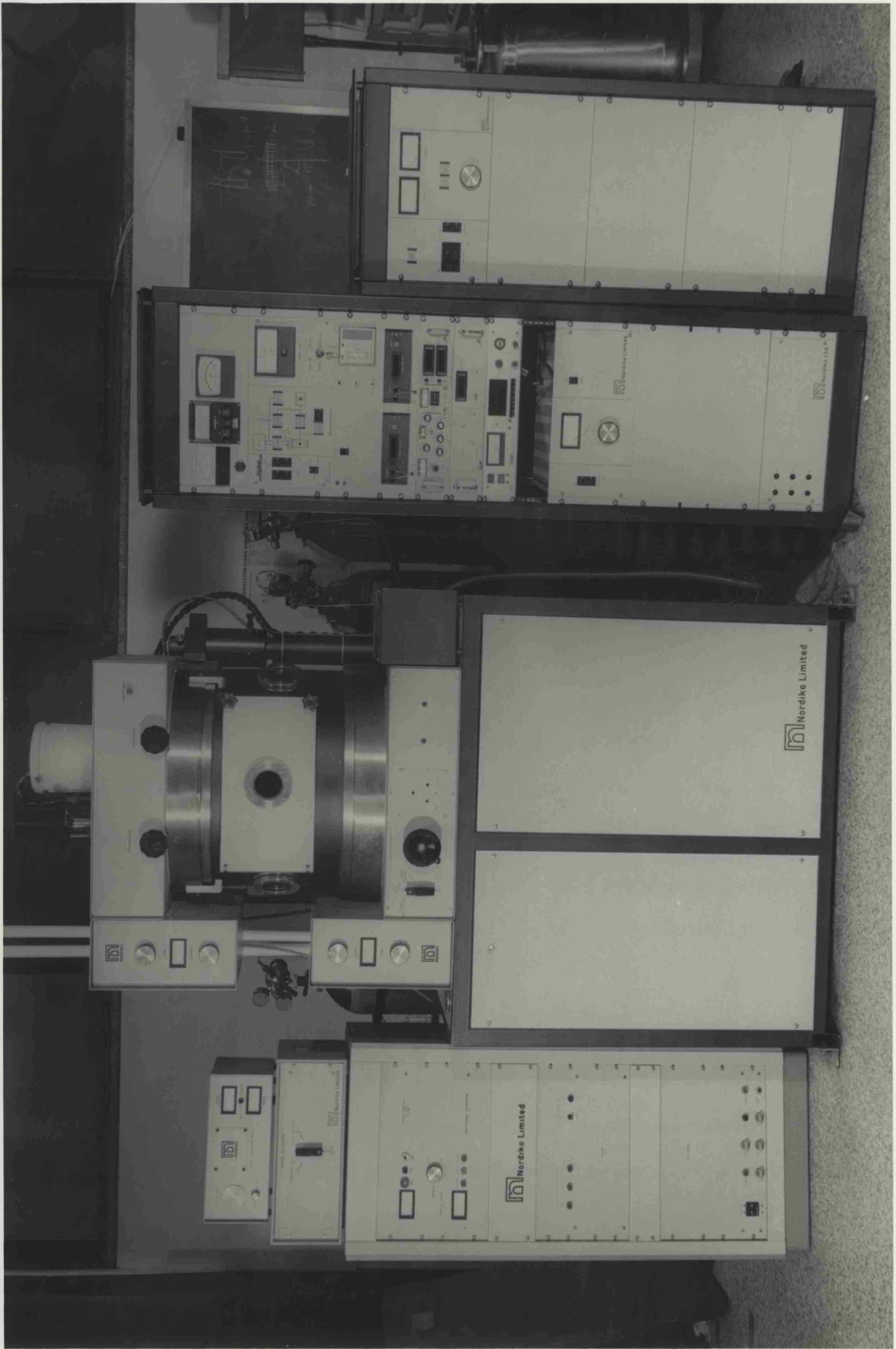


Fig 3.3 Schematic diagram of the sputtering system.

Plate 3.1 The sputtering system.



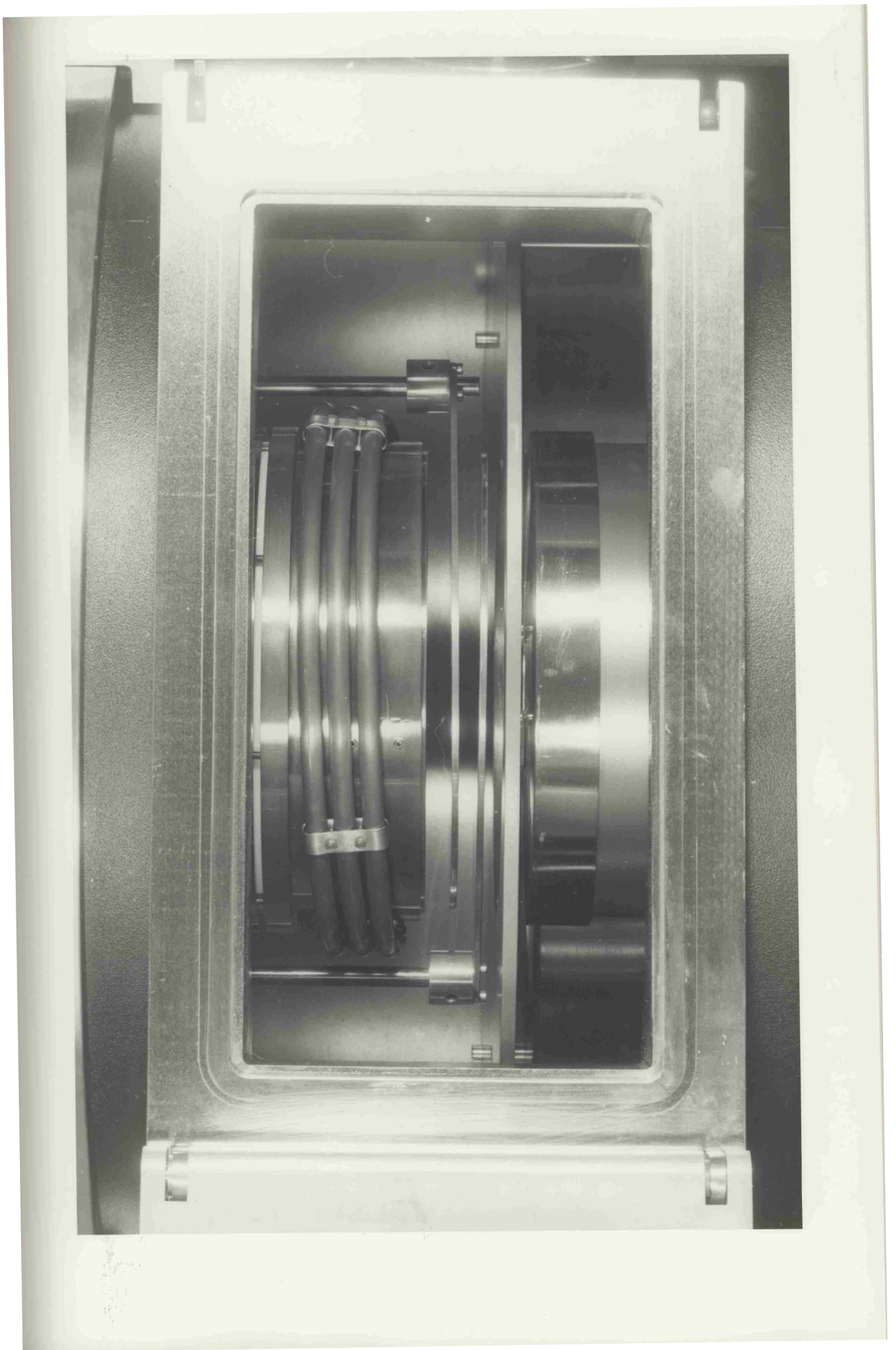
Care was taken to isolate both the manometer gauge head and the piezoelectric valves from r.f. pick-up which could result in spurious readings.

The interior of the chamber was modified in order to reduce contamination and maintain reproducibility between runs. To assist pumping, a Meisner coil of copper tubing was installed around the substrate table (see Plate 3.2). This noticeably reduced the  $H_2O$  and  $OH$  content of the chamber. The original substrate platen was replaced by an improved version which was designed and built in the Department of Physics in Leicester. To maintain stable temperatures  $\lesssim 1^\circ C$  the thickness of the oxygen-free copper was increased to 1cm with an insert for a thermocouple drilled into the side of the platen. Substrates were held in position by a stainless steel contact mask, with the substrate for electron microscopy being held beneath a shutter mechanism which could be opened and closed during a run. Thermal contact between substrates (Corning 7059 glass (24 x 24 x 1mm) or polished crystalline silicon) and the surface of the copper platen was maintained by insertion of several layers of thin aluminium foil, which also reduced the possibility of cracking the 7059 substrates when the contact mask was being tightened.

A series of aluminium evaporation masks, again of the contact type, were arranged to be rotated into position and finally lifted to locate into position on the stainless steel substrate sputtering mask (fig. 3.4). The evaporation source was itself masked down to maintain a beam of gold atoms just large enough to cover the substrate area. Thus gold contamination of the substrate table and substrate mask was eliminated.

Temperature control of the substrate platen and hence the

Plate 3.2 A view of the substrate electrode,  
surrounded by the meissner coil, two  
shutters and the evaporation source.



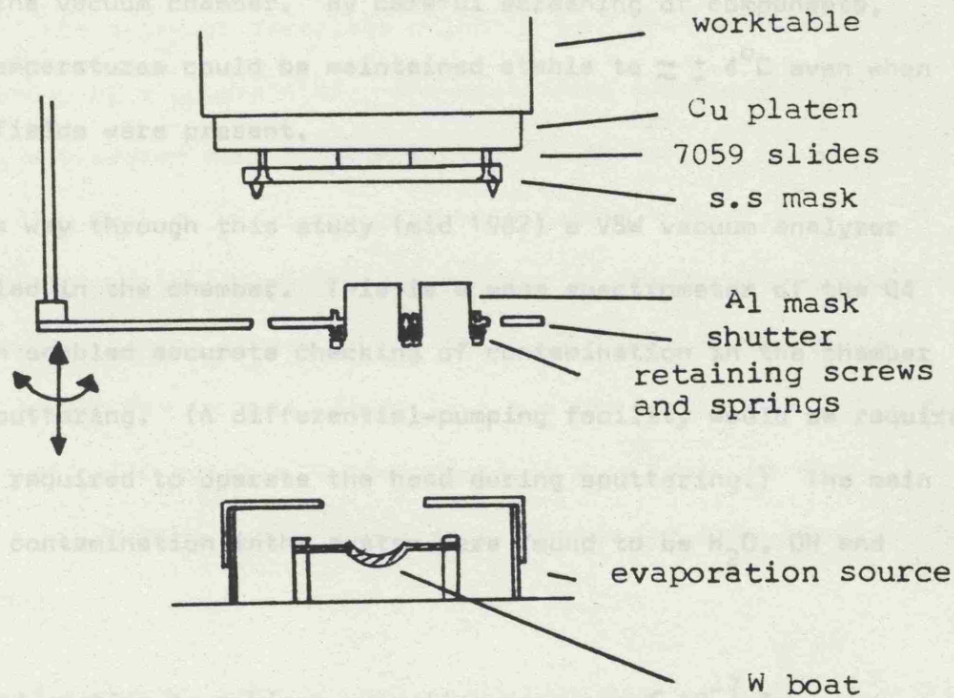


Fig 3.4 Electrode masking arrangement.

### 3.1.3 Evaporation conditions

Care was taken to reduce the possibility of life contamination. Prior to sputtering the chamber was pumped down to  $5 \times 10^{-7}$  torr and checked for contaminants, especially  $O_2$ , by the VSW vacuum analyzer. Zero-grade hydrogen and argon were then passed into the chamber through stainless steel tubes and the sputtering pressure and the flow controlled by the VG 78-7 which was suitably screened from r.f. radiation. The

substrates was obtained by a Eurotherm Temperature Controller and a 2kW transformer using two chromel-alumel thermocouples for the reference signal. One thermocouple was situated on top of the substrate heater (outside the vacuum) and the second thermocouple was positioned, electrically insulated by quartz tubing, inside the copper platen in the vacuum chamber. By careful screening of components, elevated temperatures could be maintained stable to  $\approx \pm 4^{\circ}\text{C}$  even when high r.f. fields were present.

Some way through this study (mid 1982) a VSW vacuum analyser was installed in the chamber. This is a mass spectrometer of the Q4 type, which enabled accurate checking of contamination in the chamber prior to sputtering. (A differential-pumping facility would be required if it were required to operate the head during sputtering.) The main sources of contamination in the system were found to be  $\text{H}_2\text{O}$ , OH and some  $\text{N}_2$ .

Pumpdown time to achieve operating pressure  $\lesssim 10^{-7}$  Torr was reduced by admitting oxygen-free nitrogen prior to bringing the chamber up to air and also by minimizing the time when the chamber was open to air.

### 3.1.3 Preparation conditions

Care was taken to reduce the possibility of film contamination. Prior to sputtering the chamber was pumped down to  $\lesssim 10^{-7}$  Torr and checked for contaminants, especially  $\text{O}_2$ , by the VSW vacuum analyser. Zero-grade hydrogen and argon were then passed into the chamber through stainless steel tubes and the sputtering pressure and the flow controlled by the VG 78-7 which was suitably screened from r.f. radiation. The

standard operating pressure for sputtering was  $\sim 7.4\text{mTorr}$  absolute with 30% $\text{H}_2$ .

Targets throughout this investigating were, unless otherwise stated, floated-zone (FZ) single-crystal 4" x  $\frac{1}{4}$ " intrinsic silicon discs purchased from Wacker Chemi Ltd. They were bonded by silver cement (Cerac Ltd.) onto a copper baseplate which in turn was attached to the cathode assembly by a copper stud. The sputtering electrode, nominally 8" diameter, was masked down to accommodate the 4" targets by using a steel earth ring with an aperture marginally larger than 4" but sufficiently wide so that arcing did not occur at the pressures employed. For co-sputtering, small pieces of the metal in question were evenly distributed across the target. Prior to a run the target was etched for  $\sim 30$  minutes with 200 watts r.f. power ( $\sim 2.47\text{ W cm}^{-2}$ ) with an argon pressure of  $\sim 15\text{-}20\text{mTorr}$ ; this appeared to remove the  $\text{SiO}_2$  layer on the target surface.

Several types of substrate materials were used to enable electrical transport, optical, composition and structural measurements to be made on thin films deposited during the same run. Conductivity, thermopower and visible-ultraviolet spectroscopy measurements were made on films deposited on Corning 7059 glass. Films for I.R. spectroscopy were deposited onto highly polished crystalline silicon single crystals. The electron microscopy (EM) samples were deposited onto the freshly cleaved surface of a LiF single crystal or carbon-coated mica. (The preparation of the samples for EM will be discussed in further detail in 3.4) Photoelectron spectroscopy and compositional measurements were limited to films deposited onto either aluminium foil or highly polished stainless steel slides.

Following the sputter etch of the target, with the cathode shutter

in place, the standard sputtering conditions outlined above were set up without letting the discharge extinguish. Removal of the cathode shutter started the sputtering of material up to the substrates. Substrate-to-target separation used throughout this work was 5.5cm.

On a number of occasions a gentle sputter etch of the substrates was carried out before deposition was commenced; standard conditions would be  $\sim 20\text{W}$  r.f. power, argon pressure  $\sim 20$  mTorr for 10-15 seconds. This was deemed to be unnecessary as no observable difference in the quality of the films could be detected if the substrates were suitably cleaned prior to loading into the chamber.

### 3.2 Electrical transport measurements

#### 3.2.1 D.C. conductivity

Gold electrodes were evaporated onto the samples from a tantalum boat in the sputtering system using the contact mask arrangement previously described. A gap-cell geometry was in general used in both the four- and two-probe forms for conductivity measurements. In a number of cases a sandwich-cell geometry was employed and the results compared favourably with those from the gap-cell geometry. Several gap-cell configurations were used with separations ranging from 0.8 to 8mm. Contacts were made to the electrodes using fine copper wire attached by 'silver dag' conducting paste.

D.C. dark conductivity measurements were made in two separate systems. A cryostat was designed and built for conductivity and thermopower measurements between 470K and 100K. For measurements between room temperature and 4.2K a continuous-flow helium cryostat was used.

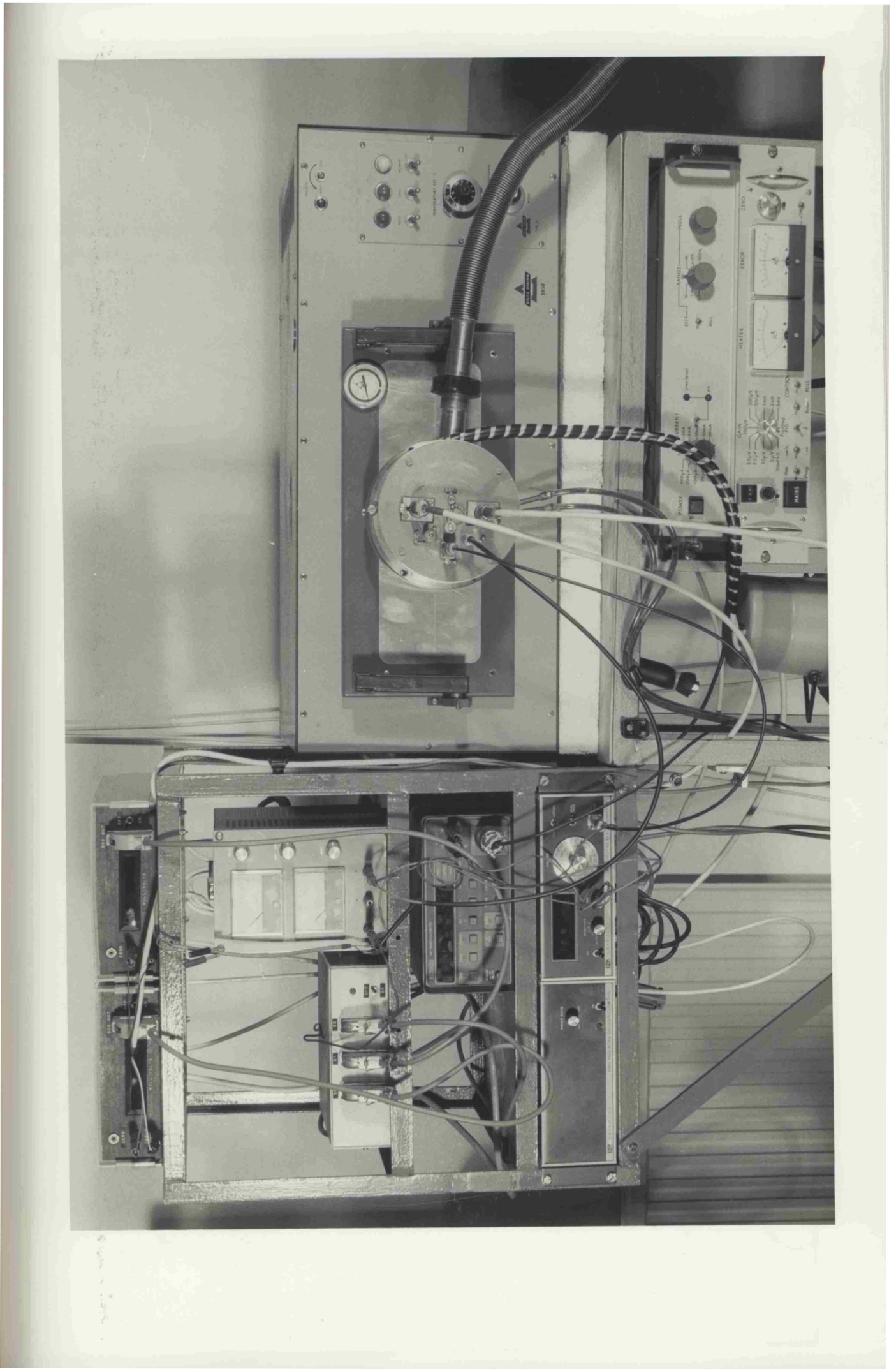
A photograph of the high-temperature d.c. conductivity and

thermopower system can be seen in Plate 3.3, with a photograph and schematic of the cryostat itself presented in Plate 3.4 and Fig. 3.5. The cryostat was built into an existing temperature-control chamber, a Delta Design Environmental Cabinet, which could hold temperatures to  $\pm 0.5^{\circ}\text{C}$ . Using an internal heater and a flow of circulating liquid-nitrogen vapour from a pressurized liquid nitrogen dewar, the temperature range 470 - 100K was accessible. Prior to making conductivity measurements the cryostat was evacuated to below  $10^{-6}$  Torr by an oil diffusion pump, with a liquid-nitrogen cold trap, backed by a rotary pump. The ultimate pressure eventually being  $\approx 10^{-7}$  Torr. The cryostat was then flushed through with helium several times and then finally filled with helium  $\approx 1$ -2psi above atmospheric pressure.

Sample temperature was determined from two copper-constantan thermocouples which were attached to the surface of the Corning 7059 glass by 'silver dag' paste, the cold junctions of which were immersed in liquid nitrogen.

A schematic of the measurement system used is shown in fig. 3.6. By slowly ramping the temperature of the Delta Design Environmental Cabinet over the required temperature range, by either manual adjustment or by means of a linear temperature programmer, the temperature dependence of the d.c. dark conductivity could be measured. Voltage was supplied to the sample by a Coutant 50V d.c. stabilized power supply and the current read by a 616 Keithley digital electrometer. Voltages from two sample thermocouples were displayed on two voltmeters (accurate to  $\sim \pm 2\mu\text{V}$ ) with BCD outputs. The output from the 616 was ADC on a Keithley 6162 isolated output/control unit with a BCD output. Sample voltage was measured by a Keithley 181 nanovoltmeter with an IEEE output. An

Plate 3.3 A photograph of the high temperature  
d.c conductivity and thermopower  
measurement system.



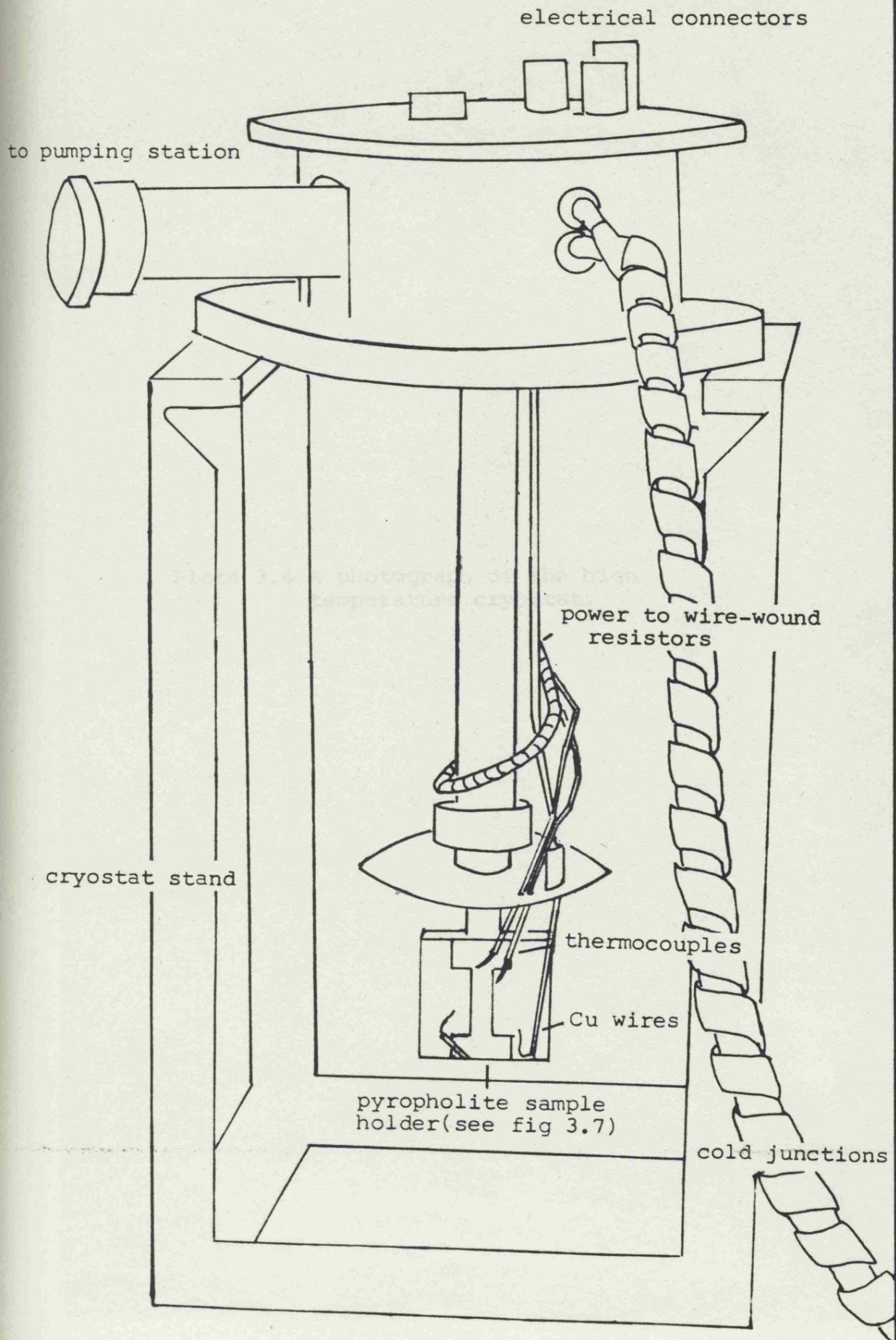


Fig 3.5 The high temperature cryostat.

Plate 3.4 A photograph of the high  
temperature cryostat.





interface unit was designed and built by the Department's Electronic Workshop to convert the three BCD outputs into IEEE format to enable the subsequent reading of the four IEEE signals by a Commodore Pet 8032 minicomputer. Information was then stored on 5 $\frac{1}{4}$ " floppy disks to enable easy access to data in future.

Measurements below 100K were made in an Oxford Instruments CF 100 continuous-flow helium cryostat, temperature control being achieved by an Oxford Instruments Precision Temperature Controller and a calibrated CLTS (cryogenic Linear Temperature Sensor) device. An ultimate temperature stability of  $\pm 0.1$ K was possible. This system was operated manually, the cryostat being initially pumped down to better than  $10^{-6}$  Torr, and the temperature slowly reduced in steps from room temperature to helium temperatures. Care was taken to ensure that the temperature had stabilized and the current reading were steady. At a number of fixed temperatures, as the temperature was again raised to room temperature, the current readings were checked. Only if current readings at a fixed temperature were the same on temperature rise and fall cycles was the measurement deemed to be reliable.

### 3.2.2 Thermoelectric power

Seebeck emf measurements were made on gap-cell samples using the high-temperature cryostat as previously described. As for d.c. conductivity measurements the thin films were deposited onto Corning 7059 glass and gold electrodes, 6.0 - 8.0mm separation, were evaporated onto the film surface. Temperature gradients across the electrode gap were maintained by activating one of the two small resistance heaters (2.5W/220 $\Omega$  vitreous wirewound resistors) which were located within the pyrophyllite sample holder (see fig. 3.7). Thermal contact between sample and the copper-heater retaining plates

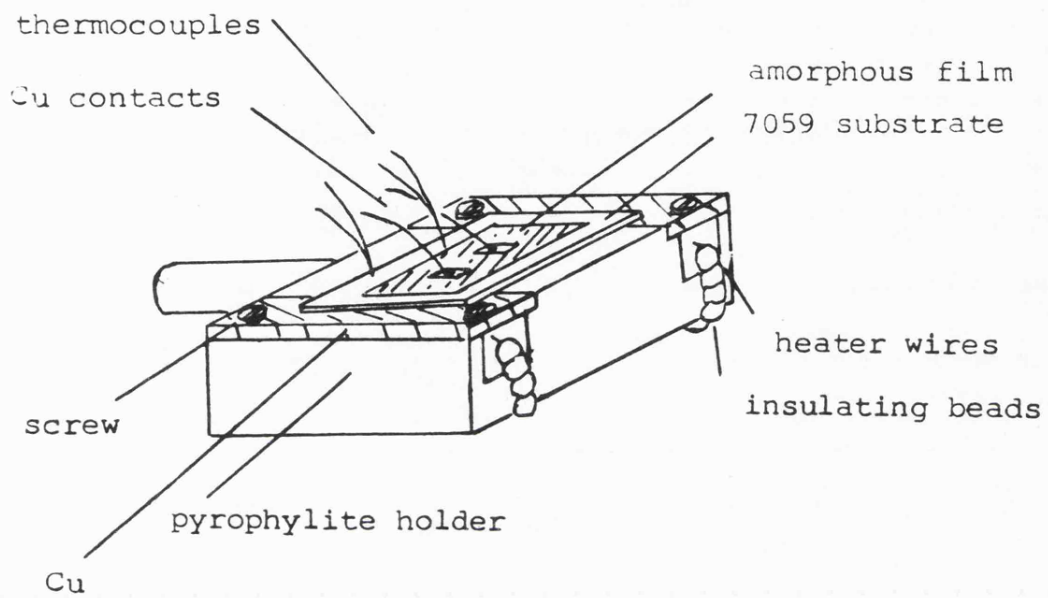


Fig 3.7 Thermopower sample holder

(fig. 3.7) was assisted by the smearing of silver conducting paste on the undersurface of the 7059 substrate. Two copper-constantan thermocouples were positioned in close proximity to the electrodes to enable accurate temperature determination.

The thermoelectric power measurement system used is represented schematically in fig. 3.6. The system is almost identical to that used in d.c. conductivity measurement except that the 50V power supply and the 181 nanovoltmeter (section A) were removed and a heater power supply  $\sim 30V$  (section B), which could be switched between heaters 1 and 2, was introduced. In this case the Keithley 616 Electrometer acted as a voltmeter with an input impedance of  $\sim 10^{14}\Omega$ . Only samples with resistance  $\lesssim 10^{11}\Omega$  were studied.

At each cabinet temperature  $T$ , at least two increments of  $\pm \Delta T_A$  and  $\pm \Delta T_B$  were made with heaters 1 and 2 (maximum  $\approx \pm 10^\circ C$ ). Owing to the time involved in obtaining steady Seebeck emf, ( $\gtrsim 30$  min) this operation was carried out manually.

### 3.3 Optical measurements

#### 3.3.1 Visible - Ultraviolet

Measurement of transmission and reflection of thin films deposited onto Corning 7059 glass were made in a Perkin Elmer 330 double-beam NIR-VIS-UV spectrophotometer whose spectral range is 2500nm - 187 nm (0.496 - 6.64eV). The reflection measurements being made with an Hitachi 60mm Integrating Sphere Accessory. Insertion of a reference sample of Corning 7059 glass in the reference beam ensured observed features were attributed to the thin film alone. The spectrophotometer was controlled by a Perkin Elmer 3500 Data Station which enabled

spectra to be stored in digital form on 5 $\frac{1}{4}$ " floppy disks. Data from disk could be transferred to the University mainframe computer (a CDC Cyber 73) by initially transferring the data onto cassettes via a Texas Instruments Silent 700 Electronic Data Terminal and subsequently reading the cassettes into the Cyber 73. (The initial disk format was incompatible with the relevant peripherals of the Cyber 73.) Alternatively the Silent 700 could act as a printer for digital output of spectra.

### 3.3.2 Infra-red

Transmission and reflection measurements were made in the infra-red regime on a Perkin Elmer 580B spectrophotometer, again using the Perkin Elmer 3500 Data Station for control and data acquisition. The 580B spectrophotometer is a double-beam instrument capable of scanning between 2.5 $\mu\text{m}$  - 50 $\mu\text{m}$  (0.496 - 0.0248eV), perfectly complementing the 330. Reflection measurements were made with a Perkin Elmer Specular Reflectance Accessory (6.5 $^{\circ}$  angle of incidence of beam to sample) using an aluminium mirror as the 100% of reflection.

Substrate material in this case was highly polished crystalline silicon (F.Z. intrinsic material 1mm thick from Wacker Chemi Ltd.) which was either hand polished to  $\sim 1\mu\text{m}$  finish or etched in a CP4 solution.

### 3.4 Electron microscopy

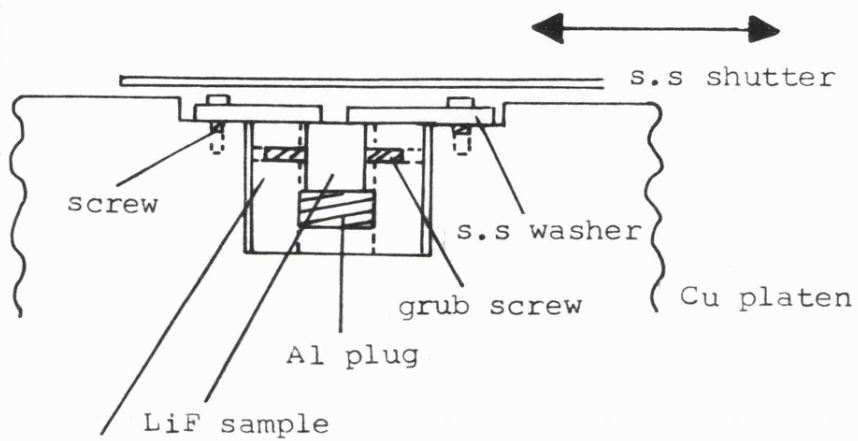
The electron microscope used in this study was a 100kV Transmission Electron Microscope (JOEL 100CX), a sophisticated instrument capable of a wide range of functions. However as transmission electron microscopy was seen as a tool to primarily 'check' the non-crystalline nature of the films by selected-area electron diffraction (SAED) and to

investigate possible microstructure [4] by bright-field imaging (BFI), many of the techniques that might be employed in a comprehensive structural examination were not employed.

Simultaneous sample preparation of films suitable for examination in the electron microscope, together with samples for electrical and optical measurements, initially proved to be a problem. The substrate platen, described earlier, was modified by making a recess into the copper surface which could hold an oxygen-free copper sample holder (see fig. 3.8). The substrate material was held between an aluminium plug and the desired stainless steel washer. The complete arrangement was slightly ( $\leq 0.2\text{mm}$ ) short of the platen surface and hence could be shielded from the plasma by a mechanical shutter which could be manually opened and closed for fixed periods of time.

In general the thin film was deposited onto LiF single crystals, cleaved to ensure a clean flat surface. A typical exposure time of the LiF crystal to the plasma was 2 - 4 minutes (120 - 240 Å). The deposited film was then 'floated off' in a very dilute solution of HF and distilled water. Great care was necessary when floating the film away from the LiF crystal; in many cases the film would explode on touching the liquid surface. The pieces of film of interest were then lifted out of the above solution using a small loop of platinum wire and then carefully dipped into a bath of pure distilled water. Care was taken not to reduce the size of the specimen any further. The final piece of specimen was then 'floated onto' a standard copper electron microscope grid.

Towards the end of this study a film was deposited onto a piece of carbon-coated ( $\sim 100\text{Å}$ ) mica (Dr. A.R. Long, Glasgow University).



Cu sample holder

Fig 3.8 LiF sample holder for E.M work.

The film was successfully removed from the mica by scoring through the carbon and floating the film off the mica in distilled water. As above, suitable specimens were then gently floated onto copper electron microscope grids.

### 3.5 Other measurements

Sample thickness measurements were made on a Rank Taylor Hobson Taly Step 4 and a Tencor Instruments Alpha Step Profileometer (Barr & Stroud Ltd.). The latter instrument was capable of very light stylus pressures, enabling step height measurements to be made on soft films. An error of  $\sim \pm 5\%$  in film thickness determination was unavoidable even with thicker films  $\sim 2\mu\text{m}$ .

Composition determination was achieved using an Electron Beam Microprobe, the characteristic X-rays being analysed by an Energy Dispersive system. By careful calibration of the metal and semiconductor host, absolute determination of the silicon metal ratio to  $\lesssim 10\%$  could be made. Approximate values for impurities with  $Z > 11$  could also be achieved.

Several other experimental methods are described in the relevant chapters, particularly that of photoemission (Chapter 5).

## CHAPTER 4

### Experimental Results

#### 4.1 a-Si:H

#### 4.2 a-Si:Cu:H and Si:Cu alloys

##### 4.2.1 D.C. conductivity

##### 4.2.2 Optical absorption

##### 4.2.3 Structural measurements

##### 4.2.4 Discussion

#### 4.3 a-Si:Au:H alloys

##### 4.3.1 D.C. conductivity and thermopower

##### 4.3.2 Optical absorption

##### 4.3.3 Structural measurements

##### 4.3.4 Discussion

#### 4.1 a-Si(H)

Sputtered films of hydrogenated amorphous silicon were prepared in the diode r.f. system as described in Chapter 3. Standard low pressures ( $P_{Ar} \sim 7.4\text{m}\tau$ ) and low powers ( $\sim 2.47 \text{ Wcm}^{-2}$ ) [46] [56] were used throughout the study, although both deposition temperature  $T_d$  and argon/hydrogen flow ratios were varied. Substrate-target separation was maintained at 5.5cm.

Someway through this investigation the initial turbo-molecular pump, a Sargent-Welsh Model 3133C, was replaced with a large diffusion pump, a Varian VH5-6. Owing to the large difference between the pumping rates of argon and hydrogen by these pumps (the diffusion pump pumps hydrogen very fast and the turbomolecular pump is at its least effective for light gases) films prepared before and after the replacement exhibited different electrical and optical properties.

The d.c. dark conductivity of sputtered a-Si:H films deposited onto substrates at various temperatures for the two pumping systems, using different argon/hydrogen partial pressure and flow rates is indicated in fig. 4.1. The first apparent feature to be observed is an irreversible change in the conductivity on heating the sample. This is most likely to be primarily attributed to the presence of water absorbed onto the surface of the gap-cell geometry samples [102] for samples 3 and 4, though not for sample 1 as some degree of annealing is evident. Subsequent heat cycling under vacuum or in an inert atmosphere (He) would result in conduction as observed in the downward heat cycle of the conductivity exhibited in the figure.

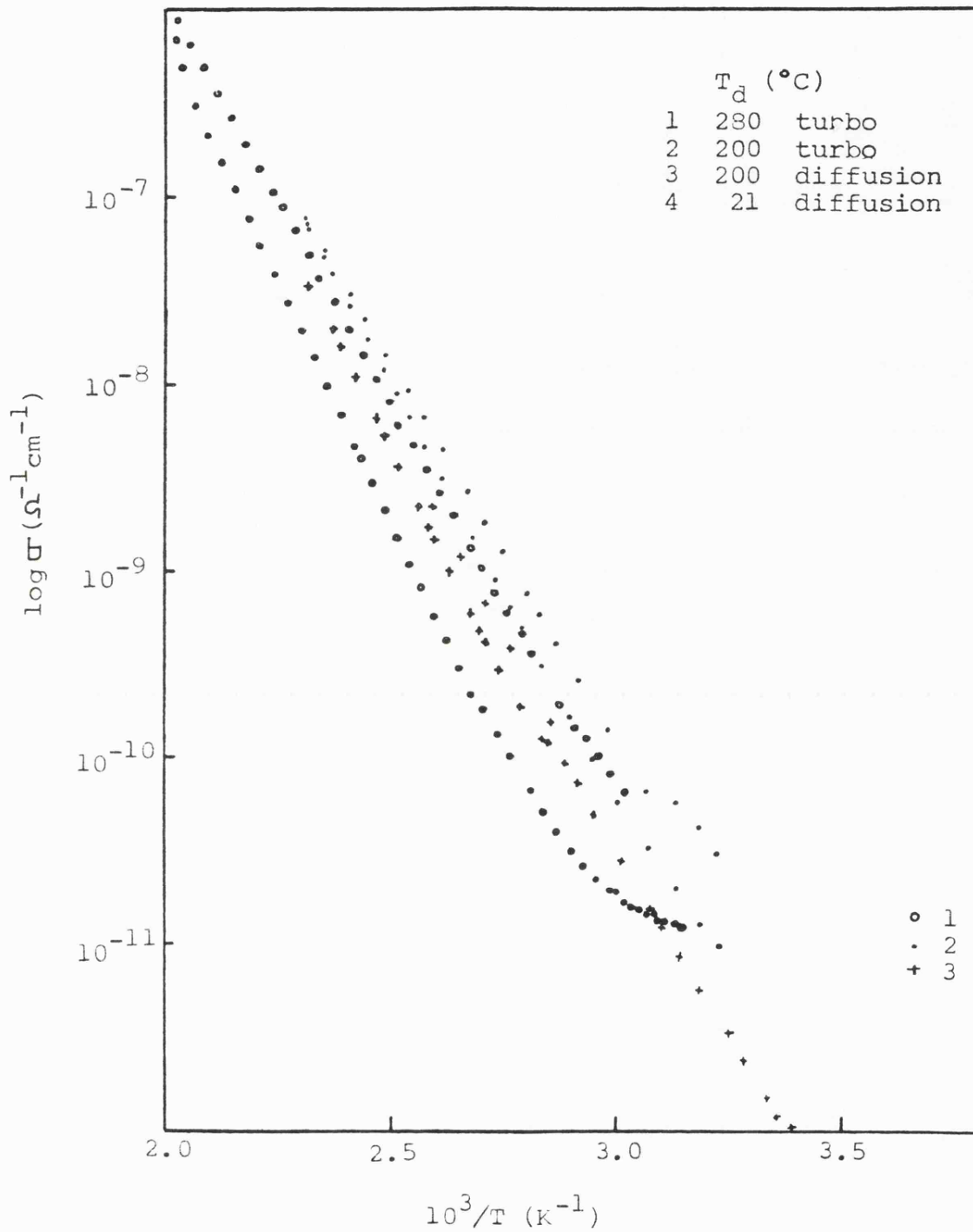


Fig 4.1  $\sigma$  vs  $10^3/T$  for a-Si:H alloys.

Conduction in all cases can be represented by a single activation energy  $E_{\sigma} = 0.85 - 0.89\text{eV}$ , indicating extended-state conduction. The conductivity prefactor  $\sigma_{10}$  varies from  $10^2 - 10^3 \Omega^{-1}\text{cm}^{-1}$  as would be expected from such a conduction process. The conductivity at 294K,  $\sigma_{RT}$  varies from  $1.5 - 3.6 \times 10^{-12} \Omega^{-1}\text{cm}^{-1}$ . These values are in general agreement with other sputtered films deposited in a similar manner; indeed it is surprising that the values of  $E_{\sigma}$ ,  $\sigma_{10}$  and  $\sigma_{RT}$  vary so little considering the variations in deposition parameters. A summary of conductivity values is displayed in Table 4.1

The deposition rates as a function of various deposition parameters are presented in Table 4.2. They vary from 0.95 to  $1.56 \text{ \AA s}^{-1}$ . The deposition temperature appears to affect the growth rate more dramatically than does the hydrogen partial pressure.

Steady-state photoconductivity was observable at room temperature on samples 1 - 4. A crude qualitative method was employed to determine this quantity. A lamp provided a white light source,  $\sim 1\text{W}$ , which was held  $\sim 10\text{cm}$  above the sample, outside the cryostat and the resultant conductivity value was then recorded. The sample was then placed into a vacuum system, which was light tight, and a similar measurement made at the same temperature. Conductivity changes of several (2 - 3) orders of magnitude on exposure to light were observed.

Optical absorption measurements in the visible at room temperature

Table 4.1

Sample Type	1	2	3	4
$E_{\sigma}$ (eV)	0.85	-	0.89	0.89
$\sigma_{\sigma}$ ( $\Omega^{-1} \text{cm}^{-1}$ )	$4.3 \times 10^2$	-	$1.43 \times 10^3$	$8.24 \times 10^2$
$\sigma_{RT}$ ( $\Omega^{-1} \text{cm}^{-1}$ )	$3.55 \times 10^{-12}$	-	$2.79 \times 10^{-12}$	$1.57 \times 10^{-12}$
$E_{\sigma}$ (eV)	-	2.00	1.96	2.03
$\alpha_{\sigma}$ ( $\text{cm}^{-1}$ )	-	$6.4 \times 10^5$	$4.5 \times 10^5$	$5.5 \times 10^5$
$\beta^{-1}$ (meV)	-	-	$1.3 \times 10^2$	$1.55 \times 10^2$
$C_H$ (at%)	-	$\sim 40$	22	31

Table 4.2

Sample Type	1	3	4
Deposition Rate $\text{\AA s}^{-1}$	0.95	1.07	1.56

Table 4.3

Sample Type	2	3	4
$2E_{\sigma}$ (eV)	-	1.78	1.78
$E_{\sigma}(n=2)$ (eV)	2.00	1.96	2.03
$E_{\sigma}(n=3)$ (eV)	1.81	1.77	1.84

gave optical absorption coefficients  $\alpha$  as a function of energy as displayed in fig. 4.2. These data can be fitted satisfactorily to the relation (after equation 1.49)

$$\alpha \hbar\omega = \text{const.}(\hbar\omega - E_0)^n$$

with  $n = 2$ . This relation is commonly observed in amorphous semiconductors. However plots with  $n = 3$  also gave good agreement with the results as can be seen in fig. 4.3. The latter power-law expression indicates linear tailing as suggested by Klazes et al [103]. However the extrapolated optical gap values  $E_0^{n=3}$  ( $T = 0$ ), using an estimated temperature coefficient of the gap  $\sim 3.3 \times 10^{-4} \text{ eV K}^{-1}$  [57], when taken in conjunction with  $E_0$  values and majority conduction by electrons (see thermopower results in 4.3.1) places the Fermi level too deep in the gap for conduction to be n-type. Table 4.3 shows the values for  $2E_0$ ,  $E_0^{n=2}$  ( $T = 0$ ) and  $E_0^{n=3}$  ( $T = 0$ ) for three of the films.

Typical infra-red transmission spectra are presented in fig. 4.4. In all cases a doublet is found at  $2100 - 2000\text{cm}^{-1}$ , the primary feature being the  $2100\text{cm}^{-1}$  absorption as is usually the case for sputtered films. This is in contrast to 'high quality' glow-discharge material where the  $2000\text{cm}^{-1}$  peak is dominant. An estimate of the hydrogen content of the films was calculated by integration of the wagging-rocking mode at  $650\text{cm}^{-1}$  and using the empirical relationship

$$C_H = 0.62 K_W \quad (4.1)$$

where  $K_W = \alpha d (\hbar\omega)$  [57] In Table 4.1 values for  $E_0$  ( $T = 0$ ),  $\beta^{-1}$  and  $C_H$  are presented for one "turbo pump" and two "diffusion pump" series of samples. For samples 3 and 4 for which only  $T_d$  was

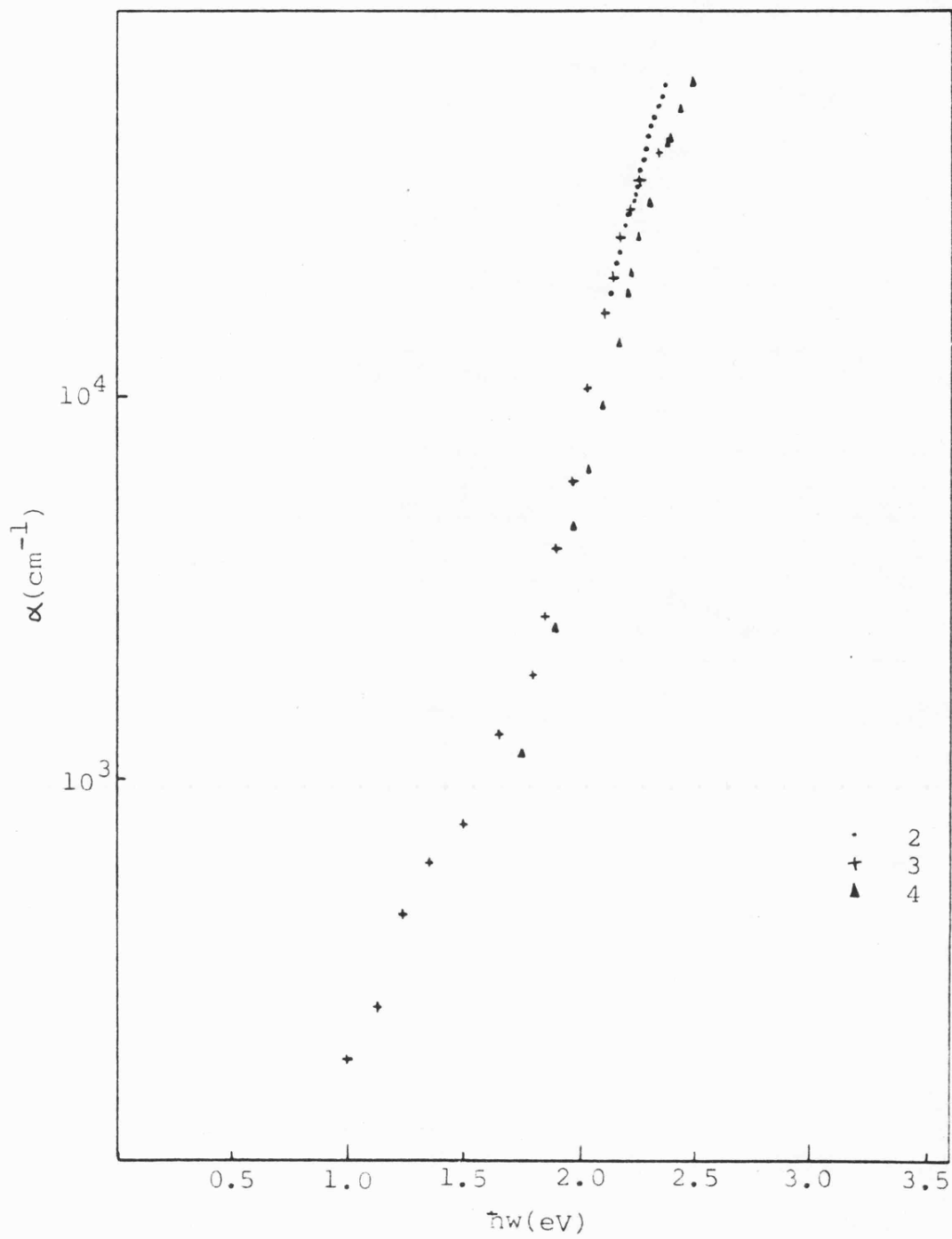


Fig 4.2  $\alpha$  vs  $\hbar\nu$  for a-Si:H alloys.

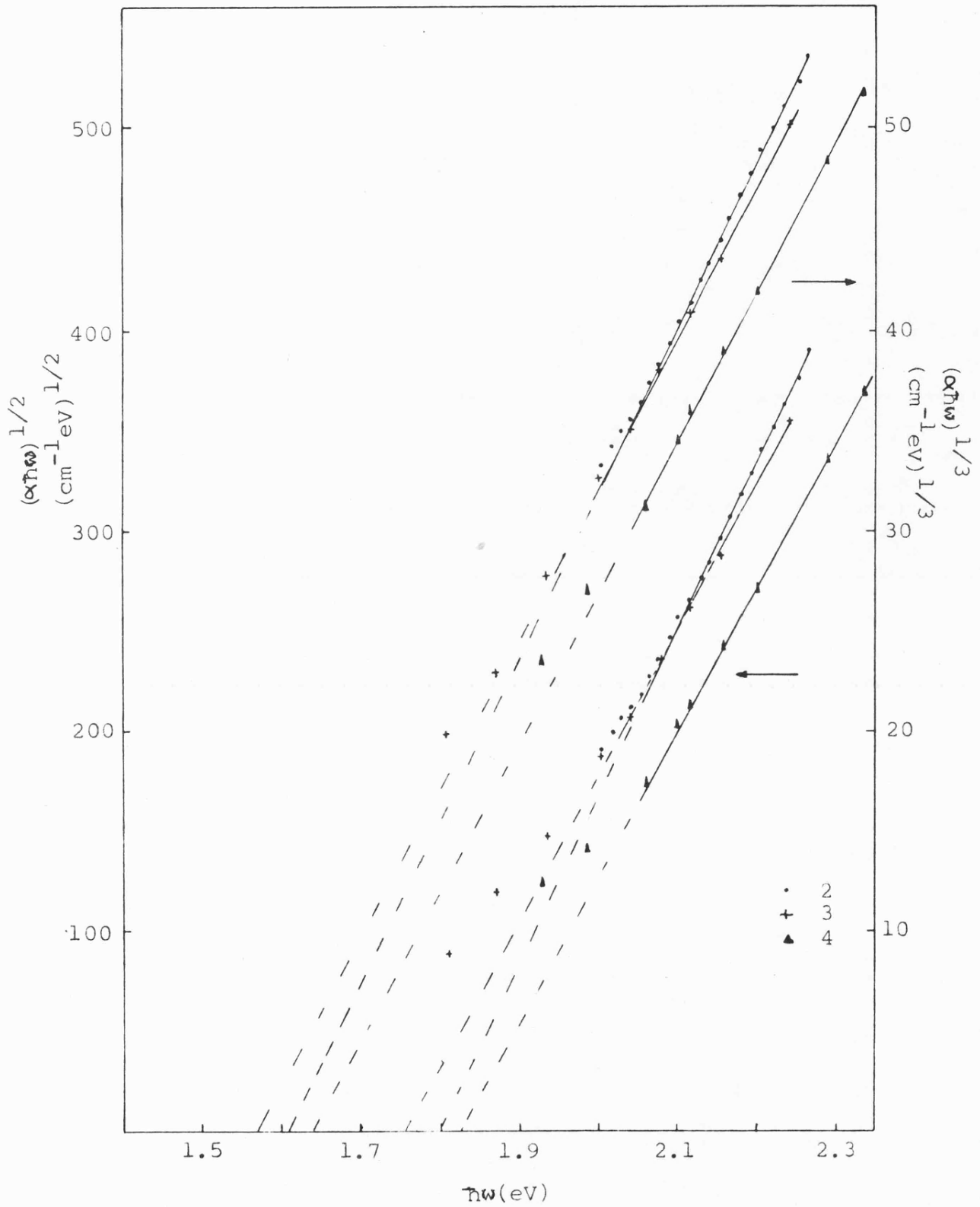


Fig 4.3  $(\alpha hw)^{1/n}$  vs  $hw$  for a-Si:H alloys.

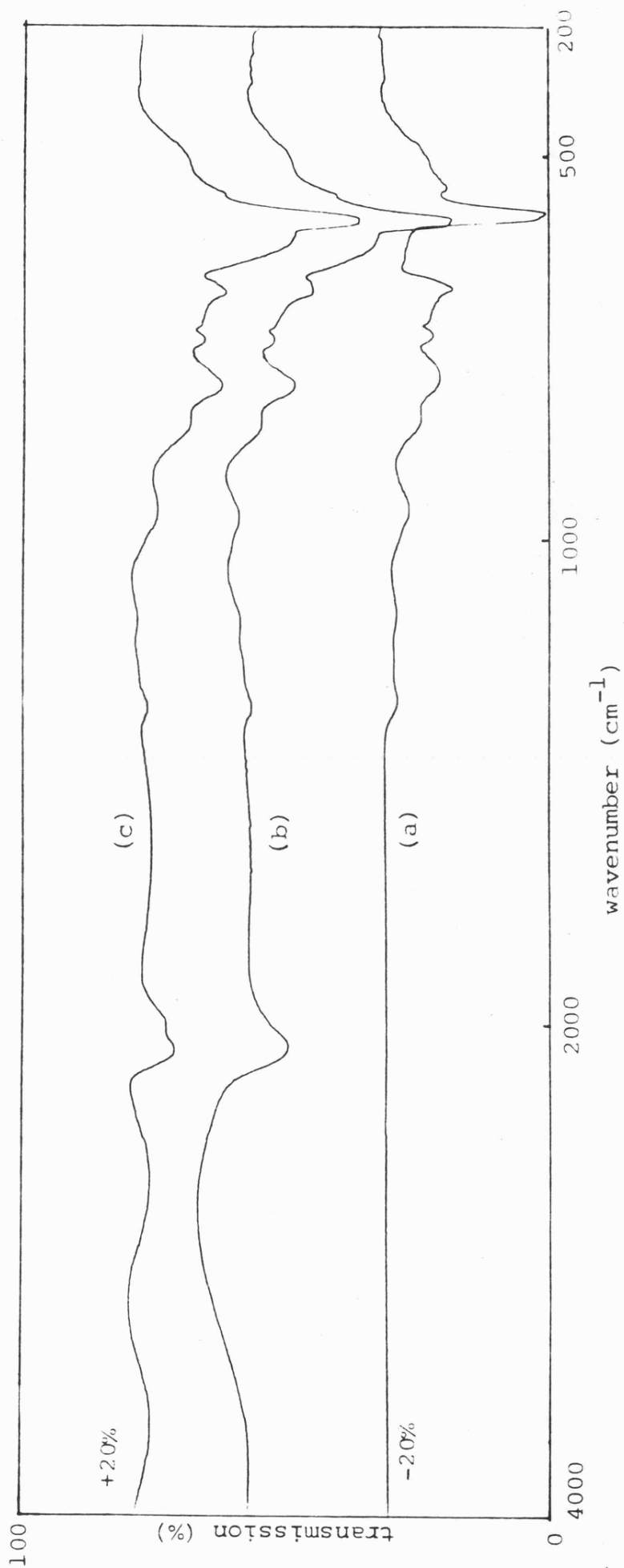


Fig 4.4 Typical IR spectra for (a) c-Si substrate, (b) a-Si:H (type 4) and (c) a-Si:H (type 1) samples. The a-Si:H spectra are not corrected for the substrate contribution.

varied (sample 4:  $T_d = 21^\circ\text{C}$ , sample 3:  $T_d = 200^\circ\text{C}$ ), results in  $C_H$  falling from 31 to 22% followed by a reduction in  $E_g(T=0)$  from 2.05 to 1.92 eV and a similar reduction in  $\beta^{-1}$  from 155 to  $134\text{meV}^{-1}$ . This is related to the increased relaxation of the network at higher deposition temperatures [104] and the fact that more efficient defect compensation by the incorporated H occurs. The reduction of  $E_g(T=0)$  for sample 2 with the highest H content ( $H \sim 40\%$ ) is most likely due to the change in plasma conditions as a result of the change in the pumping system. It should be noted that the bending modes at  $840$  and  $890\text{cm}^{-1}$ , indicative of  $\text{SiH}_2$  or  $(\text{SiH}_2)_n$  bonding, are stronger for this film.

Under standard vacuum conditions no Si-O mode was observed for as-deposited films. However, after a period of days, the characteristic Si-O mode at  $1050\text{cm}^{-1}$  [105] was formed indicating the formation of a surface layer of  $\text{SiO}_2$ . For an absolute determination of the hydrogen content of the films a more direct measurement such as hydrogen evolution or use of a nuclear reaction technique [106] is necessary.

Further, more specialised, measurements were carried out on samples prepared under the conditions required to prepare samples 3 and 4. TEM studies, to be discussed in detail in section 4.3.3, indicated a homogeneous film with no evidence of the columnar structures as reported by Knights et al [4].

Steady-state photoluminescence measurements, were carried out by Dr. Baht (Department of Physics, Sheffield University) at

11.4K using a 2.41eV excitation energy. The results are shown in fig. 4.5. A broad band, centred at about 1.3eV appears as a doublet due to interference effects from the smooth substrate. The luminescence is indicative of recombination of physically separated electrons and holes trapped in band tails [107]. The intensity of this band is approximately  $10^{-1}$  lower than that observed on 'high quality' glow-discharge a-Si:H, though this is undoubtedly affected to some extent by interference effects.

Photoemission studies, both UPS and XPS, were carried out on a variety of samples. These results are presented in Chapter 5.

Sputtered hydrogenated amorphous silicon films with distinct electrical and optical properties were prepared by controlling the deposition temperatures and the hydrogen partial pressure. The characterization of these films represents the first step in understanding the processes involved when noble metals such as Au and Cu are incorporated into the a-Si:H matrix by co-sputtering.

## 4.2 a-Si:Cu:H and Si:Cu alloys

### 4.2.1 D.C. conductivity

Chemical modification of sputtered amorphous silicon by the introduction of copper was achieved by placing small pieces of copper sheet, 5N pure (Johnson Matthey Ltd.) 3 x 3 x 1mm, uniformly on the surface of a single crystal 100mm diameter silicon target. Three sets of deposition conditions were used to prepare three distinct types of film: HI, turbo pumped,  $T_d = 200^\circ\text{C}$  with 10% H/Ar ratio (high H content); HII, diffusion pumped  $T_d \approx 200^\circ\text{C}$  with 30% H/Ar ratio (low H) and AR, diffusion pumped with an argon atmosphere (H = 0).

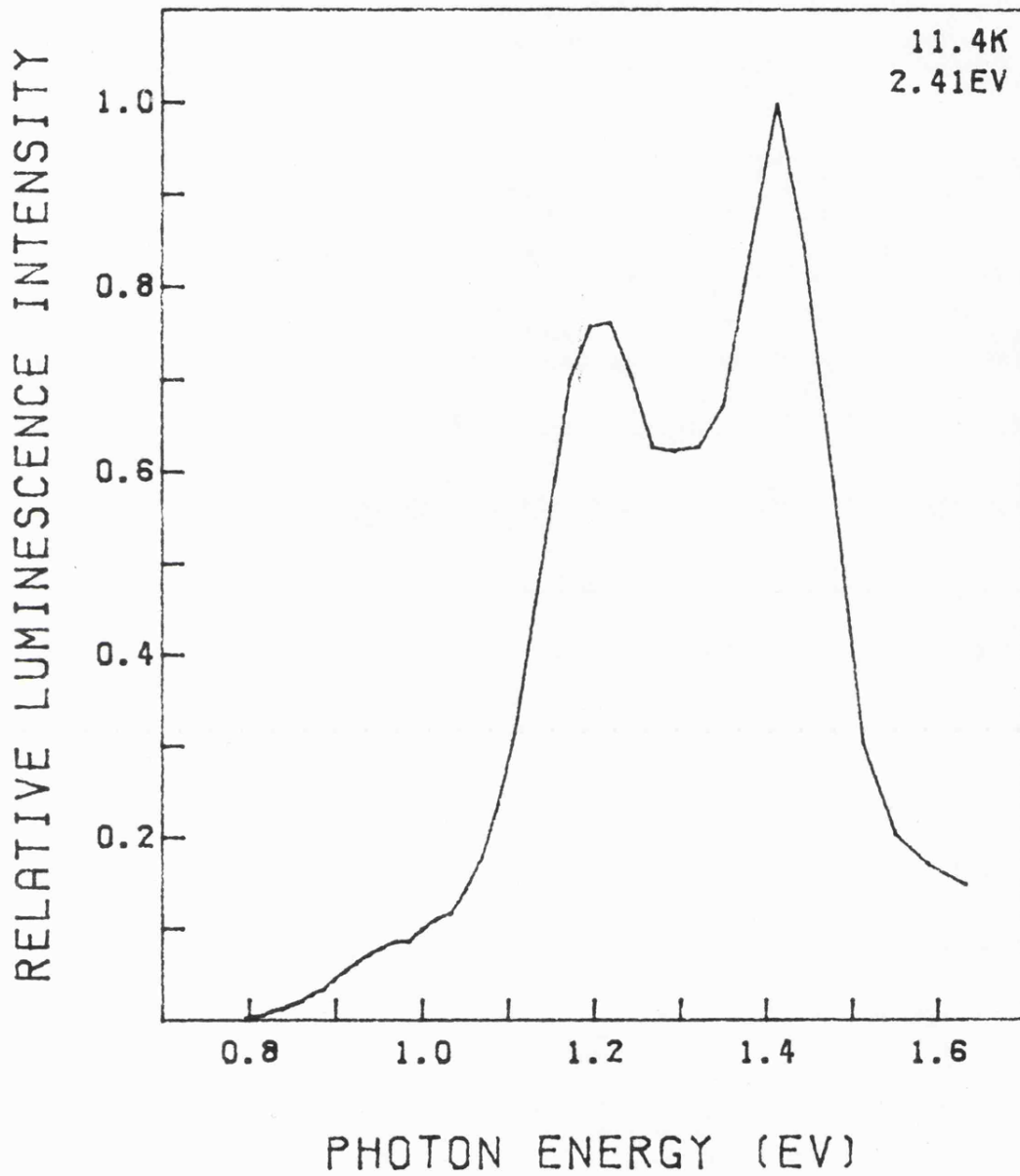


Fig 4.5 Photoluminescence from a type 3 a-Si:H sample.

Composition analysis of the silicon-copper films could not be done on a regular basis in our laboratory but several films, deposited onto aluminium foil substrates, were chemically analysed by energy dispersive analysis of the characteristic X-rays using an Electron Microprobe in the Department of Geology, Leicester University. By using polycrystalline copper and amorphous silicon films as standards, the Si:Cu ratio of the films was determined to an accuracy of  $\sim 10\%$ . Owing to the limited nature of chemical analysis available, Cu/Si surface area ratios will be used in this section to identify the samples, although for the HI series of samples reasonable estimates of the Cu content can be determined from the Cu/Si ratio. (See Table 4.4). No other elements with  $z \geq 11$  could be detected in any of the films examined. This indicates that contaminants, if present, are in quantities of less than 0.1at% in general. As can be seen from Table 4.4 the observed sputtering rates for Cu varies from 3.3 to 5.18 times the rate for Si; this compares with 5.33 reported by Glang and Maissel [108]. A distinct increase in the Cu sputtering yield relative to Si is apparent when preparation conditions change from type HI to HII. This is attributed to a change in plasma conditions.

A plot of room temperature d.c. conductivity,  $\sigma_{RT}$ , against the Cu/Si surface area ratio,  $X_{cs}$ , is shown in figure 4.6. The introduction of Cu into HI samples results in a rapid increase in conductivity for lower Cu concentrations, below  $X_{cs} \approx 2\%$  [ $\approx 7\text{at}\% \text{Cu}$ ], followed by a more gradual increase in conductivity for additional Cu beyond this point. The room temperature conductivity of type HII and ARI samples is even more insensitive than high-Cu-content HI samples to a variation

Table 4.4

Preparation Conditions Type	Cu at% by EBMA	$X_{cs}$ Cu/Si surface area ratio	Cu yield relative to Si
HI	17.6	4.96	3.55
HI	10.0	2.96	3.34
HII	22.0	4.24	5.18

Table 4.5

Preparation Conditions Type	$X_{cs}$	C (eV)	$\sigma_{OL}$ ( $\Omega^{-1} \text{cm}^{-1}$ )
HI	0.45	0.12	$2.853 \times 10^{-8}$
	0.6	0.14	$1.323 \times 10^{-6}$
	1.05	0.097	$4.27 \times 10^{-5}$
	2.1	0.036	$5.207 \times 10^{-3}$
	2.96	0.03	$1.164 \times 10^{-2}$
	4.96	0.0127	$7.543 \times 10^{-1}$
HII	2.66	0.025	$5.35 \times 10^{-1}$
	7.42	0.006	$9.276 \times 10^{-1}$

Table 4.6

Metal	Content (at%)	C (eV)	$d_{est}$ ( $\text{\AA}$ )	$S_{est}$ ( $\text{\AA}$ )
Cu	10	0.032	25	100
Cu	20	0.012	50	50
Fe	10	0.04	25	100
Fe	20	0.02	50	50

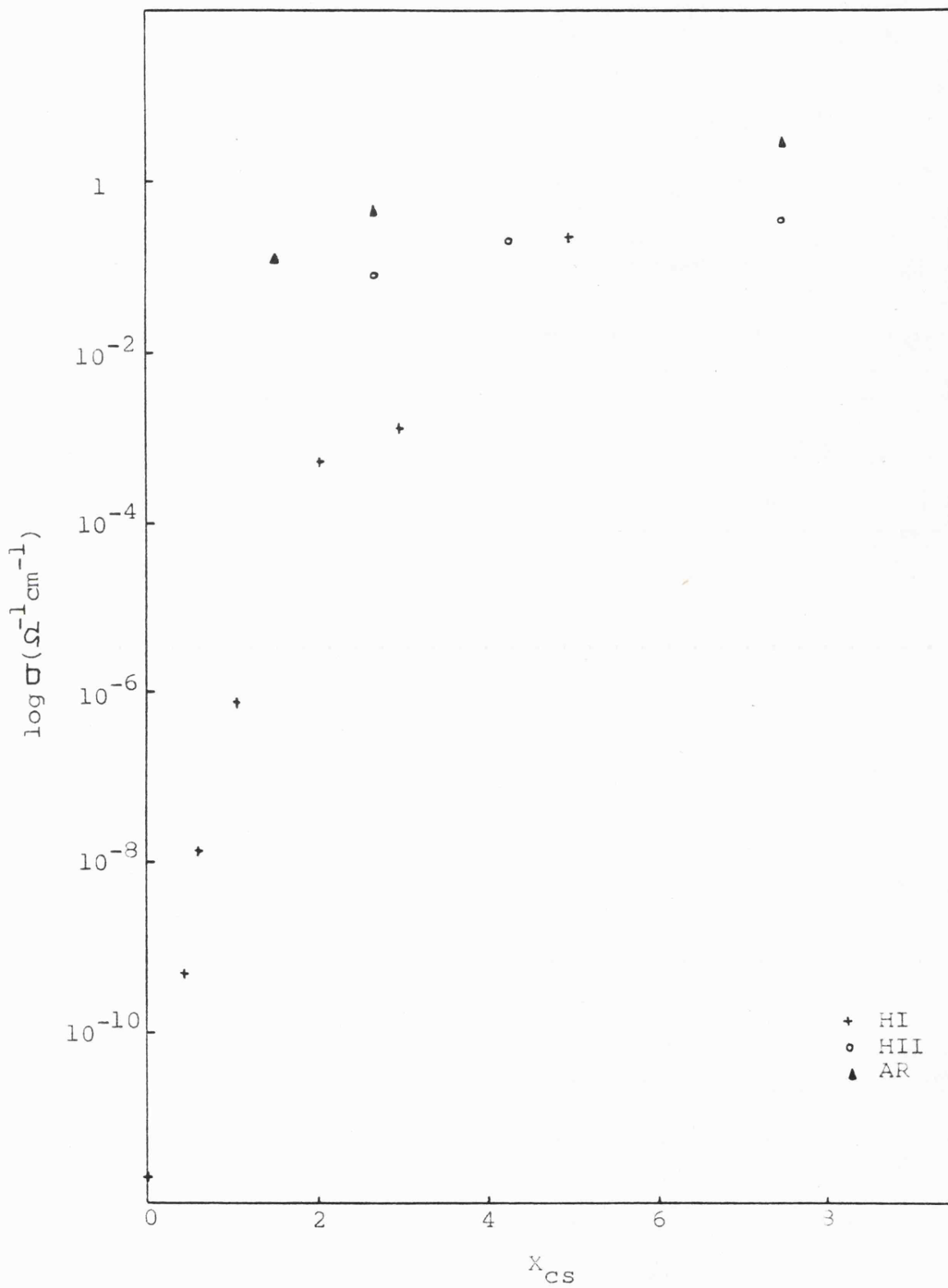


Fig 4.6  $\sigma_{RT}$  vs  $X_{CS}$  for Si:Cu:H and Si:Cu alloys.

in the Cu content, though the d.c. conductivity still increases with Cu content. This could be due, in the case of HII type mentioned, to the relatively higher Cu/Si yield and, for the unhydrogenated ARI films, the higher conductivity of the a-Si starting material [55]. Steady state photoconductivity was quenched in all films with  $X_{CS} > 0.45\%$  to a level that could not be measured by the procedure described in 4.1. In figures 4.7 and 4.8 the d.c. conductivity as a function of reciprocal temperature for a range of Cu compositions are presented for hydrogenated and unhydrogenated material respectively. For simplicity these data will be treated separately.

For the hydrogenated films, types HI and HII, there appears to be two distinct conduction mechanisms present. At high temperatures ( $T \gtrsim 267K$ ), as is most noticeable for samples with low Cu concentration there is a strongly activated region ( $E_{\sigma} \approx 0.7 - 0.8eV$  for  $X_{CS} = 0.45\%$ ). Owing to the high-temperature limit at which measurements were possible, accurate determination of the activation energy was not possible but it seems to decrease with increase of  $X_{CS}$ . The second distinct conduction region occurs below  $\approx 267K$  when the conductivity becomes less temperature sensitive. Attempts to fit this region to a simple  $\sigma = \sigma_0 \exp[-E_{\sigma}/kT]$  relationship results in  $E_{\sigma} \approx 0.049eV$  for  $X_{CS} = 0.45\%$ ; for higher Cu contents this quantity would be smaller still. This value is obviously too low for extended-state or nearest-neighbour hopping conduction to have any physical meaning.

Owing to the limited range of temperature accessible and the

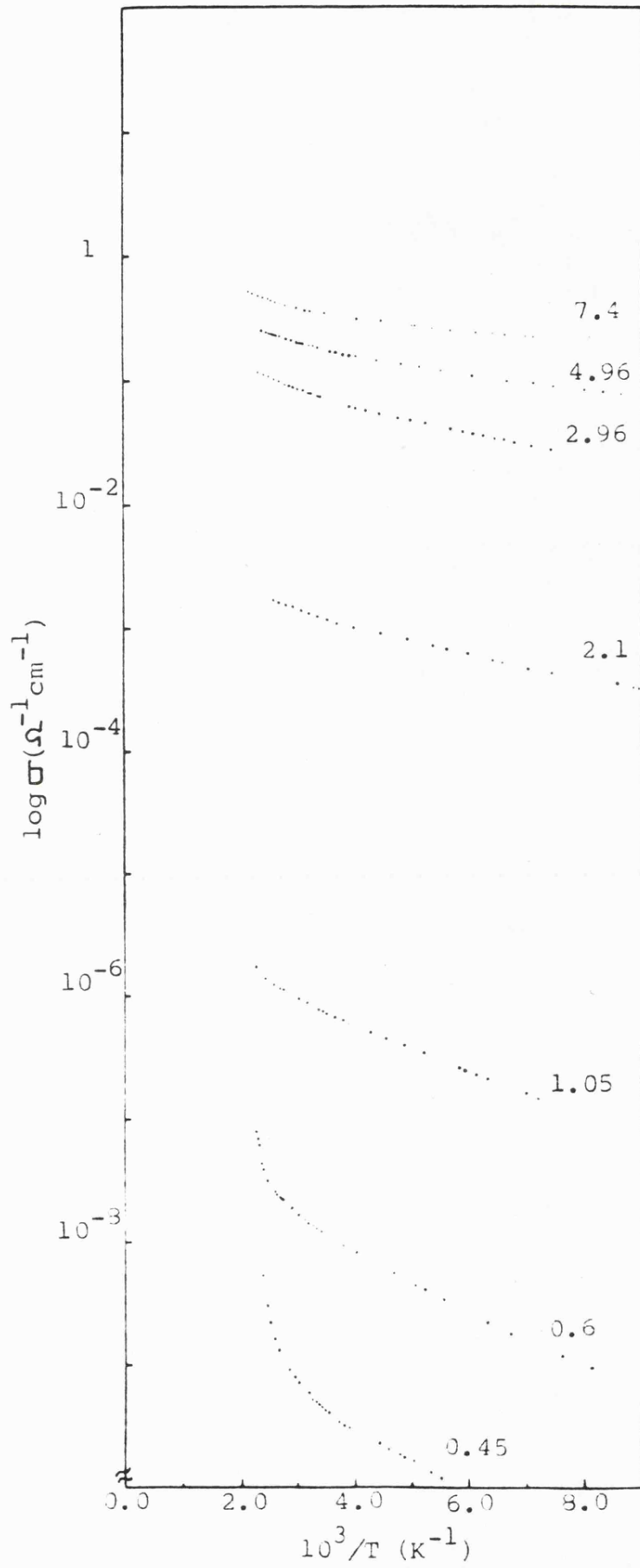


Fig 4.7  $\sigma$  vs  $10^3/T$  for Si:Cu:H films as a function of  $X_{CS}$ .

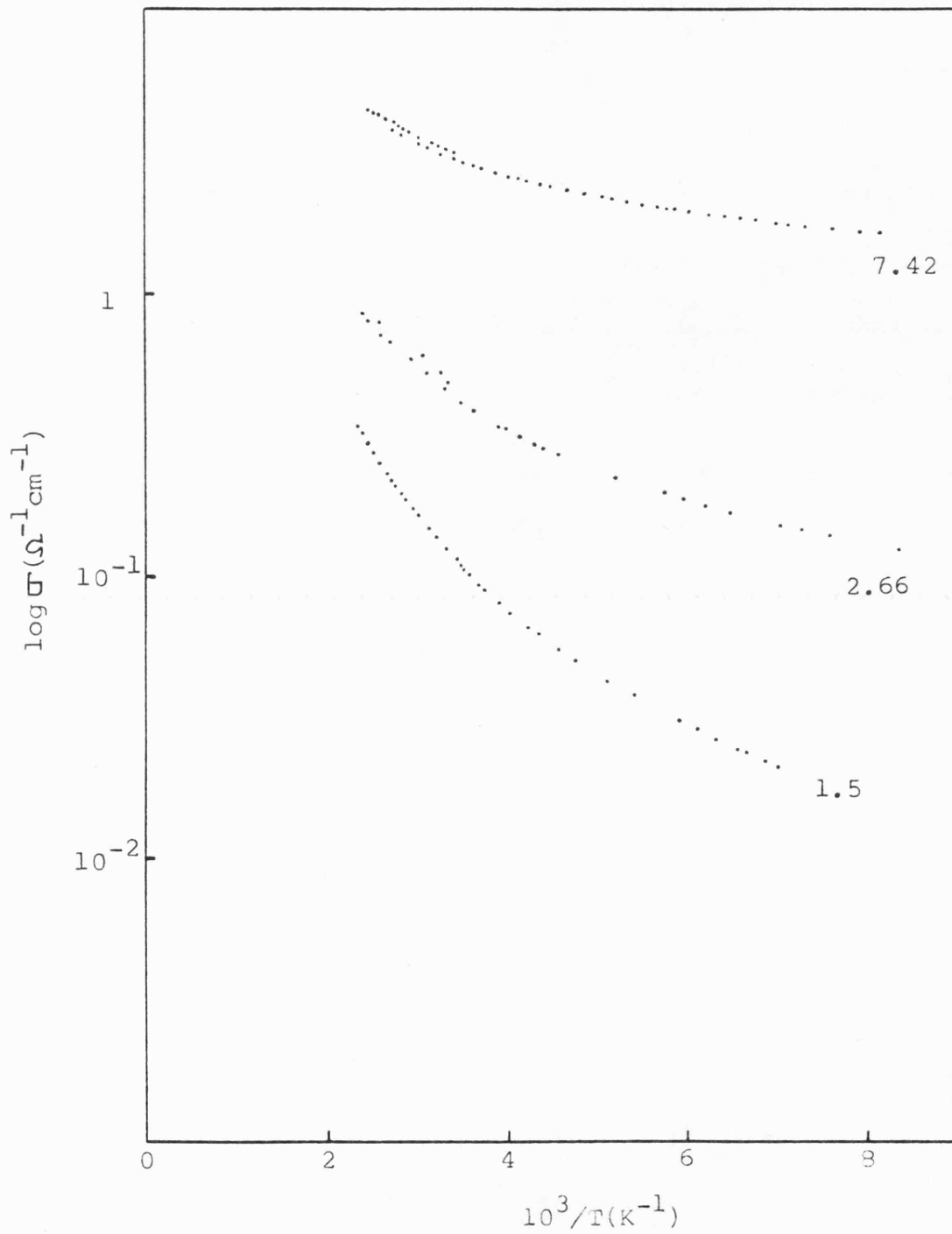


Fig 4.3  $\sigma$  vs  $10^3/T$  for Si:Cu alloys.

weak temperature dependence of the conductivity, it is possible to fit the data of the low Cu content samples,  $X_{CS} < 1.1\%$ , to plots of  $\ln \sigma$  versus both  $T^{-\frac{1}{4}}$  and  $T^{-\frac{1}{2}}$ . However, as Cu content increases to  $X_{CS} > 2\%$ , the data fits the  $T^{-\frac{1}{2}}$  relationship more favourably. In figs. 4.9 and 4.10 plots of  $\ln \sigma$  vs  $T^{-\frac{1}{2}}$  and  $T^{-\frac{1}{4}}$  are displayed for the compositional ranges  $X_{CS} < 1.05\%$  and  $X_{CS} > 1.05\%$  respectively. A temperature dependence of conductivity as  $\exp -(T_0/T)^{\frac{1}{2}}$  (equation 1.27) is indicative of variable-range hopping conduction. From the slope of the linear section of the  $\ln \sigma$  against  $T^{-\frac{1}{2}}$  plot,  $T_0$  and hence the density of states at the Fermi level  $N(E_F)$  may be determined from the relation  $T_0 = 16\alpha^3/kN(E_F)$ . Taking  $\alpha^{-1} \sim 10\text{\AA}$ , after [75], values for  $X_{CS} = 0.45, 0.6$  and  $1.05\%$  are found to lie between  $10^{19} - 10^{20} \text{ eV}^{-1} \text{ cm}^{-3}$  as presented in fig. 4.11. The anomaly at  $X_{CS} = 0.45$  is due to the high temperature thermally activated contribution to the conductivity. Thus as  $X_{CS}$  increases the number of localized states at the Fermi level rises. This result is similar to the observations of Shimizu et al [90] on transition-metal impurities in a-Si and a-Ge, where deep-level impurities such as Mn, Ni, Fe and Fe, Co, Cr [93] have been interpreted as creating localized states at the Fermi level.

A conductivity obeying a  $T^{-\frac{1}{2}}$  relationship of the form

$$\sigma_L = \sigma_{0L} \exp\left[-B/T^{\frac{1}{2}}\right] \quad (4.2)$$

with the pre-exponential  $\sigma_{0L}$  temperature dependent, has been observed in granular metal films (or cermets) where isolated metallic particles are embedded in an insulating matrix. The activation energy  $B$  is the energy required to transfer charge from

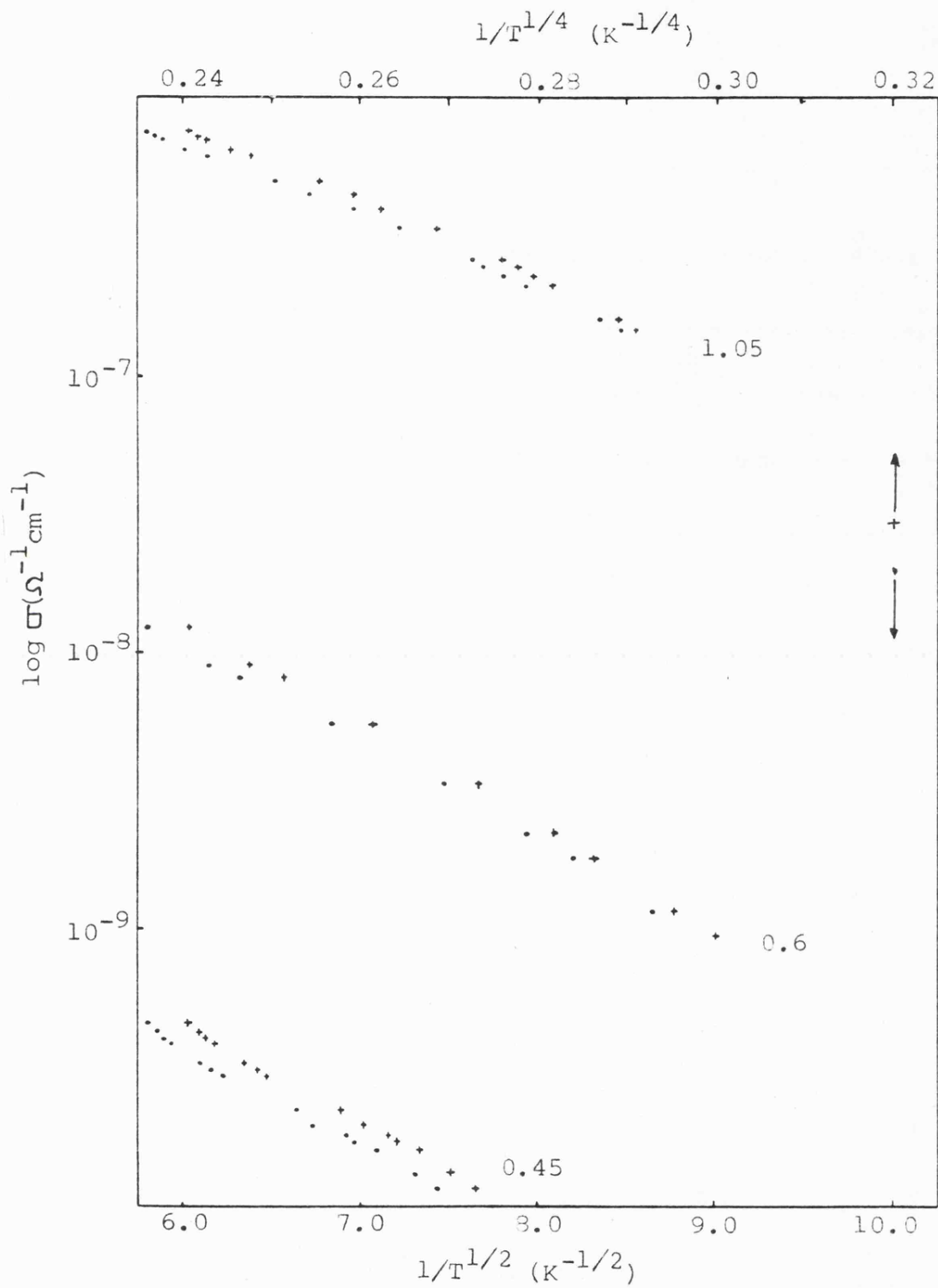


Fig 4.9  $\sigma$  vs  $T^{-1/2}$  and  $T^{-1/4}$  for Si:Cu:H alloys. ( $X_{\text{CS}} \leq 1.05\%$ )

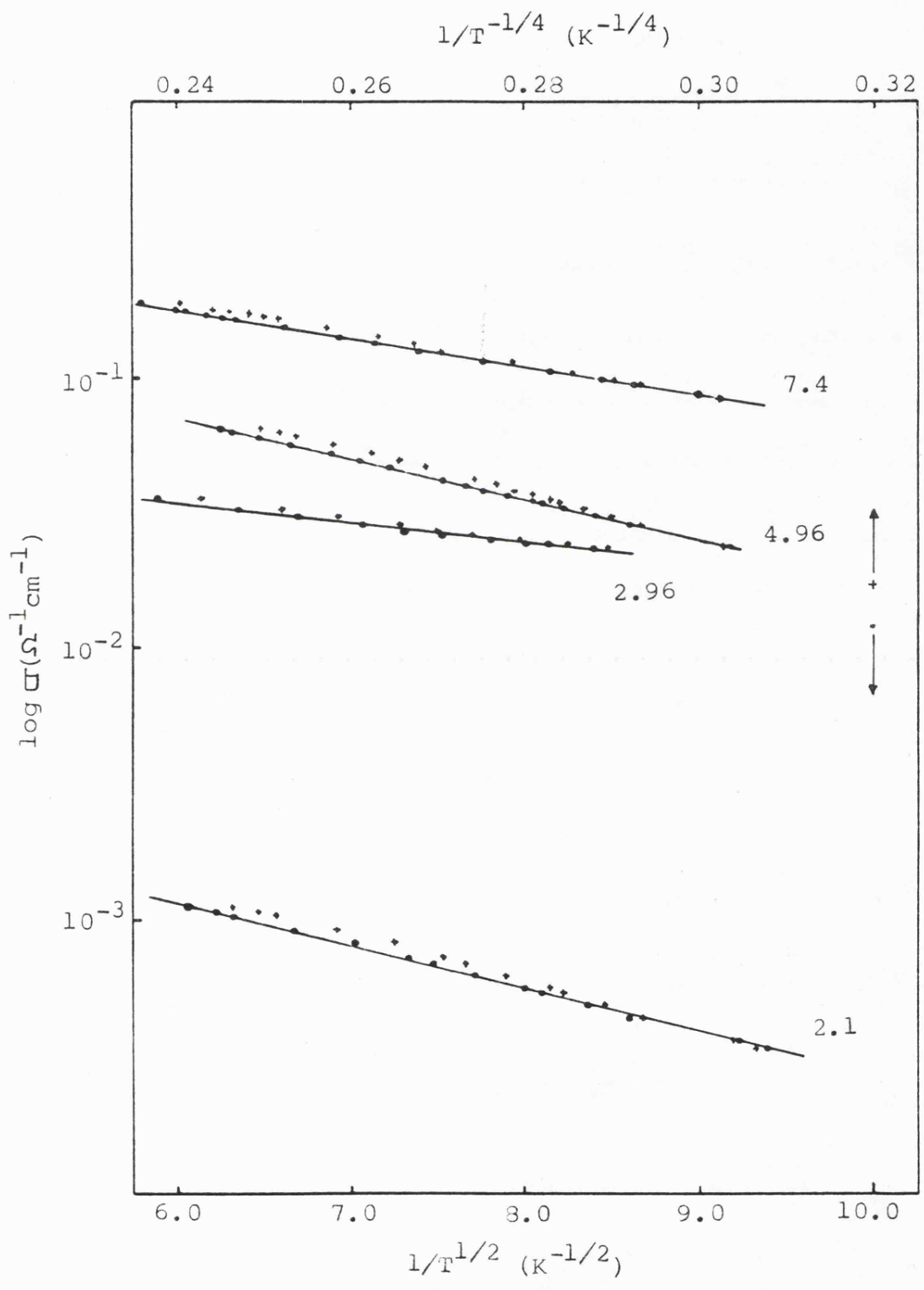


Fig 4.10  $\sigma$  vs  $T^{-1/2}$  and  $T^{-1/4}$  for Si:Cu:H alloys. ( $x_{CS} > 1.05\%$ )

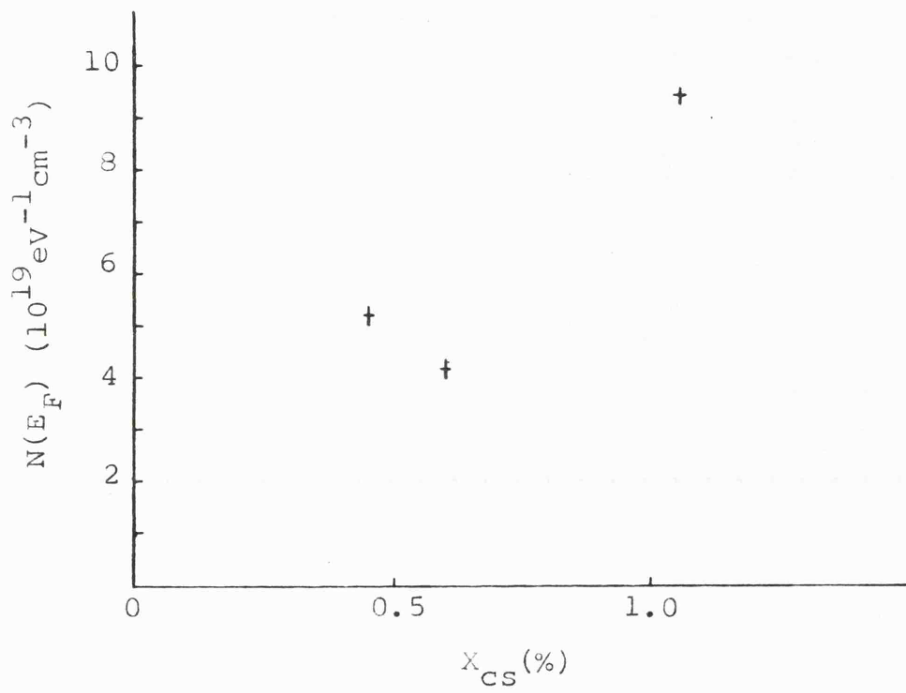


Fig 4.11  $N(E_F)$  vs  $X_{CS}$  for Si:Cu:H alloys.

one neutral metallic grain to another through the insulating medium. When the voltage difference between neighbouring metallic islands  $\Delta V \ll kT/e$

$$B = 2(C/kT)^{\frac{1}{2}} \quad (4.3)$$

after [109], where  $C = X_s E_c^0$  and  $E_c^0 = [e^2/d] f(s/d)$  with  $d$  = diameter of grain,  $s$  = separation,  $X = (2m\phi/\hbar)^{\frac{1}{2}}$ ,  $\phi$  = barrier height and  $f(s/d)$  is a function dependent on the shape and arrangement of the grains and on the interactions between the pair of charges. Characteristic plots of  $\ln \rho \sqrt{s} T^{-\frac{1}{2}}$  for a series of Au - Al<sub>2</sub>O<sub>3</sub> films are shown in fig. 4.12 [109].

The values of  $C$  and  $\sigma_{OL}$ , calculated from the results of the plots of  $\ln \rho$  against  $T^{-\frac{1}{2}}$  (figs. 4.9 and 4.10) are tabulated in Table 4.5 for films of type HI and HII. These results indicate that, over the limited range of composition studied, segregation occurs at relatively low copper concentrations  $X_{cs} \sim 1.05$  ( $\sim 3.4\text{at}\%$ ) and conduction at low temperatures ( $T < 267\text{K}$ ) is due to activated charge carrier creation and tunnelling. This type of conduction has been observed previously in a-Ge: X, with  $X = \text{Cu, Fe, Al}$ , [110] where, for concentrations  $> 10\text{at}\%\text{Cu}$  and Fe and  $30\text{at}\%\text{Al}$ , segregation and clustering of metal atoms has been observed (see Table 4.6). The agreement between films with comparable Cu content is good, indicating that similar conduction processes may be taking place in the Si:Cu:H system.

Data fitting equation 4.1 has also been reported for a-Si(O):Au and a-Si(H): Au films by Hauser [71]. From the published

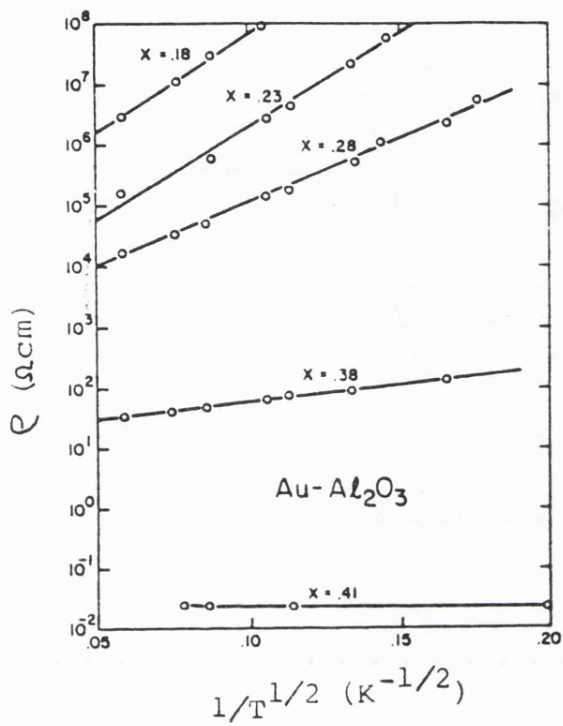


Fig 4.12  $\rho$  vs  $T^{-1/2}$  in the low field regime for Au-Al<sub>2</sub>O<sub>3</sub> films (109).  $x$ =volume fraction of Au in the films.

data, values of  $C$  are presented in Table 4.7 as a function of metal content. As expected, for equal metallic concentrations, the activation energy  $C$  is greater and the pre-exponential  $\sigma_{0L}$  lower for the insulating  $\text{SiO}_2$  than for the semiconducting a-Si:H matrix. It therefore seems likely that Au clusters are present in these films and the speculation that the  $\sigma \propto T^{-\frac{1}{2}}$  behaviour is due to percolation along quasi one-dimensional Au channels appears contentious. However, without detailed structural information on these alloys the mechanism responsible for the observed conduction behaviour will remain uncertain.

Si:Cu alloys prepared by sputtering in an argon atmosphere do not show the same conduction mechanisms as seen in the Si:Cu:H films. As shown in fig. 4.8 there is no distinct transition between competing process for any of the films, unlike the hydrogenated films. This is undoubtedly due to some extent to the higher conductivity of the a-Si host material and the absence of strongly activated conduction at high temperatures. Conductivity behaviour as  $T^{-\frac{1}{2}}$  or  $T^{-\frac{1}{4}}$  provides a satisfactory fit only over a very limited range of temperature. Hence without greatly extending the temperature range of measurement it remains unclear what the conduction processes are.

#### 4.2.2 Optical Absorption

The optical absorption coefficient,  $\alpha$ , of a series of HI type samples was measured as a function of photon energy at room temperature. The data could be fitted to the relation  $\alpha_{hw} = \text{const}(hw - E_0)^2$  as can be seen in fig. 4.13 where  $(\alpha_{hw})^{\frac{1}{2}} \propto hw$  is plotted for the range  $X_{CS} = 0$  to 4.06%. The derived values for the optical gap at room temperature,  $E_0$ , are plotted in fig. 4.14 as a function of  $X_{CS}$ . It

Table 4.7

Metal	Content (at%)	Matrix	C (eV)	$\sigma_{OL} (\Omega^{-1} \text{cm}^{-1})$
Au	14.7	SiO <sub>2</sub>	1.66	$2.632 \times 10^{-7}$
	18		0.56	$1.754 \times 10^{-5}$
	22		0.345	$1.515 \times 10^{-4}$
	25.7		0.207	$2.0 \times 10^{-3}$
	29.3		0.0733	$1.538 \times 10^{-2}$
Au	3.7	Si:H	1.163	$3.125 \times 10^{-4}$
	7.3		0.323	$2.22 \times 10^{-2}$
	11		0.1078	$3.846 \times 10^{-1}$
	14.7		0.0431	1.111

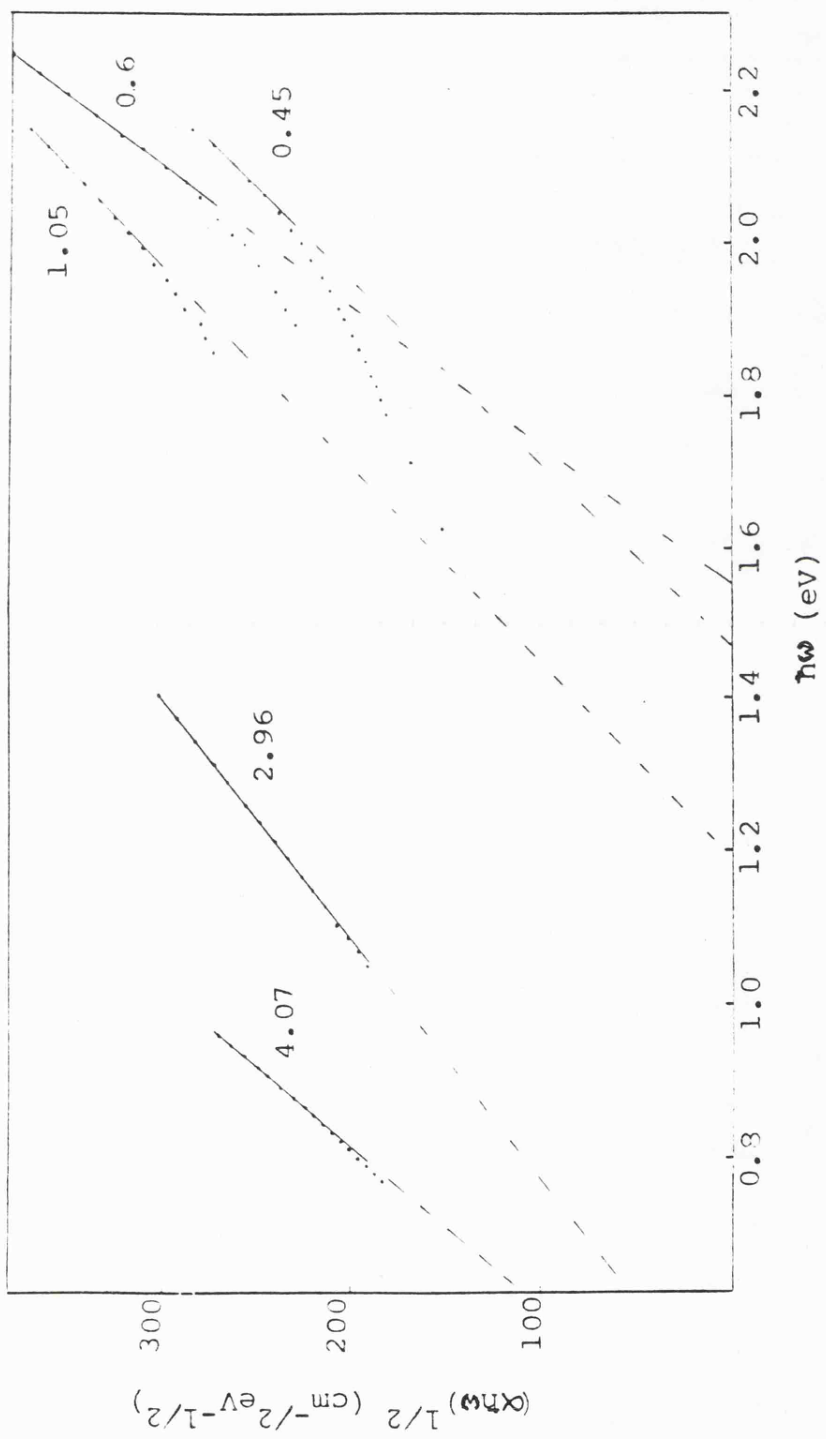


Fig 4.13  $(\alpha h\nu)^{1/2}$  vs  $h\nu$  for a-Si:Cu:H alloys, type HI, as a function of  $X_{\text{Cs}}$ .

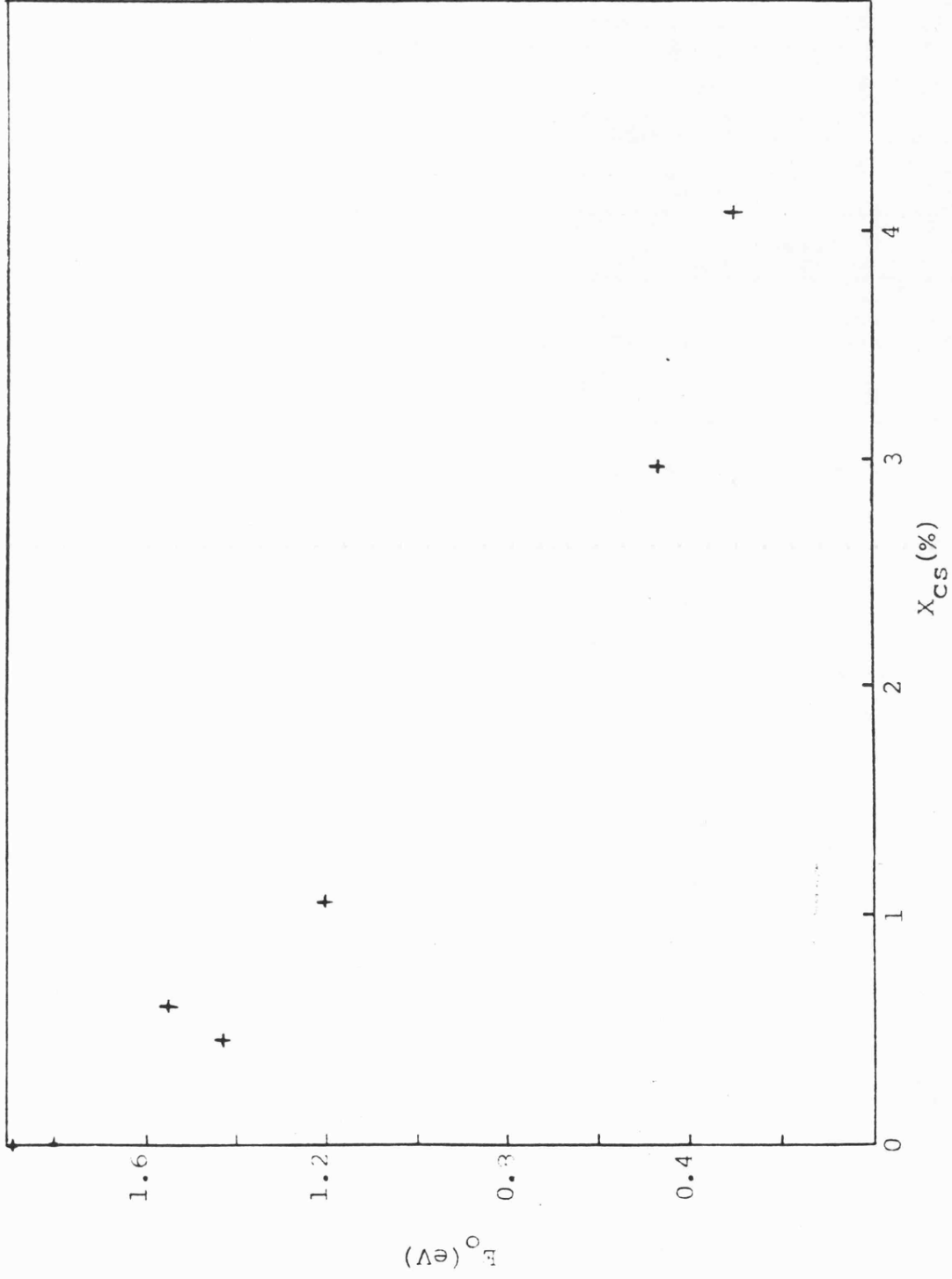


Fig 4.14  $E_0$  vs  $X_{CS}$  for Si:Cu:H (type HI) alloys.

can be seen that the quantity  $E_g$  drops relatively uniformly with  $X_{CS}$  for  $X_{CS} \lesssim 1.1\%$  and eventually saturates at  $E_g \approx 0.3 - 0.5\text{eV}$  for  $X_{CS} \gtrsim 3\%$ . It is evident, solely from the magnitude of  $E_g$  (ie  $E_g > 1.2\text{eV}$ ), that some form of amorphous phase is present for  $X_{CS} < 1.1\%$ , in agreement with the conductivity data. The initial reduction of  $E_g$  from  $1.88\text{eV}$  to  $1.42\text{eV}$  is in broad agreement with  $2E_g$ ,  $1.6$  to  $1.4\text{eV}$ , hence chemical modification of Si by Cu for  $X_{CS} < 0.5\%$  is most likely due to copper alloying with Si rather than doping.

For  $X_{CS} < 1.1\%$  the variation of  $E_g$  with Cu content  $x$  can be approximated to  $E_g(x) = E_g(0) [1 - \delta x]$ , where  $\delta$  serves as an impurity-dependent parameter representing the effectiveness of the impurity in decreasing the gap and  $E_g(0)$  and  $E_g(x)$  being the intrinsic and modified values of  $E_g$  respectively. This form of behaviour has been observed by a number of authors for a-Si/Ge and metal systems, eg Fe, Mn [91] [111], Au, Ag, Ga, Sb [112], and Sn [113]. In each case variable-range hopping conduction is observed and the reduction of  $E_g$  is a result of the growth of deep localized states near the centre of the band gap within which the Fermi level is pinned.

For  $X_{CS} \gtrsim 3\%$ , when segregation seems likely to have already occurred, the optical absorption spectrum is most likely the result of the superposition of the band features of the individual constituents of the film. Hence the derived values of  $E_g$  for these compositions is a weighted average of the energy-dependent components

of the optical absorption. The effect of any segregates which do not contribute to the optical absorption coefficient, in the energy range examined, will be to reduce the shape of the curve in fig. 4.14.

#### 4.2.3 Structural Measurements

The structural measurements made on films prepared in the early stages of this study, type HI, were limited to X-ray powder diffraction studies on films removed from their Corning 7059 substrates by scraping with a scalpel blade. Small fragments of the film were then attached to a thin fibre with araldite and placed in a goniometer at the centre of the camera. This method proved to be unsatisfactory, not only because of the sample preparation procedure, but also because of the limited amount of time available on the Debye Scherrer X-ray diffraction equipment (Dr. Russell, Dept. of Chemistry, University of Leicester).

Powder diffraction patterns for  $X_{\text{CS}} = 2.1$  and 4.24 can be seen in Plates 4.1(a) and (b) where amorphous and polycrystalline type diffraction patterns are apparent. In Plate 4.1(a) ( $X_{\text{CS}} = 2.1\%$ ) only the first halo of a-Si can be distinguished, although other features may be lost due to the poor contrast of the photograph. As  $X_{\text{CS}}$  increases to  $\approx 4.24\%$  (Plate 4.1(b)) phase separation and crystallization take place with polycrystalline copper and a variety of copper silicide phases becoming evident. No crystalline silicon peaks are seen. Our measurements indicate that, for  $X_{\text{CS}} \gtrsim 3\%$ , sputtered hydrogenated Si:Cu alloys prepared under type HI conditions are multicomponent systems.

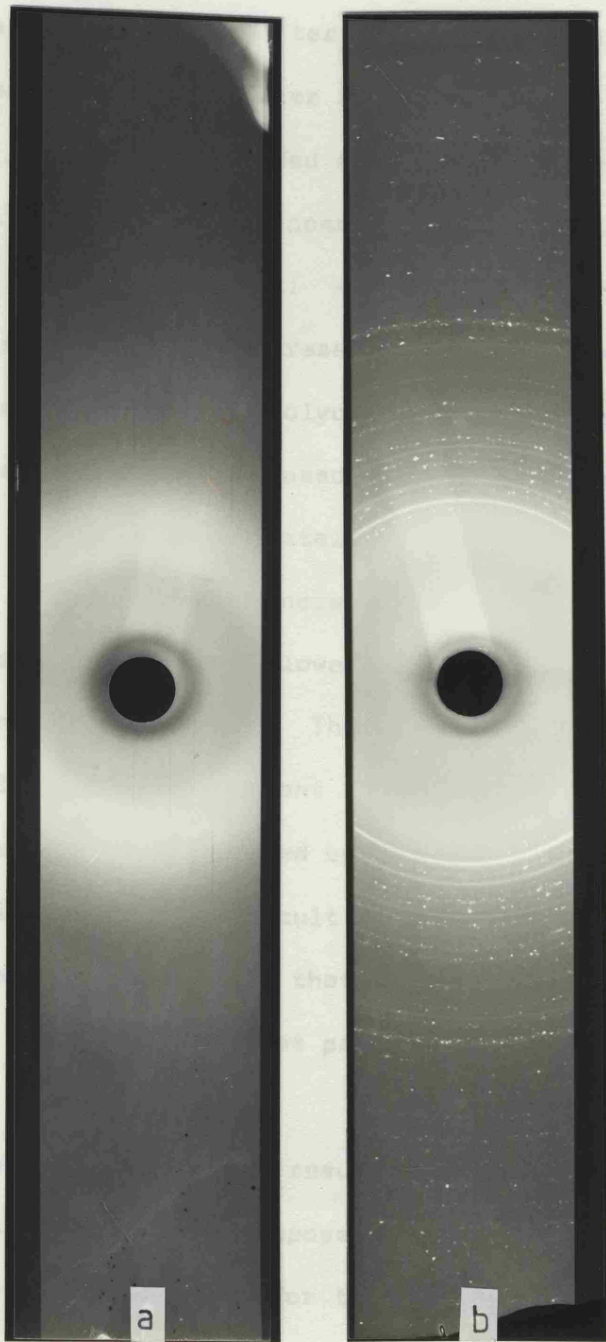
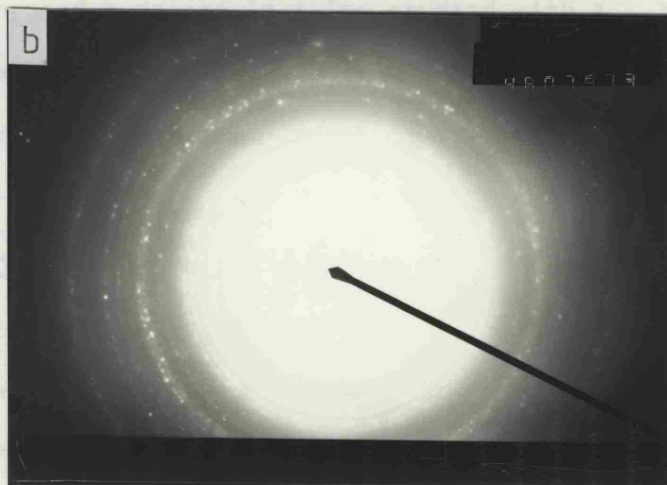
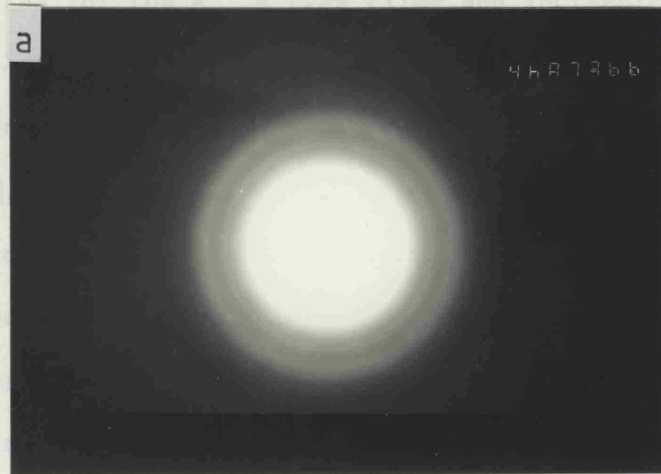


Plate 4.1 X-ray diffraction patterns for ;  
(a) a-Si:Cu:H ( $X_{CS} = 2.1\%$ )  
(b) polycrystalline Si:Cu:H ( $X_{CS} = 4.24\%$ )

Transmission electron microscopy measurements were carried out on some HII and ARI samples, after the introduction of a new substrate platten arrangement with shutter assembly for ultra-thin film preparation (3.4). This provided an alternative method of determining the structure of the silicon-copper alloys. All samples examined (HII  $X_{CS} = 2.66 - 7.42\%$  and ARI  $X_{CS} = 1.5 - 7.42\%$ ) proved to be polycrystalline or showed the presence of a polycrystalline component. In Plate 4.2(a) a polycrystalline copper silicide diffraction pattern is superimposed on the amorphous silicon halo pattern, both amorphous and crystalline phases being present in this sample ( $X_{CS} = 2.66\%$ ). As  $X_{CS}$  increases to  $\sim 7\%$ , and indeed for selected areas of samples with lower copper content, only a polycrystalline phase is found. The range of composition in which a non-crystalline phase is present is uncertain, as in general broad haloes are completely masked by the sharp rings of the crystalline phase making it extremely difficult to identify the amorphous phase. However, it can be said that all films prepared in this work with  $X_{CS} > 1.5\%$  are at least partly polycrystalline.

It is evident from these results that sputtering in a low-pressure argon atmosphere (as opposed to an argon + hydrogen atmosphere) has not prevented the tendency for the silicide formation to occur. This is in contrast to the reported behaviour for the Si:Sn:H system [113] where  $\beta$ -Sn precipitates were eliminated by the removal of hydrogen, a situation attributed to a mechanism involving preferential bonding of H to Si rather than Sn.

Transmission electron micrographs of some representative III and III films are shown in Plates 4.3(a), (b) and (c). Phase separation has occurred in all cases, with the copper-rich islands  $\sim 100 - 150\text{\AA}$  in diameter for the  $X_{\text{Cu}} = 1.1\%$  film and increasing to  $\sim 300 - 400\text{\AA}$  for larger than the  $X_{\text{Cu}} = 7.42\%$  film. The electron diffraction patterns for these films are shown in Plates 4.2(a) and (b). In this case we do not see a polycrystalline pattern, but rather a diffuse ring pattern characteristic of an amorphous matrix since copper is present in the form of small islands. The electron diffraction patterns are shown in Plates 4.2(a) and (b) as a superposition of two patterns.



The presence of a diffuse ring pattern in the electron diffraction patterns has no observable crystalline structure. The electron diffraction patterns at the magnifications shown in Plates 4.2(a) and (b) are characteristic of an amorphous matrix. The electron diffraction patterns for the sputtered films at  $T_d = 200^\circ\text{C}$  at low  $X_{\text{Cu}}$  values have a polycrystalline structure.

4.2.4 Discussion  
Sputtered films of Si:Cu:H alloys have a polycrystalline structure. The alloy exhibits a critical value,  $X_{\text{Cu}}^*$ . As the Cu concentration increases above  $X_{\text{Cu}}^*$ , the amorphous component becomes less dominant. In discussing these alloys it is convenient to divide the alloys into two groups: optical and electrical.

Plate 4.2 Transmission electron diffraction patterns for Si:Cu:H alloys of (a)  $X_{\text{Cu}} = 2.66\%$  and (b)  $X_{\text{Cu}} = 7.42\%$

1)  $X_{\text{Cu}} < 1.1\%$   
Electrical and optical measurements made on films with Cu

Transmission electron micrographs of some representative HII and ARI films are shown in Plates 4.3(a), (b) and (c). Phase separation has occurred in all cases, with the copper-rich islands  $\sim 100 - 150\text{\AA}$  in size for the  $X_{\text{CS}} = 1.5\%$  films and increasing to  $\sim 300 - 400\text{\AA}$  for  $X_{\text{CS}} = 7.42\%$ . These dimensions are considerably larger than the estimated dimensions of copper clusters given by Chopra et al [110], as reported earlier in Table 4.6. However, in this case we do not have a simple metal embedded in a semiconducting matrix since copper is also found in the silicide components of the films. The electronic conduction processes are therefore a superposition of a number of competing mechanisms.

The presence of hydrogen in films studied with  $X_{\text{CS}} > 1.5\%$  has no observable effect on the microstructure of the films at the magnifications employed - see Plates 4.3(a) and (b).

#### 4.2.4 Discussion

Sputtered Si:Cu alloys deposited onto substrates held at  $T_d = 200^\circ\text{C}$  at low pressure  $\sim 7.4\text{m}\tau$ , with and without  $\text{H}_2$  present, have a polycrystalline component when the copper content of the alloy exceeds a critical value,  $X_c$ . As the Cu concentration increases above  $X_c$  the amorphous component becomes less prevalent. In discussing these alloys it is convenient to divide the electronic, optical and structural data into two separate sections i)  $X_{\text{CS}} < 1.1\%$  and ii)  $X_{\text{CS}} > 1.1\%$ .

##### i) $X_{\text{CS}} < 1.1\%$

Electrical and optical measurements made on films with Cu

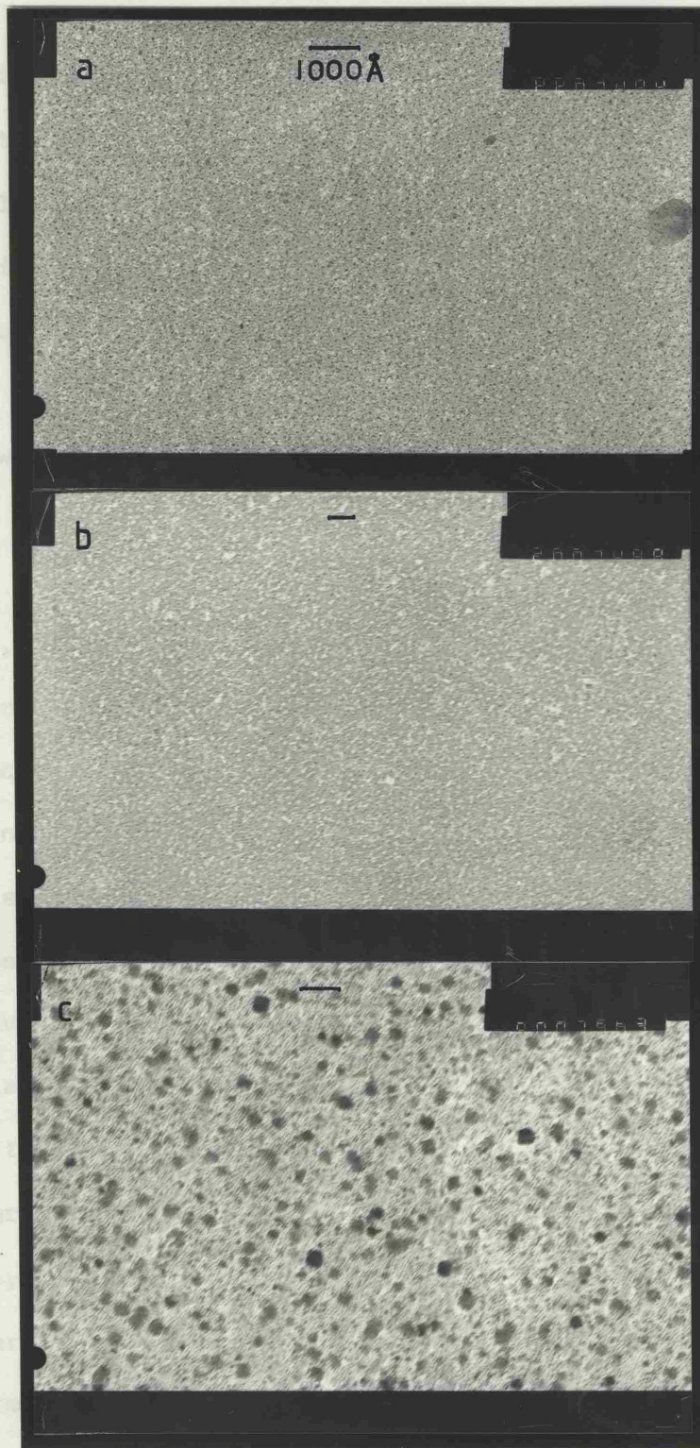


Plate 4.3 Transmission electron micrographs of thin films of (a) Si:Cu:H  $X_{CS}=2.66\%$ , (b) Si:Cu  $X_{CS}=2.66\%$  and (c) Si:Cu:H  $X_{CS}=7.42\%$ .

concentrations in this range exhibit properties which may be interpreted in terms of an amorphous Si:Cu:H alloy, although without a detailed structural investigation of these films it is impossible to discount the possibility that small metallic crystallites could be present in the amorphous matrix.

Copper, which forms deep hole traps in c-Si at  $E_v + 0.53\text{eV}$ , appears to form a similar deep impurity band of localized states in the mobility gap of amorphous silicon near mid-gap, within which the Fermi level,  $E_F$ , is pinned. Coupled with the reduction in  $E_g$ , which is an approximately linear function with  $X_{CS}$ , the thermally activated conductivity at high temperature shows a gradual reduction with increase in Cu content. Owing to the limited range of data at high temperature, the conductivity data shows only qualitative agreement. However, for  $X_{CS} = 0.45\%$   $E_g \approx 2E_\sigma$  ( $E_g = 1.42\text{eV}$ ,  $E_\sigma \approx 0.8 - 0.7\text{eV}$ ) indicating  $E_F$  lies approximately at mid-gap and that the chemical modification of Si by Cu is due to Cu alloying with Si rather than by a doping mechanism. The density of states within the impurity band,  $N(E_F)$ , increases as Cu is introduced and is identified by the introduction of variable-range hopping about  $E_F$  at low temperatures and the gradually increasing conductivity  $N(E_F)$ , as determined from  $\ln \sigma \propto T^{-1/4}$  plots varies from  $N(E_F) = 5.2 \times 10^{19} \text{eV}^{-1} \text{cm}^{-3}$  for  $X_{CS} = 0.45\%$  to  $N(E_F) = 9.5 \times 10^{19} \text{eV}^{-1} \text{cm}^{-3}$  for  $X_{CS} = 1.05\%$ . These results are in broad agreement with similar measurements made on a-Si: Ni, Mn, Fe, Co [90] [91] [93]] and Ge: Cu; Fe [110] where VRH conduction and a gradual reduction in the optical gap, in conjunction with ESR measurements, have been interpreted in a similar manner.

ii)  $X_{CS} > 1.1\%$

Direct structural measurements on films with  $X_{CS} > 1.5\%$ , irrespective of the presence of hydrogen, indicate that the films are not homogeneous, a polycrystalline phase is present in all films which becomes more dominant with increase in Cu concentration (See Plates 4.2 (a) and (b)). Electrical and optical properties of alloys prepared within this compositional range are dominated by the hetrostructure of the films. Electrical conductivity, which obeys a  $T^{-\frac{1}{2}}$  relationship at low temperatures for films containing H, HII type, can be interpreted in terms of thermally activated tunnelling between metallic grains in an amorphous semiconductor matrix. TEM measurements resolve islands of  $d \approx 100 - 150\text{\AA}$  for  $X_{CS} = 1.5\%$  and  $\approx 300 - 400\text{\AA}$  for  $X_{CS} = 7.42\%$ . However, this model is at best an oversimplification of the problem as polycrystalline copper-silicides as well as c-Cu are identified from the diffraction patterns (Plate 4.1(b)). Although the structure of the films with and without hydrogen appear similar, the d.c. conductivity of alloys without  $H_2$  may not be modelled by equation 4.2. This could be due to the great increase in conductivity of the amorphous silicon phase upon the removal of hydrogen from the plasma, resulting in a more temperature-insensitive conductivity behaviour.

The optical properties of inhomogeneous media are controlled by the individual band structures of the components of the alloy. Hence the derived values of  $E_o$  are weighted averages of the optical gaps of the individual components of the film. The values of  $E_o$ , in fig. 4.14, for  $X_{CS} > 1.5\%$  must therefore be treated as composite

quantities, and not distinct optical band gaps as was the case for  $X_{cs} < 1.5\%$ .

The range of single-phase non-crystalline Si:Cu alloys accessible by the technique employed in this study ( $X_{cs} < 1.1\%$ ) is considerably less than that obtained by co-evaporation onto liquid nitrogen cooled substrates [89] when  $0 < x < 76$  at%. The reason why phase separation is observed in films with  $X > X_{cs}$  can be attributed to a number of factors: a) The high surface mobility of Cu on a substrate held at elevated temperature; b) the low solid solubility of Cu in c-Si, ie  $9 \times 10^{-5}$  at% Cu in Si at  $\approx 800^\circ\text{C}$ , (This quantity is presented for comparative purposes as no published value for a-Si is available); c) the existence of a large number of stable crystalline compounds (see fig. 4.15).

Of these factors only a) can be controlled within the experimental arrangement available. Hence by reducing  $T_d$  drastically to  $\sim 77\text{K}$ , and by altering plasma conditions, to a low pressure of Ar, a wider range of a-Si:Cu alloys could be prepared by the co-sputtering technique.

### 4.3 a-Si:Au:H alloys

#### 4.3.1 D.C. conductivity and thermoelectric power

This dissertation presents the first systematic study of electronic, optical and structural properties of amorphous hydrogenated silicon alloyed with gold. In some respects the results are similar to those reported for the evaporated Si:Au system though many of the results are distinct to a-Si:Au:H.

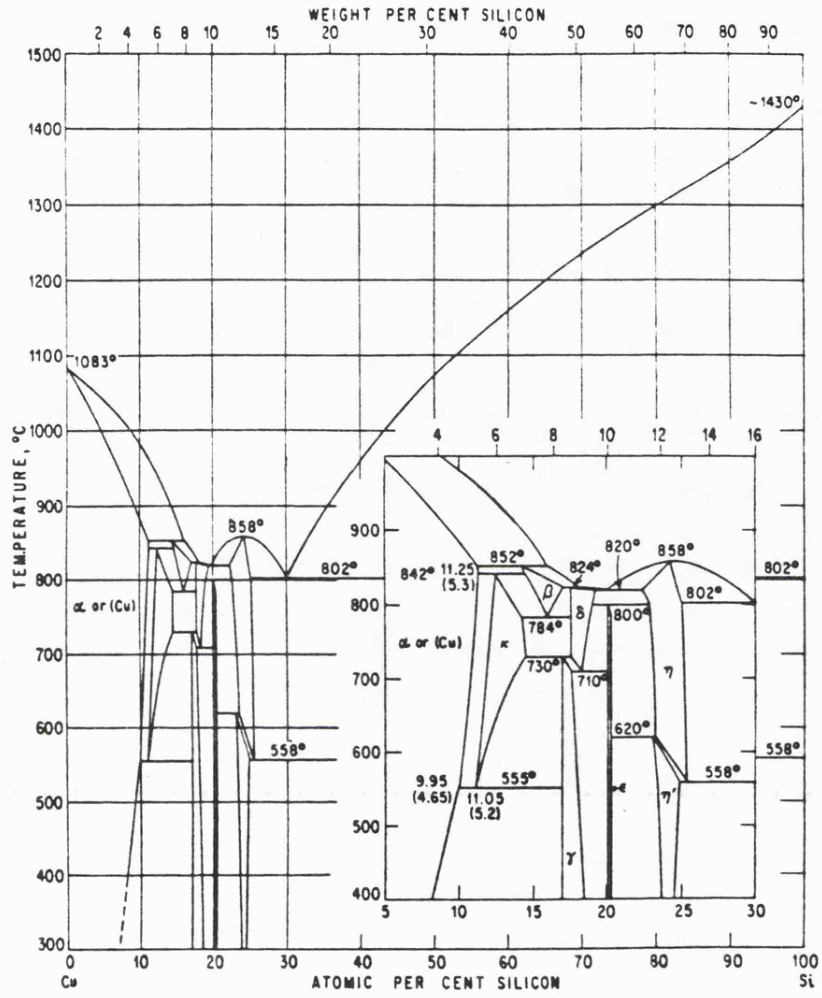


Fig 4.15 The equilibrium phase diagram for the Cu-Si system.(130)

The amorphous hydrogenated silicon-gold films were prepared by co-sputtering in an argon-hydrogen atmosphere, with small pieces of 5N pure gold (J. Matthey Ltd.) being placed on the 100mm diameter silicon target. For targets in which the Au pieces covered less than  $\sim 2\%$  of the total surface area of the target, the Au pieces were  $\sim 4 \times 4 \times 0.25\text{mm}$ , though above this percentage some of them were replaced with  $8 \times 8 \times 0.25\text{mm}$  pieces. The sputtering conditions were as described in 3.1.4 which enabled the preparation of high-quality a-Si:H in the diffusion-pumped system with deposition temperatures of  $200^\circ\text{C}$  [sample type HII] and  $21^\circ\text{C}$  [type HIII], low power  $\sim 2.47\text{Wcm}^{-2}$  and total pressure of  $\sim 7.4\text{mTorr}$  with 30%  $\text{H}_2$ .

Electrodes used throughout were gold, evaporated from a separate source in the chamber, and in general were co-planar (gap-cell arrangement) though on several occasions a sandwich-cell geometry was used. The results compared favourably, though the ease in fabrication of the gap-cell arrangement made this geometry preferable and was more widely used. Deposition of electrodes was made in the same pump-down cycle as the sputtering of the amorphous thin film. In an attempt to minimise diffusion between the electrodes and the amorphous alloy, the gold was not evaporated until substrate temperature had approached room temperature.

The gold electrodes proved in general to be ohmic for the voltages applied i.e.  $< 10^3\text{Vcm}^{-1}$ . The chemical composition of a number of the samples was determined by an electron-beam microprobe using energy dispersive analysis of the X-rays, (Mr. R. Wilson, Department of Geology, Leicester University), as was used also to a

limited extent for the Si:Cu:H system. Using polycrystalline gold and amorphous silicon as standards, an accuracy of  $\sim 10\%$  was estimated for the compositional determination of  $\sim 1\mu\text{m}$  films deposited onto thin Al-foil substrates. To the detection limit of the instrument,  $\sim 0.1$  at% for most elements with  $z > 11$ , no contaminants could be identified on any of the films analysed.

In figure 4.16  $X_{AS}$ , the Au/Si surface-area ratio for a series of target configurations is plotted against the analysed composition of the sputtered film. The results for the two deposition temperatures are similar, and agree to within the accuracy of the measuring technique. With increasing gold coverage of the cathode the effective Au/Si sputtering rate reduces from  $\approx 6.25$  at 5 at% Au to  $\sim 3.8$  at 17 at% Au. This compares with 6.0 times reported by Glang & Maisel [108] for sputtering at 1keV in Ar. The reduction can be attributed to at least two factors; the increase in the surface area of Au making poor contact with the cathode and the use of large Au pieces for high Au content samples, leading to a reduction in effective edge area of Au available to be sputtered.

The composition of films which were not analysed by EBMA has been evaluated from  $X_{AS}$  and the calibration curve of figure 4.16. It must be emphasised that, since H cannot be detected by this technique and Ar, although detectable, is not calibrated for, the Au and Si at% values are relative rather than absolute quantities.

Sputtering rates for  $T_d = 200^\circ\text{C}$  and  $21^\circ\text{C}$  were  $\sim 1.05 \pm 0.05$  and  $1.2 \pm 0.05 \text{ \AA s}^{-1}$  respectively for all  $X_{AS} > 0$ . As the deposition

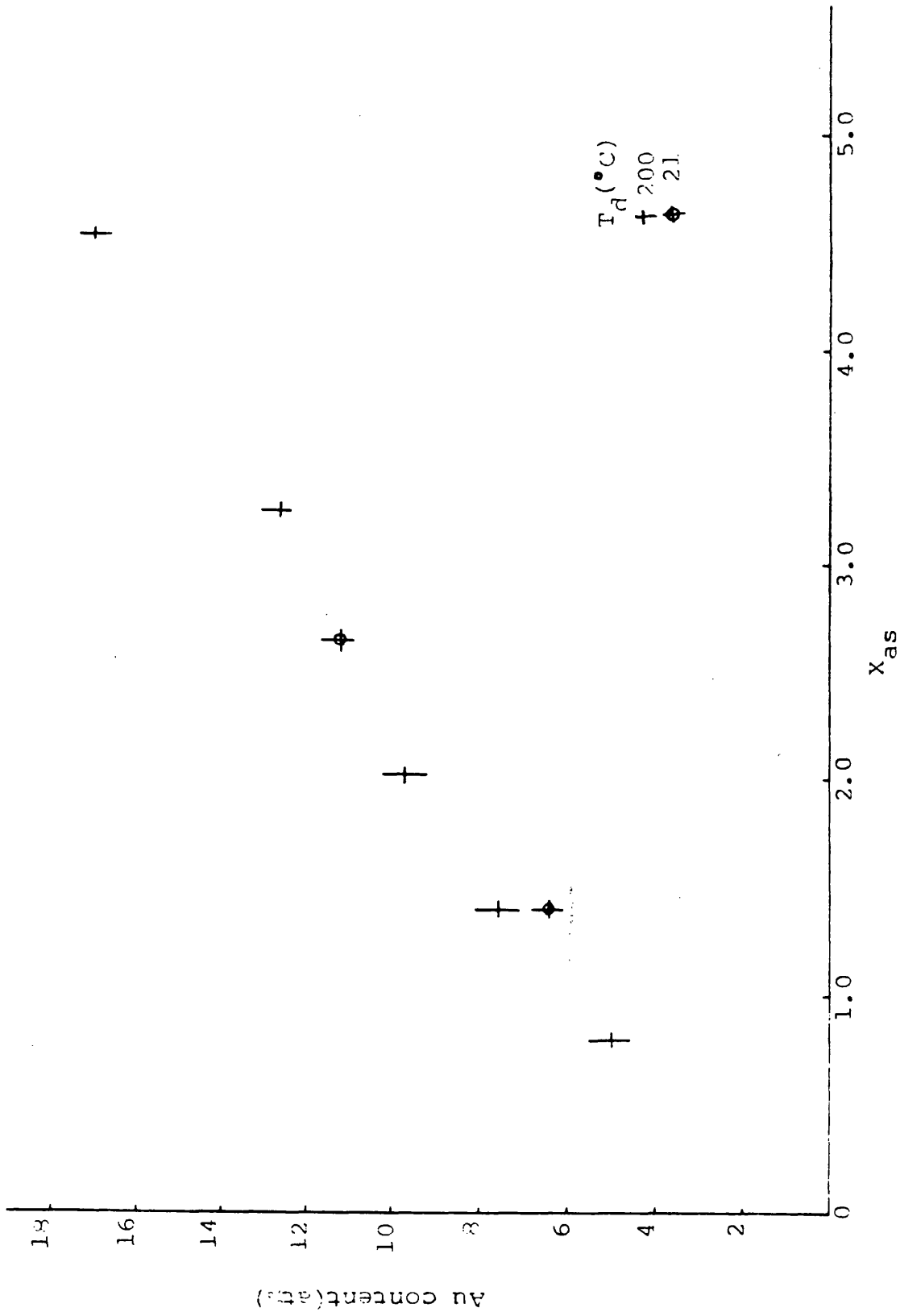


Fig 4.16 Au content vs  $X_{as}$  for a-Si:Au:H alloys.

temperature is reduced the number of atoms and molecular groups sticking and adhering to the substrate surface increases, there is an effective decrease in "re-emission coefficient" resulting in the observed increase in deposition rate.

The room-temperature d.c. conductivity,  $\sigma_{RT}$ , as a function of gold content is displayed in fig. 4.17. Very small amounts of Au  $\sim 0.26$  at% have a dramatic effect on the conductivity,  $\sigma_{RT}$ , which rises by three orders of magnitude from that of pure Si:H. For larger Au concentrations,  $x > 5$  at%, the rate of increase in conductivity slowly decreases with further Au. Conductivity values for  $T_d = 200^\circ\text{C}$  and  $21^\circ\text{C}$  films of the same  $x$  are similar, though the room-temperature deposited films have a relatively higher conductivity value for constant  $x$ . The temperature dependence of conductivity as a function of reciprocal temperature is plotted in figs. 4.18 and 4.19 for the above samples. It can be seen that the incorporation of  $\sim 0.26$  at% Au dopes the a-Si:H, reducing the activation energy  $E_{\sigma 1}$  from 0.89eV to 0.61eV and (after equation 1.11)  $\sigma_{10} = 1.4 \times 10^3$  to  $3.3 \times 10^1 \Omega^{-1} \text{cm}^{-1}$ , and at lower temperatures ( $T < 313\text{K}$ ) results in band-tail hopping with  $E_{\sigma 2} \sim 0.49\text{eV}$ . With  $E_{\sigma 1} = (E_c - E_F)_0$  or  $(E_F - E_v)_0 = 0.61\text{eV}$  and  $E_{\sigma 2} = (E_A - E_F)_0 + W$  or  $(E_F - E_B) + W = 0.49\text{eV}$  a band-tail width  $(E_c - E_A)$  or  $(E_B - E_v) \approx 0.21\text{eV}$  may be derived by assuming  $W \approx 0.09$  [114]. This value is in agreement with previous evaluations of this quantity for a-Si:H. A schematic representation of a possible energy band configuration for gold-doped a-Si:H is shown in fig. 4.20. Owing to the change in  $\sigma_{10}$  from  $1.4 \times 10^3$  to  $33 \Omega^{-1} \text{cm}^{-1}$ , and also thermoelectric power results, it seems likely that conduction is predominantly p-type with the Fermi level situated

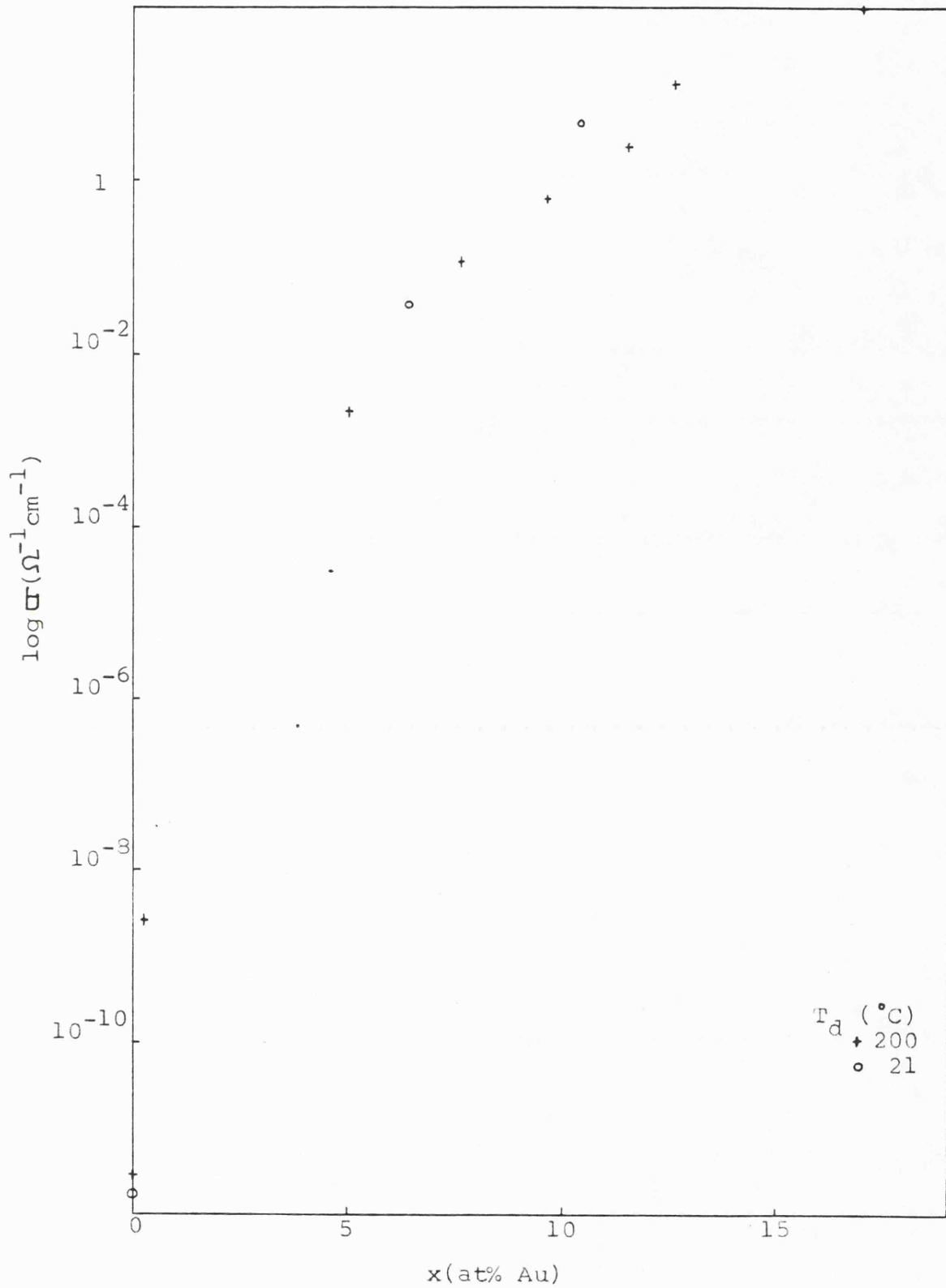


Fig 4.17  $\sigma_{RT}$  vs Au content for a-Si<sub>1-x</sub>Au<sub>x</sub>:H films.

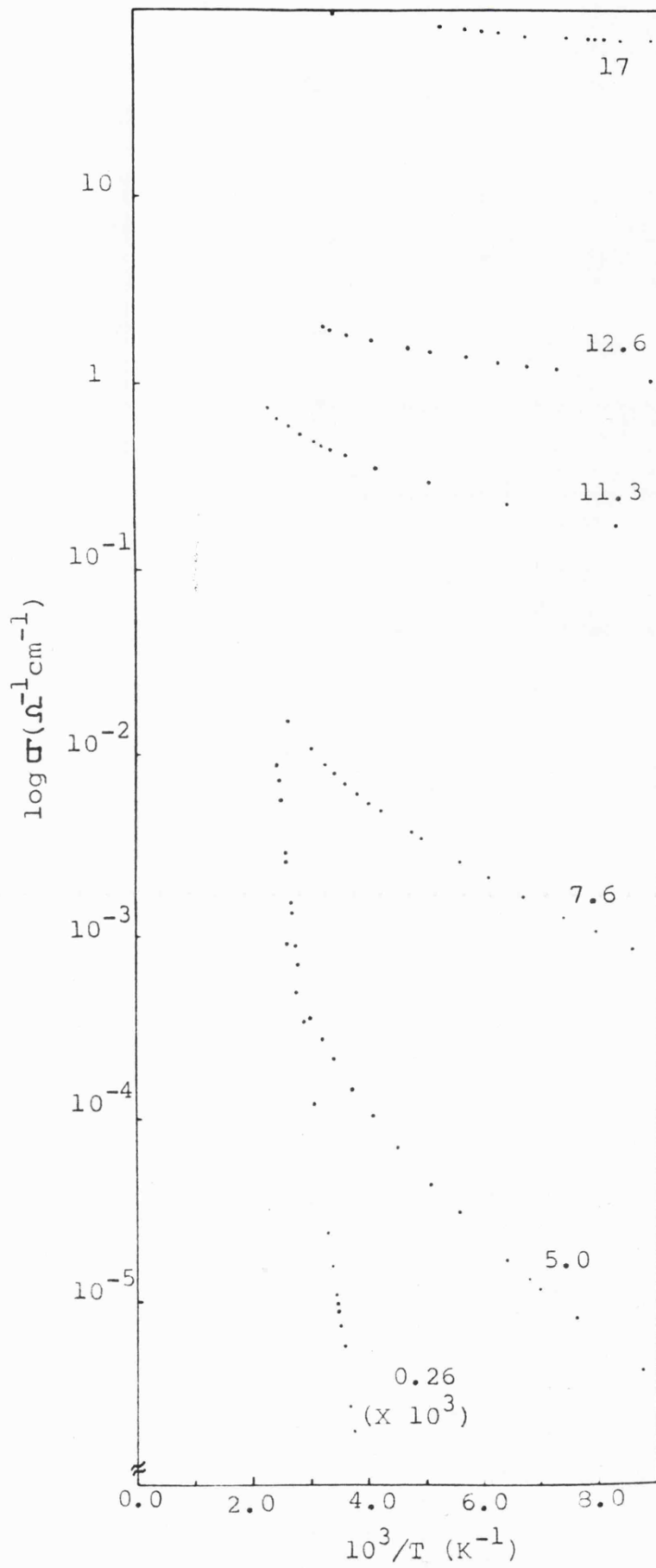


Fig 4.13  $\sigma$  vs  $10^3/T$  for  $a\text{-Si}_{1-x}\text{Au}_x\text{:H}$  alloys as a function of  $x$ .

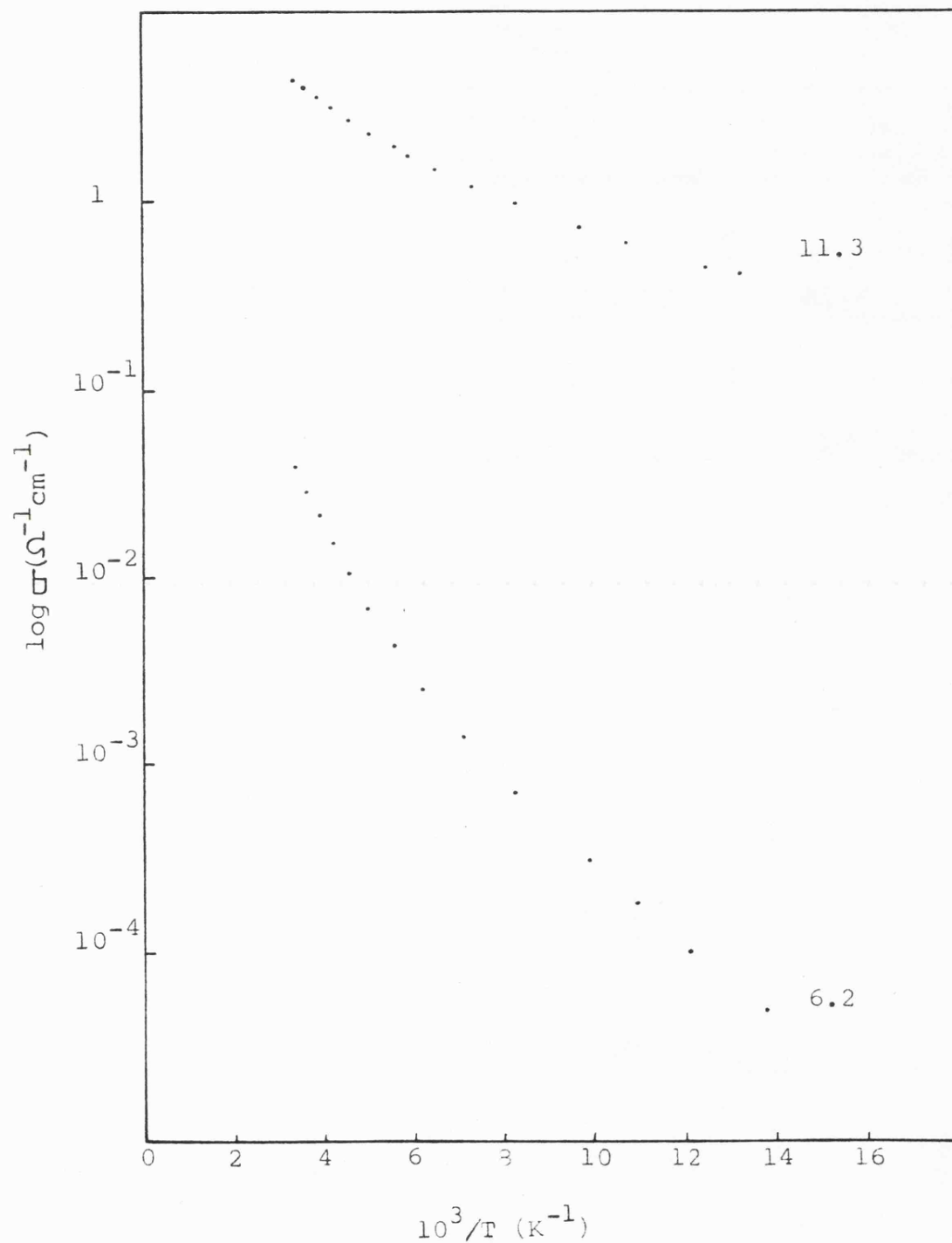


Fig 4.19  $\sigma$  vs  $10^3/T$  for  $\text{a-Si}_{1-x}\text{Au}_x\text{:H}$  films deposited at  $21^\circ\text{C}$ .

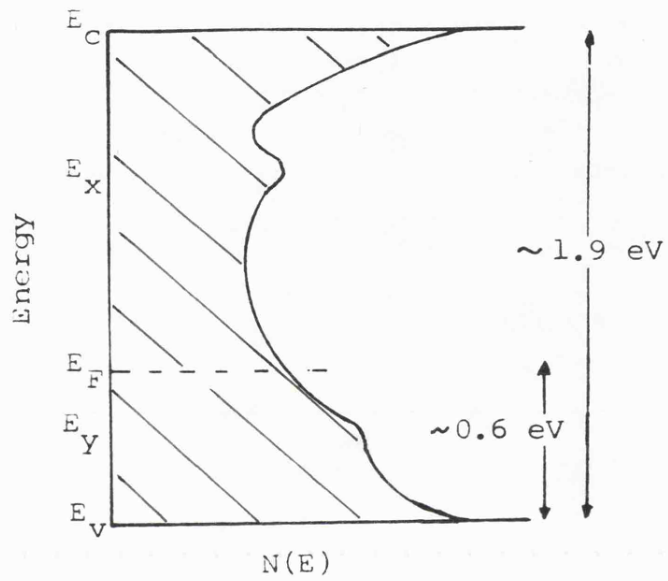


Fig 4.20 A schematic representation of a density of states distribution for  $a\text{-Si}_{99.76}\text{Au}_{0.26}\text{:H}$  film.

near  $E_y$ .

Steady-state photoconductivity as determined by the method described in (4.1) was measured for this sample. Upon illumination the conductivity rises by  $\sim 10$  times at room temperature. No photoconductivity was observed for films with  $x > 5$  at%.

Films with  $5 < x < 11.3\%$  for both deposition temperatures display variable-range hopping conduction as can be seen by the  $\ln \sigma$  against  $T^{-1/4}$  plots of figures 4.21 and 4.22 for temperatures below  $\sim 0.25 - 0.26(K^{-1/4}) \cong 256$  K. The  $T_0$  values were derived from equation 1.27

$$\sigma = \sigma_{OH} \exp - \left( \frac{T_0}{T} \right)^{1/4}$$

where  $T_0 = 16 \alpha^3 / kN(E_F)$ . They show an exponential dependence on Au content as shown in fig. 4.23. This indicates an approximately exponential increase in the density of localized states at the Fermi level,  $N(E_F)$ , with increase in Au concentration. However, when  $x \lesssim 14\%$ , it is expected that the quantity  $\alpha^{-1}$ , the decay length of the localized electrons, will increase rapidly until the wavefunction becomes completely extended for  $x > 14\%$ . With a constant  $\alpha^{-1}$  value of  $\sim 10 \text{ \AA}^{-1}$ ,  $N(E_F)$  ranges from  $1.38 \times 10^{19}$  to  $3.79 \times 10^{21} \text{ eV}^{-1} \text{ cm}^{-3}$  for  $5 < x < 11.3$ . For comparative purposes the published  $T_0$  values for co-evaporated a-Si:Au [75] are displayed in fig. 4.23. It can be seen that for a constant  $x$   $T_0(\text{HIII}) > T_0(\text{HII}) > T_0(\text{evap})$ , implying  $N(E_F)_{\text{HIII}} < N(E_F)_{\text{HII}} < N(E_F)_{\text{evap}}$ . It seems conceivable that hydrogenated material should have a slightly lower  $N(E_F)$  than evaporated material, even considering the magnitude of the impurity present. Though why  $N(E_F)$  of room-temperature deposited

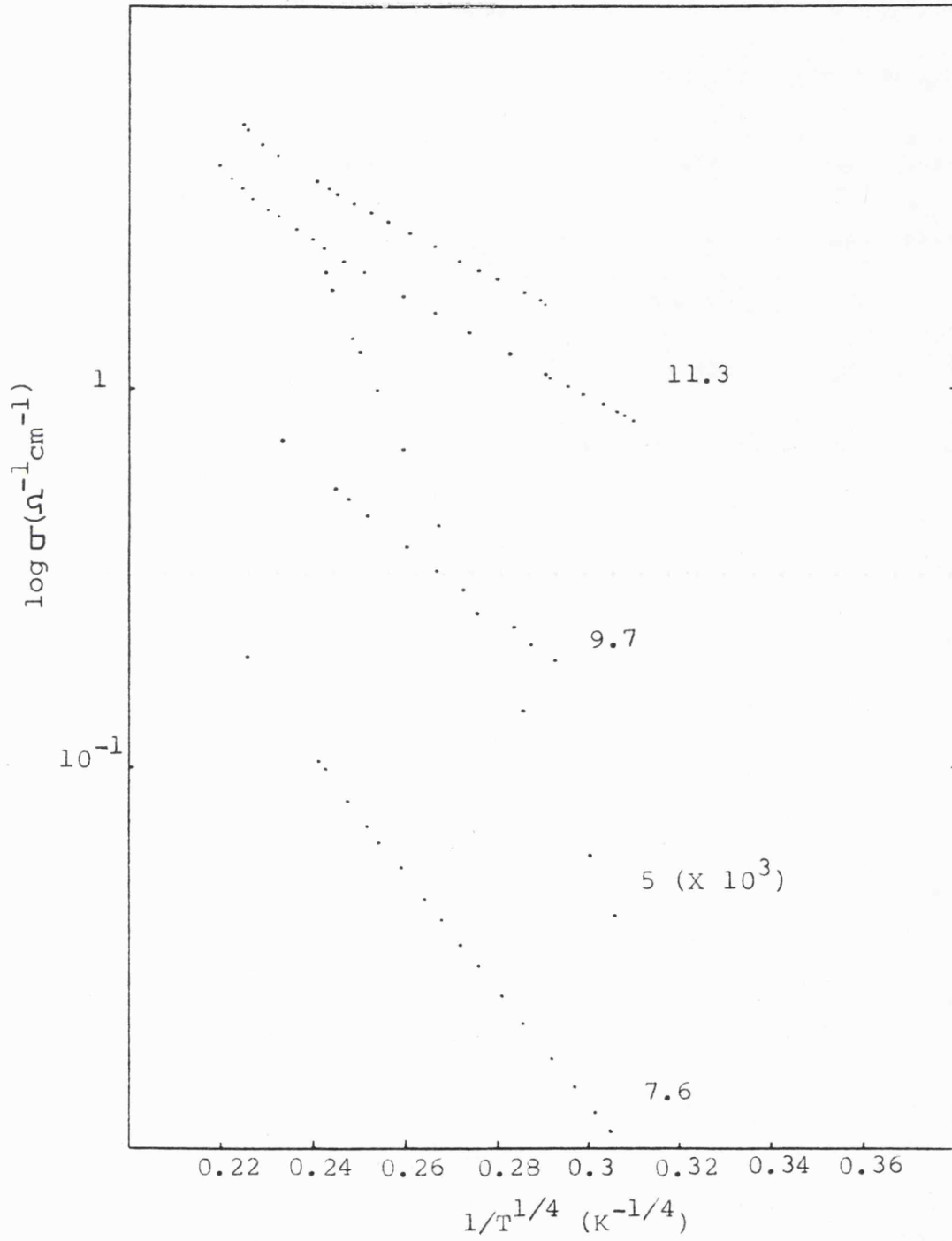


Fig 4.21  $\sigma$  vs  $T^{-1/4}$  for a-Si<sub>1-x</sub>Au<sub>x</sub>:H films deposited at 200°C.

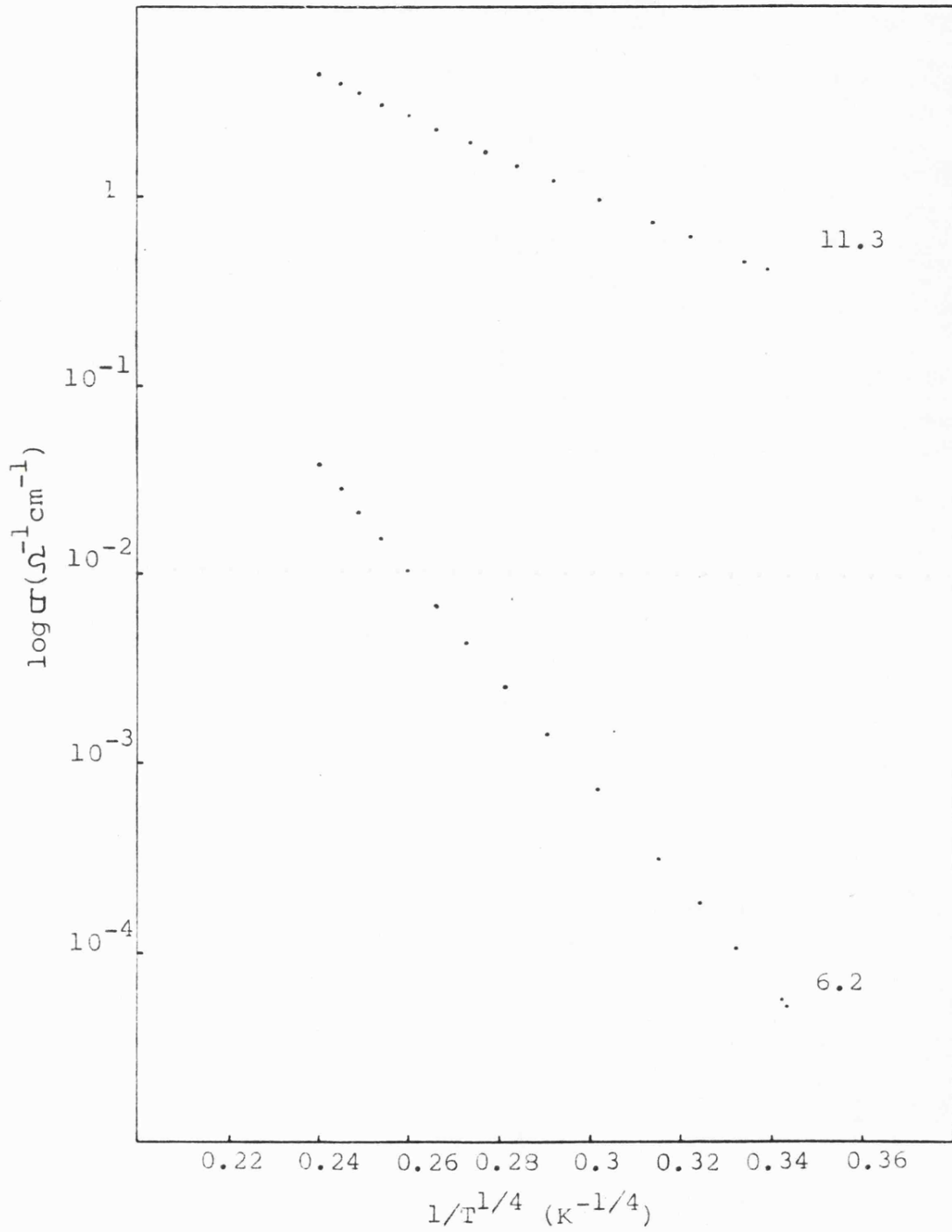


Fig 4.22  $\sigma$  vs  $T^{-1/4}$  for a-Si<sub>1-x</sub>Au<sub>x</sub>:H films deposited at 21°C.

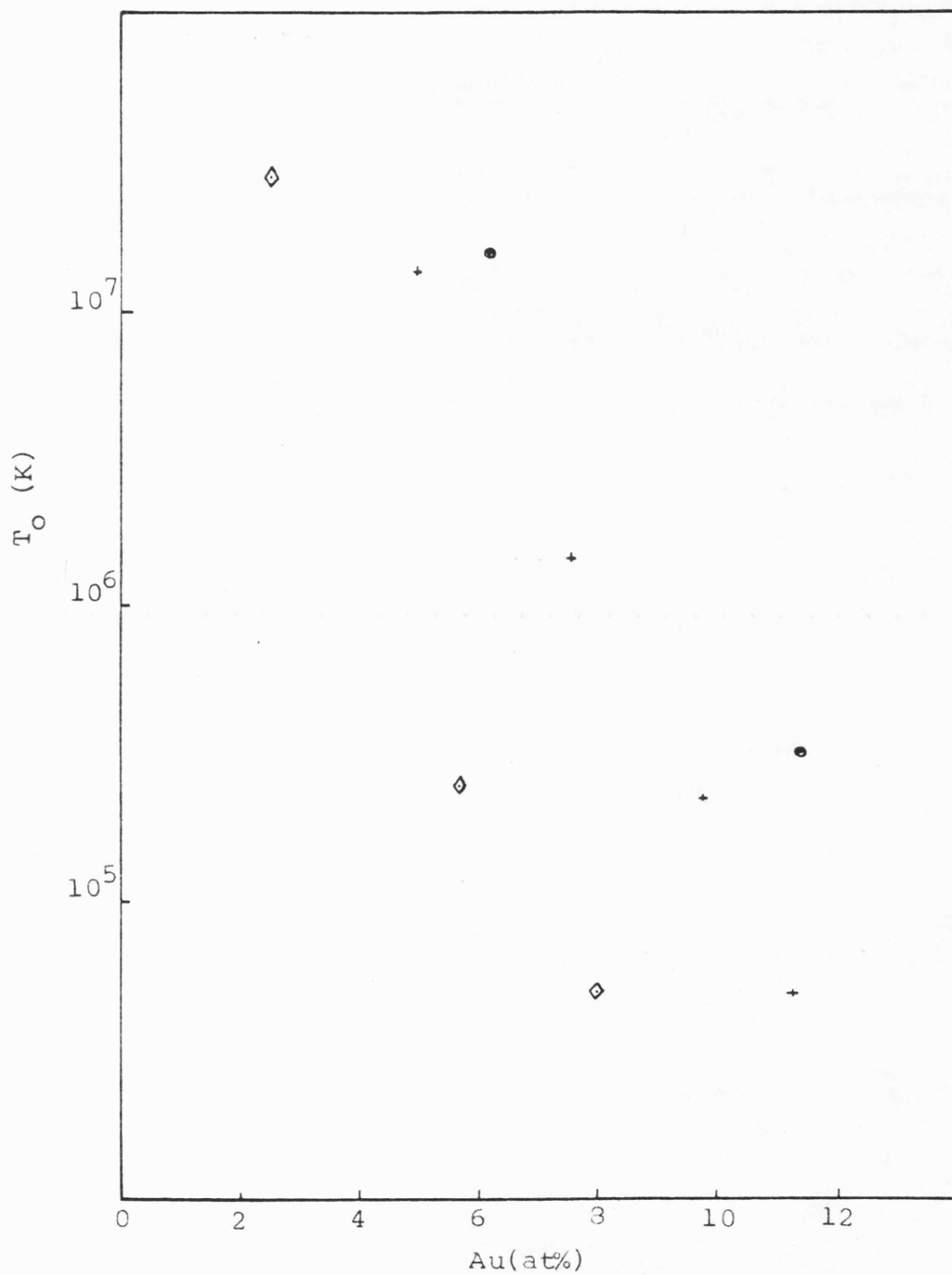


Fig 4.23  $T_0$  vs Au content for sputtered,  $T_d = 200^\circ\text{C}$  +,  $21^\circ\text{C}$  • and evaporated ◊ films. ( 68)

material should be lower than that deposited at 200°C is not understood at present.

The d.c. conductivity behaviour at high temperatures, up to ~ 140°C, for films with 5% < x < 11.3% is more strongly thermally activated than the low-temperature region which displays variable-range hopping conduction. Owing to the limited temperature range studied a high-temperature activation energy cannot be evaluated. From the reversible nature of the high-temperature conductivity it is evident that the a-Si:AuH alloys examined show no signs of crystallization.

As a result of the very gradual change in conductivity, for films with high Au content x > 11.3%, over the low-temperature range described previously, T > 77K, measurements down to very low temperatures (~ 7K) were deemed essential to investigate the conduction processes occurring at and near the metal-insulator-transition. To achieve these temperatures an Oxford Instruments continuous-flow cryostat, as described in 3.2.1, was used with liquid helium [B.O.C.]. Owing to experimental difficulties and constraints on time the low-temperature data is of a somewhat limited nature.

In fig. 4.24 the data for x = 11.3 and 12.6% is plotted on a  $\ln \sigma \propto T^{-1/4}$  graph, reaffirming the existence of variable-range hopping conduction at low temperatures. Also presented in this figure is an attempt at fitting the data to a  $T^{-1/2}$  relationship, as employed in (4.2) for the Si:Cu system; this relation does not

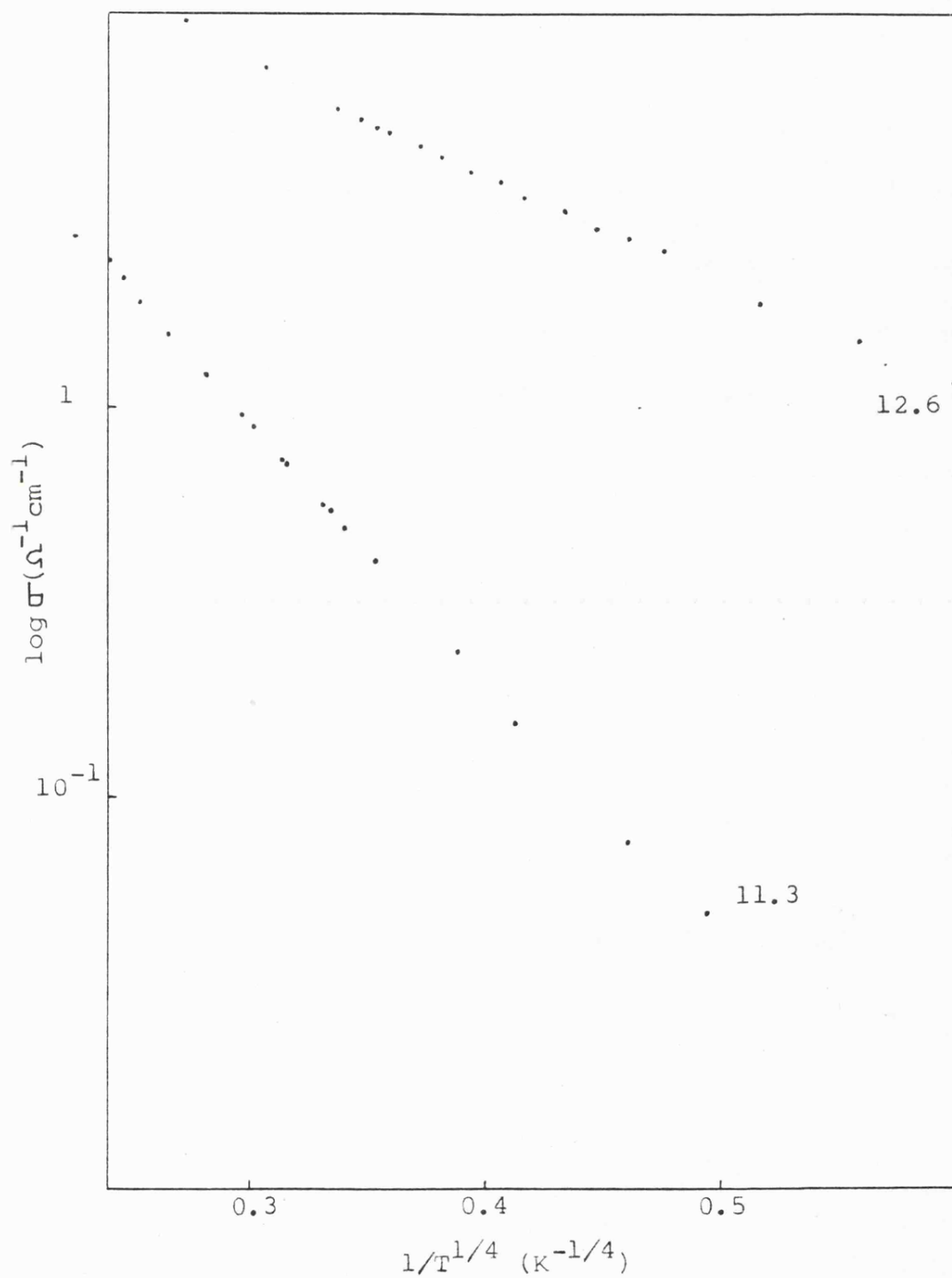


Fig 4.24  $\sigma$  vs  $T^{-1/4}$  for  $x=11.3$  and  $12.6$  at% Au.

succeed in describing the temperature dependence of the conductivity and it is concluded that a cermet-type structure does not occur for the a-Si:Au:H case unlike the Si:Cu:H alloy series deposited under similar conditions.

In fig. 4.25(a) and (b) the conductivity is plotted linearly as a function of  $T^{\frac{1}{2}}$  and  $T^{\frac{1}{3}}$  for  $x = 12.6$  and  $17\%$ . If the conductivity obeys the relationship [equation 2.1]  $\sigma(T) = \sigma(0)[1 + AT^{\frac{1}{2}}]$  or  $\sigma(T) = \sigma(0)[1 + A^1T^{\frac{1}{3}}]$  after [115] [36] the slope of the linear region obeying  $T^{\frac{1}{2}}$  or  $T^{\frac{1}{3}}$  should give a value for A and the intercept point with the conductivity axis a value for  $\sigma(0)$ . As can be seen in the figure for  $x = 12.6\%$  the A value would be negative, for positive  $\sigma(0)$ , indicating at this composition the material is not yet metallic. When  $x > 14\%$  Au, a metal-insulator transition occurs in the Si:Au system. The values of  $A = 0.153$  and  $\sigma(0) = 26.2\Omega^{-1}\text{cm}^{-1}$  for  $x = 17\%$  (fig. 4.25(a)) are in accordance with a film in which the conduction process has just become delocalized. the value of  $\sigma(0)$  the conductivity at  $T = 0$  lies below the early estimates of  $\sigma_{\min}$  for this system [24].

In fig 4.25(a) for  $x = 17\%$  the  $T^{\frac{1}{3}}$  relationship does appear to provide a superior fit to the data than that displayed in the  $\sigma$  vs  $T^{\frac{1}{2}}$  plot. This may be fortuitous as the number of data points is limited, though a similar power-law relationship has been reported by Dobson et al [36] for the a-Ge:Au system.

The thermoelectric power of the sputtered a-Si:Au:H alloys, as a function of Au content, is shown in fig. 4.26. Measurements were

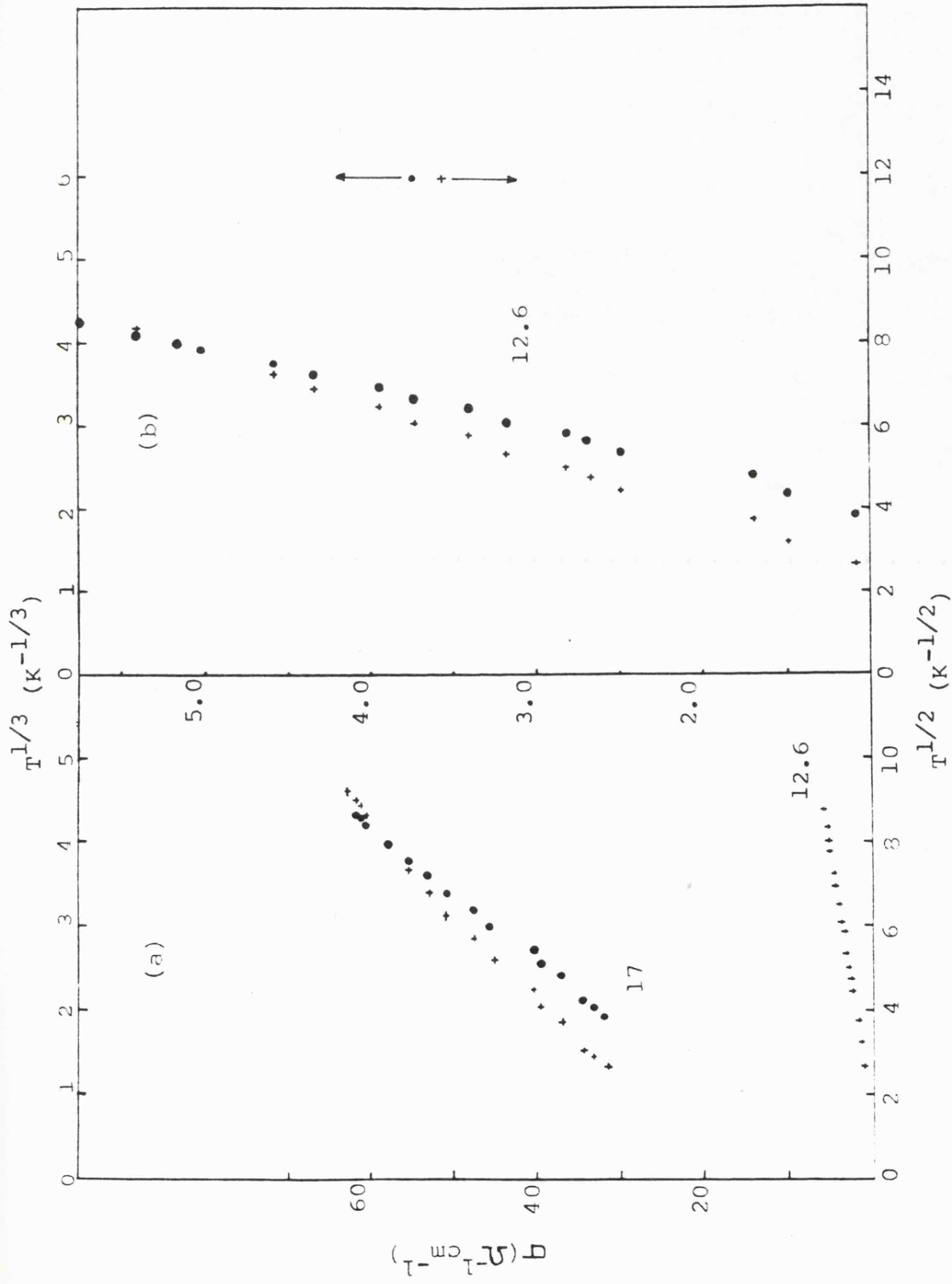


Fig 4.25  $\square$  vs  $T^{-1/2}$  and  $T^{-1/3}$  for  $x=12.6$  and 17 % Au.

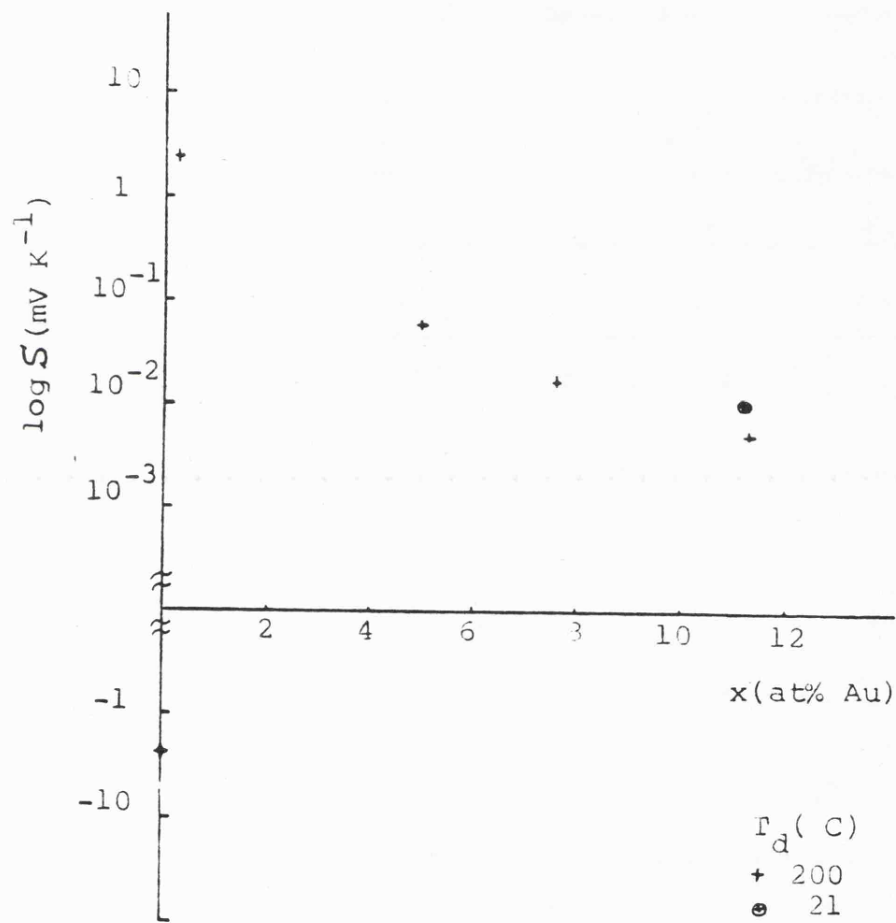


Fig 4.26  $S$  vs  $x$  for some  $a\text{-Si}_{1-x}\text{Au}_x\text{:H}$  alloys.

made at  $T \sim 310 \pm 5K$ , except  $x = 0$  where, owing to the very low conductivity of a-Si:H, the reading was taken at 358K. At  $x = 0.26\%$  the dominant conduction process changes from n-type, characteristic of a-Si:H, to p-type conduction as indicated by the change in sign of the thermopower. With increase in Au content the magnitude of the thermopower steadily decreases from  $\sim 2mVK^{-1}$  for  $x = 0.26\%$  to  $\sim 7\mu VK^{-1}$  at 11.3% as a result of the change in electronic transport mechanism from extended-state to variable-range hopping type conduction. Figure 4.27 shows the behaviour of the thermopower, as a function of temperature for the two samples containing the highest Au concentration examined,  $x = 11.2$  and 11.3% deposited at 21 and 200°C respectively. It can be seen that below  $\sim 340K$  the results show an almost linear variation with temperature for both samples in accordance with equation 1.40 [32]

$$S_h(T) = \left[ \frac{\pi^2 k^2 T}{3e} \right] \left[ \frac{d \ln \sigma(E)}{dE} \right]_{E_F}$$

It should be noted that recently the thermopower  $S_h$  for variable-range hopping has been calculated to have a square-root dependence with temperature [28]. This clearly does not fit the data in fig. 4.27.

#### 4.3.2 Optical Absorption

The optical absorption coefficient,  $\alpha$ , as a function of photon energy,  $\hbar\omega$ , is shown in figures 4.28 and 4.29 for sputtered hydrogenated silicon-gold films deposited at 200°C and 21°C respectively. In terms of the fundamental absorption edge the introduction of Au into a-Si:H gradually lowers the energy of the

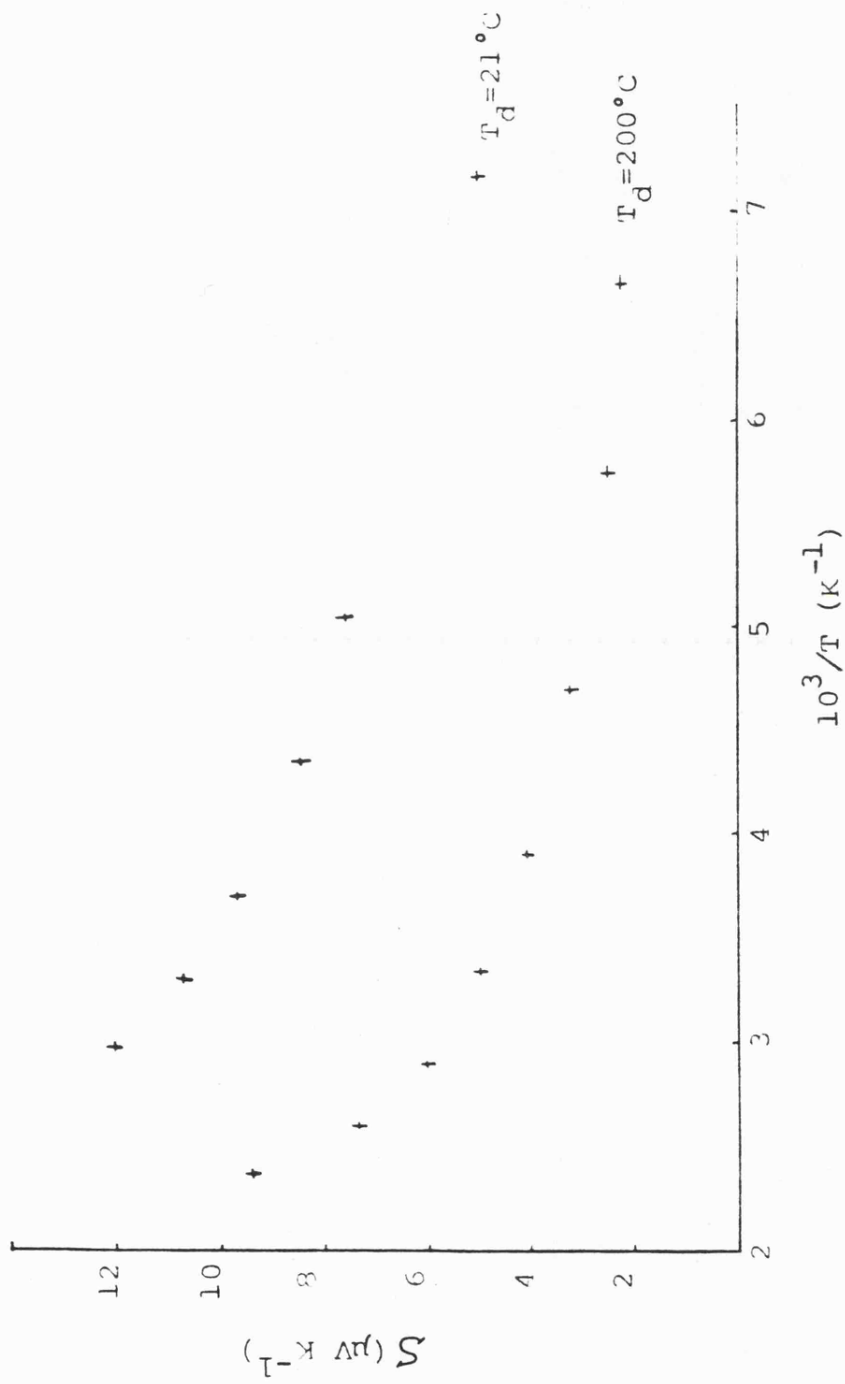


Fig 4.27  $S$  vs  $10^3/T$  for two a-Si<sub>98.7</sub>Au<sub>11.3</sub>:H alloys deposited at 200 and 21°C.

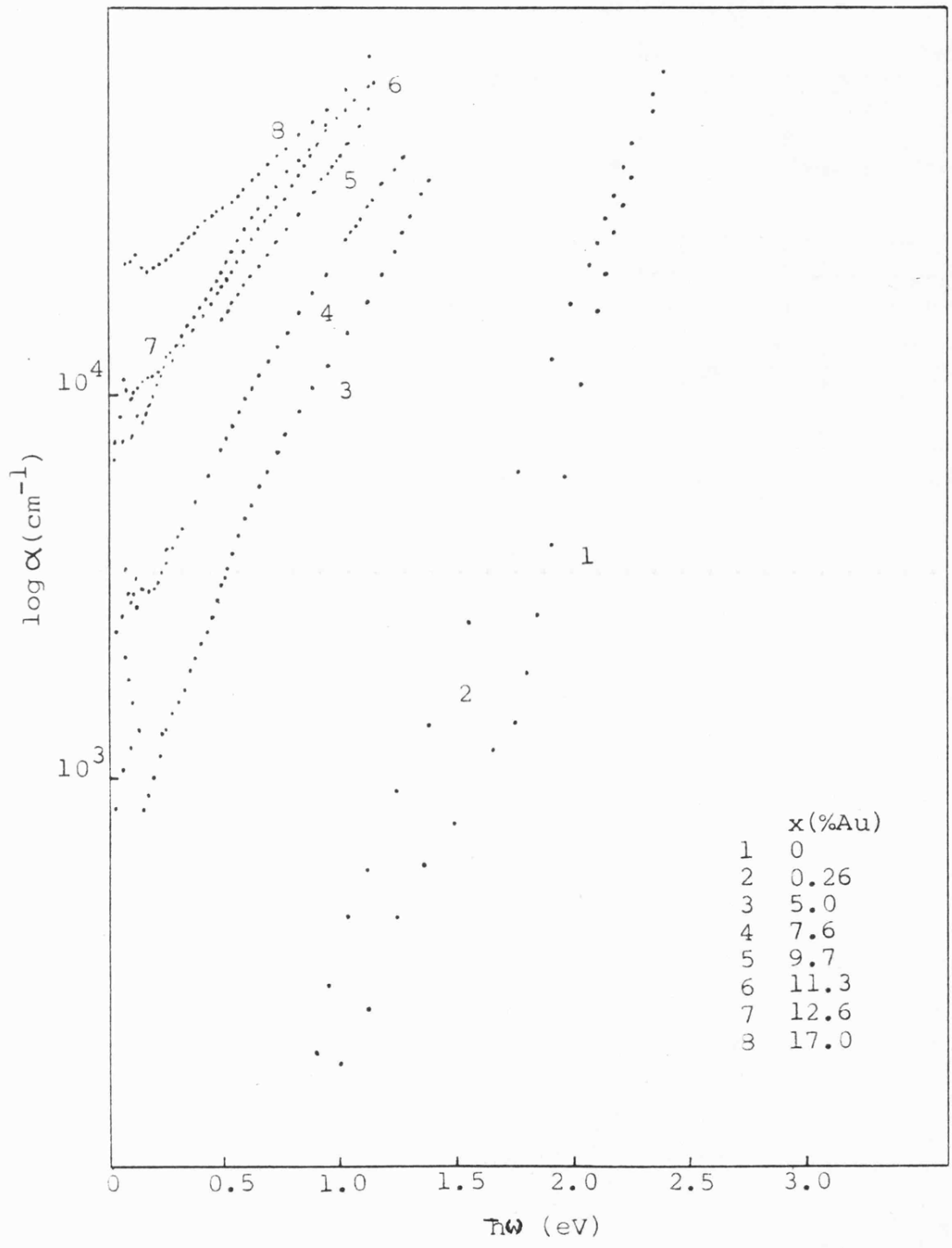


Fig 4.28  $\alpha$  vs  $h\nu$  for  $a\text{-Si}_{1-x}\text{Au}_x\text{:H}$  films deposited at  $200^\circ\text{C}$ .

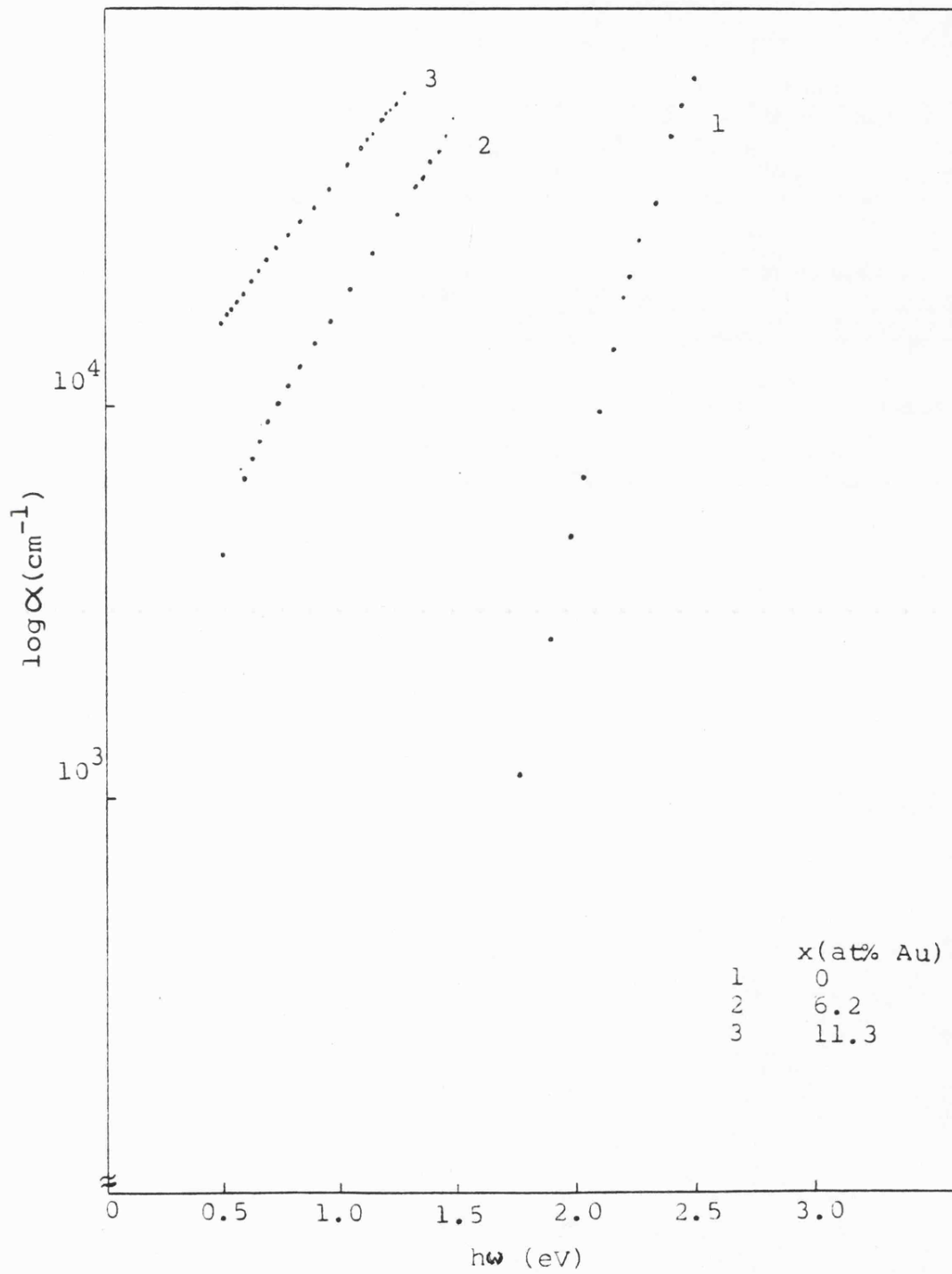


Fig 4.29  $\alpha$  vs  $h\omega$  for  $a\text{-Si}_{1-x}\text{Au}_x\text{:H}$  films deposited at  $21^\circ\text{C}$ .

absorption edge and increases the density of the localized tail states below the edge. The absorption bands centred at 0.261 and 0.248eV (2100 and 2000 $\text{cm}^{-1}$ ), 0.11 - 0.099eV (900 - 800 $\text{cm}^{-1}$ ) and 0.0806eV (650 $\text{cm}^{-1}$ ) are the silicon-hydrogen stretching, bending and rocking (or wagging) modes as observed in a-Si:H. These bands are observed, up to  $x \gtrsim 17\%$ , maintaining their characteristic frequency independent of Au concentration. The Si-O band centred at 0.130eV [1050 $\text{cm}^{-1}$ ] observed for many samples can be attributed to post-deposition oxidation of the Si:Au:H surface as opposed to bulk Si-O absorption which is found at 0.1216eV[980 $\text{cm}^{-1}$ ] [105]. The intensity of this peak steadily increases with time even for an as-deposited film stored in a desiccator. In fig. 4.30 infra-red transmission spectra for two samples (a) a-Si:H and (b) a-Si:Au:H are shown; the retention of the Si:H vibrational modes with the introduction of Au is clearly seen.

Fig. 4.31 shows plots of  $(\alpha\hbar\omega)^{\frac{1}{2}}$  vs  $\hbar\omega$  for the same series of samples as in fig. 4.28. The obtained values of  $E_g$ , extrapolated to  $E_g(T = 0)$  using a temperature coefficient  $\approx 3.3 \times 10^{-4} \text{eVK}^{-1}$  [116], are displayed in fig. 4.33. Plots of  $(\alpha\hbar\omega)^{\frac{1}{2}}$  vs  $\hbar\omega$  for  $T_d = 21^\circ\text{C}$  are presented in fig. 4.32 and the derived values of  $E_g(T = 0)$  are again plotted in fig. 4.33 along with corresponding results for evaporated a-Si:Au [68].

The introduction of hydrogen into a-Si results in an increase in the optical gap and a reduction in the density of deep lying localized states in the mobility gap. For example:  $C_H \approx 30\%$ ,  $E_g \approx 2.06\text{eV}$ ;  $C_H \approx 21\%$ ,  $E_g \approx 1.94\text{eV}$ ; and  $C_H = 0$ ,  $E_g \approx 1.5\text{eV}$ . As Au, which acts as a deep acceptor for c-Si, is introduced in small

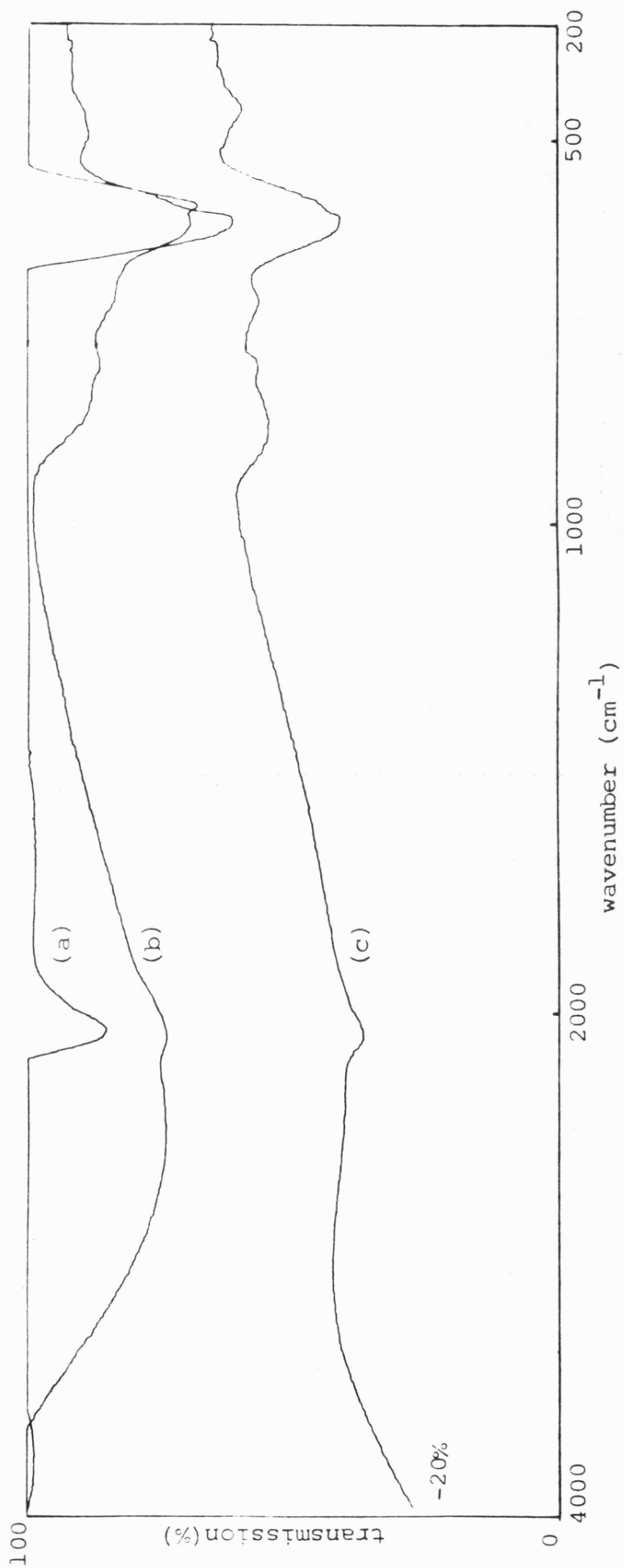


Fig 4.30 Typical IR transmission spectra for (a) a-Si:H ( $T_d=21^\circ\text{C}$ )  
 (b) a-Si<sub>99.74</sub>Au<sub>0.26</sub>:H ( $T_d=200^\circ\text{C}$ ) and (c) a-Si<sub>88.7</sub>Au<sub>11.3</sub>:H  
 ( $T_d=21^\circ\text{C}$ ).

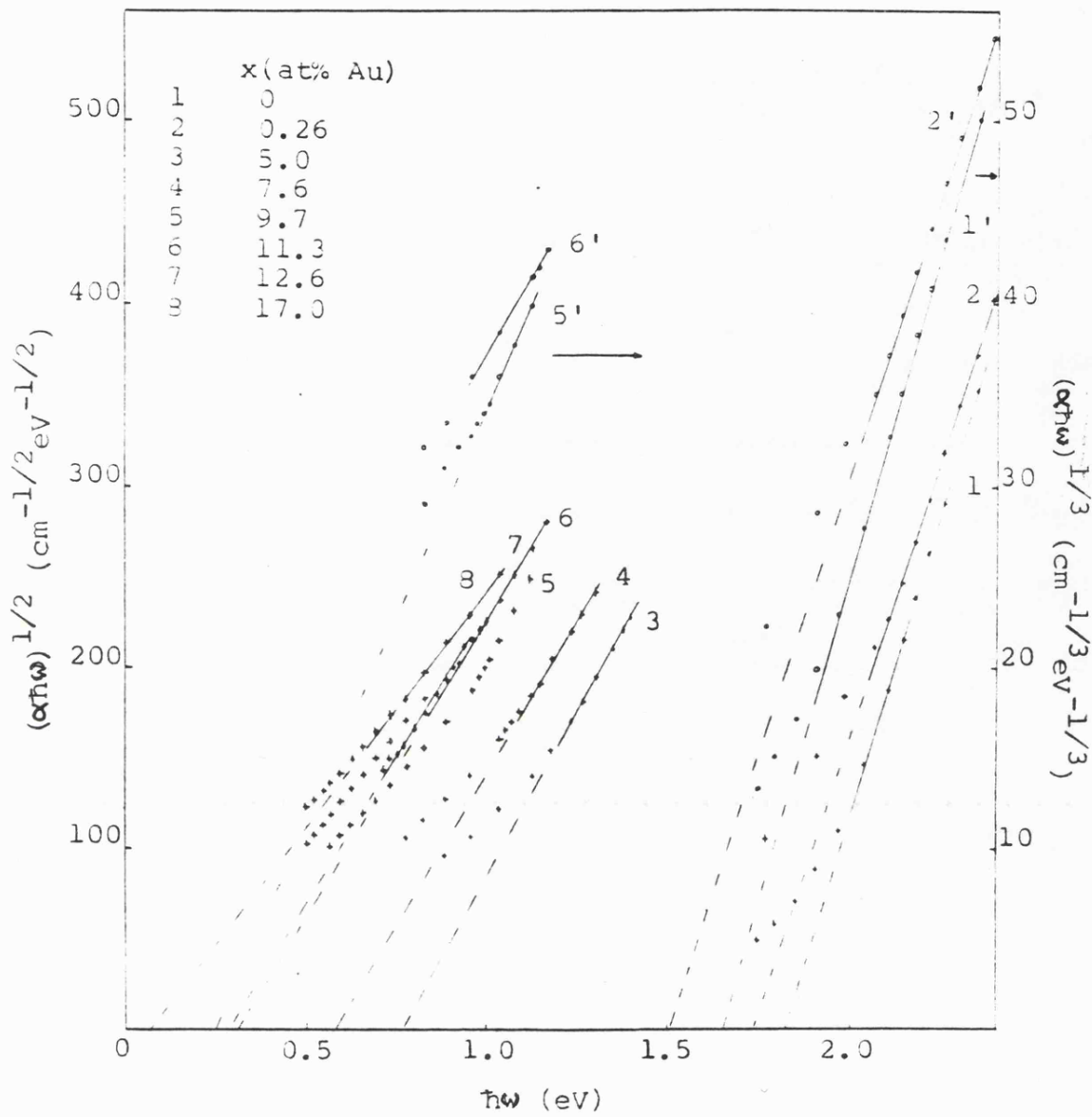


Fig 4.31  $(\alpha\hbar\omega)^{1/n}$  ( $n=2$  and  $3$ ) vs  $\hbar\omega$  for  $a\text{-Si}_{1-x}\text{Au}_x\text{:H}$  films deposited at  $200^\circ\text{C}$ .

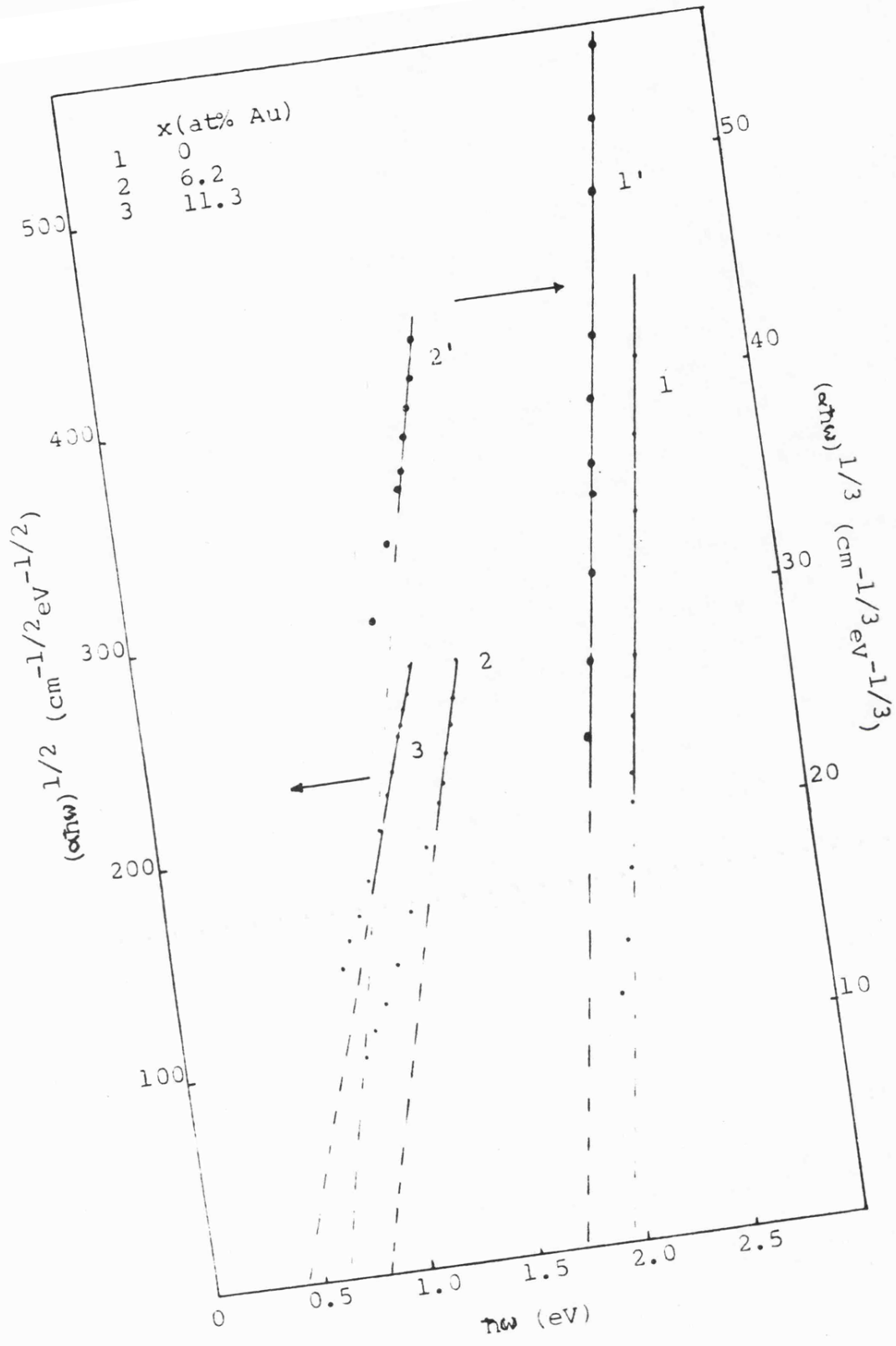


Fig 4.32  $(\alpha h\nu)^{1/n}$  ( $n=2$  and  $3$ ) vs  $h\nu$  for  $a\text{-Si}_{1-x}\text{Au}_x\text{:H}$  films deposited at 21 C.

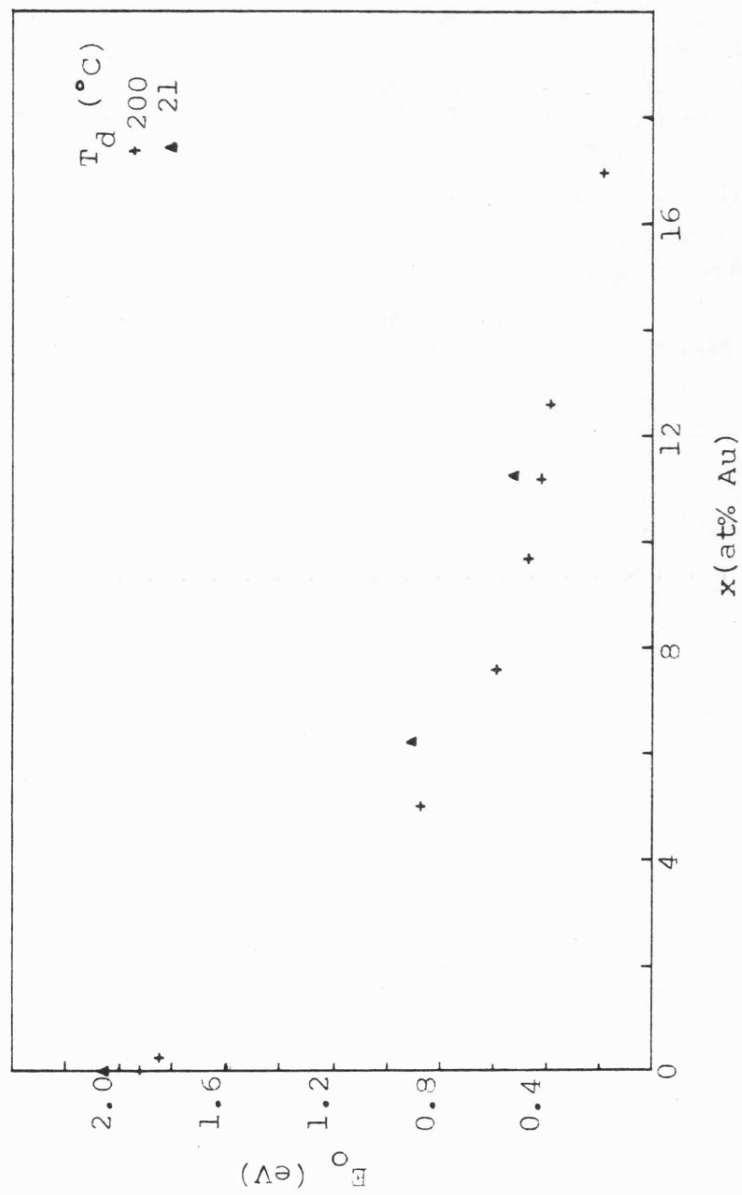


Fig 4.33  $E_O(T=0)$  vs Au content for  $a\text{-Si}_{1-x}\text{Au}_x\text{:H}$  films.

quantities ( $x \lesssim 0.26\%$ ), doping occurs and a slight reduction in the optical gap is observed. This is accompanied by an increase in the density of localized tail states, as can be inferred from the decrease in slope of the Urbach tail region, and the lowering of the Fermi level to  $\sim 0.6\text{eV}$  above the valence-band edge. It is unlikely that the presence of hydrogen will have any significant effect on the tail states which are essentially due to disorder and not defects. Additional Au ( $5 < x \lesssim 17\%$ ) rapidly reduces the size of the optical gap until at  $17\%$  Au,  $E_g(T=0) < 0.2\text{eV}$ . The reduction of  $E_g(T=0)$  with  $x$ , fig. 4.33, is significantly larger for hydrogenated high-temperature-deposited sputtered material than for the comparable evaporated alloy. This is most likely due to the initially lower density of deep localized states, such as dangling bonds, DB, which are known to exist in evaporated films of a-Si and a-Si:Au just above mid-gap [68].

The existence of a finite optical gap,  $E_g$ , for  $x > 14\%$  the composition at which the metal-insulator transition occurs, and the absence of free-carrier absorption behaviour, which might be expected to lead to an absorption varying with frequency  $\omega$  as

$$\alpha(\omega) = \alpha(0)/(1 + \omega^2 \tau^2) \quad (4.4)$$

where  $\tau$  = relaxation time, indicates that the a-Si:Au:H alloy system does not behave like a 'good' metal. An electronic transition of the type suggested by Huber et al [117], where Au switches from a dielectric to a metallic state with Si remaining semiconducting up to  $\sim 70\%$  Au, offers qualitative agreement with the observed optical data.

As a result of the independence of the Si-H vibrational frequencies to the Au concentration, it seems likely that the Au, for the concentrations investigated, is incorporated into the a-Si:H network predominantly in an interstitial manner. The broad I.R. band centred at  $\sim 0.3 - 0.5\text{eV}$ , as observed by Hauser et al [78] is, if present, much weaker than these authors reported for getter-sputtered films. However, owing to the thickness of films studied ( $t \sim 1\mu\text{m}$ ), the superposition of interference peaks on the I.R. spectra made detection of any weak or broad bands difficult.

#### 4.3.3 Structural measurements

Selected Area Diffraction (SAD) studies on thin-film structures  $200 - 700\text{\AA}$  at energies of  $60 - 100\text{keV}$  at room temperature in a JOEL 100CX TEM indicated that all specimens examined were amorphous in nature, as evidenced by the characteristic halo-type diffraction pattern (see Plate 4.4). The results of microdenoimeter traces of the diffraction patterns,  $I_T(k)$ , of samples prepared at  $T_D \sim 200^\circ\text{C}$  and  $21^\circ\text{C}$  are shown in fig. 4.34 for the compositional range  $x = 0$  to  $x = 17\%$ . It should be noted that the intensity measurement displayed in this figure,  $I_T(k)$ , includes both the elastically,  $I_e(k)$ , and the inelastic,  $I_i(k)$ , scattered electron intensities. To enable the calculation of the required RDF the inelastic scattering contribution,  $I_i(k)$ , must be eliminated. Several methods have been employed with varying degrees of success to obtain  $I_e(k)$  [8][118]. In this work only  $I_T(k)$  will be presented; hence uncertainties in the exact positions of broad weak peaks exist.

For  $x = 0$  and  $x = 0.26\%$  Au, three peaks are found centred at

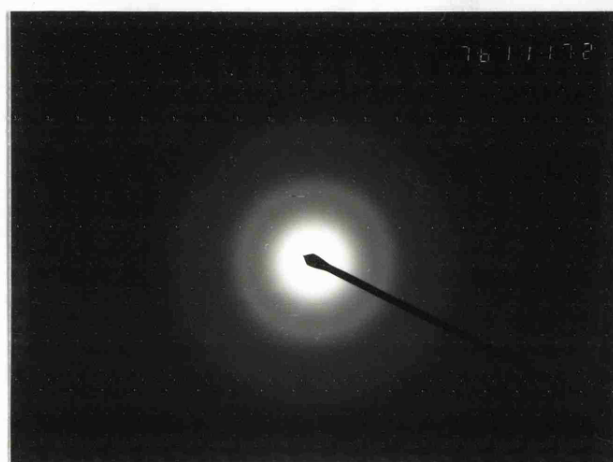


Plate 4.4 Transmission electron diffraction pattern of a-Si:H ( $T_d=200\text{ C}$  ).

Intensity

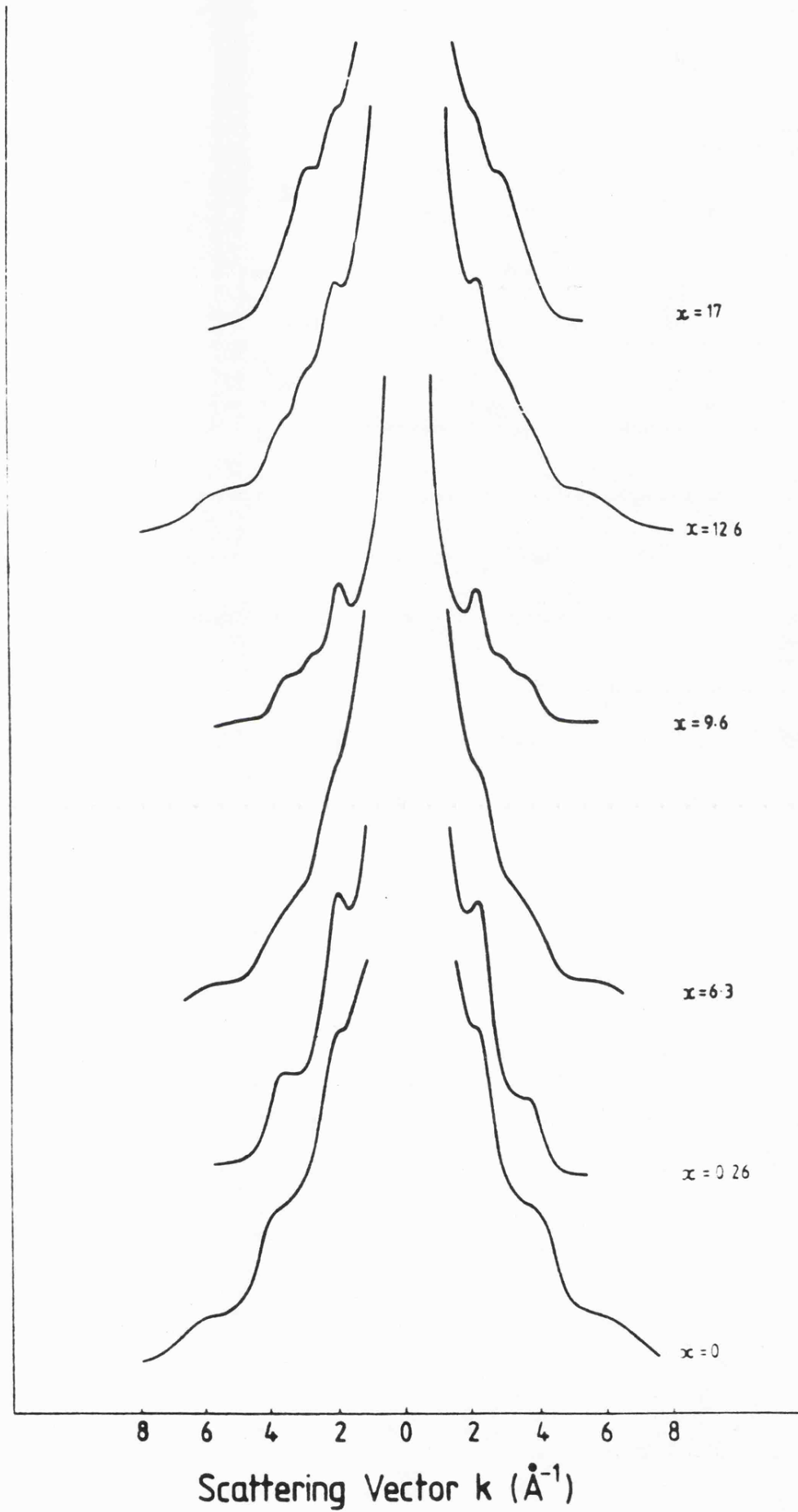


Fig 4.34  $I_P(k)$  vs  $k$  for  $a\text{-Si}_{1-x}\text{Au}_x\text{:H}$  alloys.

$\approx 2.05 \text{ \AA}^{-1}$ , 3.66 and  $5.62 \text{ \AA}^{-1}$ . These results are in agreement with the earlier work of Moss et al [119] on evaporated a-Si, though a slightly higher scattering vector value indicates a slight reduction in first- and second-nearest-neighbour separation. At  $x = 6.4\%$ , for a room-temperature deposited film, a weak side band between the first and second silicon peaks has developed which must be attributed to the presence of Au. By  $x = 9.7\%$ , for a film deposited at  $200^\circ\text{C}$ , and subsequent further increases in  $x$ , a prominent peak centred at  $\approx 2.74 \text{ \AA}^{-1}$  is found together with the three Si peaks, until at about  $x = 17\%$  it becomes impossible to resolve the second Si peak.

The results of fig. 4.34 are in broad agreement with the more extensive measurements of Ph Mangin et al [69], fig. 2.8 on evaporated a-Si:Au deposited at 77K, though these authors observe only the three a-Si peaks for  $x < 10\%$  Au. The results of the present work does not however compare favourably with the diffraction measurements of Kishimoto et al [68], (fig. 2.9) for evaporated a-Si:Au deposited at room temperature. Below 25% Au, these authors maintain that the diffraction traces observed have features similar to a-Si and, for  $x > 25\%$ , crystallization of Au is observed. From the width of the c-Au peaks, crystallite dimensions of  $\sim 20 - 30 \text{ \AA}$  were speculated. Throughout the compositional range studied in this investigation the characteristic f.c.c. peaks for Si and Au were not observed.

It is apparent from the TED results of fig. 4.34 and the previous structural work on evaporated Si:Au that the amorphous structure of Si:Au alloys are strongly dependent on deposition

parameters. However, for sputtered alloys the deposition temperature seems to have little or no effect on the diffraction pattern.

The structural description of the transformation from an a-Si phase to an amorphous eutectic-like phase, through a series of intermediate steps, does not seem inappropriate from the limited TED data available on sp-a-Si:Au:H. At compositions  $x \lesssim 6\%$ , Au is most likely incorporated interstitially, as indicated from the present IR measurements and the density measurements of Ph Mangin et al [69], and hence does not contribute to the interference function. Further reduction in the Si concentration results in a mixture of an a-Si phase and an a-eutectic phase, as indicated by the presence of the peak at  $\approx 2.74 \text{ \AA}^{-1}$ , which is observed in both the amorphous [69] [70] [72] and liquid phases [74]. The a-eutectic phase is seen as a close-packed structure with a high degree of Si-Au bonding.

It is evident that these results, in conjunction with the absence of any irreversible discontinuity in the d.c. conductivity which could be attributed to crystallization, show that the alloys are stable over a wide range of temperature ie  $T_d = 200^\circ\text{C}$ ,  $T_{\text{cry.}} > 515\text{K}$  for  $x < 12.6\%$  and  $T_{\text{cry.}} > 294\text{K}$  for  $x = 17\%$  and  $T_d = 21^\circ\text{C}$  samples. As no conscious effort was made to measure the exact crystallization temperature for each composition, it is impossible to ascertain whether the incorporation of Ar in the film, as can be seen from the results of EBMA (fig. 4.35) and XPS (Chapter 5) studies, does make the amorphous film more stable as reported by

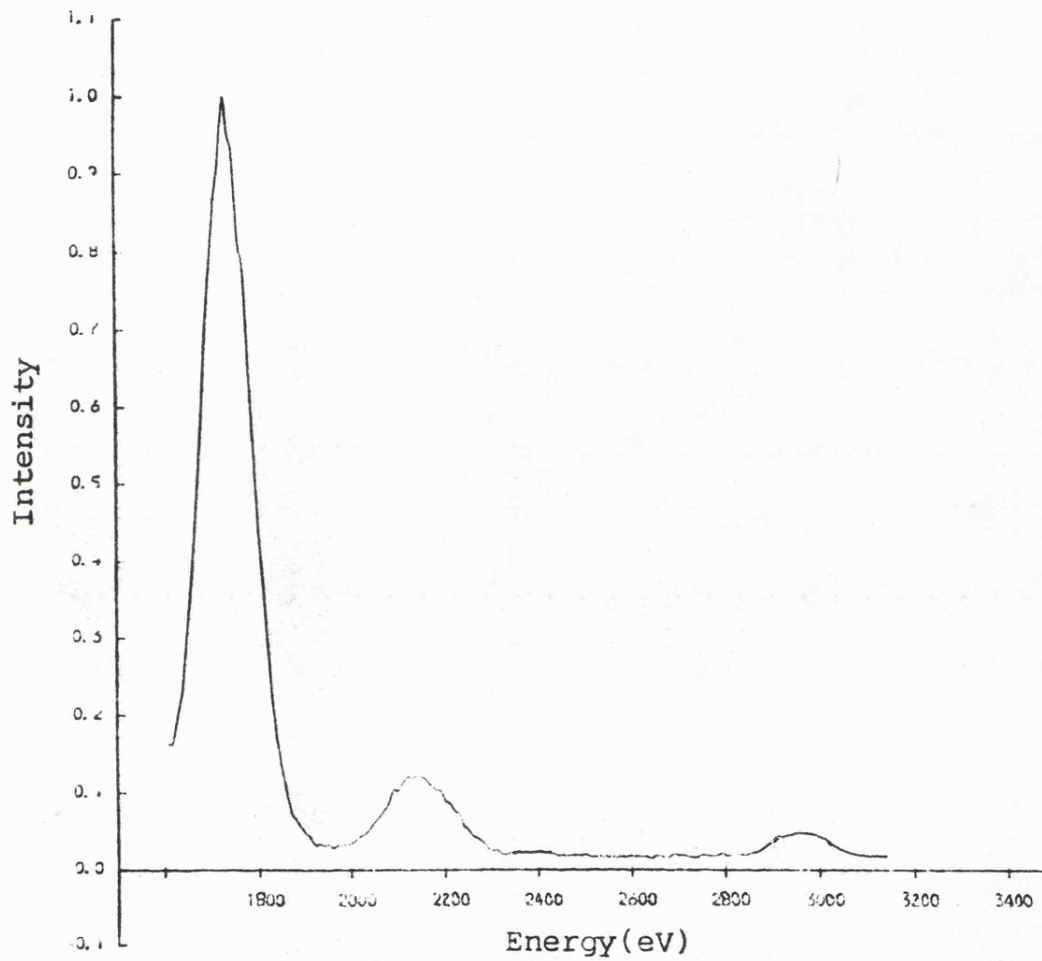


Fig 4.35 Intensity of X-ray emission vs Energy for an a-Si:Au:H film deposited onto an Al foil substrate. The peaks are, from left to right Si, Au and Ar respectively.

Hauser [70]. Owing to the absence of any Ar standards, an absolute evaluation of the Ar content of the films could not be achieved; hence only a comparative study of the relative Ar content of films with varying Au concentrations was carried out. Fig. 4.36 shows the variation of the Ar peak height, normalized to the peak intensity at  $x = 0$  for a-Si:H,  $T_d = 200^\circ\text{C}$ , with Au content over the range of composition studied. A gradual reduction in the Ar fraction of the alloys with increase in  $x$  is observed for both deposition temperatures. Argon contents of 0.5 to 7 at% have been reported in the literature for sputter-deposited a-Si:H films [57] [120], 0.8 - 3.9 at% for a-Si:Sn:H films [113] and  $\sim 1$  at% for a-Si:Au alloys ( $x = 75$ ) [70]. An empirical inverse correlation between Ar pressure  $P_{\text{Ar}}$  and Ar content has been found [120]; hence one may expect a relatively high  $\approx 3$  at% Ar component for films deposited under the conditions described in (3.1.3) with  $x = 0$ . It is unclear at present why the Ar content of the films decreases with  $x$ . It must be noted that the sample  $x = 30\%$ , which displayed a yellowish colouration as opposed to the silvery grey of the other films with  $x > 5\%$ , was not homogeneous and had a thin layer  $\sim 1000\text{\AA}$  of c-Au covering the surface as determined by Alpha Step measurements. This Au coating will result in a more abrupt decrease in Ar signal than otherwise might be expected.

Bright-field transmission electron micrographs (TEMs) were made on the films used in the TED studies at room temperature in the JOEL 100CX. The results can be seen in Plates 4.5(a) - (e) for  $T_d = 200^\circ\text{C}$  and Plates 4.6(a) and (b). For  $T_d = 21^\circ\text{C}$ .

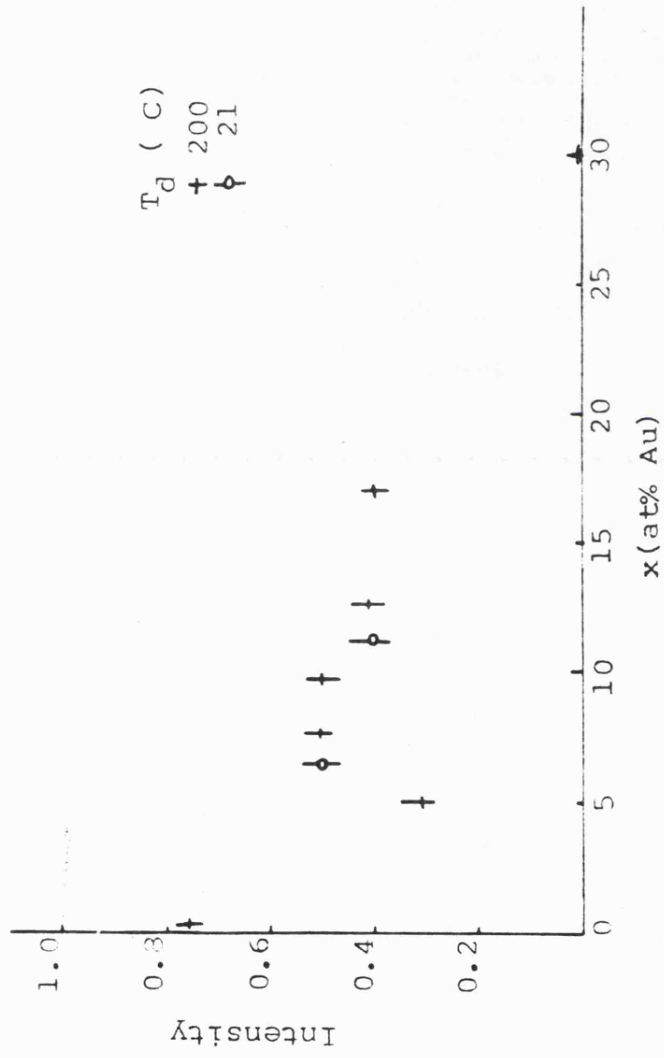
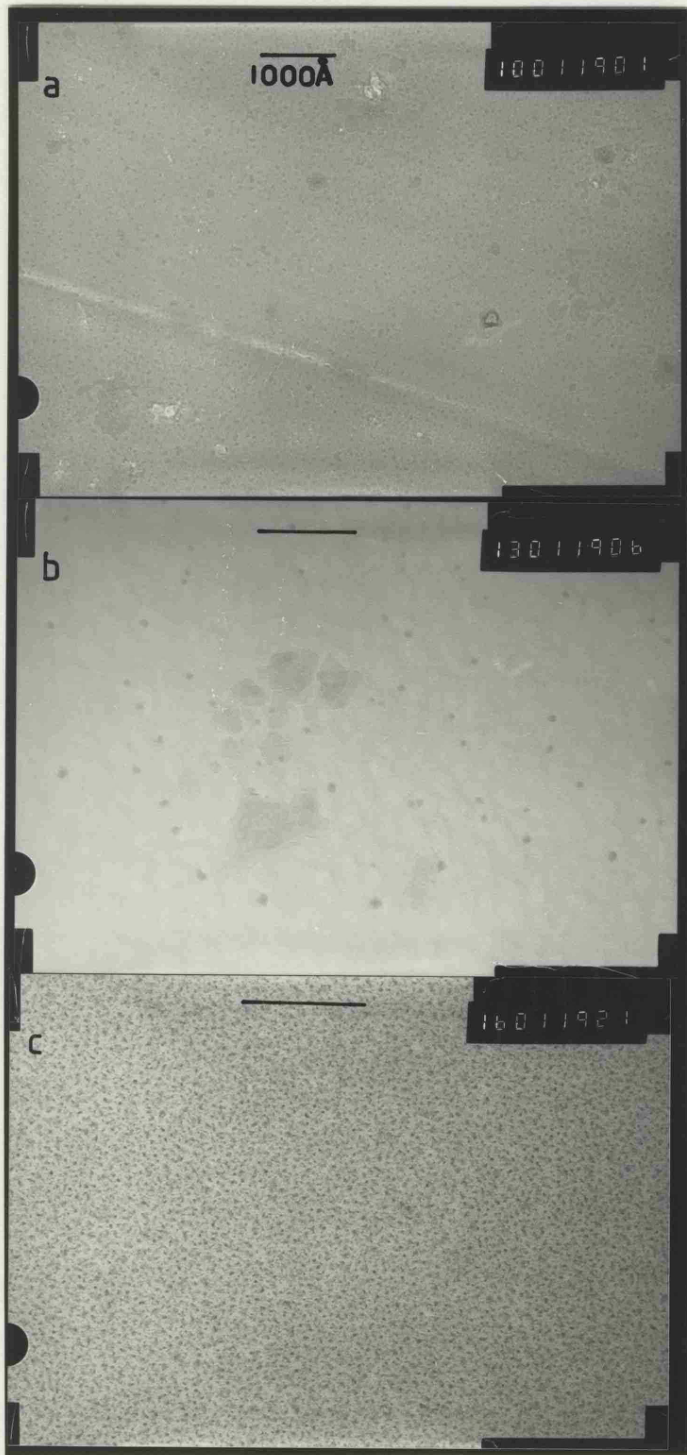


Fig 4.36 Normalized Ar peak height vs Au content.

Plates 4.5 (a)-(e). Transmission electron micro-  
graphs of a-Si<sub>1-x</sub>Au<sub>x</sub>:H alloys of  
varying Au content x.



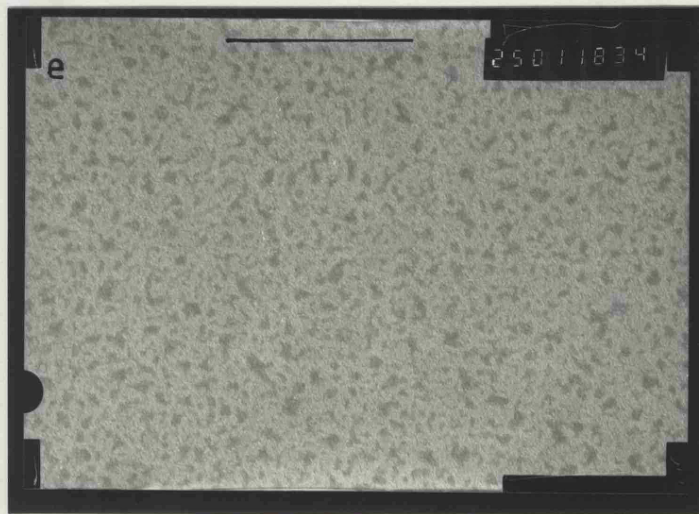
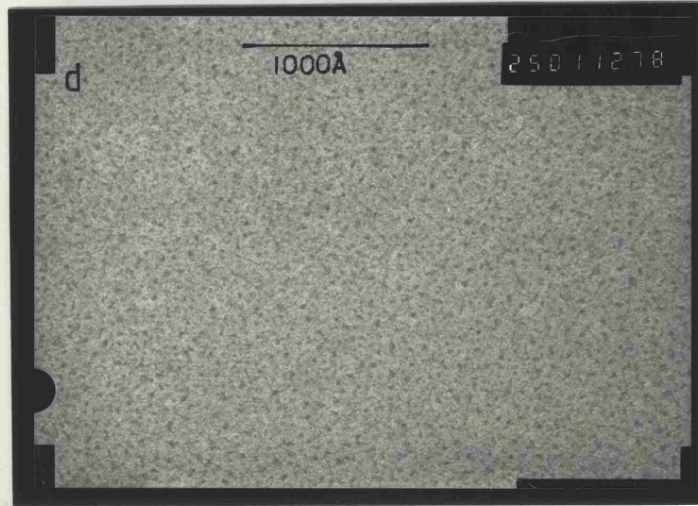
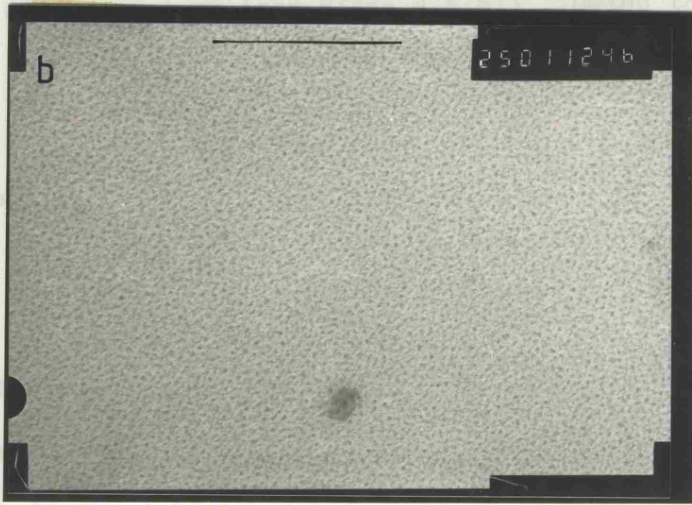
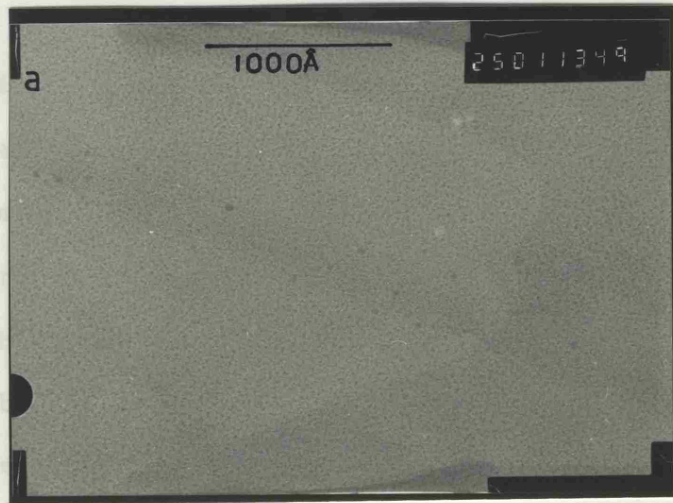


Figure 1. Plate TEM transmission electron micrographs of  
a-Si<sub>1-x</sub>Ge<sub>x</sub> alloys deposited at 21°C,  
(a) x=0.2 and (b) x=11.2% Au.

Plate 4.6(a) is a bright-field TEM for a-Si:H deposited at 200°C. The density of fine structure < 20Å being resolvable at 250kX magnification is reported by the density regions resolved with films of different features have they are probably either from the stage. The incorporation of 0.26% Au in the film has no discernible effect on the magnification. Note the thin surface; this off' process.



In Plate 4.6(b) the microstructure is similar to those shown in Plate 4.6(a) and (b). A fine structure < 20Å can be seen throughout the film with a resolvable fine structure < 12Å as a background. Using 250kX magnification on x = 12.5% (see fig. 4.5(d)), structure within the high-density regions is found to be

Plate 4.6 Transmission electron micrographs of a-Si<sub>1-x</sub>Au<sub>x</sub>:H alloys deposited at 21°C. (a) x=6.2 and (b) =11.3% Au.

Plates 4.5(a) and (b) are high-magnification bright-field images of room-temperature deposited films. In Plate 4.5(a) (x = 4.2%)

In Plate 4.5(a) a bright-field TEM for a-Si:H deposited at 200°C is shown, fine structure  $< 20\text{\AA}$  being resolvable at this magnification. There is no evidence of the columnar morphology as reported by Knights et al [4] (see Plate 4.7). The dark high-density regions  $\sim 60 - 90\text{\AA}$ , in which the fine structure may be resolved were seen, to varying degrees, throughout this study on films of differing composition and deposition temperature. As these features have been previously reported for a-Ge [12] and a-Si:Cu [89] they are probably due to some form of contamination of the film either from the substrate or from a post-deposition preparation stage. The incorporation of 0.26%Au in the film has no discernable effect on the microstructure (see Plate 4.5(b)). Owing to the higher magnification employed, fine structure on the scale  $\lesssim 12\text{\AA}$  is detectable. Note the thin platelets of fragmented film lying on the substrate surface; this is evidence of the explosive nature of the 'floating off' process.

In Plates 4.5(c), (d) and (e) where  $x = 9.7, 12.6$  and  $17\%$  the microstructure of the thin specimens has changed dramatically from those shown in Plates 4.5(a) and (b). Dark high density regions  $\lesssim 24\text{\AA}$  can be seen throughout the film with a resolvable fine structure  $\lesssim 12\text{\AA}$  as a background. Using 250kX magnification on  $x = 12.6\%$  (see fig. 4.5(d)), structure within the high-density regions is found to be  $\lesssim 8\text{\AA}$ , a dimension similar to the fine-structure background.

Plates 4.6(a) and (b) are high-magnification bright-field images of room-temperature deposited films. In Plate 4.6(a) ( $x = 6.2\%$ )

the high-density regions and the fine-structure background have features on a scale  $\lesssim 10^3$ . The feature which crosses the micrograph from right to left, which has a series of dark bands, is most likely the edge effect, associated with it, is most likely the edge effect. The  $x = 0.75$  film (Plate 4.5(V)), with fine regions  $\lesssim 10^3$ .

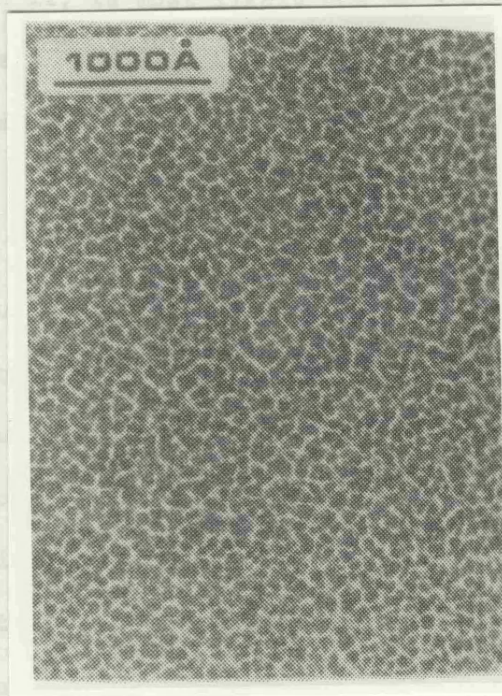


Plate 4.7 Transmission electron micrograph of a glow-discharge deposited a-Si:H film exhibiting structural inhomogeneity.(4)

Both of these features appear to be independent of deposition temperature.

These measurements should be given as only a preliminary investigation into the microstructure of a-Si:H alloys. Further more detailed measurements are required before a satisfactory structural model can be presented for this system.

#### 4.3.4 Discussion

Amorphous Si<sub>1-x</sub>Ge<sub>x</sub>H alloys, over the compositional range 0 < x < 0.175, have been prepared by the co-sputtering technique at

the high-density regions and the fine-structure background have features on a scale  $\lesssim 8\text{\AA}$ . The feature which crosses the micrograph from right to left, which has a series of dark regions,  $\sim 20 - 50\text{\AA}$  across, associated with it, is most likely due to a substrate defect. The  $x = 11.3\%$  film (Plate 4.6(b)) is in many ways the same as Plate 4.5(d), with fine structure down to  $\sim 8\text{\AA}$  and high-density regions  $\lesssim 16\text{\AA}$ .

Structural measurements on a-Si:Au:H films containing  $x = 0.26\%$  Au show little or no change from that observed for a-Si:H. As the Au content of the amorphous films increases to  $x \approx 6.2\%$  features both in TED (a diffraction peak centred at  $\sim 2.74\text{\AA}^{-1}$ ) and in TEM (dark high-density regions with  $d \approx 10\text{\AA}$ ), can be distinguished along with the intrinsic a-Si:H structural features. With the addition of further Au the dimensions of the high-density regions, within which structure down to  $\sim 10\text{\AA}$  can be resolved, increases to  $\sim 25\text{\AA}$  in conjunction with the growth of the diffraction peak at  $2.74\text{\AA}^{-1}$ . Both of these features can be specifically attributed to the presence of Au in the a-Si:H matrix in a form which, over the range studied, appears to be independent of deposition temperature.

These measurements should be seen as only a preliminary investigation into the microstructure of a-Si:Au:H alloys. Further more detailed measurements are required before a satisfactory structural model can be presented for this system.

#### 4.3.4 Discussion

Amorphous  $\text{Si}_{1-x}\text{Au}_x\text{:H}$  alloys, over the compositional range  $0 < x < 17\%$ , have been prepared by the co-sputtering technique at

low pressure in an Ar/H<sub>2</sub> atmosphere. As the majority of this work was carried out on films deposited at  $T_d = 200^\circ\text{C}$ , unless otherwise stated, the discussion of the results will be made in terms of an a-Si:Au:H alloy prepared at this temperature.

The addition of small amounts of Au  $\sim 0.26\%$  to a-Si:H results in doping of the amorphous semiconductor, the Fermi level falling from 0.89eV below the conduction band (fig. 4.37(a)) to  $\sim 0.6\text{eV}$  above the valence band and nearest-neighbour hopping conduction being observed for  $T < 313\text{K}$ . The d.c. conductivity rises by over three orders of magnitude at room temperature. A schematic of an energy-band diagram, as proposed earlier, is shown in fig. 4.37(b) and does appear to fit the d.c. conductivity, thermoelectric power and optical absorption data. From this model the width of the valence-band tail states  $(E_V - E_A) \approx 0.21\text{eV}$ , assuming  $W \sim 0.09\text{eV}$  [114], in accordance with previously published estimates of this quantity [7], and the Fermi level  $E_F$  is situated near to  $E_V$ . Au incorporated into the a-Si:H matrix in these quantities has little or no effect on the structure of the a-Si:H film as determined by the electron microscopy techniques employed in this work, or by bright-field TEM and selected-area electron diffraction. Increasing the Au content of the film beyond 5% results in an increase in room-temperature conductivity (see fig. 4.17) the observation of variable-range-hopping type conduction at  $T < 265\text{K}$  and a gradual reduction in  $E_0$  with increase in  $x$ . It is evident that for  $x > 5\%$  chemical modification of Si by Au occurs with  $E_F$  being situated just above the top of the valence-band tail states. The derived values of  $T_0$  as a function of  $x$  can

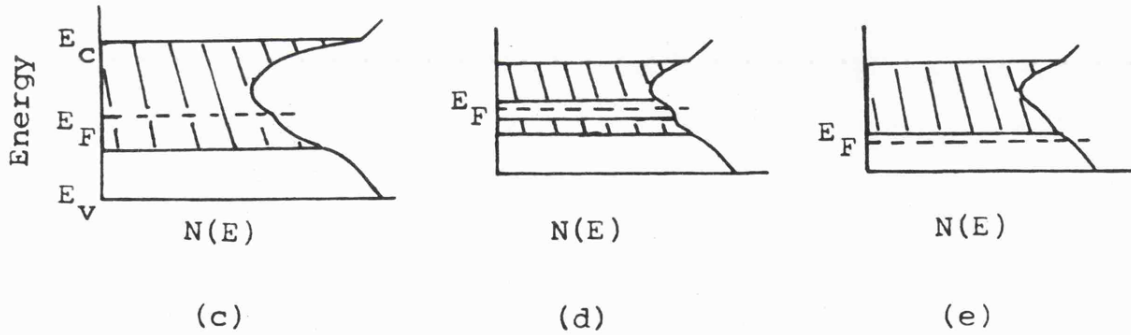
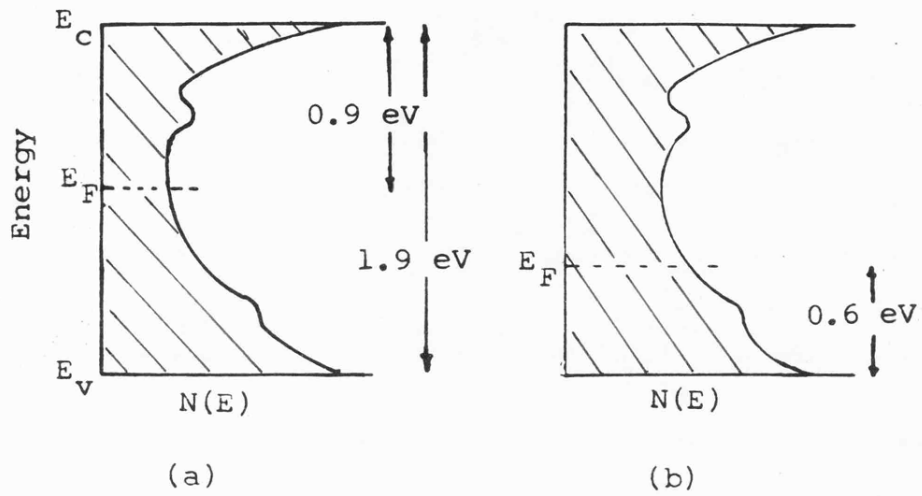


Fig 4.37 Schematic density of states distribution for the  $a\text{-Si}_{1-x}\text{Au}_x\text{:H}$  system with  $x=$  (a) 0, (b) 0.26, (c) 9.7, (d)  $> 14\% \text{Au}$  after (75) and (e)  $> 14\% \text{Au}$ .

be seen in fig. 4.23 and, assuming a constant value of  $\alpha$  at  $\approx 10^8 \text{ cm}^{-1}$ , these correspond to  $N(E_F) = 1.375 \times 10^{19}$  for  $x = 5\%$  and  $N(E_F) = 1.34 \times 10^{23} \text{ eV}^{-1} \text{ cm}^{-3}$  for  $x = 12.6\%$ . Figure 4.37(c) displays a possible energy-band configuration for this composition range, a deep band of localized states growing above the valence-band tail states with addition of further Au. It should be noted that over this range of Au concentration,  $5 < x < 12.6\%$ , the values of  $T_0$ , and hence  $N(E_F)$ , for films prepared in this study are different to those of Morigaki et al [75] as displayed in fig. 4.23, indicating  $N(E_F)_{210^\circ\text{C}} < N(E_F)_{200^\circ\text{C}} < N(E_F)_{\text{eV}}$ . In conjunction with this observation the reduction in optical gap,  $E_0$ , is seen to occur more rapidly for the sputtered as compared to evaporated material (see fig. 4.33). It is possible that the incorporation of hydrogen into the Si:Au films in the present work, which is known to reduce the density of localized states within the gap, is sufficient to account for the variation in  $N(E_F)$ , as dangling-bond states near mid-gap are known to exist in evaporated a-Si:Au [68]. However why  $N(E_F)_{210^\circ\text{C}} < N(E_F)_{200^\circ\text{C}}$  is not understood at present.

The addition of further Au to compositions beyond the metal-insulator transition, at  $x = 14\%$  results in a finite optical gap  $E_0 \approx 0.2 \text{ eV}$  for  $x = 17\%$ , (the evaluation of an  $E_0$  of this magnitude from the  $(\alpha \hbar \omega)^{\frac{1}{2}}$  vs  $\hbar \omega$  plots is somewhat doubtful for such high  $x$ -values and this quantity should therefore be viewed with caution) and a metallic conduction behaviour. Conductivity measurements at low temperature, down to  $\sim 7\text{K}$ , indicate a  $\sigma(T) = \sigma(0) [1 + AT^n]$  relationship with  $n = \frac{1}{2} - \frac{1}{3}$ , though owing to the limited data available the exact evaluation of the exponent  $n$  is uncertain. This type of

conduction behaviour has been interpreted as being indicative of electron-electron correlation effects [35] [36] and has been observed in the a-Ge:Au and c-Si:P. With an exponent of  $n = \frac{1}{2}$ ,  $\sigma(o) = 26.2 \Omega^{-1} \text{cm}^{-1}$ , a value below the early estimates of  $\sigma_{\text{min}} \approx 100 \Omega^{-1} \text{cm}^{-1}$  [24] and  $A = 0.153$ . Both quantities are in good agreement with the results of similar measurements on evaporated a-Si:Au [115] and indicate that the concept of a minimum metallic conductivity does not appear to be suitable for this particular system. The observation of metallic conduction behaviour in conjunction with the small but finite optical gap and the absence of free-carrier behaviour can be explained in terms of two possible density-of-states configurations. In figure 4.37(d) a schematic of the energy-band diagram suggested by Morigaki et al [75] can be seen where states within the band  $E_z$  have become extended due to the strength of the overlap of the wavefunctions between adjacent Au atoms. Alternatively in fig. 4.37(e)  $E_F$  has been pushed down through the localized band-tail states, through the mobility edge, and into the extended-states at the top of the valence band. From the existing data it is difficult to ascertain which of these processes is occurring. The I.R. photoconductivity measurements of Kishimoto et al [68] may be interpreted in terms of an impurity-band type model, but the reduced optical gap values of the present work seem to indicate that the second model, in which  $E_F$  falls into the valence band is the most favourable picture.

Why differences exist between the optical and electronic properties of evaporated and sputtered a-Si:Au alloys is not understood at present. However it seems likely that they are related

to structural differences of the alloys prepared by these techniques. In the present work, for compositions above  $x \approx 6.2\%$ , (for a film with  $T_d = 21^\circ\text{C}$ : Plate 4.6(a)), the film's structure has changed from the featureless micrograph of a-Si:H with fine structure  $\lesssim 10\text{\AA}$  (Plate 4.5(a)) to an alloy which exhibits high-density regions  $\sim 12\text{\AA}$  which grow to  $\sim 25\text{\AA}$  for  $x = 17\%$ . In all cases a fine structure of  $< 12\text{\AA}$  can be seen throughout the thin film independent of the Au concentration. A diffraction peak centred at  $\sim 2.74\text{\AA}^{-1}$  in addition to the observed Si peaks at  $2.05\text{\AA}^{-1}$ ,  $3.66\text{\AA}^{-1}$  and  $5.61\text{\AA}^{-1}$  (fig. 4.34), is also seen to develop with Au content. It is apparent that at a certain composition  $x_A$ , where  $0.26 > x_A > 6.2\%$  the amorphous film changes its structure from a doped a-Si:H film to a Si:Au:H alloy with the growth of high-density regions and the subsequent development of the peak in the interference function at  $2.74\text{\AA}^{-1}$  which is related to Au within the alloy. The diffraction measurements of the present work are in broad agreement with the work of Ph Mangin et al [69] on evaporated a-Si:Au where similar peaks are observed, though the Au related peak at  $2.74\text{\AA}^{-1}$  is only observed for  $x > 10\%$ . In contrast Kishimoto et al [68] report Si peaks only for  $x < 25\%$ . Hence from the limited diffraction data available on the a-Si:Au system it seems likely that the structure of the film depends strongly on deposition parameters and the specific techniques employed.

TEM measurements, in conjunction with d.c. conductivity and optical absorption measurements, indicate that for the sp-a-Si:Au:H system, the deposition temperature, at least over the temperature

range 21 - 200°C, is of little importance for  $x > 5\%$  when Au is alloying with Si. It is however important to remember that 20 - 30% H is incorporated into these films at  $x = 0$  and  $\sim 3$  to  $\approx 1.5\%$  Ar over the range of composition studied. Hence it is perhaps not unexpected that the structure of evaporated and sputtered alloys should appear slightly different.

In the a-Si:Au system two electronic transitions take place; for  $x = 14\%$  Au switches from a dielectric to a metallic state and at  $x \approx 70\%$  Si switches from its semiconducting to metallic state [117] [88]. This can be structurally modelled by assuming the existence of an a-Si phase and an a-eutectic like phase. For low Au concentrations the a-Si phase is dominant, though as Au is gradually increased a series of intermediate phases, composites of the a-Si and a-eutectic phases, takes place until the a-eutectic phase is achieved at  $\approx 70\%$  Au [69]. As the tetrahedrally bonded a-Si phase is semiconducting and the close-packed structures of the a-eutectic phase is metallic with a high degree of Si-Au bonding, it is apparent that the two electronic transitions can occur as the Au content of the alloy varies. In the present study, with  $0 < x < 17\%$ , only one of the electronic transitions can be observed and the major structural component is the a-Si like phase. For  $x < 6\%$  it seems likely that Au is predominantly bonded in an interstitial manner, as inferred from the compositional invariance of the Si-H bonding in the I.R. and the mass-density measurements of Ph Mangin et al [69] on evaporated a-Si:Au. As the Au content is increased further, an intermediate type of phase is made of predominantly tetrahedrally coordinated a-Si:H, as indicated by the three Si diffraction peaks, but

there is also an a-eutectic contribution as evidenced by the observation for a peak at  $2.74\text{\AA}^{-1}$ . With additional Au, the peak centred at  $2.74\text{\AA}^{-1}$  develops, the a-eutectic component increases and the metal-insulator transition occurs.

In an attempt to determine which of the two possible energy-band configurations (fig. 4.37(d) and (e)) occurs, photoelectron spectroscopy (UPS and XPS) was employed on a series of sp a-Si:Au:H alloys. These results are presented in the following chapter.

## CHAPTER 5

### Photoemission

- 5.1 Introduction
- 5.2 Experimental
- 5.3 Results and discussion

### 5.1 Introduction

Photoelectron Spectroscopy is an extremely powerful technique which enables detailed examination of the electronic structure of a system. When light, of energy  $\hbar\omega$ , is incident on a sample with work function  $\phi < \hbar\omega$ , electrons with kinetic energy  $E_{KE}$  are emitted (see fig. 5.1). The energy of initial unperturbed state of the electron is

$$E_i = \hbar\omega - E_{KE} - \phi \quad (5.1)$$

Hence by careful manipulation of  $\hbar\omega$  and  $E_{KE}$  the band structure of the system can, in principle, be studied.

A schematic representation of the basic experimental arrangement required to study photoelectron emission can be seen in fig. 5.2. Photons of energy  $\hbar\omega$  from a monochromatic source (eg a gas-discharge lamp, X-ray tube, synchrotron) create photoelectrons which are ejected from the sample and subsequently generate a current,  $I(E, \hbar\omega)$ , in the analyser. A judicious choice of which experimental parameters to vary and to keep constant must be made. In the present work  $I$  is only a function of photon energy  $\hbar\omega$  and electron energy  $E$ , as the other quantities are kept fixed and the analyser integrates over a spread of angles  $\theta_e$ .

Interpretation of experimental photoelectron spectra can be made in terms of the "Three-Step Model" of photoemission which has been widely used and accepted since the early work of Berglund et al [122]. This model views the photoemission process as a sequence of three independent steps:-

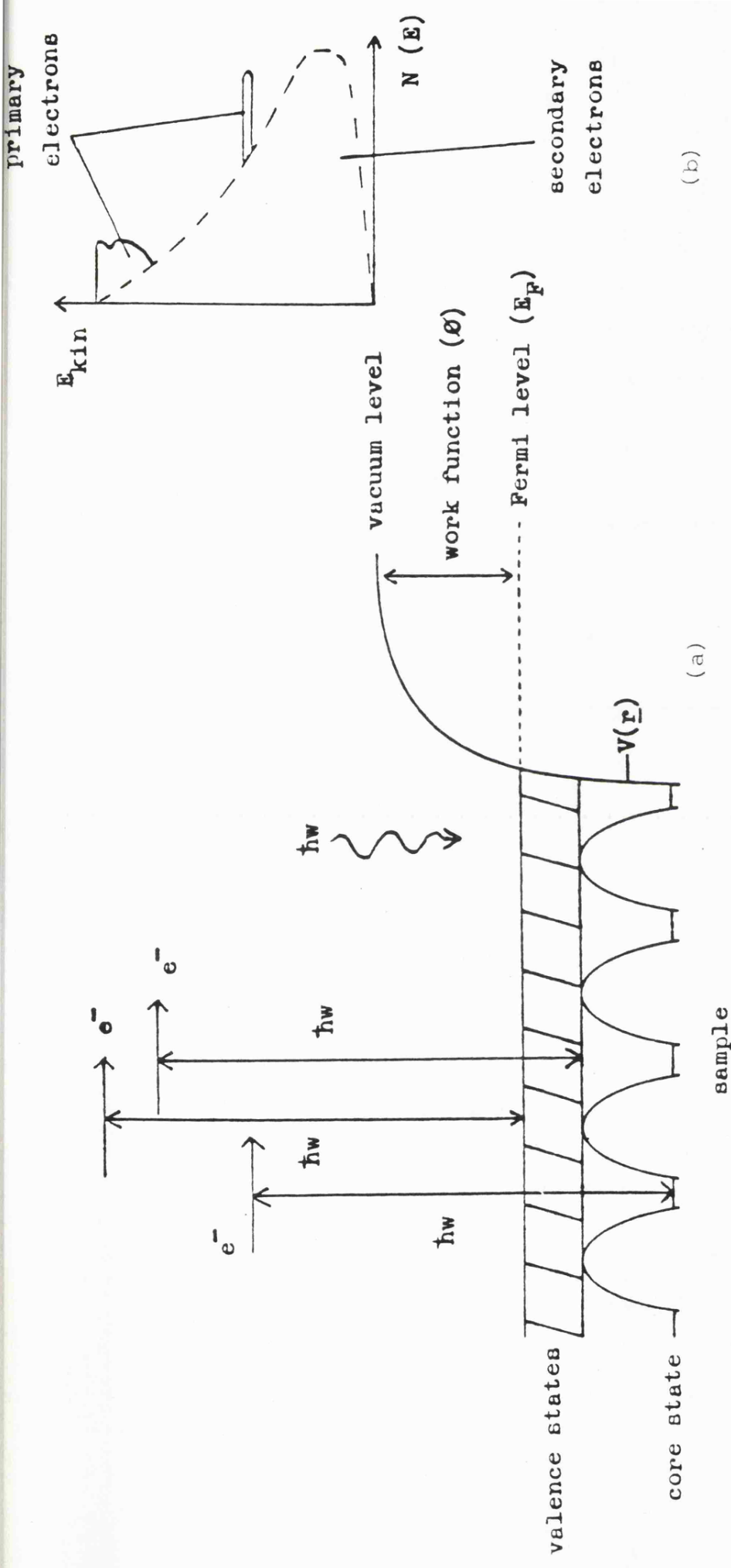


Fig 5.1 The photoemission process

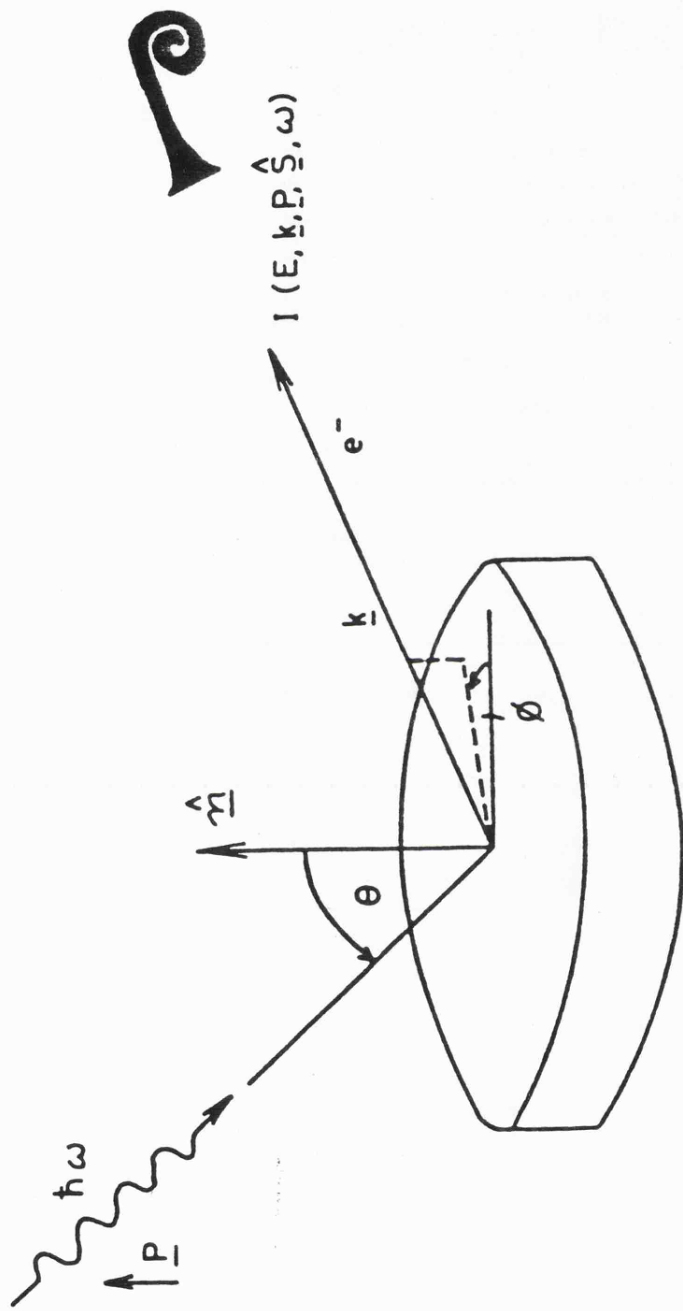


Fig 5.2 Schematic of the photoemission experiment.

- 1) Optical excitation of an electron from an initial state with an energy  $E_i$  to a final state with energy  $E_f$ .
- 2) Electron transport through the solid, normally involving scattering.
- 3) Escape through the sample surface into the vacuum where it is collected.

Only a small fraction of photoexcited electrons reach the surface without inelastic collisions with other electrons to produce the primary current,  $I_p$ . The majority are scattered with an energy loss in one or more collisions and contribute to the background of secondaries producing a current  $I_s$ . Hence

$$I(E, \hbar\omega) = I_p(E, \hbar\omega) + I_s(E, \hbar\omega) \quad (5.2)$$

Applying the three-step model to the primary current  $I_p(E, \hbar\omega)$  gives

$$I_p(E, \hbar\omega) = P(E, \hbar\omega) \times T(E) \times D(E) \quad (5.3)$$

Where  $P(E, \hbar\omega)$  is the distribution of photoexcited electrons,  $T(E)$  is the transmission function and  $D(E)$  the escape function for electrons reaching the surface.

Both  $T(E)$  and  $D(E)$  are found to be smooth functions of energy,  $E$ , beyond the low-energy cut off and hence are not expected in themselves to give structure in  $I_p(E, \hbar\omega)$ . When a similar treatment is applied to  $I_s(E, \hbar\omega)$  the distribution of secondary electrons is found to be structureless, hence the  $I_s(E, \hbar\omega)$  contribution can be seen as a

relatively smooth distribution rising with increase in binding energy as indicated in fig. 5.1(b). In an amorphous system where  $\underline{k}$  is no longer a good quantum number the primary current can be related to the one-electron density of states as

$$P(E, \hbar\omega) \approx \text{const } N(E - \hbar\omega)N(E) \quad (5.4)$$

where  $N(E - \hbar\omega)$  is the density of initial states and  $N(E)$  is the density of final states. The approximately constant pre-factor includes the optical matrix elements for the system which are, for an amorphous system, of less significance than in the crystalline case owing to the relaxation of the  $\underline{k}$  selection rules. As  $N(E)$  normally has little structure in an amorphous material, we may regard  $I_p(E, \hbar\omega)$  as a reflection of the initial density of states weakly modulated by the matrix elements and the smooth distributions of  $T(E)$  and  $D(E)$ . Hence the structure of fig. 5.1(b) can be considered to represent to a good approximation the density of the initial states of the amorphous sample.

Photoelectron spectroscopy is very much a surface-sensitive technique as although photons, typically  $\hbar\omega$  is 5 - 1500eV, penetrate into the sample to a depth of greater than  $100\text{\AA}$ , inelastic scattering of the electrons leads to an escape depth of between  $\sim 4$  and  $40\text{\AA}$ . Surface contamination is therefore extremely detrimental and atomically clean surfaces are required. This necessitates the use of UHV conditions and in situ sample cleaning.

When an electron is photoejected from the valence band the potential  $V(\underline{r})$  has little effect on the energy of the electron. Hence examination of the primary photocurrent  $I_p(E, \hbar\omega)$  gives a direct

mapping of the valence band as described earlier. However when the incident photons have sufficient energy to excite core levels (eg by using X-ray frequencies), the potential  $V(\underline{r})$  becomes more important in controlling the binding energy of the photoelectron.

X-ray induced Photoelectron Spectroscopy (XPS) may be used for elemental analysis of a specimen by identifying the characteristic binding energies of the core levels present (see fig. 5.9), hence the acronym ESCA ie Electron Spectroscopy for Chemical Analysis. Information concerning the local chemical environment of specific elements can be achieved by examining the exact value of the binding energy of the core level and assessing the magnitude of the chemical shift, if present. The binding energy of a core state is determined by the attractive potential of the nuclei and the repulsive Coulomb interaction with other electrons. When chemical modification of the environment of an atom occurs, a spatial rearrangement of the valence charges of the particular atom leads to a new potential  $V'(\underline{r})$ . In the ion-point approximation the chemical shift of a core level is related to the atomic environment through the local Madelung potentials. For two different compounds A and B containing the element in question, the chemical shift  $\Delta E_i(A,B)$  can be expressed as

$$\Delta E_i(A,B) \propto [ V_i^A - V_i^B ] \quad (5.5)$$

where  $V_i^A = \sum_{j \neq i} q_j^A / R_{ij}$  with  $R_{ij}$  the separation between atoms  $i$  and  $j$  and  $q_j$  is the charge on atom  $j$ . For example the 2p level of Al has a binding energy of 72.6eV in Al metal and an energy of 75.3eV in  $Al_2O_3$  indicating a chemical shift of 2.7eV.

In the present work both UPS, Ultra-Violet Photoelectron Spectroscopy and XPS were employed to examine the valence band structure (UPS) and core levels (XPS) of a series of a-Si<sub>1-x</sub>Au<sub>x</sub>:H samples.

## 5.2 Experimental

Photoelectron spectroscopy involves the detection of electrons emitted from the first few layers of atoms at the surface of a sample and, as mentioned, is very sensitive to surface cleanliness and contamination. A sample exposed to a gas at a pressure of  $10^{-6}$  Torr that has a sticking coefficient of unity will accumulate a monolayer of residual gas in 1 sec. Thus, operating at a chamber pressure of  $10^{-10}$  Torr, approximately  $3\frac{1}{2}$  hours passes before a monolayer of gas can form on the sample surface.

The photoelectron spectrometer used in the present study was an ESCA spectrometer designed and built in the Department of Physics, University of Leicester for the study of liquid metals. Usage of the system was kindly granted by Dr. C. Norris.

A schematic representation of the system is shown in fig. 5.3 where the specimen lies at the focus of a number of apertures. The system comprises an X-ray source, capable of providing Mg and Al K<sub>α</sub> emission ( $h\nu = 1253.6$  and  $1486.6$  eV respectively) for XPS work, a He discharge lamp for UPS, a hemispherical analyser for electron detection and an argon sputter gun for removal of surface contamination. The experimental chamber was manufactured from stainless steel and was pumped by a series of three UHV diffusion pumps, each with a liquid-nitrogen cold trap, backed by rotary pumps. As the system has been

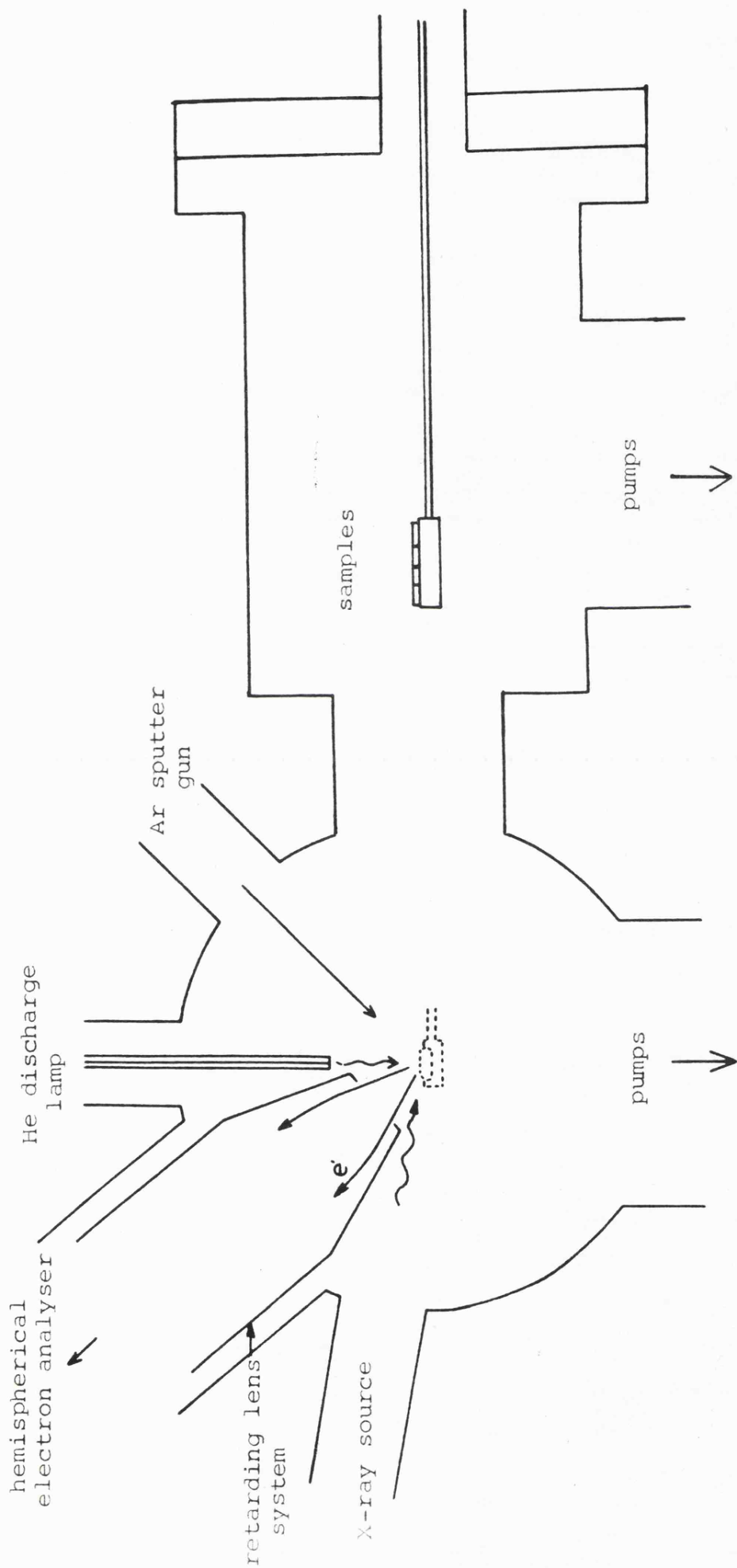


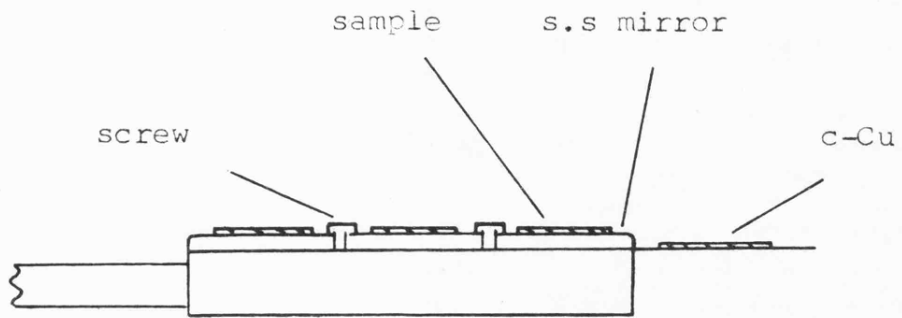
Fig 5.3 Schematic of the photoelectron spectrometer

described in some detail elsewhere [123] no further description is given here.

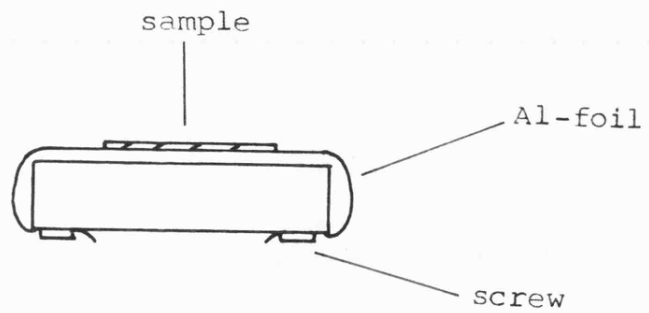
Sputtered films of a-Si:H and a-Si<sub>1-x</sub>Au<sub>x</sub>:H deposited onto polished stainless-steel substrates for  $T_d = 200^\circ\text{C}$  and Al foil for  $T_d = 21^\circ\text{C}$  were removed from the previously described sputtering system and immediately transferred into a UHV sample holder ( $\sim 10^{-6}$  Torr). A series of samples were then removed and attached to the micromanipulator, enabling examination of up to four samples in one pumpdown cycle, which was subsequently bolted onto a stainless-steel chamber flange. (See figures 5.3 and 5.4). The system was then baked out to  $\sim 120^\circ\text{C}$  for the  $T_d = 200^\circ\text{C}$  samples and  $65^\circ\text{C}$  for the  $T_d = 21^\circ\text{C}$  samples for several days. Upon removal of the bake-out ovens a chamber pressure of  $\sim 10^{-10}$  Torr was readily achieved.

### 5.3 Results and discussion

Early XPS measurements were made on samples deposited onto stainless steel substrates held at  $T_d = 200^\circ\text{C}$ . For samples with  $x = 0, 11.3, 12.6$  % Au, the presence of Fe and Ni was indicated when the samples were centrally positioned under the gas-discharge lamp. As these elements are components of stainless steel, it was deemed that either i) the argon sputter gun was sputtering stainless steel onto the specimen, ii) the X-ray gun was not focused exactly onto the specimen; the dimensions of the discharge could mean that it "saw" both film and substrate, or iii) both i) and ii) were contributing. To discriminate between these possibilities a further set of samples  $x = 0, 6.2, 11.2$  % Au ( $T_d = 21^\circ\text{C}$ ) were deposited onto Al foil substrates. A larger specimen surface area was employed with the Al foil being attached onto the sample holder



(a)



(b)

Fig 5.4 Sample holders, type (a) and (b).

from beneath with stainless-steel screws (see fig. 5.4(b)). With the latter sample geometry, no Al signal was observed when the sample was suitably positioned under the He discharge lamp. Hence, with the UPS spectra on  $T_d = 21^\circ\text{C}$  and  $200^\circ\text{C}$  samples appearing identical, it seems likely that the impurity elements detected by XPS on the stainless-steel substrates were not present, in sufficient quantities at least, in the specimen areas investigated by UPS. For this reason, unless otherwise stated, all UPS measurements will be treated independent of deposition temperature.

In fig. 5.5 UPS spectra at  $h\nu = 21.2\text{eV}$  for a-Si:H films are shown before and after an argon sputter etch. Prior to the etch the dominant feature present is the wide band centred approximately at  $\sim -7\text{eV}$  which is due to the O 2p states. Removal of the thin oxide layer results in the characteristic a-Si:H valence-band structure which can be divided into three broad regions. From the top of the valence band to  $\sim -4\text{eV}$  the signal is attributed to the Si 3p orbital; structure between  $-5$  to  $-8.5\text{eV}$  to H 1s states and the peak at  $\sim -9.5\text{eV}$  to the Ar 3p orbital. The Si 3s derived states and the hybridized 3s - 3p states form a broad and structureless distribution between  $-6$  and  $-14\text{eV}$  [124], although owing to the secondary electron contribution, these cannot be resolved in the figure. These results are in many aspects similar to those of previous UPS studies [125] [126] where the amorphous film was prepared in situ for P.E. measurements. Von Roedern et al [124] report the presence of two peaks, denoted A and B, centred at approximately  $-6$  to  $-7\text{eV}$  and  $-10$  to  $-11\text{eV}$  and have assigned the A-B separations  $\sim 5\text{eV}$  to polyhydride and  $\sim 4.2\text{eV}$  to

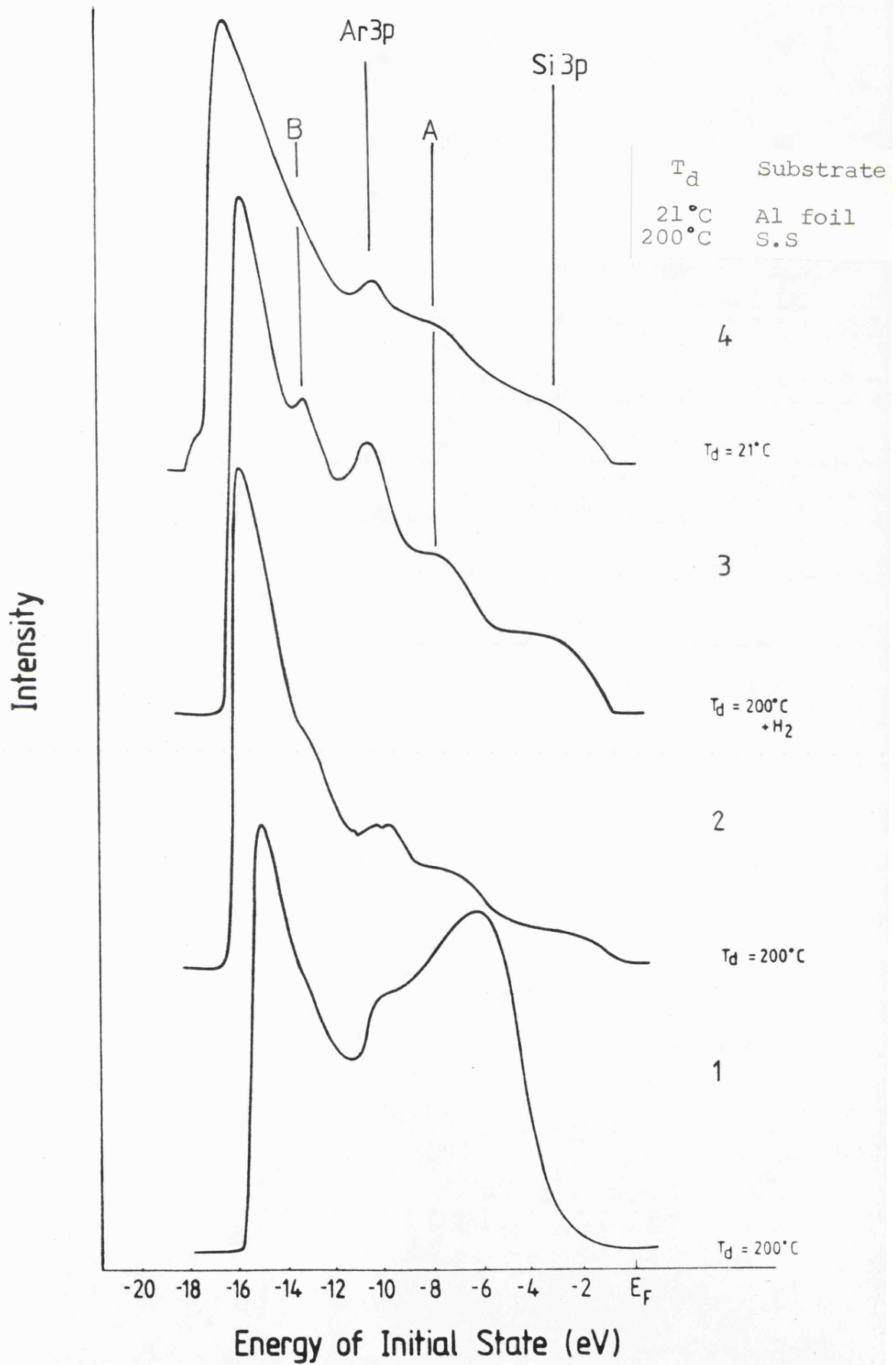


Fig 5.5 UPS spectra ( $h\nu=21.2\text{eV}$ ) of a-Si:H alloys as a function of surface preparation and deposition temperature. 1= as deposited film; 2, 3 and 4 after Ar sputter etch. ( 3 after  $10^{-6}$   $\text{H}_2$  for 5 min. )

dihydride bonding configurations. The cluster-model calculations of Ching et al [127], although assigning relatively higher binding energies, show agreement in A-B separation energies, the peak A being assigned to Si3p/H1s bonding states and B with Si3s/H1s bonds. In the present work only the peak A can be identified, due to the strong secondary contribution. Hence it is not possible to determine whether SiH<sub>3</sub> or SiH<sub>2</sub>-type bonding is predominant on the top ~ 10<sup>8</sup> Å layer of the specimens examined.

From the position of the Fermi level,  $E_F$ , as determined from the sharp Fermi edge observed in the spectrum of Cu, the separation  $E_F - E_V$  can be estimated. D.C. conductivity and optical absorption measurements in Chapter 4 indicate the separation between  $E_F$  and the top of the valence band is ~ 1eV. The UPS spectra in fig. 5.5 show a significantly smaller separation,  $E_F - E_V \sim 0.4\text{eV}$ . As the position of  $E_F$  is strongly dependent on the H content of the sample and it has been reported that exposure of the surface to the atomic hydrogen can modify the gap [125], an attempt was made to enhance the hydrogen content of the samples surface. In fig. 5.5 the result of exposing the sample to ~ 10<sup>-6</sup> τ of H<sub>2</sub> for 5 minutes can be observed. In order to maximise the atomic hydrogen component all ion gauges were switched on to maximum filament current. It is however doubtful where much atomic hydrogen would reach the sample surface. It should be noted that the peak at ~ 12eV can be observed, although it is weaker for exposures ~ 10<sup>-8</sup> τ for the same time duration. Little effect can be seen at the top of the valence band where the separation  $E_F - E_V$  remains low.

From the A-B separation it seems likely that polyhydride-type bonding is dominant at the surface of the film, as has been reported by Ley et al [126] for the a-Si:F(H) system.

The apparent anomaly between  $E_F - E_V$  derived from bulk and PES (surface) could be due to the severe surface damage that the a-Si:H must experience on Ar-ion bombardment.

A reduction of the work function,  $\phi$ , by  $\sim 1\text{eV}$  for  $T_d = 21^\circ\text{C}$  relative to  $T_d = 200^\circ\text{C}$  a-Si:H films is apparent. This is the result of a more disordered surface, and most likely a less dense film, being formed at the lower deposition temperature which has the effect of lowering  $\phi$ .

In fig. 5.6 are shown UPS spectra at  $h\nu = 21.2\text{eV}$  for films of varying Au content. The Au 5d band can be seen to lie between -4 to -8eV with two peaks  $5d_{3/2}$  and  $5d_{5/2}$  centred at  $\sim 6.6$  and  $-5\text{eV}$  produced by spin-orbit coupling. With increasing Au content the separation between the peaks increases (see fig. 5.7) and the density of states at the top of the valence band can be seen to rise. However, owing to the secondary background contribution, it is difficult to evaluate accurately this increase.

The gradual increase in 5d peak separation from  $\sim 1.4$  to  $1.6\text{eV}$  is still considerably less than the bulk metal value of  $\sim 2.5\text{eV}$ , indicating that the d-orbital of Au is mixing with the sand p orbitals of Si. This results in the observed increase in state density at the top of the valence band. Also included in fig. 5.7 is the separation



Fig 5.6 UPS spectra ( $h\nu=21.2\text{eV}$ ) of various  $a\text{-Si}_{1-x}\text{Au}_x\text{:H}$  alloys.

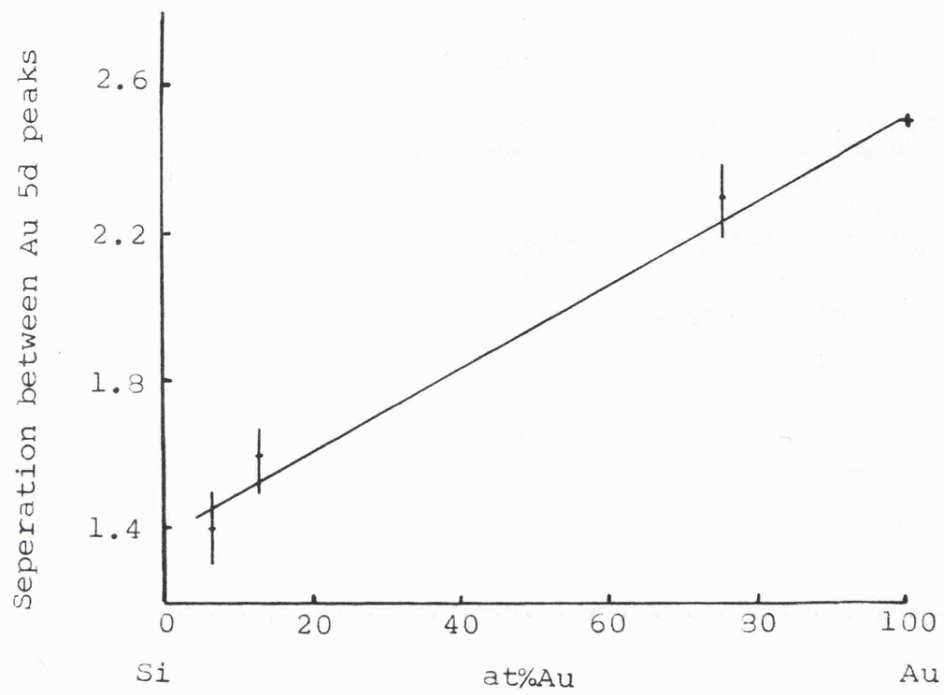


Fig 5.7 Au 5d peak seperation vs Au content.

for  $\text{Au}_3\text{Si}$  derived from a PE study of Au overlayers on C-Si (111) [128].

The results of figures 5.6 and 5.7 for the a-Si:Au:H system are in many respects similar to those of Fukushima et al [129] on the a-Au:Ge system where the samples were prepared by co-evaporation inside the spectrometer. In fig. 5.8 XPS spectra for the a-Au:Ge system are shown. A similar increase in width of the 5d peak separation accompanied by a rapid increase of states at the top of the valence band can be observed with a transition from semiconducting to metallic behaviour occurring somewhere between 10 - 30 %Au.

It is evident that the MIT in the a-Si<sub>1-x</sub>Au<sub>x</sub>:H system can be suitably explained as arising from delocalization of states at the top of the valence band and not as the result of a transition from localized to extended states of a d-band within the mobility gap [75]. Of interest is the depth of the Au 5d band in Si, which can be found at higher binding energies than in the pure metal. This result is in agreement with theoretical calculations of Bisi et al [128] on the  $\text{Au}_3\text{Si}$  system when the authors find the Au 5d band is shifted to lower energies with a decrease in energy separation between the two main d-band structures.

XPS spectra for two films,  $x = 0$  and 12.6%Au can be seen in fig. 5.9. In each case the Ar 2p peak at  $\sim 249\text{eV}$  ( $2p_{1/2} \sim 250.6\text{eV}$  and  $2p_{3/2} \sim 248.5\text{eV}$ ) can be identified in quantities greater than 1 - 2 at %. (the detection limit of the instrument). However it is not possible to equate this to the EBMA results, although the peak intensity was always found to be stronger for the a-Si:H film rather

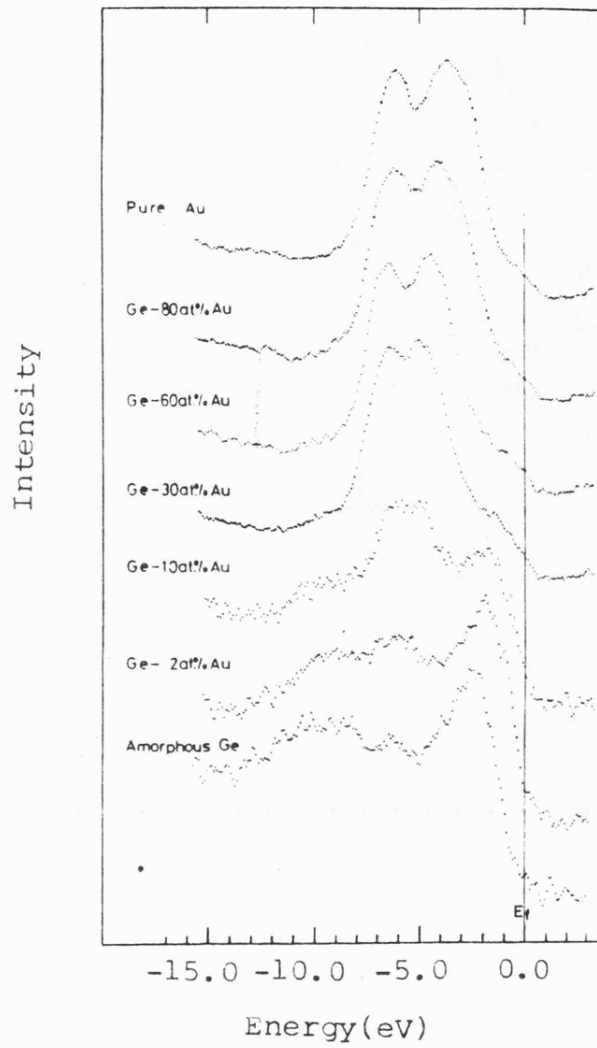


Fig 5.8 XPS valence band spectra for a-Au<sub>1-x</sub>Ge<sub>x</sub> alloys.(129)

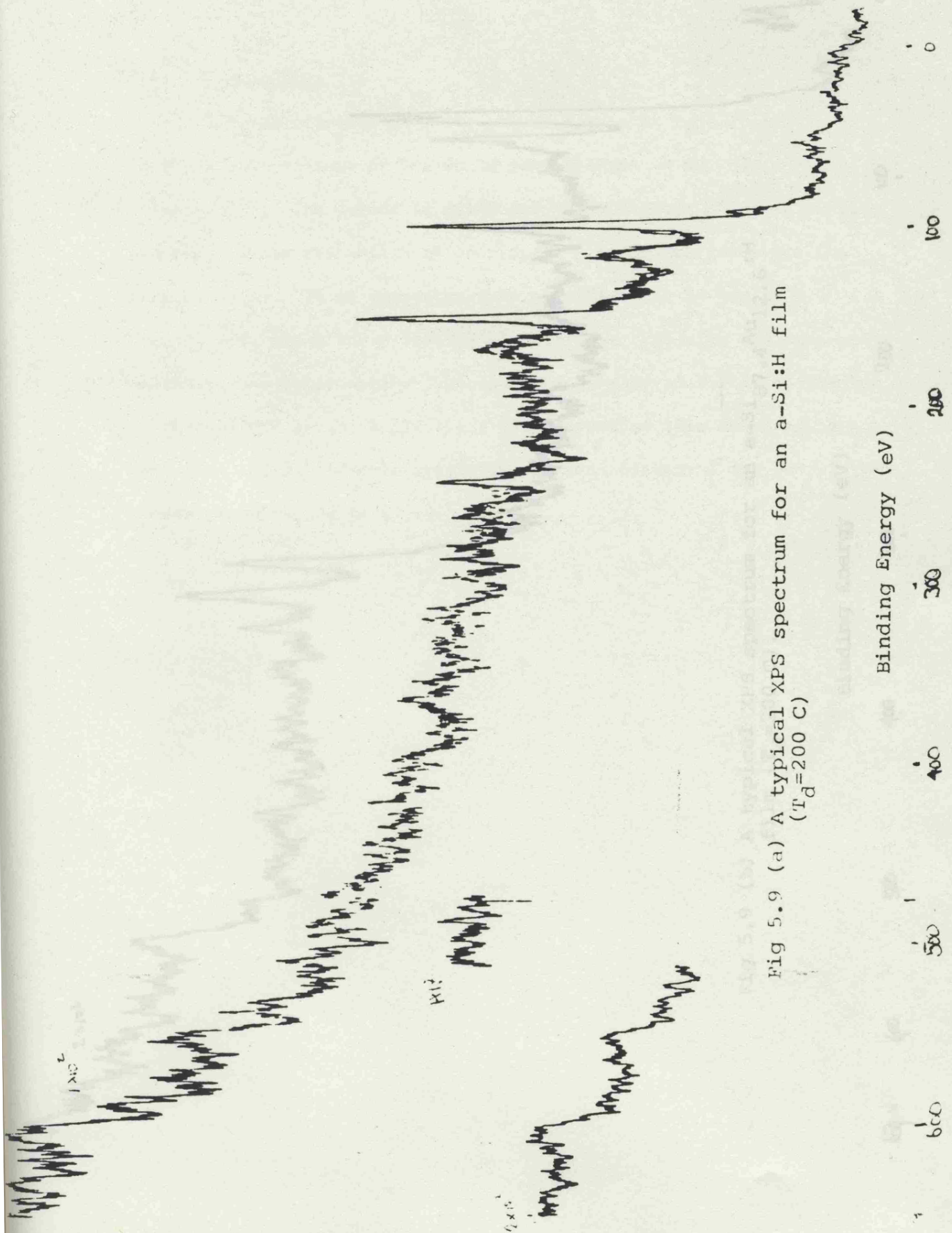


Fig 5.9 (a) A typical XPS spectrum for an a-Si:H film  
 ( $T_d=200$  C)

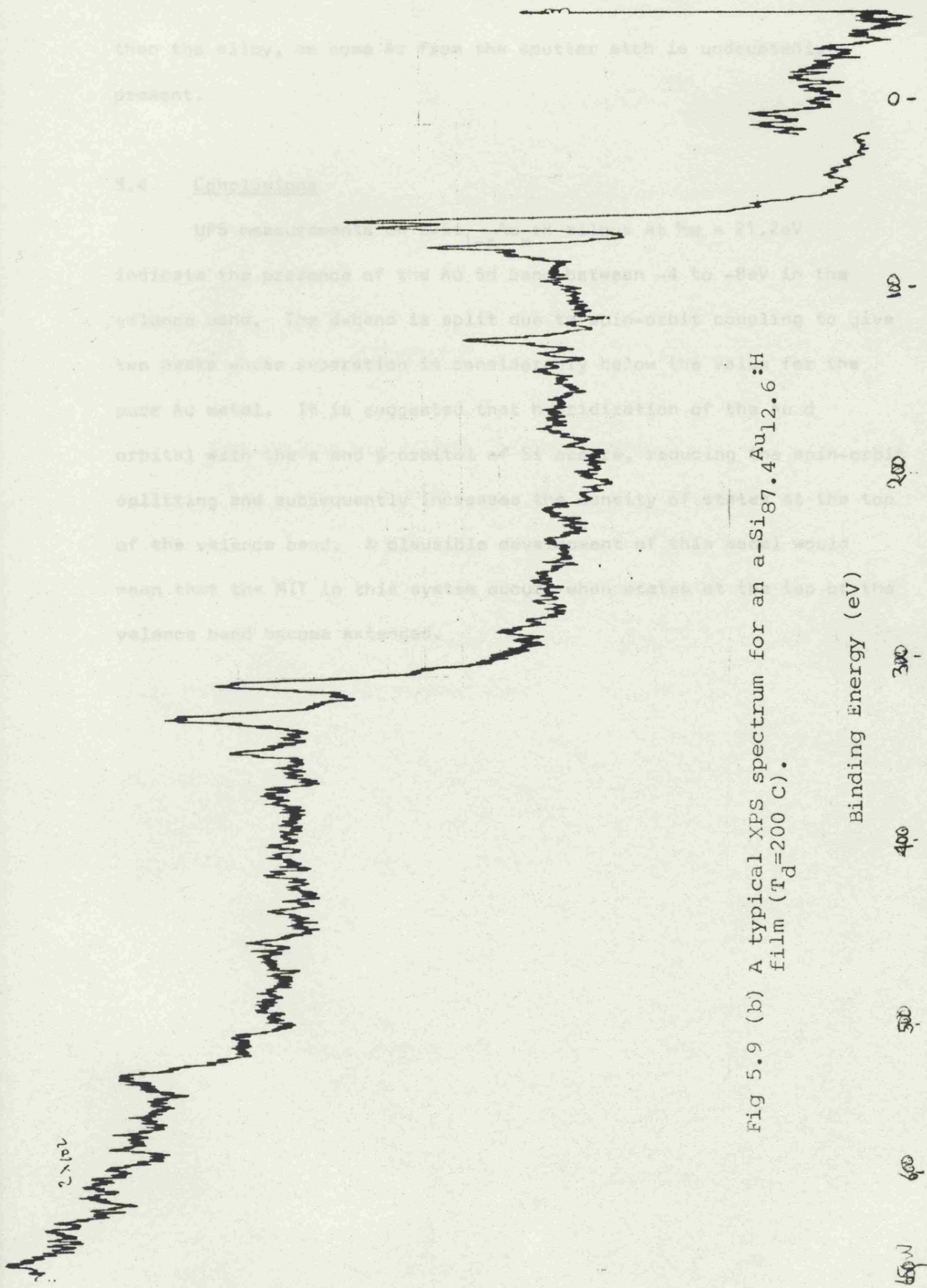


Fig 5.9 (b) A typical XPS spectrum for an a-Si<sub>87.4</sub>Au<sub>12.6</sub>:H film ( $T_d=200$  C).

than the alloy, as some Ar from the sputter etch is undoubtedly present.

#### 5.4 Conclusions

UPS measurements on a-Si<sub>1-x</sub>Au<sub>x</sub>:H alloys at  $\hbar\omega = 21.2\text{eV}$  indicate the presence of the Au 5d band between -4 to -8eV in the valence band. The d-band is split due to spin-orbit coupling to give two peaks whose separation is considerably below the value for the pure Au metal. It is suggested that hybridization of the Au d orbital with the s and p orbital of Si occurs, reducing the spin-orbit splitting and subsequently increases the density of states at the top of the valence band. A plausible development of this model would mean that the MIT in this system occurs when states at the top of the valence band become extended.

CHAPTER 6

Conclusions and suggestions for further  
work

6.1 Conclusions

6.2 Suggestions for further work

## 6.1 Conclusions

This dissertation describes the first detailed examination of the electronic, optical and structural properties of sputtered hydrogenated Si:Cu and Si:Cu alloys. As the preceding chapters contain conclusions relating to each of the two alloy series, the discussion in this section will be restricted predominantly to a comparison of the two systems.

Although Cu and Au both have full d-bands and a free s electron (see Table 6.1), the results of 4.2 and 4.3 indicate that Cu and Au behave differently when incorporated into the a-Si:H matrix. For similar deposition conditions it was shown, 4.2, that for the Si:Cu:H and Si:Cu systems with  $X_{\text{CS}} \gtrsim 1.1\%$  ( $\sim 3.5\%$ Cu) phase separation takes place with the alloy having the tendency to form a copper silicide with the precipitation of polycrystalline Cu. The Si:Au:H system proves to be more stable and alloys containing in excess of 17%Au can be formed, without any evidence of crystallinity as confirmed by TED. It is worth noting that the reduction of the spin-orbit splitting of the Au 5d band indicates that Au is not present in the Si host in the form of small clusters which would be difficult to detect by TED. The structural invariance, as detected by UPS and TEM, of a-Si:Au:H films deposited between 21 - 200°C indicates that the range of stable alloys that could be formed even at room temperature is likely to be extensive.

It is well documented that Cu is more reactive than Au in forming compounds, as expected from the higher ionization potential

TABLE 6.1

Element	Electronic Configuration	1st Ionization Potential (eV)
Cu	[Ar] 3d <sup>10</sup> 4s <sup>1</sup>	7.73
Ag	[Kr] 4d <sup>10</sup> 5s <sup>1</sup>	7.58
Au	[Xe] 4f <sup>14</sup> 5d <sup>10</sup> 6s <sup>1</sup>	9.23

for Au. This is supported by the existence of Cu in I, II, and III valence states whereas Au is predominantly found only in valence state III. Hence the existence of a large number of stable crystalline Si:Cu structures, as can be seen in the Si:Cu equilibrium phase diagram (fig. 4.15), as opposed to the equivalent phase diagram (see fig. 2.7) for the Si:Au system where crystalline compounds are formed only at, or very close to the eutectic composition. These results indicate that the Si:Cu system should be more likely to form a polycrystalline alloy or degrade from an amorphous state to a polycrystallite meta-stable state than the equivalent Si:Au alloy.

All Si:Cu alloys prepared in this work, with or without hydrogen present in the discharge, for  $X_{CS} \gtrsim 1.1\%$  proved to be inhomogeneous with phase separation occurring. The electronic and optical properties of these alloys were governed by this multi-component structure.

A comparison between the optical and electronic properties of low-Cu content a-Si:Cu and the equivalent compositional range for a-Si:Au indicates that, although the optical gaps,  $E_g$ , reduce in a similar manner for both systems (see fig. 4.14 and 4.33) the d.c. conductivity behaviour differs dramatically. The introduction of 0.26%Au to the a-Si:H host increases the room temperature dark conductivity,  $\sigma_{RT}$ , from  $\sim 2 \times 10^{-12}$  to  $4 \times 10^{-9} \Omega^{-1} \text{cm}^{-1}$ . For a comparable increase in  $\sigma_{RT}$  for the Si:Cu system  $\sim 1.8\%$  Cu ( $X_{CS} = 0.5\%$ ) is required.

In both cases the dominating conduction process at low temperatures is variable-range-hopping conduction at the Fermi level,  $E_F$ , which is situated near the centre of the mobility gap for the a-Si:Cu system and just above the top of the valence band for a-Si:Au:H. For the equivalent impurity element concentration the value of the variable-range-hopping parameter  $T_0$  for Cu is  $\sim 1.97 \times 10^6$  as opposed to  $\sim 5 \times 10^7$  for Au. By assuming a decay length for the wavefunctions,  $\alpha^{-1} \sim 10 \text{ \AA}^{-1}$  for both elements  $N(E_F)$  values of  $9.4 \times 10^{19} \text{ eV}^{-1} \text{ cm}^{-3}$  for Cu and  $3.7 \times 10^{18} \text{ eV}^{-1} \text{ cm}^{-3}$  for Au may be derived for an incorporated concentration  $X \sim 1.05\%$ . The discrepancy between  $N(E_F)$  for the addition of Cu or Au could possibly be explained by assuming  $\alpha_{\text{Au}}^{-1} \sim 2\alpha_{\text{Cu}}^{-1}$ . However, this would seem to be rather unlikely and it is more reasonable to accept that Cu atoms are more efficient at creating states in the mobility gap than Au, at least for low concentrations. This in turn must be related to the bonding configurations of the noble metal atoms in the two systems. As in the a-Si:Au: system for  $x \lesssim 6\% \text{ Au}$ , the Au atoms are predominantly incorporated in an interstitial manner it is suggested that the more reactive Cu atoms are primarily bonded substitutionally in the a-Si:H network.

## 6.2 Suggestions for further work

i) By sputtering Si:Cu alloys at reduced temperatures the compositional range of stable amorphous alloys should be enhanced. Subsequent examination of the electronic and optical properties of this alloy series in the neighbourhood of the M.I.T. could discover the nature of the transition in this system.

ii) A more detailed understanding of the a-Si:Au:H system could be achieved by extending the low-temperature range of d.c. conductivity measurements, particularly near the critical M.I.T. concentration of  $x = 14\%$

iii) As the hybridization of the Si s-p states with the d-states of Au has a significant effect on the optical and electronic properties of a-Si:Au:H, examination of the a-Si:Ag system, where the Ag 4-d band is deeper and narrower than the Au 5-d band, could prove to be useful in extending our understanding the behaviour of simple noble metals incorporated in semiconducting hosts.

## REFERENCES

1. S. R. Ovshinsky, Phys. Rev. Letts. 21 (1968) 1450
2. W. E. Spear and P. G. LeComber, Sol. State Commun., 17 1975  
1193
3. A. I. Andrievskii, I. D. Nabitovish and Ya. V. Voloshchuk, Sov.  
Phys. Crystallog. 5 (1960) 349
4. J. C. Knights and R. A. Lujan, Appl. Phys. Lett. 35 (1979) 244
5. D. A. Anderson, Phil. Mag. 35 (1977) 17
6. A. E. Owen, Contemp. Phys. 3 (1970) 227
7. N. F. Mott and E. A. Davis, Electronic Processes in Non-Crystalline  
Materials 1979 (Oxford: Clarendon Press)
8. A. Barna, P. B. Barna, G. Radnoczi, L. Toth and P. Thomas,  
Phys. Stat Sol. (a) 41 (1977) 81
9. E. A. Stern, Sci. Am. 234 (1976) 96
10. J. C. Knights, T. M. Hayes and J. C. Mikkelson Jr., Phys. Rev.  
Letts. 39 (1977) 712
11. M. L. Radee and A. Howie, Phil. Mag. 25 (1972) 1001
12. J. D. Bernal and J. Mason, Nature 188 (1960) 910
13. G. N. Greaves and E. A. Davis, Phil. Mag. 29 (1974) 1201
14. R. J. Bell and P. Dean, Phil. Mag. 25 (1972) 1381
15. J. C. Phillips, J. Non-Cryst. Sol. 34 (1979) 153

16. J. C. Phillips, *J. Non-Cryst. Sol.* 43 (1981) 37
17. G. Weiser, D. Ewald and M. Milleville, *Phil. Mag.* B40 (1979) 291
18. A. F. Ioffe and A. R. Regel, *Prog. Semicond.* 4 (1960) 137
19. P. W. Anderson, *Phys. Rev.* 109 (1958) 1492
20. J. T. Edwards and D. J. Thouless, *J. Phys. C.* 5 (1972) 807
21. A. I. Gubanov, *Quantum Electron Theory of Amorphous Conductors* 1963 (New York: Consultants Bureau)
22. N. F. Mott, *Adv. Phys.* 16 (1967) 49
23. M. H. Cohen, H. Fritzsche and S. R. Ovshinsky, *Phys. Rev. Lett.* 22 (1969) 1065
24. N. F. Mott, *Phil. Mag.* 26 (1972) 1015
25. E. A. Davis and N. F. Mott, *Phil. Mag.* 22 (1970) 903
26. P. Nagels, *Amorphous Semiconductors, Topics in Applied Physics*, Vol. 36, ed M. H. Brodsky 1979 (New York: Springer Verlag) 113
27. A. J. Grant and E. A. Davis, *Sol. Stat Commun.* 15 (1974) 565
28. P. N. Butcher, *Linear and Non-Linear Electron Transport in Solids*, eds. J. T. De Vreese and V. E. Van Doren 1976 (New York: Plenum Press)
29. A. Miller and S. Abrahams, *Phys. Rev.* 120 (1960) 745
30. N. F. Mott, M. Pepper, S. Pollitt, R. H. Wallis and C. J. Adkins, *Proc. R. Soc. a* 345 (1975) 169

31. H. Fritzsche, Sol. Stat. Commun. 9 (1971) 1813
32. M. Cutler and N. F. Mott, Phys. Rev. 181 (1969) 1336
33. I. P. Zvyagin, Phys. Stat. Sol. (b) 54 (1972) 733
34. H. Overhof, Phys. Stat. Sol. (b) 67 (1975) 709
35. T. F. Rosenbaum, R. F. Milligan, M. A. Paalanen, G. A. Thomas and R. N. Bhatt, Phys. Rev. B27 (1983) 7509
36. B. M. Dodson, W. L. McMillan, J. M. Mochel and R. C. Dynes, Phys. Rev. Lett. 46 (1981) 46
37. E. Abrahams, P. W. Anderson, D. C. Licciardello and T. W. Ramakrishnan, Phys. Rev. Lett 42 (1979) 693
38. W. Gotze, Sol. Stat. Commun. 27 (1978) 1393
39. N. F. Mott, Commun. on Physics 1 (1976) 203
40. H. R. Phillip and H. Ehrenreich, Phys. Rev. 129 (1963) 1550
41. T. M. Donovan, W. E. Spicer, J. M. Bennett and E. J. Ashley, Phys. Rev. B2 (1970) 397
42. A. Abraham, J. Tauc and B. Velicky, Phys. Stat. Sol. 3 (1963) 767
43. J. Tauc, Amorphous and Liquid Semiconductors (1974) (London Plenum Press) ed. J. Tauc
44. R. E. Smith, J. Non-Cryst. Sol. 8/10 (1972) 598
45. A. J. Lewis, G. A. N. Connell, W. Paul, J. R. Pawlik and R. J. Temkin Int. Conf. on Tetrahedrally Bonded Amorph. Semicond. A.I.P. Conf. Proc. 20 (1974) 27

46. M. H. Brodsky, M. Cardonna and J. J. Cuomo, Phys. Rev. B16 (1977) 3556
47. J. C. Knights and G. Lucovsky, CRC Critical Reviews in Sol. State and Met. Sci. (1980) 211
48. R. C. Chittick, J. Non-Cryst. Sol. 3 (1970) 255
49. E. A. Davis, J. Non-Cryst. Sol. 4 (1970) 107
50. F. Urbach, Phys. Rev. 92 (1953) 1324
51. D. L. Wood and J. Tauc, Phys. Rev. B5 (1972) 3144
52. J. D. Dow and D. Redfield, Phys. Rev. B5 (1972) 594
53. W. E. Spear, Proc. 5th Int. Conf. on Amorphous and Liquid Semiconductors, Garmisch-Partenkirchen (1973) 1
54. G. A. Connell, Amorphous Semiconductors Topics in Applied Physics Vol. 36 ed. M. H. Brodsky 1979 (New York: Springer-Verlag), 73
55. A. J. Lewis, Phys. Rev. B13 (1976) 2565
56. M. J. Thompson, M. Alkaisi and J. Allison, Rev. de Phys. Appl. 13 (1978) 625
57. W. Paul and D. A. Anderson, Sol. Energy Meter 5 (1981) 229
58. S. Iizima, H. Okushi, A. Matsuda, S. Yamasaki, K. Nakagawa, M. Matsumura and K. Tanaka, Proceed. 11th Conf. on Solid State Devices, Tokyo (1979) Jap. J. of Appl. Phys. 19 (1980) 521
59. M. Suzuki, T. Maekawa, Y. Koskimoto and T. Bandow, Proceed. 9th Int. Conf. on Amorphous and Liquid Semiconductors (1981) pt 2. C4 - 623

60. A. R. Mirza, A. J. Rhodes, J. Allison and M. J. Thompson,  
Proceed. 9th Int. Conf. on Amorphous and Liquid  
Semiconductors (1981) pt. 2. C4 - 659
61. P. D.'Antonio and J. H. Konnert, Phys. Rev. Lett 43 (1979) 1169
62. A. J. Leadbetter, A. A. M. Rashid, N. Colenutt, A. F. Wright and  
J. C. Knights, Sol. State Commun. 38 (1981) 957
63. R. Bellissent, A. Chenevas-Paule and M. R. Roth, Physica B & C  
117/118 (1983) pt. 2. 941
64. T. D. Moustakas and H. P. Maruska, Appl. Phys. Lett 43 (1983)  
1037
65. B. Von Roedern, L. Ley and M. Cardona, Phys. Rev. Lett 39  
(1980) 1576
66. W. Klement Jr., H. Williams and P. Duwez, Nature 187 (1960) 869
67. M. Von Allem, S. S. Lau, M. Maenpaa and B. Y. Tsaur, Appl. Phys.  
Lett. 36 (1980) 205
68. N. Kishimoto and K. Morigaki, J. of Phys. Soc. of Japan, 46  
(1979) 497
69. Ph Mangin, G. Marchal, C. Mournay and Chr Janot, Phys. Rev. B21  
(1980) 3047
70. J. J. Hauser and J. Tauc, Phys. Rev. B17 (1978) 3371
71. J. J. Hauser, Sol. State Commun. 34 (1980) 321
72. H. S. Chen and D. Turnbull, J. of Appl. Phys. 38 (1967) 3646
73. J. Dixmier and A. Guinier, Mem. Sci. Rev. Metall. LXIV (1967) 53

74. R. M. Waghorne, V. G. Rivlin and G. I. Williams, J. Phys. F. 6 (1976) 147
75. K. Morigaki, Phil. Mag. B42 (1980) 979
76. N. Nishida, M. Yamaguchi, T. Furubayashi, K. Morigaki, H. Ishimoto K. Ono, Sol. State Commun. 44 (1982) 305
77. B. Stritzker and H. Wuhl, Proceed. 12th Int. Conf. Low Temperatures, Kyoto (1970) 339
78. E. Hauser, J. Tauc and J. J. Hauser, Sol. State Commun. 32 (1979) 385
79. J. Macneil and E. A. Davis, Proceed. 10th Int. Conf. on Amorphous and Liquid Semiconductors (1983) pt. 1, 145
80. N. Kishimoto, K. Morigaki, K. Murakami, A. Shimizu and A. Hiraki Phys. State. Sol. (b) 80 (1977) K113
81. M. N. Brodsky and R. S. Title, Phys. Rev. Lett. 23 (1969) 581
82. N. Kishimoto, K. Morigaki, T. Sano, M. Iwami and A. Hiraki, Proceed. 7th Int. Conf. on Amorphous and Liquid Semiconductors (1977) 490
83. T. Sano, M. Iwami, A. Hiraki and K. Morigaki, Sol. State Commun. 23 (1977) 971
84. E. Hauser, R. J. Zirke, J. Tauc, J. J. Hauser and S. R. Nagel, Phys. Rev. Lett. 40 (1978) 1733
85. M. L. Theye, Phys. Rev. B2 (1970) 3060
86. B. Moraghar and L. Schweitzer, Phys. State Sol. (b) 30 (1977) 491
87. B. G. Bagley and F. J. De Salva, Bull. Am. Phys. Soc. 21 (1976) 385

88. A. Hiraki, A. Shimizu, M. Iwami, T. Narusawa and S. Komuja  
Appl. Phys. Lett. 26 (1975) 57
89. H. Suto and H. Ishikawa, Trans. Japn Inst. Met. 17 (1976) 596
90. T. Shimizu, M. Kumeda, I. Watanabe and Y. Noumi, J. Non-Cryst.  
Sol. 35/36 (1980) 645
91. T. Shimizu, M. Kumeda, I. Watanabe and K. Kamono, Sol. State  
Commun. 26 (1978) 445
92. G. Marchal, Ph Mangin and Chr. Janot, Sol. State Comm. 18 (1976)  
739
93. J. Abzamir and M. M. Collver, Sol. State Commun. 30 (1979) 425
94. G. Hertel, D. J. Bishop, E. G. Spencer, J. M. Rowell and R. C.  
Dynes, Phys. Rev. Lett. 50 (1983) 743
95. A. S. Edelstein, S. R. Ovshinsky, E. Sadate-Akhavi and J. Wood,  
Sol. State Commun. 41 (1982) 139
96. S. Herd, K. N. Tu and K. Y. Ahn, Appl. Phys. Lett. 42 (1983) 597
97. P. Mrafko and P. Duhaj, Phys. State Sol. (a) 22 (1974) 151
98. M. Von Allmen, S. S. Lau, M. Maenpaa and B. Y. Tsaur, Appl. Phys.  
Lett. 37 (1980) 84
99. T. Tien, G. Ottaviani and K. N. Tu, J. Appl. Phys. 54 (1983) 7047
100. J. H. Keller and R. G. Simmons, I.B.M. J. Res. Develop 23 (1979) 24
101. J. Tardy and R. Meaudre, Phil. Mag. B48 (1983) 571
102. M. Tanielian, M. Chatani, H. Fritzsche, V. Smid and P. D. Persans,  
J. Non-Cryst. Sol. 35/36 (1980) 575

103. R. H. Klazes, M. H. L. M. van den Broek, J. Bezemer and S. Radelaar  
Phil. Mag. B45 (1982) 377
104. W. Paul, G. A. N. Connell and R. J. Temkin, Advan. Phys. 22  
(1973) 529
105. R. A. Street and J. C. Knights, Phil. Mag. B43 (1981) 1091
106. P. John, I. M. Odeh, M. J. K. Thomas, M. J. Tricker, J. I. B. Wilson,  
J. B. A. England and D. Newton, J. Phyc. C. 14 (1981) 309
107. R. A. Street, Proceed. 9th Int. Conf. on Amorphous and Liquid  
Semiconductors (1981) pt. 1 C4 - 283
108. L. I. Maissel and R. Glang, Handbook of Thin Film Technology, 1970  
(New York: McGraw-Hill) 4-40
109. B. Abeles, P. Cheng, M. D. Coults and Y. Arie, Adv. Phys. 24  
(1975) 407
110. K. L. Chopra, P. Nath and A. C. Rastogi, Phys. State Sol. (a)  
27 (1975) 645
111. P. Nath, D. K. Pandya and K. L. Chopra, Phys. State Sol. (a)  
34 (1976) 405
112. M. Zavetova, S. Koc and J. Kenek, Recent Advances in Science and  
Technology of Materials, Ed. A. Bishay, Vol. 1 Plenum Press:  
New York (1974) 285
113. D. L. Williamson, R. C. Kerns and S. K. Deb, J. Appl. Phys. 55  
(1981) 2816
114. D. I. Jones, W. E. Spear and P. G. LeComber, J. Non-Cryst. Sol.  
20 (1976) 259
115. N. Nishida, M. Yamaguchi, T. Fumbayashi, K. Morigaki, H. Ishimoto  
and K. Ono, Tech Report ISSP Ser. A No. 1222 (1982)

116. E. C. Freeman and W. Paul, Phys. Rev. B20 (1979) 716
117. E. Huber and M. Von Allmen, Phys. Rev. B28 (1983) 2979
118. M. Gandais, M. L. Theye, S. Fissons and J. Boissonade, Phys. State Sol. (b) 58 (1973) 601
119. S. C. Moss and J. F. Graczyk, Phys. Rev. Lett. 23 (1969) 1167
120. T. D. Mostakas, J. Elect. Mat. 8 (1979) 391
121. T. M. Donovan, Phys. Rev. Lett. 27 (1971) 1794
122. C. N. Berglung and W. E. Spicer, Phys. Rev. A 136 (1964) 1030
123. M. K. Gardiner, PhD Thesis, (1984) University of Leicester
124. B. Von Roedern, L. Ley, M. Cardona and F. W. Smith, Phil. Mag. B40(1979) 433
125. R. J. Smith and M. Strongin, Phys. Rev. B24 (1981) 5863
126. L. Ley, H. Richter, R. Karcher, R. L. Johnson and J. Reichardt, Proceed. 9th Int. Conf. on Amorphous and Liquid Semiconductors (1981) pt. 2. C4 - 753
127. W. J. Ching, D. J. Lam and C.C. Lin, Phys. Rev. Lett. 42 (1979) 805
128. O. Bisi, C. Calandra, L. Bracovich, I. Abbati, G. Rossi, I. Lindau and W. E. Spicer, J. Phys. C. 15 (1982) 4707
129. J. Fukushima, K. Tamura, H. Endo, K. Kishi, S. Ikeda, S. Minomura J. de Phys. 35 (1974) C4 - 261
130. M. Hansen and K. Anderko. Constitution of Binary Alloys, 2nd Edn. 1958 (New York: McGraw-Hill)

## APPENDIX

## ABBREVIATIONS

a	amorphous
ev	evaporated
g	glassy
l	liquid
sp	sputtered
AES	auger electron spectroscopy
BFI	bright-field imaging
CFO	Cohen, Fritzsche and Ovshinsky
CRN	continuous random network
DB	dangling bond(s)
EBMA	electron beam microanalysis
EM	electron microscopy
ESCA	electron spectroscopy for chemical analysers
EXAFS	extended x-ray absorption fine structure
FZ	floated zone
LMQ	laser induced melting, mixing and quenching
LRO	long range order
MIT	metal-insulator transition
NNH	nearest neighbour hopping
PE	photoemission
RDF	radial distribution function
SAED	selected area electron diffraction
SANS	small angle neutron scattering
SEM	scanning electron microscopy
SRO	short range order
TCR	temperature coefficient of resistance
TED	transmission electron diffraction
TEM	transmission electron microscopy
UPS	ultra-violet photoelectron spectroscopy
VRH	variable range hopping
XPS	X-ray induced photoemission spectroscopy